

AFOSR-TR- 83 0078

AD-A261 703



Approved for public release;  
Distribution Unlimited

DISTRIBUTION STATEMENT A  
Approved for public release  
Distribution Unlimited

DTIC  
ELECTE  
MAR 05 1993  
S B D

Washington  
State University

DEPARTMENT OF PHYSICS

**AIR FORCE OFFICE OF SCIENTIFIC RESEARCH**  
**Contract F49620-91-C-0093**

**Annual Report**  
**January, 1993**

---

**DEFECT INITIATION/GROWTH AND ENERGY DISSIPATION**  
**INDUCED BY DEFORMATION AND FRACTURE**

**J. Thomas Dickinson**  
**Washington State University**

**Department of Physics and**  
**Materials Science Program**  
**Pullman, WA 99164-2814**

**Reproduction in whole or part is permitted for any purpose of the United States Government.**

**Approved for public release; distribution unlimited.**

**93-04637**



313p8

98

3

4

013

REPORT DOCUMENTATION PAGE

Form Approved  
OMB No. 0704-0188

1a. REPORT SECURITY CLASSIFICATION UNCLASSIFIED			1b. RESTRICTIVE MARKINGS		
2a. SECURITY CLASSIFICATION AUTHORITY			3. DISTRIBUTION / AVAILABILITY OF REPORT  APPROVED FOR PUBLIC RELEASE DISTRIBUTION UNLIMITED		
2b. DECLASSIFICATION / DOWNGRADING SCHEDULE					
4. PERFORMING ORGANIZATION REPORT NUMBER(S)  FRACTO1992			5. MONITORING ORGANIZATION REPORT NUMBER(S)		
6a. NAME OF PERFORMING ORGANIZATION		6b. OFFICE SYMBOL (if applicable)	7a. NAME OF MONITORING ORGANIZATION  AIR FORCE OFFICE SCIENTIFIC RESEARCH DIRECTORATE OF AEROSPACE SCIENCES		
6c. ADDRESS (City, State, and ZIP Code)  WASHINGTON STATE UNIVERSITY PULLMAN, WA 99164-2814			7b. ADDRESS (City, State, and ZIP Code)  AFOSR/NA BLDG 410 BOLLING AFB DC 20332-6448		
8a. NAME OF FUNDING / SPONSORING ORGANIZATION  AFOSR		8b. OFFICE SYMBOL (if applicable)  NA	9. PROCUREMENT INSTRUMENT IDENTIFICATION NUMBER  F41650-91-C-0093		
8c. ADDRESS (City, State, and ZIP Code)  AFOSR/NA Bolling AFB DC 20332-6448			10. SOURCE OF FUNDING NUMBERS		
			PROGRAM ELEMENT NO. 61105F	PROJECT NO. 302	TASK NO. AS
			WORK UNIT ACCESSION NO.		
11. TITLE (Include Security Classification)  DEFECT INITIATION/GROWTH AND ENERGY DISSIPATION INDUCED BY DEFORMATION AND FRACTURE					
12. PERSONAL AUTHOR(S)  J. THOMAS DICKINSON					
13a. TYPE OF REPORT  ANNUAL TECHNICAL		13b. TIME COVERED FROM 6/15/91 TO 12/14/92		14. DATE OF REPORT (Year, Month, Day)  JAN 14, 1992	
15. PAGE COUNT  290					
16. SUPPLEMENTARY NOTATION					
17. COSATI CODES			18. SUBJECT TERMS (Continue on reverse if necessary and identify by block number)		
FIELD	GROUP	SUB-GROUP	DEFORMATION, CRACK PROPAGATION, FRACTURE, PARTICLE EMISSION, FRACTO- EMISSION INTERFACIAL FAILURE, CRAZING, ELECTRICAL TRANSIENTS, MICROCRACKING, SURFACE CHARGE, FRACTOGRAPHY, CRYSTAL DEFECTS, SCANNING TUNNELING MICROSCOPY, PHOTOLUMINESCENCE.		
19. ABSTRACT (Continue on reverse if necessary and identify by block number)					
<p>Based on our capabilities to a) detect and characterize particle release from surfaces on fast time scales, b) to measure rapid electrical transients, and c) to obtain high resolution topographical information utilizing scanning tunneling and atomic force microscopy, we present new results on the time sequence of events leading up to defect initiation and growth which ultimately leads to fracture. We employ dynamic methods as well as post-fracture examination in polymers, ceramics, metals, and interfaces. We emphasize mechanisms, with interpretation and connections between these results and the creation and evolution of defects in materials under mechanical stress. In many cases, the information we are acquiring has important implications concerning dissipation of energy (e.g., plastic deformation, microcracking, crack branching, and crack deflection) which play critical roles in controlling the strength and toughness of materials.</p>					
20. DISTRIBUTION / AVAILABILITY OF ABSTRACT <input checked="" type="checkbox"/> UNCLASSIFIED/UNLIMITED <input type="checkbox"/> SAME AS RPT. <input checked="" type="checkbox"/> DTIC USERS			21. ABSTRACT SECURITY CLASSIFICATION  UNCLASSIFIED		
22a. NAME OF RESPONSIBLE INDIVIDUAL  W. F. Jones			22b. TELEPHONE (Include Area Code)  202 767-0470		22c. OFFICE SYMBOL

# TABLE OF CONTENTS

	page
I. TECHNICAL SUMMARY	1
II. INTRODUCTION	2
III. MOLECULAR EMISSION DUE TO BOND SCISSIONS IN POLYMERS	4
IV. ELECTRON AND PHOTON EMISSION FROM POLYCARBONATE	17
V. ELECTRON AND PHOTON EMISSION FROM POLYETHYLENE	58
VI. TRANSPORT AND RECOMBINATION ON FRACTAL LATTICES	85
VII. VOLATILE EMISSION DUE TO CRAZING IN POLYSTYRENE	116
VIII. ELECTRICAL TRANSIENTS GENERATED BY ADHESIVE PEEL	141
IX. STM OBSERVATIONS OF METALLIC GLASS FRACTURE SURFACES	177
X. XENON EMISSION FROM Xe-IMPLANTED ZIRCONIA	222
XI. WORK IN PROGRESS	246

CONTENTS

<b>Accession For</b>	
NTIS GRA&I	<input checked="" type="checkbox"/>
DTIC TAB	<input type="checkbox"/>
Unannounced	<input type="checkbox"/>
Justification	
By	
Distribution/	
Availability Codes	
Dist	Avail and/or Special
A-1	



## **I. TECHNICAL SUMMARY**

During the deformation of materials, a sequence of events occurs which results from stress being applied to the inherent microstructure and flaw distributions in all materials. Eventually, these events culminate in catastrophic damage or failure. We have been probing this time sequence of events using dynamic methods as well as post-fracture examination in polymers, ceramics, metals, and interfaces. These probes include time-resolved measurements of particle emission (fracto-emission), electrical transients during interfacial failure, and the use of scanning tunneling microscopy of fracture surfaces. We present new results in these areas with emphasis on mechanisms and interpretation and connections between these results and the creation and evolution of defects in materials under mechanical stress. In many cases, the information we are acquiring has important implications concerning dissipation of energy (e.g., plastic deformation, microcracking, crack branching, and crack deflection) which play critical roles in controlling the strength and toughness of materials.

## II. INTRODUCTION

What follows is a short summary and significance of the work to be described.

**III. Molecular Emission Due to Bond Scissions in Polymer Fracture.** In Section III we present the results of a simple but carefully executed experiment involving detection of molecular CO from the fracture of polycarbonate. Through elimination of artifacts we show that chain cleavage is the source of this emission and provides a way to "count" such events. This work will appear in J. Materials Research.

**IV. Electron and Photon Emission from Polycarbonate.** In section IV we discuss the electron and photon emission from the deformation and fracture of polycarbonate. We observe emissions during the onset of neck formation (very carefully established to be real) and intense emission during fracture itself. These signals are attributed to bond breaking induced excitations relaxing via radiative/non-radiative recombination events. A novel method of monitoring deformation and fracture by passing a light beam through the gauge of the sample was devised. These measurements allow accurate correlations of defect growth and emission to be measured. This method also permits a determination of instantaneous crack velocity which allowed us to determine a threshold crack speed for the onset of detectable electron emission ( $\sim 5$  m/s). A model is proposed for the sequence of events causing the emission. This manuscript has been submitted to J. Polym. Sci. B: Polym. Phys. Ed.

**V. Electron and Positive Ion Emission from High Density Polyethylene.** In Section V we present a careful investigation of pre-fracture emission from deformation of high density polyethylene (HDPE). Previous workers have indicated that electron emission during deformation in HDPE was due to bond breaking. Our work shows that for HDPE, this is not the case. Instead, we show that tribological loading with metals (e.g., stainless steel) produce signals entirely like those observed earlier. We show the importance of an intimate metal/polymer contact (producing contact electrification), followed by mechanically induced separation of charge and subsequent dynamic stimulation of the polymer surface due to energetic charge motion (surface flashover). This manuscript has been submitted to J. Appl. Phys.

**VI. Transport + Recombination Kinetics on a Fractal Network.** Section VI deals with an investigation of the rather surprising behavior of the "tails" in the emission from fracture seen for several materials, namely emissions that continue for  $10^2 - 10^3$  s after fracture. The shape of these curves relate to the manner in which the material is excited during fracture as well as the subsequent transport and recombination processes yielding the emission. We show that we obtain very good fits to the observed decay data by the use of a bimolecular recombination model occurring on a fractal lattice. The result of the curve fitting is a fractal dimension of the recombination path which is related directly to the dimension of the lattice. This manuscript has been submitted to J. Materials Research.

**VII. Ar Atom Emission to Characterize Craze Formation and Growth in Polystyrene.** Section VII discusses the study of crazing during deformation of polystyrene (PS) and high impact polystyrene (HIPS) using an emission signal. We preloaded the samples in Ar by soaking them in an atmosphere of Ar until the samples were saturated. Upon deformation in a vacuum system, a mass spectrometer could easily detect the formation, growth, and ultimate linking of crazes. We designed an optical technique to also monitor this process and showed excellent correlation in their rates, *provided* the crazes intersect the free surface. We show that the emission of such a volatile species reflects the growth of crazes that intersect the surface, as well as changes in the connectivity of the craze network. This manuscript has been submitted to J. Polym. Sci. B: Polym. Phys. Ed.

**VIII. Electrical Transients Generated During Adhesive Failure.** Using common 3M Magic Tape on a clean Cu substrate we have developed a new technique for examining the micromechanical events that accompany peeling of a pressure sensitive adhesive. The method used was to measure the current generated by the detachment process, a consequence of the contact charging established during and after the time of adhesive bond formation. A model for the current generation is presented and shown to qualitatively be correct. We explored in time events which ranged from 0 to 200 Hz and which corresponded to structures at the peel zone down to  $\sim 10 \mu\text{m}$  in size. These electrical measurements are a potentially new way to obtain in a time resolved fashion insight into the micromechanical processes accompanying peeling on even smaller size and faster time scales. This is Part I of a two part paper; Part II deals exclusively with fluctuations and is still in preparation. These papers will be submitted to an adhesion journal.

**IX. Scanning Tunneling Microscope Observations of Metallic Glass Fracture.** The work presented in section IX deals with the fundamental question of the fracture behavior of metallic glasses and the role of plasticity in amorphous metals. We observe on size scales of  $\sim 10\text{-}100 \text{ nm}$  a number of features which indicate considerable plasticity, including slip band formation, fingering in the crack front, and evidence of shear deformation.

**X. Xenon Emission from Zirconia.** In this section we present measurements of the emission of atomic Xe from Xe-implanted cubic zirconia which has been shown in previous studies to have increased hardness. The Xe is embedded within a 50 nm range of the surface in the form of solid and fluid inclusions. We put this surface into tension by three-point flexure loading until fracture. The resulting emissions are very intense and were correlated with extensive lateral cracking in the region of the Xe implantation layer.

**XI. Work in Progress.** Projects currently under way include: the emission of occluded volatiles during deformation of polycarbonate, the emission of occluded volatiles during the fracture of polystyrene and their relation to the temperature of the fracture surface, measurements of electrical signals accompanying interfacial failure of metal-oxide structure, chemi-emission of electrons from titanium metal as a probe of inelastic deformation processes, and the imaging of point defect clusters generated by plastic deformation in MgO single crystals.

### **III. Molecular CO emission accompanying fracture of polycarbonate: evidence for chain cleavage**

J. T. Dickinson, L. C. Jensen, S. C. Langford

*Physics Department, Washington State University, Pullman, WA 99164-2814 USA*

R. P. Dion

*The Dow Chemical Company, Designed Thermoplastics Research, Midland, MI 48667 USA*

L. Nick

*Institute of Physical Chemistry, Technical University of Clausthal,*

*D-W-3392 Clausthal-Zellerfeld, Germany*

#### **Abstract**

When polycarbonate is loaded in tension at room temperature to failure, a certain percentage of the chains are believed to undergo cleavage due to the constraints of entanglements. We present direct evidence that accompanying fracture of polycarbonate, CO molecules are released due to bond scissions.

(Received:

**Keywords:** polymer fracture, fracto-emission, neutral emission, mass spectroscopy

The fracture of high molecular weight glassy polymers is believed to involve the rupture of polymer chains anchored on either side of the crack tip by geometrical entanglements. However, little direct experimental evidence exists for this chain rupture in bulk samples, due to the relatively small number of chains broken in well controlled fracture events.<sup>1,2</sup> Brown, Deline, and Green have used surface analysis techniques on the fracture surfaces of specially designed block copolymers to provide evidence for polymer chain cleavage.<sup>3</sup> An alternate strategy is to observe the dynamic evolution of low molecular weight fragments produced by the cleavage of polymer chains in vacuum. However, quantitative measurements of species due to bond-breaking have been troubled by interference from the emission of volatiles entrained during sample manufacture and storage, including products of incomplete polymerization.<sup>4,5</sup> Significant concentrations of occluded volatiles can remain in bulk samples even after days under high vacuum conditions. However, the development of sensitive quadrupole mass filters allows the use of self supporting thin films, which can be efficiently degassed under high vacuum. Furthermore, the polymerization of polycarbonate can be very complete, leaving negligible amounts of low molecular weight polymerization products. We report here molecular emissions accompanying the fracture of polycarbonate thin films which we attribute to the rupture of polymer chains. Fracture of the polycarbonate chain yields the distinctive molecule CO; in samples free from entrained N<sub>2</sub>, CO is readily distinguished from typical contaminants. For comparison purposes, we also present measurements of the corresponding emissions from bulk polycarbonate samples, which contain significant amounts of occluded N<sub>2</sub>.

The polycarbonate used in this work was Calibre® 300-10 provided by The Dow Chemical Company. Thin (50-75  $\mu\text{m}$ ) films of polycarbonate were cast from methylene chloride solution. Care was taken to avoid the incorporation of dust particles, which serve as stress concentrators and lead to premature failure. The films were baked at 100 °C for 12 hours to remove the residual solvent, and cooled over a two hour period. Slower cooling yielded brittle films with higher yield stresses<sup>6</sup> which often failed in a tearing, slow crack growth mode; low emission intensities resulted

from this slow crack growth. Dogbone samples with a gauge width of about 5 mm were cut from the cast films with scissors.

Thicker polycarbonate samples were milled into dogbones from 3.2 mm injection molded test specimens. The gauge section of these samples was 1.5 cm long and  $3.2 \times 3.2 \text{ mm}^2$  in cross section. The room temperature diffusivity of  $\text{CO}_2$  in polycarbonate is about  $5 \times 10^{-9} \text{ cm}^2/\text{s}$ ,<sup>7</sup> which corresponds to a  $1/e$  time for the pump out of occluded  $\text{CO}_2$  from these 3.2 mm-thick samples of about 25 days. The  $1/e$  time for the pumpout of volatiles is proportional to the square of the material thickness, so that the corresponding decay constant for the pumpout of films with thickness  $\sim 80 \text{ }\mu\text{m}$  is on the order of ten minutes. Although the diffusivity of CO in polycarbonate was not found, comparisons of CO and  $\text{CO}_2$  diffusion constants for other polymers suggest that the diffusion constants for these two gases are similar.<sup>8</sup> Thus we expect the pump-out of CO to be similar to that of  $\text{CO}_2$ .

The samples were mounted in a tensile loading apparatus in an ultrahigh vacuum system and kept under vacuum for typically 24 hours prior to testing. Some films were given additional heating and exposed to vacuum for several days. With or without heating, the 24 hr exposure to vacuum was sufficient for thorough removal of CO from the thin film samples. The background pressure at the time of the experiment was typically  $10^{-6} \text{ Pa}$ . The neutral emission was monitored with a UTI 100C quadrupole mass spectrometer (QMS), where the front of the electron impact ionizer mounted about 5 mm from the gauge section of the sample. The applied load was monitored with a Scaime force transducer with a 90 N adapter for the thin film samples and a 4500 N adapter for the bulk samples. Deformation was introduced from the outside of the vacuum through a stainless steel bellows.

The 3.2 mm thick dogbone samples yielded intense emission at mass 28, but much of this emission could be attributed to occluded  $\text{N}_2$ . The mass 28 signal and applied load from a 3.2 mm thick sample are shown in Fig. 1. This sample was kept under vacuum for about 24 hours prior to testing. Strong emission at mass 28 is noted at the onset of yield and later at fracture. The signal at mass 28 also increases significantly during cold drawing. As the time under vacuum is

insufficient to remove occluded  $N_2$  and  $CO_2$ , these gases may contribute substantially to the signal at mass 28. An estimate of their contribution may be made by comparing the signal at mass 28 to the signals at mass 14 and 44.  $N_2$  characteristically produces peaks at masses 14 and 28 in the ratio of 1:10 in our instrument, due to the production of  $N^+$  in the ionizer. Similarly,  $CO_2$  characteristically yields signals at mass 44 and 28 in the ratio of 10:1. The observed ratio of mass 44 to mass 28 is about 1:2, indicating that the contribution of  $CO_2$  to the mass 28 signal is no more than about 5%. Similarly, the ratio of mass 14 to mass 28 is about 1:20, indicating that perhaps 50% of the mass 28 signal is due to  $N_2$ . Due to sample to sample variation in the fracture/emission process, the uncertainty in the observed ratios is rather large. We may therefore conclude that although a significant portion of the observed signal at mass 28 is due to occluded  $N_2$ , a major share of mass 28 signal (~45%) from bulk polycarbonate is due to the emission of CO. Nevertheless, the *origin* of the CO (occluded vs. bond breaking) is not clearly determined from fracture of thick samples.

Although occluded gases are difficult to remove from the 3.2 mm thick samples, time exposed to vacuum does affect their concentration significantly. This was especially evident in the emissions at yield, which depend on the concentration of occluded gases in the near-surface region of the specimen. Near the surface, removal by diffusion to the surface and subsequent desorption is especially efficient and confirmed by significant reductions in the deformation induced emissions for long pumping times. This supports our conclusion that occluded gases can be efficiently removed from thin films where at most the surface is only a few tens of microns from the center of the sample. This was confirmed by fracture measurements at mass 18 ( $H_2O$ ) on cast films [this is the most intense signal accompanying the fracture of bulk polycarbonate]. Thin film fracture yielded no detectable signal due to absorbed water. Similar tests at mass 14 ( $N^+$  from  $N_2$ ) and mass 32 ( $O_2$ ) also showed no emissions. Thus we are confident that the concentration of occluded gases in the thin films is negligible after pumping for several hours.

While the contribution of occluded gases to emissions from thin films can be negligible, contributions from external sources must be carefully distinguished due to the low signal intensities

involved. CO is readily desorbed from moving metal parts, especially the metal bellows in the loading apparatus. The contribution of moving metal parts to the observed signal was determined by tensile testing metal wires (free of CO) with strengths similar to that of the thin films. During loading, small emissions are observed which were due to the motion of the bellows; in addition, a small, broad peak is observed somewhat after fracture. However, no increase in emission is observed at fracture. Thus any burst in emission at mass 28 accompanying the fracture of polycarbonate films can be confidently attributed to the sample and not to the sudden motion of metal parts.

Typical mass 28 emissions during loading and fracture of a thin film are shown in Fig. 2. The timing of the onset of loading, necking and fracture were determined to within 30 ms from simultaneous videotaped observations. The small increase in the background following the onset of drawing and the slow peak observed immediately after fracture are consistent with emission due to the motion of the bellows. However, the sharp burst at fracture is entirely due to the fracture of the film itself. This burst is shown on an expanded time scale in Fig. 2(b). All samples exhibiting fast fracture yielded such CO bursts. Flawed samples (usually due to an incorporated dust particle) exhibited slow crack growth at low elongations with little necking or yielding. These specimens emitted negligible mass 28 signal at fracture; i.e., the low number of CO molecules emitted per unit time during slow crack growth in these samples could not be distinguished from the background. Fast fracture may yield more CO due to a higher bond scission probability (due to fewer disentanglements) and, of course, a shorter duration of fracture causes a higher rate of emission. (The sensitivity of an electron bombardment ionizer is proportional to the *density* of gas in the ionizer at a given instant).

CO<sub>2</sub> emissions (mass 44) were very small and difficult to distinguish from artifacts even for fast fracture. Given the signal-to-noise ratio of our detection system and the size of the mass 44 artifacts, we estimate that the ratio of CO<sub>2</sub>/CO is  $\leq 1/15$ .



An order of magnitude estimate of the number of emitted CO molecules accompanying fast fracture,  $N_{CO}$ , can be deduced from the area of the peak (the detected charge),  $Q_{detected}$ , which we estimate to be 10 pC in Fig. 2.

$$N_{CO} \sim \frac{Q_{detected}}{S \tau \eta_{geom}}, \quad (1)$$

where  $S$  is the quadrupole detection efficiency measured at mass 28,  $\tau$  is the average time required for a CO molecule to pass through the ionizer, and  $\eta_{geom}$  is the geometric collection efficiency of the ionizer, accounting for the solid angle it subtends as viewed from the sample. The quadrupole sensitivity at mass 28 was estimated by filling the chamber with a known pressure of  $N_2$  while monitoring the quadrupole signal. With  $S \sim 0.3$  A/torr  $\sim 6 \times 10^{-18}$  A/molecule (i.e. amps per molecule inside the quadrupole ionizer),  $\tau \sim 54$   $\mu$ s (assuming thermal velocities at 300 K), and  $\eta_{geom} \sim 0.028$ ,  $N_{CO} \sim 1.1 \times 10^{12}$  molecules. This corresponds to  $4 \times 10^{14}$  molecules/cm<sup>2</sup> of nominal fracture surface area.

One envisions highly strained, thermally stimulated chains breaking at a C-O bond adjacent to the carbonyl radical as shown in Fig. 3. This bond is a weak bond in the polycarbonate structure,<sup>9</sup> so it is reasonable to expect the polymer chain to cleave at this point. This bond scission could result in non-adiabatic relaxation of the strain energy in the chain ends, producing a phenoxy end radical remaining attached to the chain end and a free carbon monoxide molecule. Electron transfer during the bond scission could well favor CO release. In the simplest scenario, one CO molecule is produced for each chain scission. A similar reaction could produce CO<sub>2</sub> and a phenyl end radical. Both products are observed during thermal- and photo-decomposition of polycarbonate. CO<sub>2</sub> and CO are also produced in  $\gamma$ -irradiated polycarbonate in the ratio of about 1:5.<sup>10</sup> At this point, our measurements indicate a much smaller ratio; CO is by far the principle product observed from mechanical bond breaking.

An estimate of the number of broken bonds expected in the case of fracture may be made on the basis of the entanglement density and average distance between entanglements in

polycarbonate, where we assume that no disentanglements occur. Geometrical considerations require that a minimum of  $(\rho\delta/2)$  entanglements per unit area be destroyed in the formation of the fracture surface, where  $\rho$  is the entanglement density and  $\delta$  is the mean distance between entanglements. From the data of Donald and Kramer<sup>11</sup> ( $\rho \sim 2.0 \times 10^{20}$  entanglements/cm<sup>3</sup>,  $\delta \sim 4.4$  nm), we estimate that a minimum of  $6 \times 10^{13}$  chains/cm<sup>2</sup> must be broken to form a fracture surface with an area equal to the cross section of the thin film. Thus the estimated number of CO molecules is roughly an order of magnitude higher than the number of broken chains required for the formation of a planar fracture surface.

The large number of broken bonds is consistent with computer models of fracture in disordered media. Given sufficient disorder, the number of broken bonds in a two dimensional system tends to scale as  $L^{1.7}$ , where  $L$  is the system size.<sup>12</sup> This is well in excess of the number of bonds required to form a linear (in two dimensions) fracture surface, which scales as  $L^{1.0}$ . Despite the experimental uncertainties involved, the data above are consistent with excess broken bonds, which would constitute an extended damage zone in the near-surface region of both fracture surfaces.

As noted above, the mass 28 signals due to chain cleavage during the fracture of thick (cross section  $3.2 \times 3.2$  mm<sup>2</sup>) polycarbonate are obscured by signals due to occluded gases. Although these signals are sources of interference in the present work, their intensities during deformation can be shown to reflect changes in diffusivity of the gas through polymer. Currently, we are studying the processes responsible for the changing diffusivity by intentionally introducing gases such as Ar and D<sub>2</sub>O and monitoring the resulting emissions intensities during deformation of polycarbonate.

In this work, the CO emission accompanying the fracture of *thin film* polycarbonate is direct evidence for bond cleavage during fracture. The lack of detectable CO<sub>2</sub> emission suggests a *favorable dissociation route* accompanying fracture. The number of broken bonds implied by CO emission from the thin films is of the same order of magnitude as the number geometrically required for the formation of the fracture surface, but perhaps as much as a factor of ten higher.

The number of broken bonds detected by this method ( $1 \times 10^{12}$ ) is well below the sensitivity of present ESR techniques and has the advantage of being relatively insensitive to radical reactions subsequent to fracture. This allows measurements at room temperature and higher, which are inaccessible to present ESR methods. Its applicability to other polymers depends on the existence and emission of suitable fragments and the ability to cast suitable films. For some polymers, such as polystyrene and poly(methyl methacrylate), one may have to account for possible unzipping reactions initiated by radicals formed during the fracture process. We anticipate that time resolved acquisition of these emissions could provide insight into such post-fracture events. With further development and careful sample preparation, the use of time-resolved mass spectroscopy has significant potential as a quantitative measure of bond breaking during fracture.

We wish to acknowledge support for this work from Dow Chemical Co., the Air Force Office of Scientific Research through Contract AFOSR-F49620-91-C-0093, and the Washington Technology Center.

## REFERENCES

1. H. H. Kausch, *Polymer Fracture*, 2nd Edition (Springer Verlag, Berlin, 1987).
2. E. H. Andrews and P. E. Reed, in *Failure in Polymers: Molecular and Phenomenological Aspects*, (Springer Verlag, Berlin, 1978), pp. 1-66.
3. H. R. Brown, V. R. Deline, and P. F. Green, *Nature* **341**, 221 (1989).
4. M. A. Grayson, C. J. Wolf, R. L. Levy, and D. B. Miller, *J. Polym. Sci. Polym. Phys.* **14**, 1601 (1976).
5. N. S. Enikolopian, L. S. Zarkhin, and E. V. Prut, *J. Appl. Polym. Sci.* **30**, 2991 (1985).
6. R. J. Morgan and J. E. O'Neal, *J. Polym. Sci. Polym. Phys.* **14**, 1053 (1976).
7. F. J. Norton, *J. Appl. Polym. Sci.* **7**, 1619 (1963).
8. V. Stannett, in *Diffusion in Polymers*, edited by J. Crank and G. S. Park, (Academic Press, London, 1968), pp. 41-73.
9. L. H. Lee, *J. Poly. Sci. A* **2**, 2859 (1964).
10. Y. Hama and K. Shinohara, *J. Polym. Sci. A-1* **8**, 651 (1970).
11. A. M. Donald and E. J. Kramer, *J. Polym. Sci. Polym. Phys.* **20**, 899 (1982).
12. L. de Arcangelis, A. Hansen, H. J. Herrmann, and S. Roux, *Phys. Rev. B* **40**, 877 (1989).

**FIGURE CAPTIONS**

1. (a) Emission at 28 amu and (b) load accompanying the fracture of a relatively thick ( $3.2 \times 3.2 \text{ mm}^2$  cross section) dogbone sample of polycarbonate.
2. Neutral emission at mass 28 from a thin polycarbonate film (a) during loading and fracture and (b) the peak at fracture shown on a faster time scale.
3. Possible bond breaking sequence for the release of gaseous CO.

# Mass 28 from the Tensile Fracture of Polycarbonate

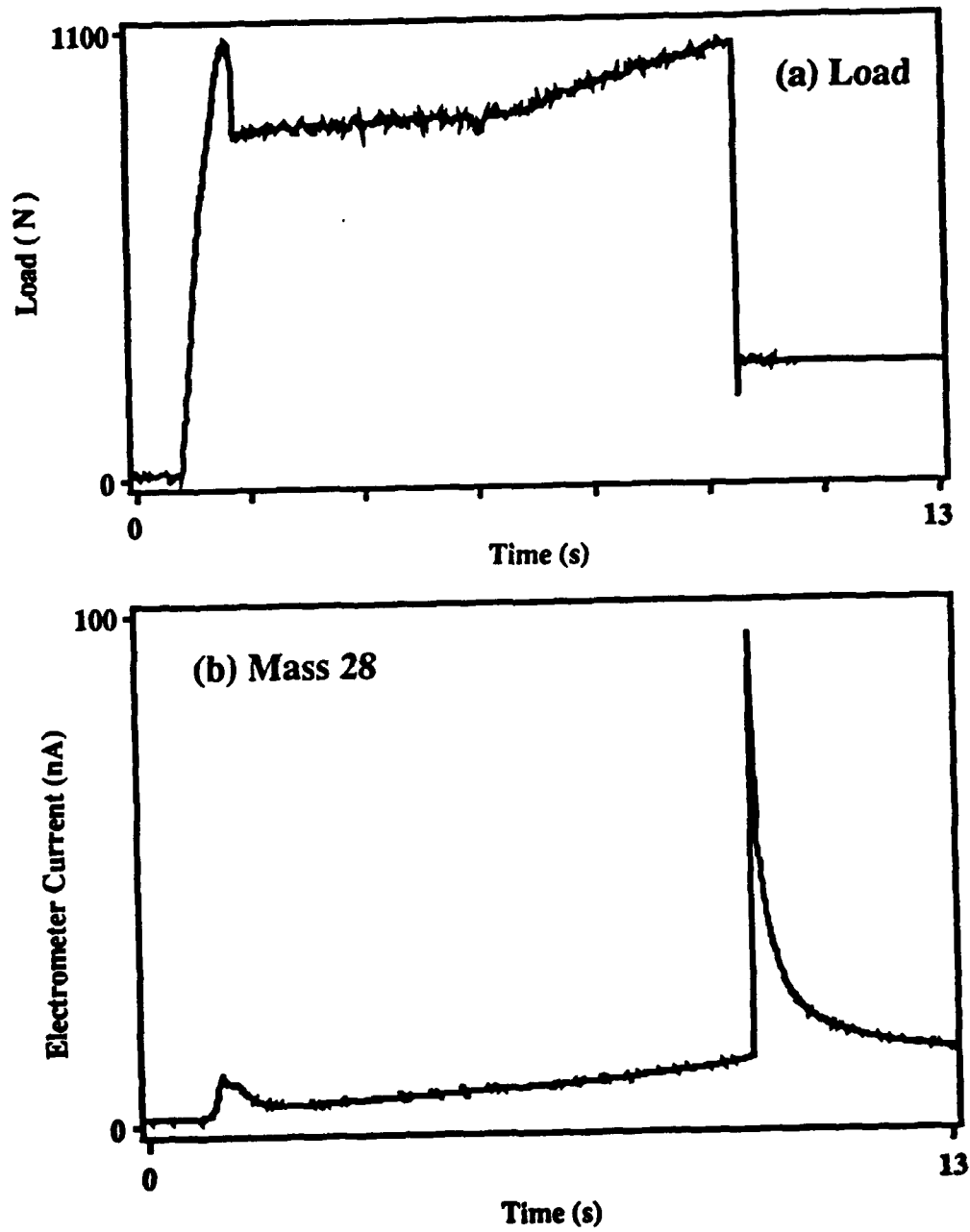


**FIG. 1**

**Mass 28 Signal During the Tensile Fracture  
of Thin Polycarbonate Film**

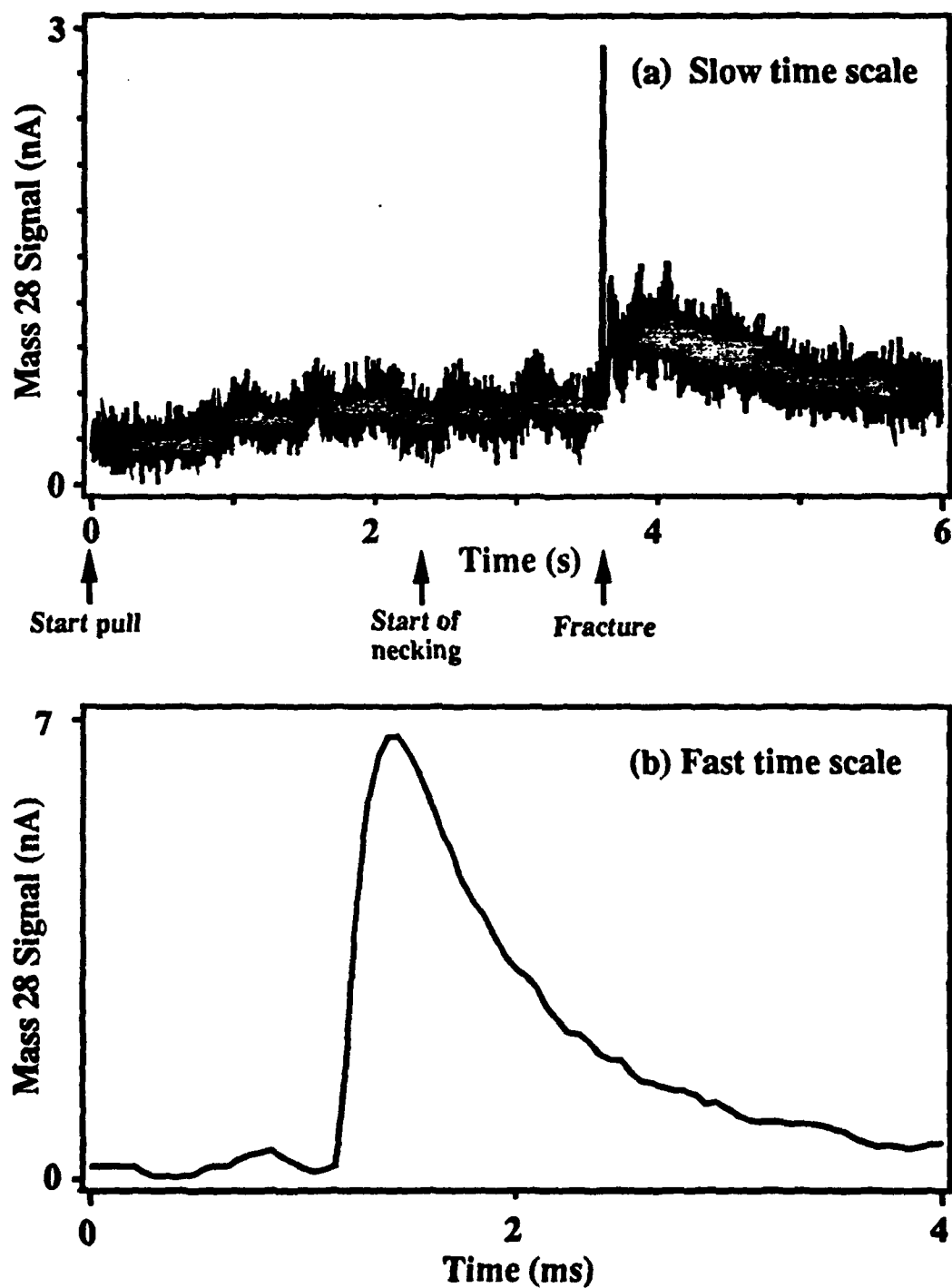
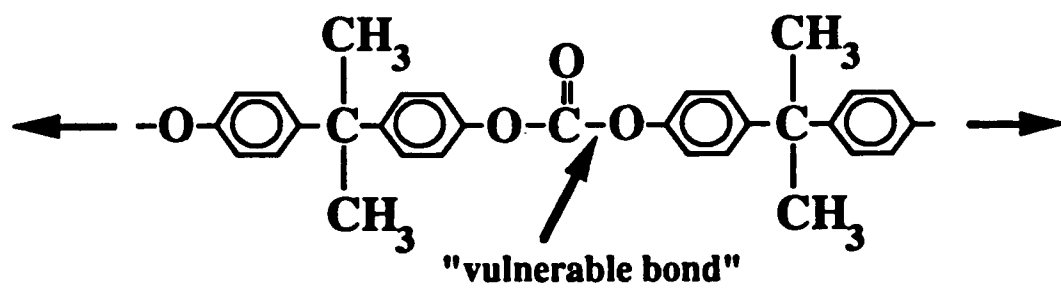
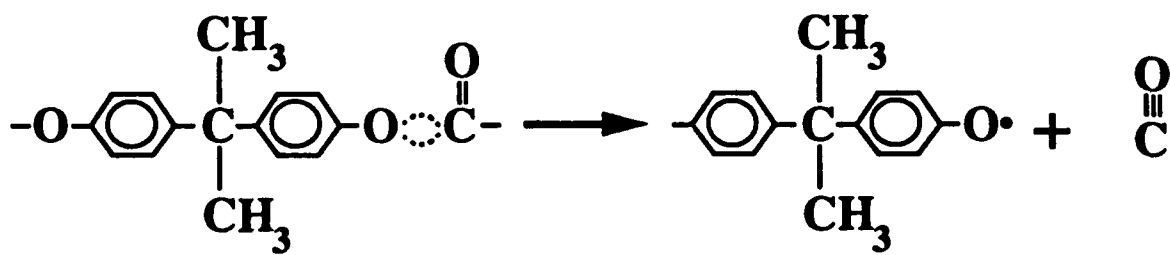


**FIG. 2**



**Mechanically Strained PC Chain**



**Excited Chain End**

**Release of CO**

**Fig. 3**



#### **IV. Electron and Photon Emission Accompanying Deformation and Fracture of Polycarbonate**

**K. A. ZIMMERMAN, S. C. LANGFORD, J. T. DICKINSON, Physics Department, Washington State University, Pullman, WA 99164-2814 and R. P. DION, The Dow Chemical Company, Designed Thermoplastics Research, Midland, MI 48667**

##### **Synopsis**

Electron and photon emission accompanying tensile loading and failure of polycarbonate show weak emissions during the onset of neck formation and intense emissions during the fracture event itself. These results are interpreted in terms of formation of active species by bond breaking followed by emission driven by energy released by recombination. Fast time scale measurements *during* fracture show that intense electron and photon emission typically begins about 50  $\mu$ s prior to the completion of fracture and is most intense at the completion of fracture. The gradual onset reflects the final stages of growth of the failure-initiating defect. Defect growth was monitored by measuring the intensity of a light beam transmitted through the gauge length of the sample; the transmission is sensitive to scattering by surface and bulk defects. A marked decrease in transmission begins some tens of ms prior to fracture due to scattering from the fracture-initiating defect. These measurements allow accurate correlations of defect growth with the onset of the electron and photon signals.

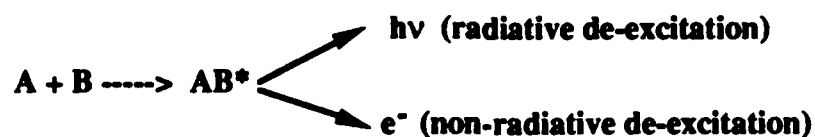
**Keywords:** fracture, fracto-emission, polymer, polycarbonate, defect growth, optical transmission

## INTRODUCTION

Deformation and failure of many materials results in the emission of photons, electrons, ions, and neutral particles which we refer to collectively as fracto-emission. The character of these emissions can be sensitive probes of deformation, bond-breaking, and interfacial failure. Fast detectors and electronics allow the sampling of fracto-emission components on ms to ns time scales; these fast time scales are inaccessible to many other probes of fracture processes. In this work we apply fracto-emission and light transmission measurements to the study of defect growth and fracture in a ductile polymer, polycarbonate.

Electron emission (EE) and photon emission (phE) accompanying the loading and failure of polymers has been reported by several workers.<sup>1-9</sup> Observations of electron and positive ion emission accompanying the loading and fracture of neat polycarbonate have been previously reported.<sup>9</sup> Mechanisms for these emissions have been reviewed elsewhere,<sup>5</sup> although a number of unresolved questions remain. For amorphous polymers the most likely scenario involves two pathways. During the fracture event itself, it is possible that direct molecular excitations are occurring due to non-adiabatic processes associated with bond breaking. The radiative decay of such excitations would yield photon emission, while decay by nonradiative, Auger-like transitions, would yield electron emission. Direct, radiative transitions would have fluorescent life-times of  $10^{-7}$  -  $10^{-9}$  s.

Decay involving intersystem crossings or transport/recombination processes could result in decay lifetimes of anywhere from  $10^{-7}$  s to  $10^2$  s. For instance, bond scissions could readily produce active species, denoted here A and B, which would eventually recombine to produce localized excited states. The decay of these excited states would yield the observed emissions:



This mechanism is similar to those suggested by Krylova for radiated polymers<sup>10</sup> and Dickinson et al. for fractured polymers.<sup>11</sup> Other models we have proposed<sup>12</sup> involve macroscopic charge separation (creating charge patches) during fracture; these models do not seem to be appropriate for neat polymers such as polycarbonate, polyethylene, and polymethyl methacrylate. In these materials, we do not observe consistent evidence for strong charge separation. In contrast, intense charge separation is observed during the failure of interfaces between these polymers and metals or other dissimilar materials; this interfacial failure yields very intense emission phenomena which are explained in terms of processes involving these high concentrations of electrical charge.<sup>13,14,15</sup>

In the case of thermally stimulated luminescence from irradiated polymers, Partridge has argued that the emitted light is generated by recombination of electrons with positive ions, rather than free radicals.<sup>16</sup> This conclusion is based on the poor correlation between the luminescence behavior and free radical concentrations (measured with ESR) under different sample treatments (dose, optical bleaching, and annealing). Similar arguments have been presented by Zlatkevich.<sup>17</sup> Furthermore, Blake and Randall<sup>18</sup> showed that in  $\gamma$ -irradiated polyethylene, isothermal thermoluminescence intensities could be increased by the application of an electric field, which would promote the motion of trapped charge carriers (electrons). These are strong arguments in support of an electron/positive ion recombination mechanism for the EE and phE accompanying fracture. Finally, using electron scavengers, Sakaguchi et al.<sup>19-21</sup> have shown with ESR that high yields of ionic species result from bond scissions in polypropylene, polyethylene, and polytetrafluoroethylene.

In this work, we first describe the behavior of EE and photon emission (phE) on a slow time scale during loading, showing the small but reproducible emissions observed during yielding and drawing. We then focus on fast time scale observations of the intense emissions immediately prior to and during catastrophic failure; these measurements shed light on the sequence of events leading to ultimate failure. To establish correlations between these emissions and the progress of defect growth, somewhat novel measurements of light transmission along the *length of the sample* were made. Although scattered light prohibits simultaneous phE measurements, light transmission

can easily be measured synchronously with EE. Illumination conditions were chosen to optimize sensitivity to either (a) scattering from surface defects formed during drawing (which ultimately lead to failure) or (b) scattering from defects in the bulk of the sample (with little sensitivity to surface defects). Comparisons between these signals and the fracto-emission signals allows for time-resolved reconstruction of certain key events preceding fracture on very rapid time scales.

## EXPERIMENTAL

Polycarbonate (Calibre® 300-10) was provided by The Dow Chemical Company in the form of compression molded bars,  $6.3 \times 1.3 \times 0.32 \text{ cm}^3$ . This material has molecular weights  $M_w = 42,400$  and  $M_n = 21,900$ , and a glass transition temperature  $T_g = 159^\circ\text{C}$ . The bars were machined into dogbone shapes with gauge cross sections of  $3.2 \times 3.2 \text{ mm}^2$ . The samples were clamped into a vacuum compatible loading apparatus positioned between the electron and photon detectors. After pumping the system down to a pressure of about  $100 \mu\text{Pa}$ , the samples was loaded to fracture in tension.

The loading and detection apparatus are described in detail in Ref. 5. Electron emission was detected by a Galileo Electrophysics Model 4821 Channeltron electron multiplier (CEM) mounted 2-3 cm from the gauge length of the sample. A +300 V bias on the front cone of the CEM allowed for the efficient collection of electrons escaping the sample regardless of their initial energy, provided that the path between the point of emission and the CEM was unobstructed. The very short "escape depth" of electrons from solid materials make EE measurements quite surface sensitive—in contrast to phE. Necessarily, all EE measurements were carried out in vacuum. When only phE or light transmission measurements were required, the experiments were often carried out in air. A major challenge was the choice of appropriate sensitivity for the CEM due to great sample-to-sample variations in peak EE intensity. To obtain maximum sensitivity during the early stages of crack growth, the detector was often allowed to saturate during the later stages of crack growth. Examples of both saturated and unsaturated signals are provided.

Photon emission was detected with an EMI Gencom 9924QB photomultiplier tube (PMT), sensitive to wavelengths in the 180-600 nm range. The PMT was mounted opposite the CEM, 1-2 cm from the sample surface. The transparency of polycarbonate to visible light ensured the relatively efficient detection without regard to the intervening material between the point of emission and the detector.

To monitor the weak signals during loading, the output of the CEM and PMT were pulse counted. In the pulse counting mode, the CEM and PMT were operated at high gain, where single photon or electron counting events produce detectable pulses of current. The amplified pulses were amplitude discriminated and counted over 3 ms intervals using a multichannel analyzer. Loading rates for the pulse counting work were typically about 3 mm/s, corresponding to a strain rate of  $0.11 \text{ s}^{-1}$ . The tensile force applied to the sample was monitored by a Scaime 60 g force transducer with a 1000 lb adapter mounted outside the vacuum system. The output of the force transducer was digitized with a LeCroy 6810 transient recorder at 50  $\mu\text{s}$  intervals. As noted above, great care was taken to avoid slipping in the clamps, which can produce extraneous emissions due to abrasion.<sup>15</sup>

Much lower CEM and PMT gains were employed to study the intense, short lived emissions during catastrophic crack growth. The CEM and PMT outputs were digitized with LeCroy TR8828 transient recorders. The signals were amplified and integrated with a 50 ns time constant, then digitized at 50 ns intervals. As the load cell was not fast enough to provide information on these time scales, these samples were equipped with resistive strain gauges (Omega 3/120LY41) mounted near one end of the gauge length. The strain gauge resistance formed one leg of a balanced Wheatstone bridge. The output of the bridge was differentially amplified and digitized at 200-500 ns intervals. Time response of the gauge and circuitry was less than 10  $\mu\text{s}$ .

Light transmission measurements proved to be sensitive to the onset of necking and crack growth. Light from a red LED was directed through the gauge length of the sample and detected with a fast photodiode (response time less than 1 ns). To maximize the detected signal, the ends of the sample were polished. The output of the photodiode was digitized at 50 ns intervals with a

LeCroy 8828 transient recorder. Light scattering measurements are particularly sensitive to the presence of defects larger than the wavelength of the light employed, here about 600 nm. The relatively poor collimation of the LED light resulted in a great deal of internal reflection along the gauge length of the sample; thus this signal was sensitive to the presence surface defects larger than about 600 nm. The LED signal was also sensitive to changes in the sample cross-section at the onset of necking.

Optical transmission measurements were also made using the highly collimated beam of a HeNe laser (633 nm). These measurements were performed in air rather than vacuum to allow room for the necessary optics. Careful attention to the optical condition of the entrance and exit surfaces of the samples was required to minimize the effect of small sample motions during loading. These surfaces (at either end of each sample) were polished by applying a solvent and clamping the surfaces between glass slides; the samples were then annealed for 20-30 minutes at 100 °C. The experiment was performed in an Applied Test Systems Universal Tester equipped with a light-tight box. The samples were loaded in tension at a rate of 1.27 mm/s, corresponding to a strain rate of  $0.042 \text{ s}^{-1}$ . Care was taken to keep the light beam away from the sample surfaces as it passed through the gauge section; i.e., the high degree of collimation allowed the laser beam to pass through the interior of the sample without interacting with the surface along the gauge section. Thus the transmitted intensity was insensitive to surface defects, but still sensitive to scattering from defects in the central portion (bulk) of the sample. The transmitted intensity was monitored by a photovoltaic cell with a time response of 50  $\mu\text{s}$ . The large active area of the photovoltaic cell rendered the detected signal insensitive to small motions caused by vibrations during loading.

## RESULTS

Polycarbonate is a model amorphous thermoplastic which typically displays extensive cold drawing prior to fracture in tensile tests. In machined samples, failure generally results from the

progressive growth of defects produced in the machining process. These defects grow by a tearing mechanism, yielding the characteristic "diamond-like cavities" shown in Fig. 1(a). When one of these defects grows to sufficient size, catastrophic failure ensues. The curvature of the fracture surface of Fig. 1(b) shows that defect growth proceeded continuously through half the sample cross section prior to catastrophic failure. [The progress of defect growth is a critical factor in understanding the failure of polymers during deformation.] Note that the resulting fracture surface is covered with small flap-like structures, shown in Fig. 1(c).

Typical EE and phE measurements during loading and fracture in vacuum are shown in Fig. 2. Due to the relatively low emission intensities and the long duration of the loading process, these emissions were pulse counted. By far the most intense emission occurs at fracture. The emission fracture is actually much more intense than indicated in Fig. 2 due to the "pile up" of pulses from the CEM; these overlapping pulses cannot be individually resolved and are thus undercounted. After fracture, EE and phE decay over 10-30 ms. In addition, as we show below, intense, coincident EE and phE *bursts* can be observed for several seconds following fracture.

Of considerable interest are the weak but significant emissions prior to fracture. The EE count rate rises above background ( $\sim 1$  count/s) shortly before tensile yield [at arrow (i)] and stays above background until fracture. Modest EE bursts are also observed at the onset of necking at arrow (i) and later in the drawing process [at arrow (ii)]. Both pre-fracture bursts in Fig. 2 coincide with load drops, although some load drops are not associated with EE bursts. The lack of a one-to-one correspondence between EE bursts and load drops may be due to the detection geometry. In the absence of a direct, line-of-sight path from a localized EE source to the detector, the electric field of the CEM may draw the emitted electrons back to the sample, ultimately preventing their escape and detection. Both load drops and EE bursts may be associated with localized strain softening events. These bursts are not associated with slipping in the clamps which results in tribologically induced emission.<sup>15</sup> If observed, slipping generally occurs prior to the onset of neck formation, where the stress at the interface between the clamp and the sample is higher. Further, slipping generally yields much stronger EE.

**This page intentionally left blank.**



At the onset of neck formation, weak phE can be observed. In Fig. 2 this phE is obscured by the high phE background of the uncooled PMT. By cooling the PMT to decrease background and loading the sample more rapidly to increase the emission rate, the signal-to-noise ratio was increased sufficiently so that phE at the onset of neck formation was observable, as shown in Fig. 3. The sample was loaded at a rate of 1.2 mm/s, corresponding to a strain rate of  $0.04 \text{ s}^{-1}$ . This test was performed in vacuum to avoid any possible phE due to chemiluminescence in the presence of atmospheric oxygen. The data were acquired at 50 ms/channel and have been integrated somewhat to average out the effect of the remaining background counts. The phE peak at the onset of neck formation (marked with an arrow) is clearly observed along with a continuous build up of phE during drawing.

Figures 4(a) and 4(b) shows pulse-counted phE and EE data some seconds after the fracture event, which is marked by an arrow. Coincident EE and phE bursts are often observed at random intervals long after fracture. The coincidence of these bursts is evident in Fig. 4(c), where the vertical lines connect coincident events. Their duration is much less than a single counting interval (3 ms) and their intensity slowly decreases with time after fracture. Similar EE and phE bursts have been observed following interfacial failure between polymers and inorganic substrates; these bursts have been shown to result from rapid, surface discharge events on highly charged surfaces created by interfacial failure.<sup>22</sup> Since there is little reason to expect significant charge densities on the fracture surfaces of neat polymers, we suspect that the bursts observed in Fig. 4 are due to transient, mechanical relaxation events, perhaps involving the flap-like structures shown in Fig. 1(c). Long after fracture, the surface (including the flaps) will be covered by patches of unreacted species left over from random fluctuations in the initial distribution of species.<sup>23</sup> After fracture, much of the plastic strain experienced by these flaps will begin to relax, occasionally bringing two flap surfaces into intimate contact. If patches of one active species (e.g., electrons) are rapidly brought into contact with patches of the other (e.g., positive ions), recombination can lead to a transient burst of emission. It should be emphasized that in order to see both phE and EE,

these reactions must occur at a free surface where electrons are able to escape and reach the detector.

The intense EE and phE signals immediately before and during fracture are shown in Fig. 5, along with the output of a strain gauge attached to the sample. The strain measurements have been shifted in time to account for the time required for the stress wave from the fracture surface to reach the strain gauge. (The time delay was determined to within  $\pm 5 \mu\text{s}$  using the speed of sound along the length of the sample and the distance from the fracture surface to the strain gauge.) The oscillations in the strain following fracture are due to stress waves reflected from the end of the sample and the fracture surface. The first drop in strain indicates the time interval associated with rapid crack growth.

The EE and phE signals in Fig. 5 begin at roughly the same time, about  $30 \mu\text{s}$  *before* the apparent completion of fracture. Both signals grow in intensity as the strain drops. The loss of noise-like structure in the EE signal near its peak indicates that the CEM is saturated at this point and therefore ceases to reflect the actual EE intensity. (The CEM was operated at high gain in order to detect EE as early in the course of fracture as possible.) The recovery of the CEM is indicated by the recovery of the fluctuating component of the signal some  $35 \mu\text{s}$  later. A large number of small EE pulses (single counts) are observed over the next  $200 \mu\text{s}$ ; the accompanying phE is somewhat less intense.

In the great majority of fracture events, the peak emissions are quite close to the completion of fracture, as indicated by the first minimum in strain. Although the first minimum in strain which is accompanied by a strong phE burst [marked by arrow (i)] as well as rapidly increasing EE, the most intense phE occurs somewhat later [marked by arrow (ii)]. (As the CEM is still saturated, the EE shows only a shoulder rather than a peak at this point.) The fracture surface of this sample was unique in that ligaments were observed along two edges of the sample, suggesting that the delayed phE is due to the delayed failure of these ligaments. The high phE intensity produced by ligament failure may be related to the unusually high ligament strain at failure. Despite the relatively small amount of material broken during ligament failure, the emission rate would be enhanced by bond

breaking during cold drawing as well as potentially high crack velocities during ligament failure. As noted below, fracto-emission intensities depend strongly on crack velocity, which would be enhanced by the high stresses immediately prior to ligament failure. Thus the failure of small but highly strained ligaments could readily yield emissions as intense as the relatively slow "tearing" of the bulk material during catastrophic failure.

Another set of EE and phE signals recorded during fracture of another specimen appears in Fig. 6. Again, the CEM was operated at high gain and thus saturated soon after the onset of catastrophic failure. In this fracture event, EE and phE bursts are observed at arrows (i) and (ii), well before the onset of catastrophic crack growth. The intermittent character of the emission suggests that the crack jumped at least twice prior to catastrophic failure. Characteristic features on the fracture surface are consistent with oscillations in crack velocity prior to catastrophic failure. Ultimate failure does not occur until after arrow (iii), where EE and phE rise dramatically. Significantly, the interval between the onset of emission [arrow (i)] and the onset of catastrophic failure [near arrow (iii)] is similar to the interval between strain oscillations after fracture, suggesting that catastrophic failure was precipitated by a stress wave generated by the first crack jump and reflected from the end of the sample. To the resolution of the strain measurements ( $\pm 5 \mu\text{s}$ ), the phE peak coincides with the first minimum in strain, marked by arrow (iv), and thus coincides with the completion of fracture.

The EE of Fig. 6(a) shows a tendency to burst after fracture. The periodicity of these EE bursts is also similar to that of the strain oscillations following fracture, suggesting that reflected stress waves may influence the emission process after fracture as well. We propose that the deformation of surface material by reflected stress waves was sufficient in this case to produce microscopic motion of one or more surface flaps, which would promote recombination of active species by bringing portions of two flaps into intimate contact.

The timing of the EE relative to the failure event is more precisely determined by simultaneous EE and Light Emitting Diode (LED) light transmission measurements, shown in Fig. 7. (LED light scattered out of the sample prohibits simultaneous phE measurements.) Here the EE

signal was acquired at lower CEM gain. The EE signal shows no sign of saturation near the peak, and should therefore accurately represent the EE intensity in this region. We take the minimum in the photodiode output, marked by arrow (ii) to indicate the completion of fracture. The onset of EE is marked by arrow (i), about 15  $\mu\text{s}$  prior to the completion of fracture. The delayed onset of EE in Fig. 7 relative to those of Figs. 5 and 6 may be due to lower CEM sensitivity. However, the sudden onset of EE in Fig. 7 suggests that the defect which precipitated fracture was situated on the side of the sample away from the detector; the electron collection efficiency would then be very small until the defect grew through the sample and opened a direct line-of-sight path to the detector. The EE peak nearly coincides with the minimum in the transmission curve, which identifies the completion of fracture. Note that the EE peak immediately *follows* the period of most rapid bond breaking, rather than coinciding with it. We attribute this brief delay to the enhanced electron escape probability as the crack opens (after the completion of fracture). During fracture, the narrow crack limits the number of electrons which can escape to the detector. For the first 2-3  $\mu\text{s}$  after fracture, the increased collection efficiency due to the opening crack more than compensates for the rapidly falling emission rate. The subsequent decay is highly non-exponential, consistent with an emission process involving recombination of active species rather than the direct decay of simple, isolated excitations.

The LED light transmission measurements of Fig. 7 indicate a relatively sharp transition from slow defect growth to catastrophic crack growth about 8  $\mu\text{s}$  prior to the completion of fracture; this was typical of transmission measurements acquired on this time scale. The fracture surfaces also show evidence of a transition from a slow to rapid crack growth mode. In Fig. 1(b) the surface formed in slow crack growth shows a dense pattern of radial steps, while the surface formed in catastrophic crack growth [Fig. 1(c)] has fewer (or smaller) steps which are almost parallel. In most cases, the fracture-initiating defect had grown through half the gauge cross section before the onset of catastrophic failure. However, moderately intense EE is observed at least 10  $\mu\text{s}$  before the onset of catastrophic failure. This suggests that the crack velocity

immediately prior to catastrophic failure is significant, and that the transition to catastrophic crack growth is often continuous.

LED transmission data were also recorded during the loading of polycarbonate. LED data and the corresponding load are shown in Fig. 8. The LED signal drops slowly during the initial stages of loading [starting at (i)], peaks briefly at the onset of cold drawing [at arrow (ii)], then drops sharply. We attribute the small increase in transmission at (ii) to the development of surface curvature and/or variations in refractive index during the necking processes; under appropriate conditions, light which would otherwise be scattered from surface defects can be weakly focused onto the photodiode, briefly increasing the transmission signal. As the neck propagates along the gauge of the sample, the transmission signal drops slowly. The decrease in transmission gradually accelerates as fracture becomes imminent [arrow (iii)], and finally drops precipitously at failure [arrow (iv)]. On this time scale, the LED signal drops markedly a full second before fracture, long before the load begins to drop. Immediately prior to fracture, the LED signal is only 40% of its initial intensity. At this point, changes in the transmission are most likely dominated by the growing crack. The rapid acceleration in crack velocity immediately prior to failure make it unlikely that two large defects coexist at this point. This is confirmed by microscopic examination of the sample after fracture. Thus the drop in transmission immediately prior to fracture is generally dominated by the scattering from an isolated fracture-initiating defect.

An expanded view of the LED data of Fig. 8 early in the loading process is shown in Fig. 9. The drop in transmission tracks the increase in applied load through the early stages of yielding. The total drop in transmission prior to yield is about 16%. As noted below, this drop is far in excess of that due to scattering in the bulk material under load. It is also much greater than the decrease in cross sectional area of the gauge length at these strains ( $\sim 1\%$ ). We attribute the majority of the increased scattering prior to yield to growing defects nucleated at sites of machining damage; the latter are known to nucleate surface crazes.<sup>24</sup> Since the transmission of the poorly collimated LED light depends strongly on total internal reflection at the sample surfaces, the transmitted intensity is quite sensitive to the presence of surface defects.

From Fig. 8, it is clear that the transmission is already dropping rapidly 1 s before fracture. An expanded view of the LED and load signals in this region are shown in Fig. 10. On this time scale, the gradually accelerating decrease in transmitted intensity is quite clear. The drop in transmission is a far more sensitive indicator of impending failure than the load. On this time scale, the LED signal is dropping rapidly 200 ms prior to failure, while the load does not drop significantly until about 50 ms before failure. As noted above, most of the drop in transmission at this point may be attributed to the growth of the largest defect, which ultimately precipitates fracture.

The LED and EE signals accompanying catastrophic crack growth in this fracture event are shown in Fig. 11 on an expanded time scale. The CEM sensitivity is high, to observe EE during "subcritical" crack growth. Thus, like the EE signals of Figs. 5 and 6, the EE of Fig. 11 shows signs of saturation during rapid crack growth. (Since the electron detector is saturated, the position of the EE peak relative to the LED signal is not meaningful). The first EE is observed about 25  $\mu$ s before the completion of fracture. Consistent with the steady growth of the EE in Fig. 11, the fracture surface of this sample showed no signs of crack arrest prior to catastrophic failure; i.e., the fracture surface was consistent with a relatively slow, continuously growing defect during the initial stages of crack growth, which would account for the lack of significant EE bursts prior to fracture.

The photodiode output can be used to estimate the crack speed immediately prior to catastrophic failure. At this point, the crack itself is the dominant scattering center, and to first order the photodiode output is proportional to the cross sectional area of the intact material ahead of the crack tip. The intact area at the onset of catastrophic failure  $A_0$ , can be estimated from fractographic observations, and by comparing the area of the fracture surface produced during catastrophic failure with the associated drop in transmission, the light intensity signal can be calibrated relative to the area produced. In Fig. 11, the change in the photodiode output during catastrophic failure corresponds to about 0.12 mV/mm<sup>2</sup> fracture surface area. The geometry of the crack front prior to catastrophic failure is well approximated by a quarter circle [see Fig. 1(b)], with a crack length equal to the radius of the circle. The crack velocity can then be expressed as

$$\frac{dr}{dt} = \frac{0.12 \text{ mV/mm}^2}{(\pi A)^{1/2}} \frac{dI}{dt} \quad (1)$$

where  $r$  is the crack length,  $A$  is the crack area, and  $I$  is the photodiode output. The area  $A$  may be estimated by integrating the observed transmission intensity; in the time region of interest,  $A$  remains within 20% of  $A_0 = 8 \text{ mm}^2$ .

Crack velocity estimates made on the basis of the LED data of Fig. 11 are shown in Fig. 11(b). The rapid acceleration of the crack prior to catastrophic failure is quite evident. The EE signal also clearly begins at a modest crack velocity, about 5 m/s. This indicates a threshold in crack velocity for the detection of EE due to fracture. Since the onset of phE is essentially in coincidence with the onset of EE (from Figs. 5 and 6), both emission signals exhibit the same threshold in crack velocity.

The crack velocity during catastrophic failure is  $\sim 300 \text{ m/s}$ . The dramatic increase in EE intensity immediately prior and during catastrophic failure appears to be much greater than the increase in the rate of fracture surface formation. This is due in part to the increase in electron escape probability as the crack opens enhances the observed emission markedly. However, the major factor is probably a strongly nonlinear dependence of EE on crack velocity and/or stress intensity.

Some idea of the relative importance of scattering from surface and bulk defects was obtained by comparing transmission measurements using an LED with measurements using a well collimated HeNe laser beam. Typical laser transmission measurements are shown in Fig. 12. Here the laser timing signal is again compared with the output of a strain gauge. The slow decrease in signal as the sample draws is real, but small (about 3%). Drawing is associated with a significant increase in the amount of sample traversed by the light beam ( $\sim 10\%$ ); but given the transparency of polycarbonate, this is unlikely to account for a 3% decrease in transmission. We attribute the majority of the increase in scattering to inhomogeneities in the bulk associated with the drawing process, e.g., shear bands. The relatively small drop in laser transmission during

drawing suggests that the order of magnitude larger decrease in LED light transmission is due to the growth of surface flaws.

Like the LED data, the transmitted HeNe light signal shows an accelerating decrease in intensity as fracture becomes imminent. This region of the data is shown on an expanded time scale in Fig. 13. The transmitted intensity is dropping markedly at an accelerating rate 60 ms before the completion of fracture. About 20 ms before fracture, a small drop in load is also observed. Because the laser beam passes through the interior of the sample, the effect causing this drop must extend to the bulk. As noted above, the curvature of the fracture surfaces produced in this work indicate that the fracture-initiating defect has often grown through half the gauge cross section prior to the onset of catastrophic failure. Defects of this size would scatter a major fraction of the laser beam. Thus, we attribute this drop in transmission to the intersection of the growing defect with the laser beam.

## DISCUSSION

Electron and photon emission generally requires localized energies on the order of eV per atom, which are typical of bond energies. Thus we expect EE and pHE to reflect bond breaking events as opposed to less energetic processes such as the sliding of polymer chains past one another (reptation). EE and pHE signals therefore provide evidence for bond breaking during the deformation and fracture of polymers.

The chemistry of the polycarbonate (PC) employed in this study is based on the structure shown in Fig. 14. Under tensile strain, chain rupture is expected to occur at one of the C-O bonds adjacent to the carbonyl group. This is the "weakest" bond of the chain, lacking the resonance stabilization of the phenyl groups. Photolysis of this bond yields phenyl and phenoxy radicals;<sup>25</sup> similar radicals may be generated by mechanical bond breaking. Alkyl radicals due to hydrogen abstraction are also observed. CO and smaller amounts of CO<sub>2</sub> are produced as by-products of phenyl and phenoxy radical production in photolysis by  $\gamma$ -rays. Significantly, we have recently observed CO emission accompanying the fracture of PC films,<sup>26</sup> suggesting that phenyl and



phenoxy radicals are produced in mechanical as well as photolytic bond breaking. Phenoxy radicals are expected to serve as electron traps,<sup>27</sup> and could release electrons (species A) thermally or upon recombination with phenyl or other phenoxy radicals. The corresponding hole traps would be positive radical ions involving carbonyl and/or phenyl groups. Hama and Shinohara suggest that these radical ions serve as luminescence centers (species B) in thermally stimulated luminescence of irradiated PC.<sup>13</sup> Thermally stimulated electron emission from PC following exposure to radiation has been attributed to similar charged and neutral radicals.<sup>28</sup>

Although a spectrum of the phE would be extremely helpful in identifying the species responsible for fracture related phE, the relatively small amount of total phE accompanying fracture of neat PC render spectroscopy impractical. However, we have performed spectroscopy on the much more intense emissions from glass-filled PC.<sup>29</sup> The peak in spectra acquired during and following fracture in vacuum occurs at 375 nm, in fairly close agreement with the peak in the PC fluorescence spectra reported by Gupta et al.<sup>30</sup> Thus phE during failure of glass/PC interfaces appears to involve processes similar to UV-induced fluorescence, and it is possible that phE during fracture of neat PC is also of similar origin. Gupta et al. attribute the fluorescence they observe to the decay of the first excited state of the aromatic carbonyl singlet.<sup>30</sup> They identify this state as the reactive excited state responsible for the photo-Fries mechanism for photo-decomposition in polycarbonate. Although speculative, we suggest that the singlet state may be an intermediate state in mechanical chain scission as well as photo-induced scission. The low quantum fluorescence yields ( $< 0.05$ )<sup>30</sup> reported by Gupta et al. are consistent with the modest phE intensities observed here. On the basis of this identification, we attribute the phE during crack growth to the decay of excited aromatic carbonyl state produced during bond scission.

EE at fracture is more difficult to explain due to the difficulty of delivering the energy provided by recombination or relaxation (usually associated with a decrease in electron energy) to an emitted electron (requiring an increase in electron energy). This process probably involves the recombination of the mobile electron with a positive phenyl radical, with the transfer of energy to a second, nearby electron via an Auger process. It is also possible that free electrons are produced

by a free radical reaction, e.g., the recombination of negative phenoxy radicals with neutral phenoxy or phenyl radicals.

The production of the electrons, charged radicals, and other electronic excitations during mechanical bond rupture is a key step in the emission process, and one which may seem unlikely given the speed of electronic relaxations relative to atomic displacements. This difficulty is overcome to a large degree by the coupling of the electronic energy levels with atomic displacements.<sup>31</sup> Charge redistribution along strained backbone bonds will tend to decrease the electron densities in strained bonds and increase the electron densities in nearby unstrained bonds. This redistribution is similar to the atomic displacements which accompany the electronic excitation of F-centers in alkali halides,<sup>32</sup> and the numerous examples of atomic displacements accompanying the DIET (Desorption Induced by Electronic Transitions) process.<sup>33</sup> In the polycarbonate chain, the unstrained C=O bond of the carbonyl group would therefore gain electron density at the expense of electron density in the adjacent C-O bonds. The proximity of the unstrained C=O and strained C-O bonds facilitates this charge transfer and may contribute to the weakness of the C-O bonds under mechanical loading. Electron transfer to the C=O bond changes the C=O bond length; after rupture of the C-O bond fracture, the C=O displacement will relax slowly (relative to electronic relaxations), and the probability of the associated electronic relaxation will be considerably reduced until after this relaxation is completed. Thus the efficiency of molecular charge separation depends strongly on time required to "break" the C-O bond. If this time is long relative to the time required for the atomic relaxation of the C=O distortion, the probability of charge separation and subsequent fracto-emission become negligible. This may help explain the extraordinary sensitivity of fracto-emission intensities to crack speed,<sup>34</sup> where higher crack speeds would result in higher frequencies of successful charge transfer events. We are currently carrying out *ab initio* calculations on strained molecules, e.g., H<sub>2</sub>CO, to probe for the resulting electron energy and charge density shifts due to deformation.

In this light, the low intensity of the continuum EE observed during cold drawing may be due to the low number of bonds broken during cold drawing or to the relatively slow separation of

the molecular fragments. Both factors may be important. As noted above, the rate of bond breaking prior to strain hardening is expected to be low. Prior to strain hardening, drawing is believed to leave the network of chain entanglements in the polymer largely intact,<sup>35</sup> and thus should not require extensive bond breaking. This is consistent with ESR measurements of free radicals produced in the deformation of semi-crystalline polymers, which detect little if any free radical production until the onset of strain hardening, i.e., after the neck has formed through the entire gauge length of the material.<sup>36</sup>

Neck formation appears to involve somewhat higher rates of bond breaking. Both EE and *phE* measurements show increased intensities during neck formation, i.e., at the onset of yield. Neck formation involves a small, localized region, which would explain the lack of a significant ESR signal at this point. Moiré interferometry *strain* measurements made by Theocaris and Hadjiiosiph show extremely high, localized strains at the point of neck formation,<sup>37</sup> usually in the vicinity of a surface defect. The high magnitude of the associated stresses can hardly be less than those during strain hardening, where bond breaking can be observed by ESR. These very high strains may facilitate the rapid separation of molecular fragments after bond breaking and increase the efficiency of EE and *phE* processes. Similar events may account for the other transient EE bursts prior to fracture, which are accompanied by load drops similar to those during neck formation.

The growth of surface defects during the cold drawing process was readily detected in the LED light transmission experiments. Morgan and O'Neal have made detailed observations of the growth of surface defects in PC.<sup>24</sup> In the early stages of loading, crazes develop at surface flaws and grow until they are typically about 10  $\mu\text{m}$  deep. Defects of this size scatter visible light efficiently, and account for our observed decrease in light transmission during the early stages of loading. As the defects are incorporated into the necked region, craze growth ceases due to the difficulty of growth into the oriented polymer. Subsequent defect growth occurs by a tearing mechanism, yielding the diamond-like cavities of Fig. 1(a). The change in growth mechanism explains the slower decrease in light transmission after yielding. When the largest defect reaches a

critical length, often by the coalescence of diamond-like cavities, failure ensues. As ultimate failure in ductile polymers frequently initiates at such flaws,<sup>24,38</sup> they are of considerable importance in terms of failure mechanisms.

As fracture becomes imminent, the fracture-initiating defect generally begins to dominate the light scattering process; thus the light transmission measurement in the ms prior to fracture reflect the rate of surface area formation and thus the crack velocity. The crack velocity corresponding to the onset of detected EE in Fig. 8 is estimated to be about 5 m/s. We believe this velocity is a reasonable estimate of the point at which EE becomes significant on  $\mu$ s time scales (i.e., with count rates on the order of 1 MHz or higher).

The most intense EE and phE signals are observed during the fracture event itself, where crack velocities of 300 m/s are typical. These intense emissions reflect the high number of bonds broken during surface formation. The rate of bond breaking during catastrophic crack growth may be enhanced by craze formation. (This enhancement is not expected in thin PC films, where crazing is hindered.) Craze formation often accompanies rapid crack growth in bulk PC,<sup>39</sup> and involves a substantial amount of bond breaking.<sup>40</sup> Recent scanning tunneling microscope (STM) observations of PC fracture surfaces indicate that the average craze fibril diameter in samples similar to those employed in this study is under 3 nm.<sup>41</sup> This very small fibril diameter, coupled with the high entanglement densities characteristic of PC, require correspondingly high numbers of disentanglements (mostly by bond breaking) to form the craze. The enhancement of emission intensities due to crazing should be larger for the phE, due to the ease with which photons can escape the crazed material.

The phE and EE bursts observed long after fracture suggest that excitations produced during fracture itself can relax suddenly long after the fracture event itself. As noted above, deformation and fracture can produce long lived free radicals.<sup>28,36</sup> Although the probability of radical recombination is high immediately following fracture, a large number of free radicals will be isolated from potential recombination partners and remain for some time. This accounts for the presence of weak EE and phE long after fracture. We propose that the phE and EE bursts

observed after fracture are due to mechanical relaxation events at the surface which redistribute remaining active species, bringing pairs into close proximity and leading to transient, rapid recombination. Because both EE and phE bursts are observed, the relevant relaxations must occur at or near the surface. These relaxations might involve the flap-like surface features often observed on PC. These surface "flaps" are under tension during fracture, and being quite thin, are extensively deformed.<sup>24</sup> Inhomogeneous relaxation of the flaps after fracture would move the surfaces of adjacent flaps past one another, facilitating recombination of active species near the surface. If sufficiently violent, these microscopic tribological events could in principle also excite trapped charge carriers to yield EE and phE directly.

## CONCLUSIONS

EE and phE measurements accompanying the deformation of polycarbonate in tension are consistent with significant rates of bond breaking at the onset of cold drawing (EE bursts). Although these emissions are relatively weak, we feel that they more reasonably reflect actual rates of bond breaking than previously reported EE from polyethylene, which may have been dominated by sample abrasion in the clamps. In this study, we took great care to avoid such artifacts, and therefore feel comfortable attributing the emissions from PC prior to failure to deformation-induced bond breaking.

Failure in these PC samples was initiated at diamond-shaped cavities formed along the gauge length at sites of pre-existing flaws. LED and laser transmission measurements show that for strain rates on the order of  $0.1 \text{ s}^{-1}$  a single defect dominates the light scattering process as much as 1 s prior to failure. The fracture-initiating defect grows through a significant portion (roughly half) of the gauge cross section by about 30 ms prior to fracture. Some tens of  $\mu\text{s}$  prior to ultimate failure, the fracture-initiating defect grows rapidly—sometimes continuously, sometimes intermittently. When the crack speed reaches values on the order of 5 m/s, significant electron emission and photon emission are observed. At this velocity the rate of bond breaking and the probability of producing the appropriate active species in any given bond breaking event become

sufficient for the generation of observable EE and pH E on the time scales (ns- $\mu$ s) appropriate to catastrophic crack growth. The crack velocity during catastrophic crack growth is significantly higher, on the order of 300 m/s, and is accompanied by intense EE and pH E emission. Although these measured times apply specifically to the geometry employed in this work, they can provide a new real-time probe of the growth of the fracture-initiating defect. This information is not readily obtained from post-mortem fractographic studies.

The very high time resolution available with light and particle detection has great potential in unraveling the dynamics of very short events, including rapid crack growth. This information can have direct implications to the process of energy dissipation during deformation and fracture, which in polymeric materials generally depends on crack velocity.<sup>42,43</sup> Further, the atomic and molecular scale of particle and photon emission can often be exploited to obtain information on atomic and molecular processes accompanying deformation and fracture. For instance, these emissions can be useful in distinguishing between bond breaking vs chain sliding in various deformation processes. The understanding of deformation and fracture on the molecular level in turn facilitates the prediction of the consequences of material failure and the development of new materials with desirable properties.

### ACKNOWLEDGMENTS

This work was supported by the Dow Chemical Company, the Air Force Office of Scientific Research Contract AFOSR-F49620-91-C-0093, and the Washington Technology Center.

## REFERENCES

1. A. M. Polyakov and N. A. Krotova, Dokl. Akad. Nauk SSSR 151, 130 (1963), [Dokl. Phys. Chem. 150, 575 (1963)].
2. V. A. Zakrevskii and V. A. Pakhotin, Vysokomol. Soyed. A14, 568 (1975), [Polym. Sci. USSR 17, 653 (1975)].
3. V. A. Zakrevskii and V. A. Pakhotin, Fiz. Tverd. Tela. (Leningrad) 20, 371 (1978), [Sov. Phys. Solid State 20, 214 (1978)].
4. I. E. Kurov, A. V. Movshovich, and V. P. Novoshilov, Mekhanika Kompositnykh Materialov 4, 579 (1983) [Mech. Comp. Mater. 12, 411 (1983)].
5. J. T. Dickinson, in *Non-destructive Testing of Fibre-reinforced Plastics Composites*, Vol. 2, edited by John Summerscales, (Elsevier Applied Science, London, 1990), pp. 429-482.
6. J. T. Dickinson, L. C. Jensen, and S. K. Bhattacharya, Makromol. Chem. Macromol. Symp. 7, 129 (1987).
7. J. Fuhrmann, G. H. Scherer, and R. Hoffmann, Polym. Commun. 27, 164 (1986).
8. J. Fuhrmann, G. H. Scherer, and L. Nick, Makromol. Chem. 188, 2241 (1987).
9. Leo Nick, Ph. D. thesis: Technical University of Clausthal, 1988.
10. I. V Krolova, Uspekhi Khimii 55, 2138 (1976).
11. J. T. Dickinson, E. E. Donaldson, and M. K. Park, J. Mater. Sci. 16, 2897 (1981).
12. J. T. Dickinson, L. C. Jensen, and A. Jahan-Latibari, J. Mat. Sci. 19, 1520 (1984).
13. J. T. Dickinson, "Fracto-Emission Accompanying Adhesive Failure," in *Adhesive Chemistry—Developments and Trends*, edited by L. H. Lee (Plenum Publishers, New York), 1984.
14. J. T. Dickinson, in *Adhesive Bonding*, L. H. Lee, ed., (Plenum Press, New York, 1991), pp. 395-423.
15. J. T. Dickinson, L. C. Jensen, and R. P. Dion, "Fracto-Emission from High Density Polyethylene: Bond Breaking vs Tribological Stimulation," submitted to J. Appl. Phys.

16. R. H. Partridge, in *Radiation Chemistry of Macromolecules*, Vol. I, edited by M. Dole, (Academic Press, New York, 1973), pp. 193-222.
17. L. Zlatkevich, *Radiothermoluminescence and Transitions in Polymers*, (Springer-Verlag New York, 1987), pp. 22-27.
18. A. E. Blake and K. J. Randle, *J Phys. D* 10, 759 (1977).
19. M. Sakaguchi, H. Kinpara, Y. Hori, S. Shimada, and H. Kashiwabara, *Polymer* 25, 944 (1984).
20. M. Sakaguchi, H. Kinpara, Y. Hori, S. Shimada, and H. Kashiwabara, *Polym. Commun.* 26, 142 (1985).
21. M. Sakaguchi, H. Kinpara, Y. Hori, S. Shimada, and H. Kashiwabara, *J. Polym. Sci. Polym. Phys. Ed.* 25 1431 (1987).
22. J. T. Dickinson and E. E. Donaldson, *J. Adhesion*, 24, 199 (1987).
23. D. Toussaint and F. Wilczek, *J. Chem Phys.* 78, 2462 (1983).
24. R. J. Morgan and J. E. O'Neal, *Polymer* 20, 375 (1979).
25. Y. Hama and K. Shinohara, *J. Polym. Sci. A-1* 8, 651 (1970).
26. J. T. Dickinson, L. C. Jensen, S. C. Langford, R. P. Dion, L. Nick, to appear in *J. Mater. Res.*
27. Y. Hama, K. Nishi, K. Watanabe, and K. Shinohara, *J. Polym. Sci. Polym. Phys.* 12, 1109 (1974).
28. I. V. Krylova, and I. A. Rodina, *Zh. Fiz. Khim.* 61, 1688 (1987) [*Russ. J. Phys. Chem.* 61, 884 (1987)].
29. J. Fuhrmann, Leo Nick, J. T. Dickinson, and L. C. Jensen, "Photon emission during deformation of glass-fiber reinforced bisphenol-A polycarbonate," to appear in *J. Appl. Poly. Sci.*
30. A. Gupta, R. Liang, J. Moacanin, R. Goldbeck, and D. Klinger, *Macromol.* 13, 262 (1980).
31. M. E. Eberhart, D. P. Clougherty, and J. N. Louwen, *MRS Bulletin* 16(4), 53 (1991).



32. M. Hirai, *Rev. Solid State Sci.* 4, 431 (1990).
33. *Desorption Induced by Electronic Transitions: DIET IV*, edited by G. Bets and P. Varga, (Springer Verlag, Berlin, 1991).
34. J. T. Dickinson and L. C. Jensen, *J. Polymer Sci., Polymer Phys.* 20, 1925 (1982).
35. A. M. Donald and E. J. Kramer, *J. Mater. Sci.* 17, 1871 (1982).
36. A. Peterlin, *J. Polym. Sci. C* 32, 297 (1971).
37. P. S. Theocaris and C. Hadjiiossiph, *Eng. Fracture Mech.* 12, 241 (1979).
38. P. L. Cornes, K. Smith, and R. N. Haward, *J. Polym. Sci. Polym. Phys. Ed.* 15, 955 (1977).
39. M. J. Doyle, *J. Mater. Sci.* 18, 687 (1983).
40. E. J. Kramer, *Adv. Polym. Sci.* 52/53, 1 (1983).
41. D. M. Kulawansa, S. C. Langford, and J. T. Dickinson, *J. Mater. Sci.* 7, 1292 (1992).
42. W. Döll, *Adv. Polym. Sci.* 52/53, 104 (1983).
43. S. P. Gross, J. Fineberg, M. R. Morder, H. L. Swinney, *Phys. Rev. B* 45, 5146 (1992).

## FIGURE CAPTIONS

- FIG. 1** SEM micrographs of polycarbonate fracture surfaces showing: (a) typical diamond-like cavities formed during cold drawing; (b) a typical fracture surface; and (c) a close up of the flap-like structures on the fracture surface. In (b), failure initiated in the lower left-hand corner. Immediately prior to failure, the crack front defined a arc reaching from the upper left corner of the sample to the lower right corner. Crack growth through the remaining portion of the sample proceeded at very high velocities.
- FIG. 2.** (a) EE, (b) pH<sub>E</sub>, and (c) load accompanying loading and fracture of PC. The EE and pH<sub>E</sub> signals are plotted as counts per 12 ms interval.
- FIG. 3.** Smoothed pH<sub>E</sub> data accompanying the loading and fracture of PC. The PMT was cooled to reduce the pH<sub>E</sub> background and thus allow the observation of pH<sub>E</sub> at the onset of neck formation. The time of neck formation is indicated by the arrow. The relatively long duration of drawing compared with Fig. 1 is due to the relatively low strain rate employed ( $0.04 \text{ s}^{-1}$  vs  $0.11 \text{ s}^{-1}$ ) and the greater strain at fracture ( $\sim 50\%$  vs  $\sim 10\%$ ).
- FIG. 4.** (a) EE and (b) pH<sub>E</sub> accompanying loading and fracture, showing EE and pH<sub>E</sub> bursts long after fracture. These bursts are shown on an expanded time scale in (c) to show the coincidence of the EE and pH<sub>E</sub> bursts. The data are displayed as counts per 18 ms interval. The low intensity of the EE burst at fracture is due to the undercounting of overlapping (piled up) pulses from the CEM.
- FIG. 5.** Digitized (a) EE, (b), pH<sub>E</sub>, and (c) strain gauge output during fracture. The strain signal has been shifted to account for the time required for the strain wave to reach the gauge.

**FIG. 6.** A second set of digitized (a) EE, (b), pH<sub>E</sub>, and (c) strain measurements during fracture. Again, the strain signal has been shifted to account for the travel time of the strain wave.

**FIG. 7.** (a) EE and (b) transmitted light intensity (LED) accompanying catastrophic crack growth.

**FIG. 8.** (a) Transmitted light intensity (LED) and (b) applied load over the entire duration of deformation and fracture.

**FIG. 9.** (a) The initial drop in LED signal and (b) rise in load from Fig. 7, shown on an expanded time scale.

**FIG. 10.** (a) LED signal and (b) load immediately prior to ultimate failure from Fig. 7.

**FIG. 11.** (a) EE and (b) LED signal accompanying catastrophic crack growth from Fig. 7..(b) also displays an estimate of the crack velocity based on the LED signal and Eq. 1; the vertical axis for the crack velocity estimate appears on the right.

**FIG. 12.** (a) Transmitted light intensity (laser) and (b) strain gauge output accompanying loading and fracture.

**FIG. 13.** (a) Laser signal and (b) strain gauge output immediately prior to ultimate failure from Fig. 12, shown on an expanded time scale.

**FIG. 14.** Part of a polycarbonate chain showing the region containing the weaker bonds.

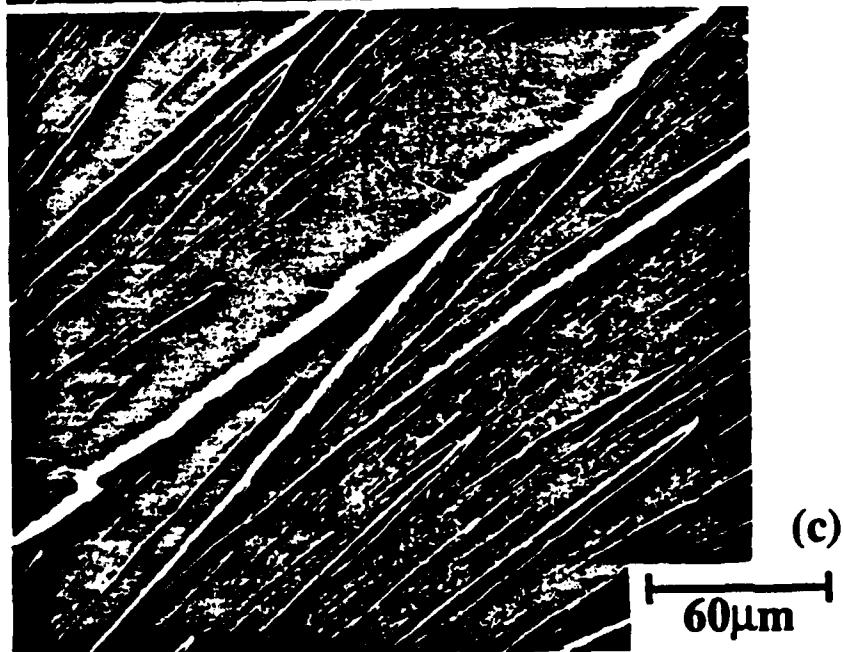
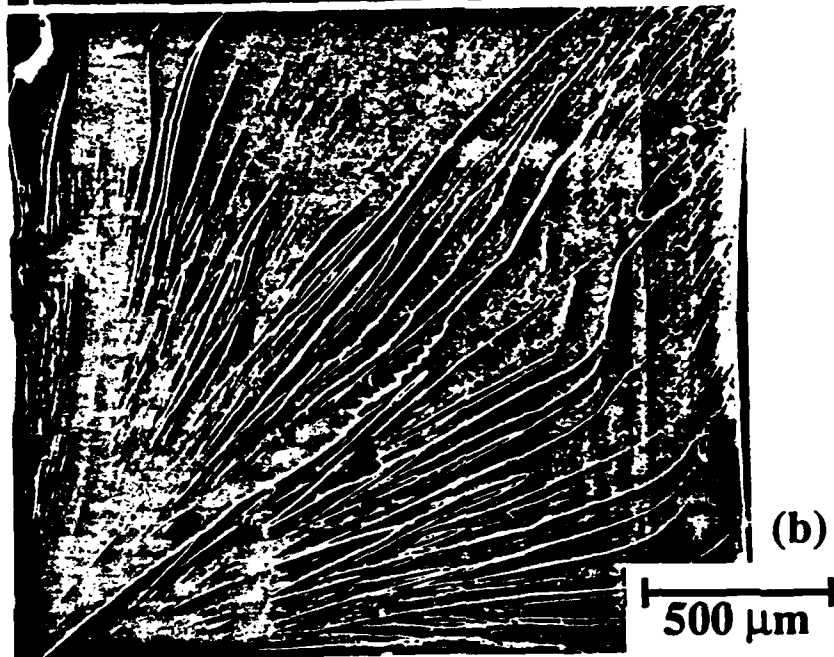
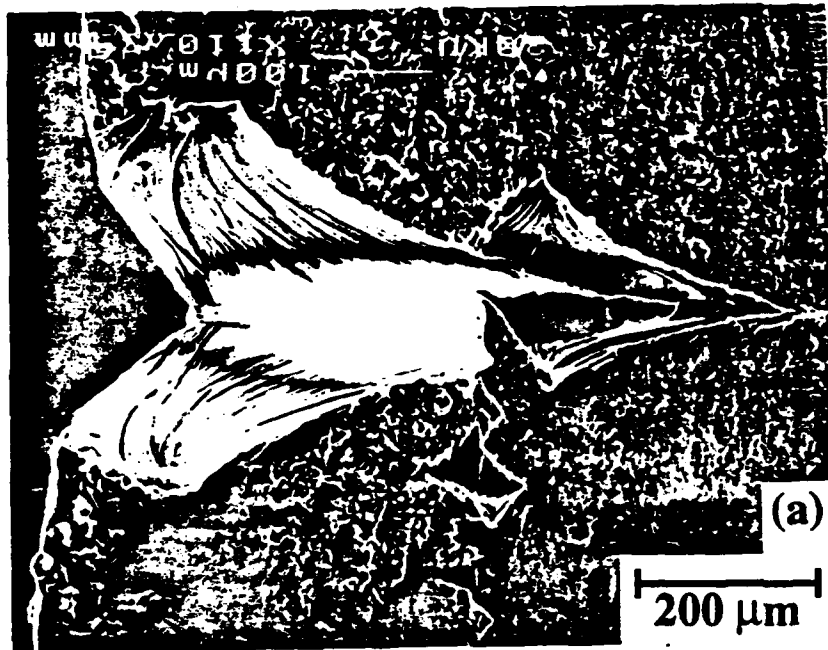


FIG. 1

## EE, Phe, and Load from the Fracture of Polycarbonate

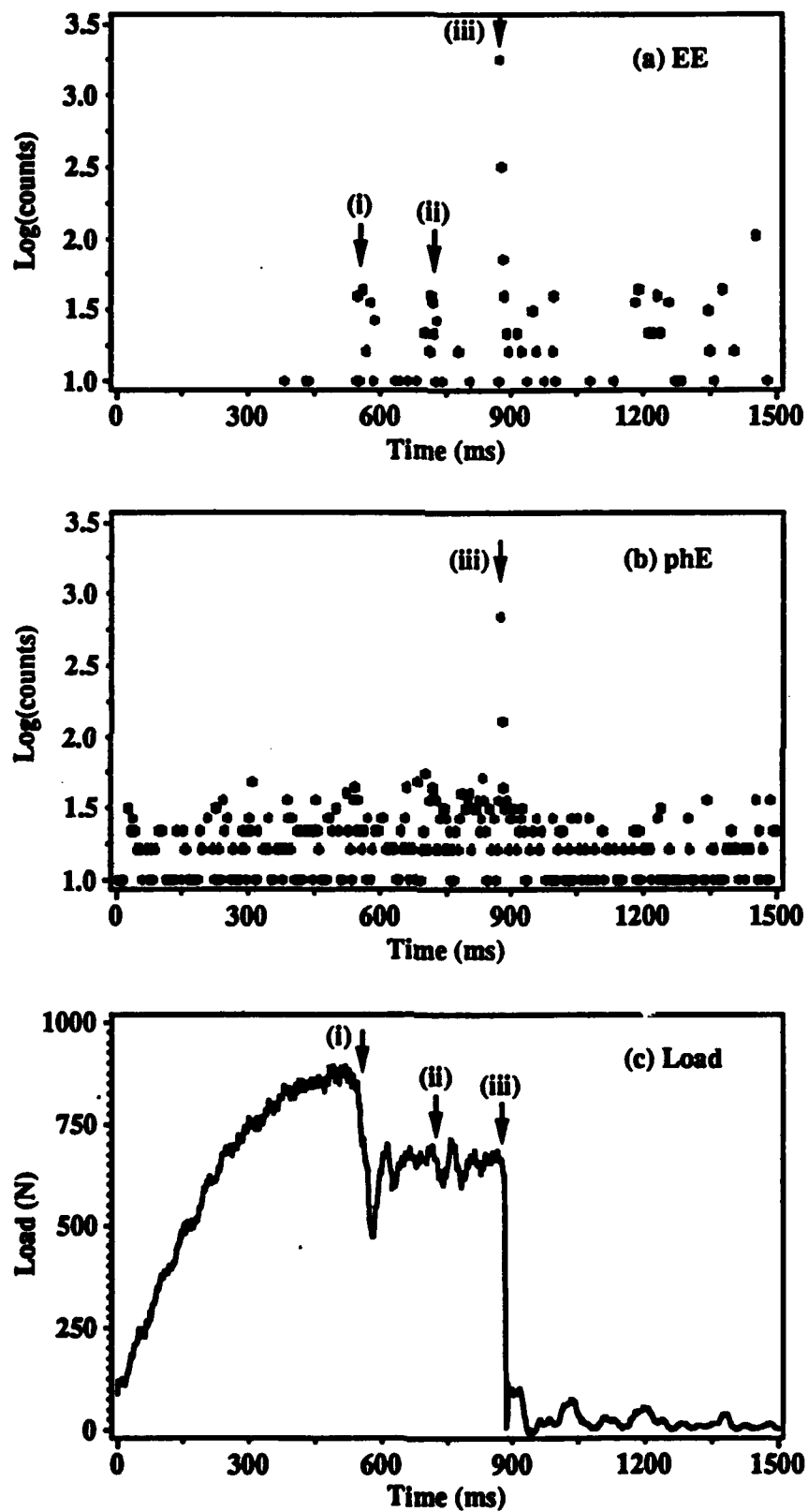
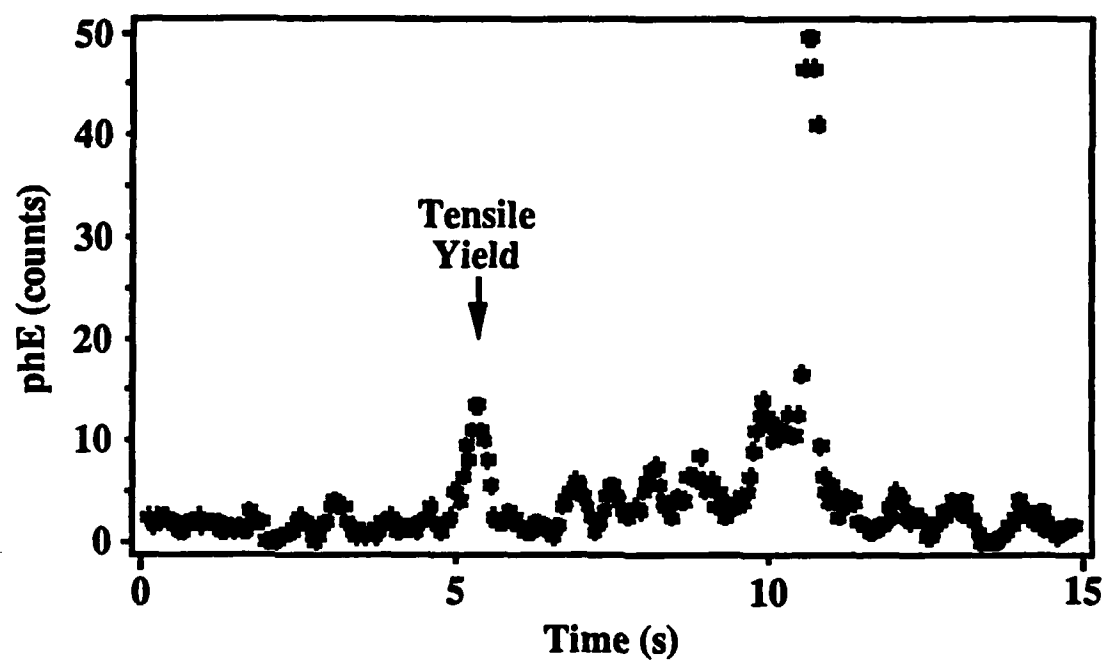


FIG. 2

### phE During Deformation and Fracture of Polycarbonate



**FIG. 3**

## EE and phE from the Fracture of Polycarbonate

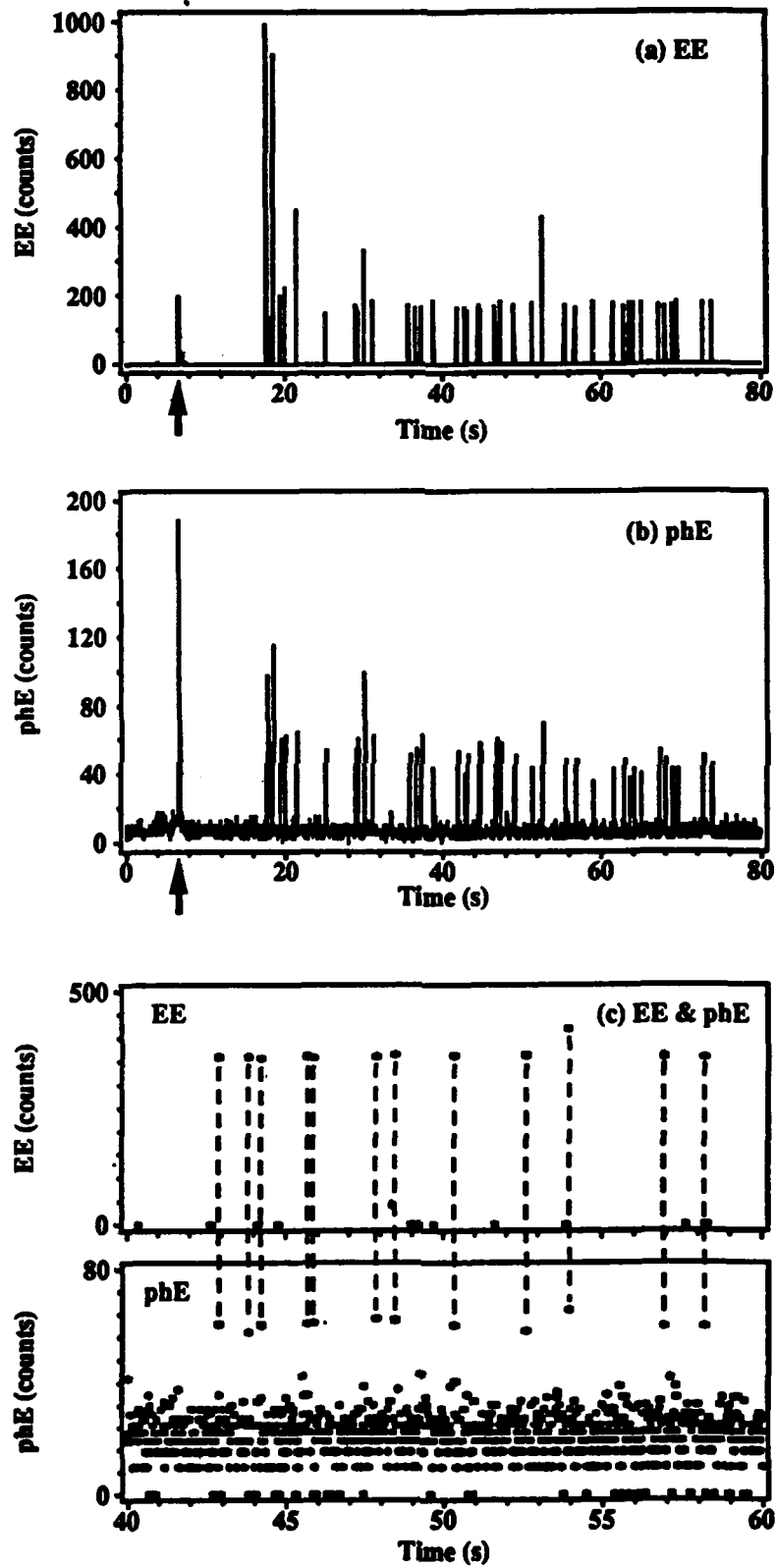


FIG. 4

## EE, phE, and Strain from the Fracture of Polycarbonate

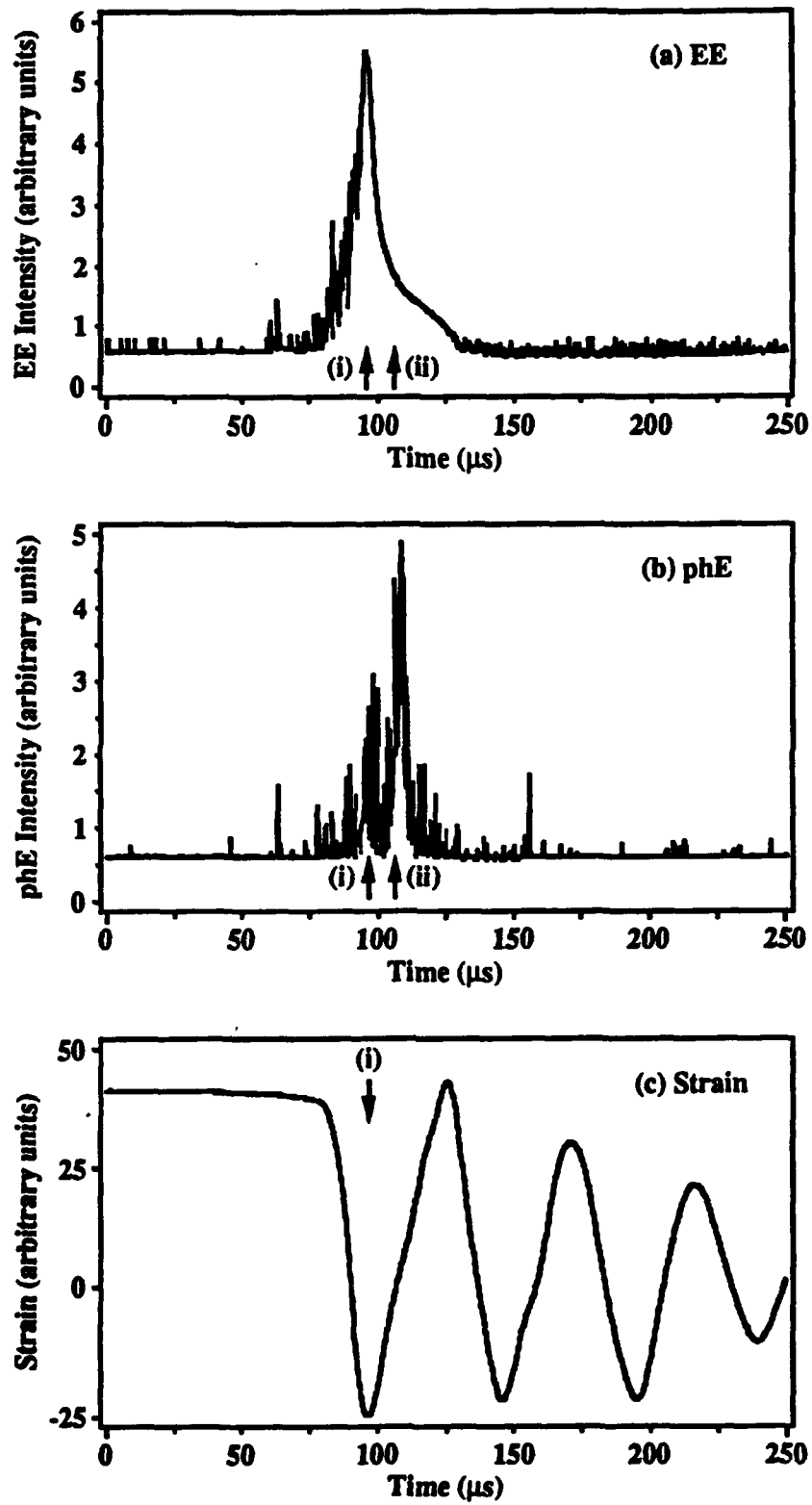


FIG. 5



## EE, phE, and Strain from the Fracture of Polycarbonate

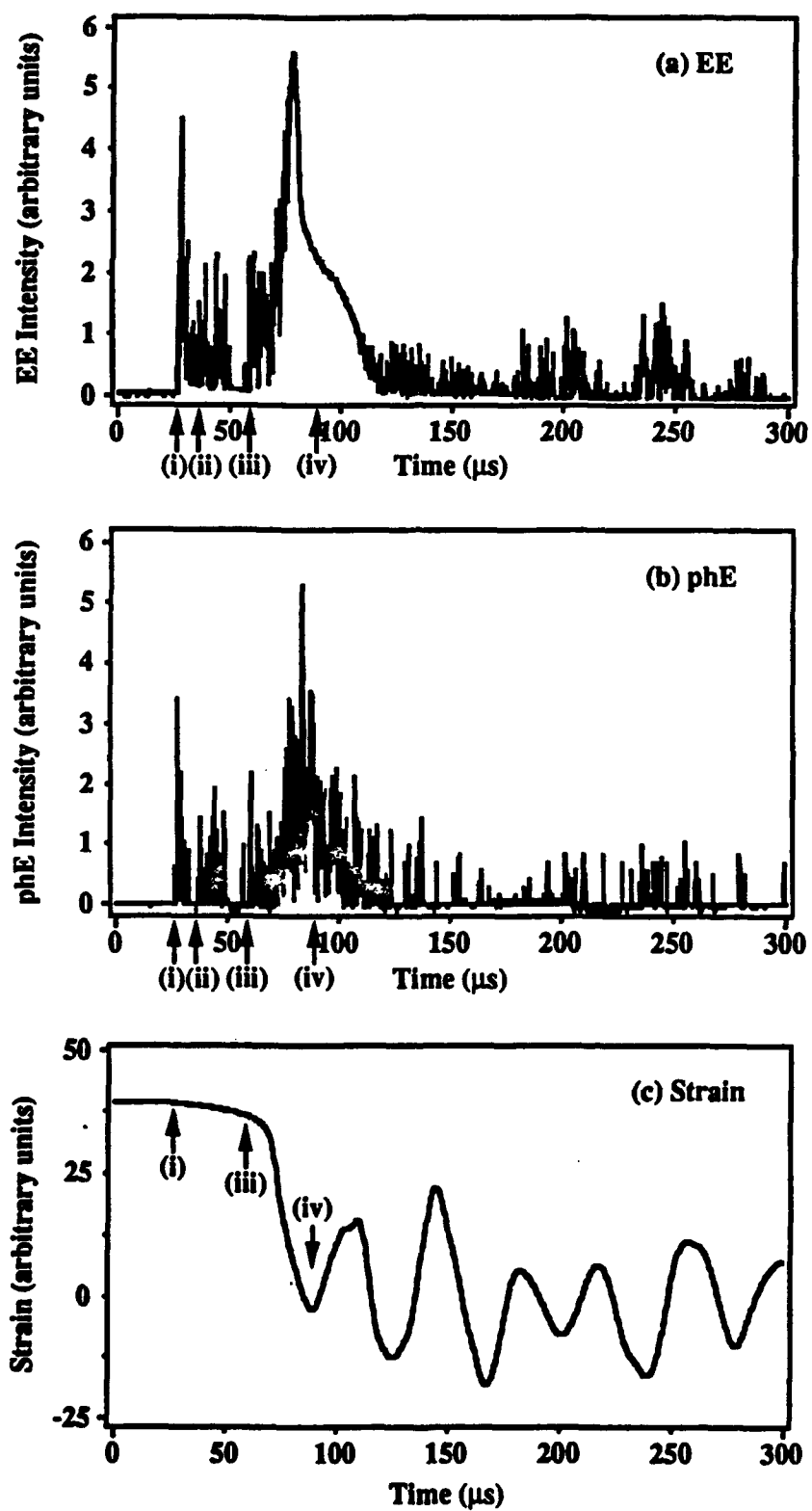


FIG. 6

# EE and LED Signal from the Fracture of Polycarbonate

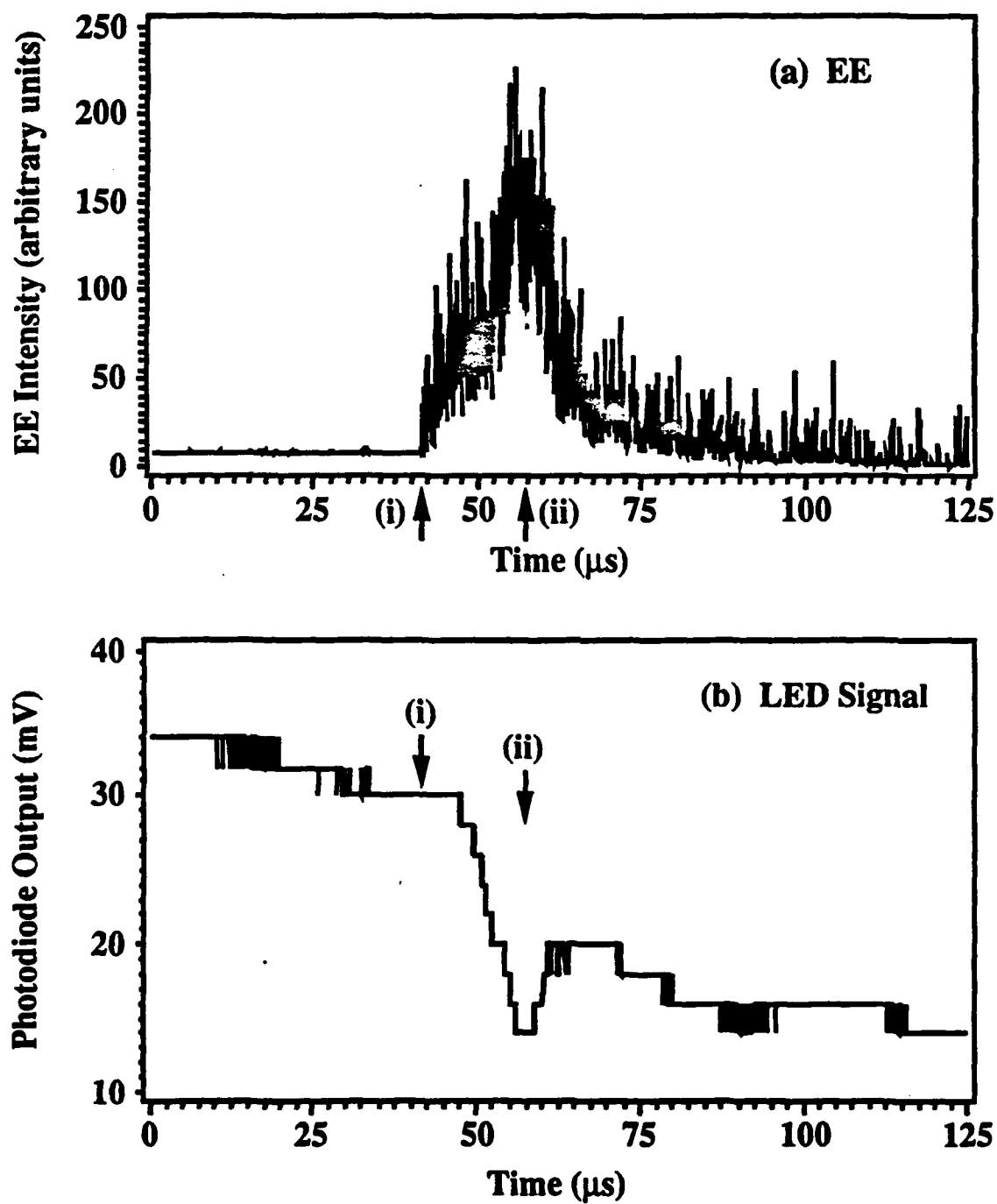
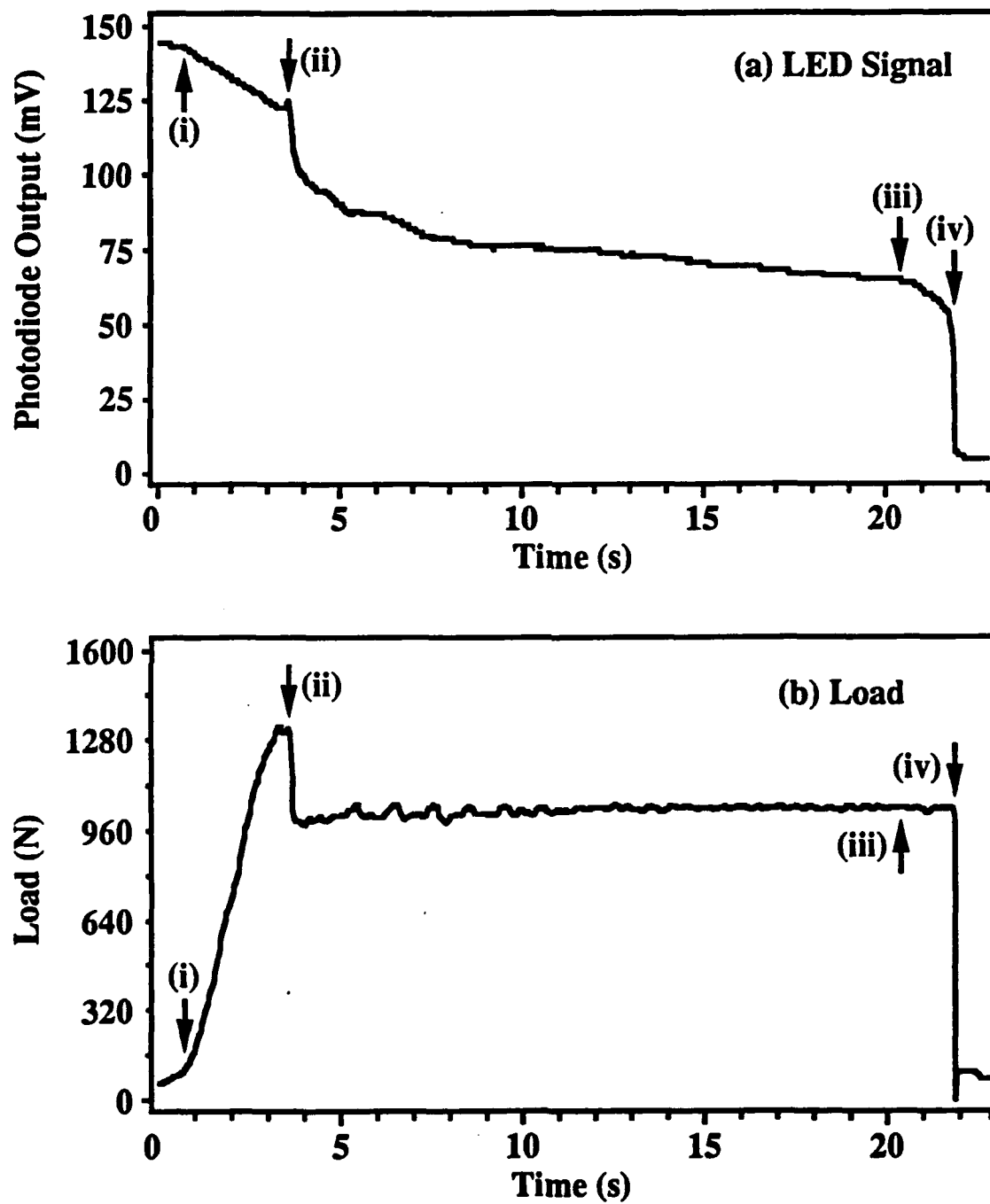
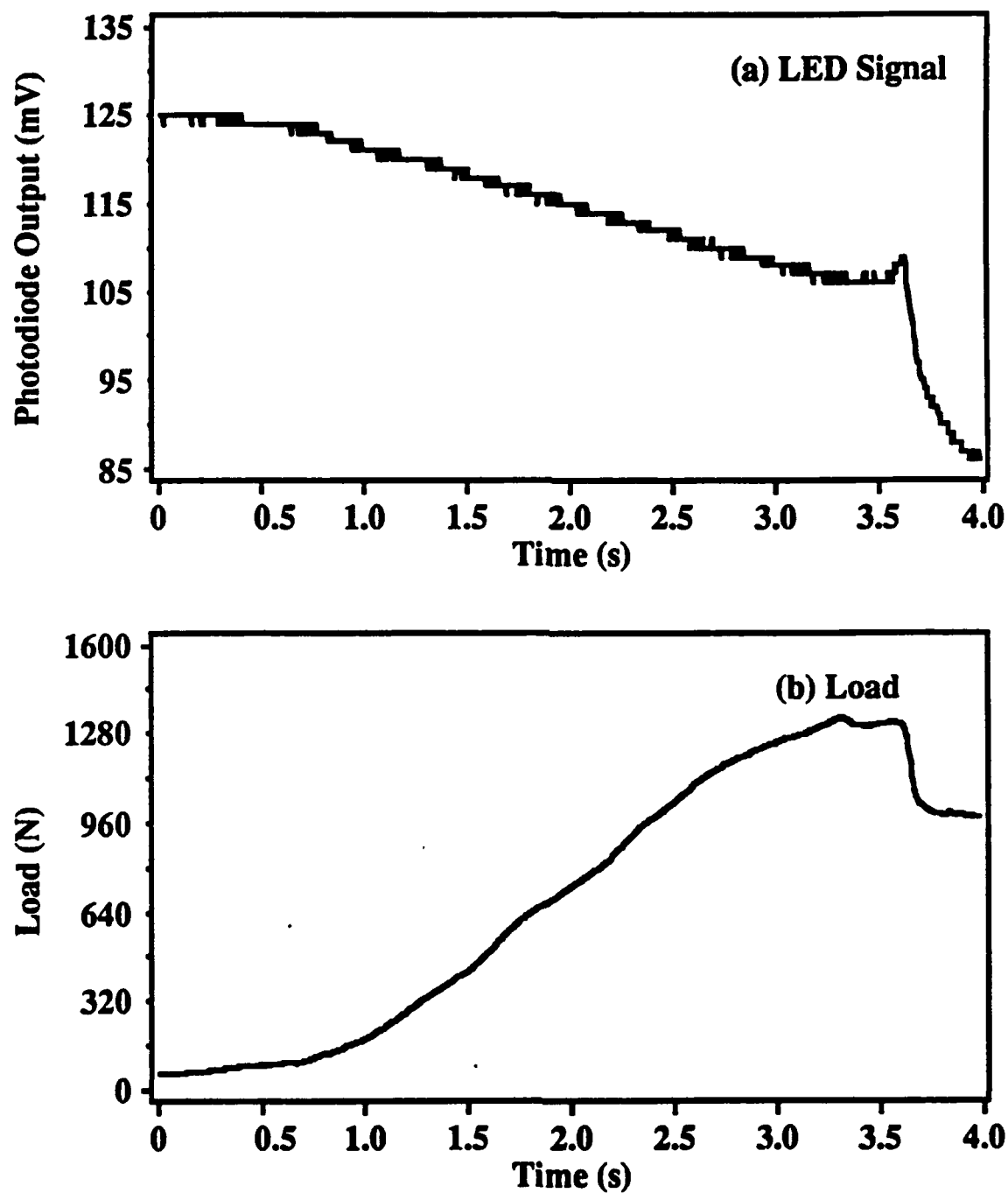


FIG. 7

**LED Signal and Load from Fracture of Polycarbonate****FIG. 8**

**LED Signal and Load from Fracture of Polycarbonate****FIG. 9**

# LED Signal and Load from Fracture of Polycarbonate

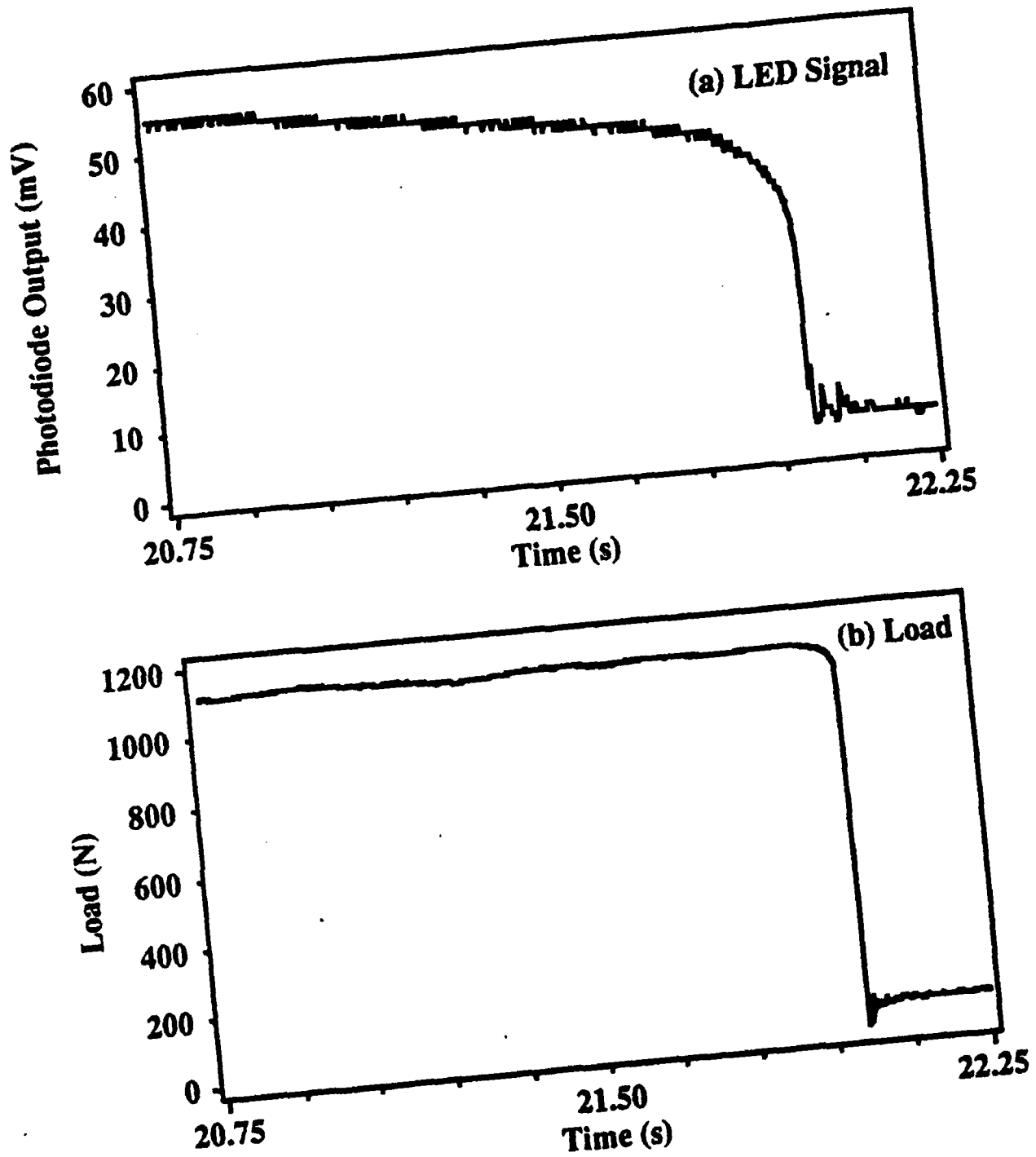
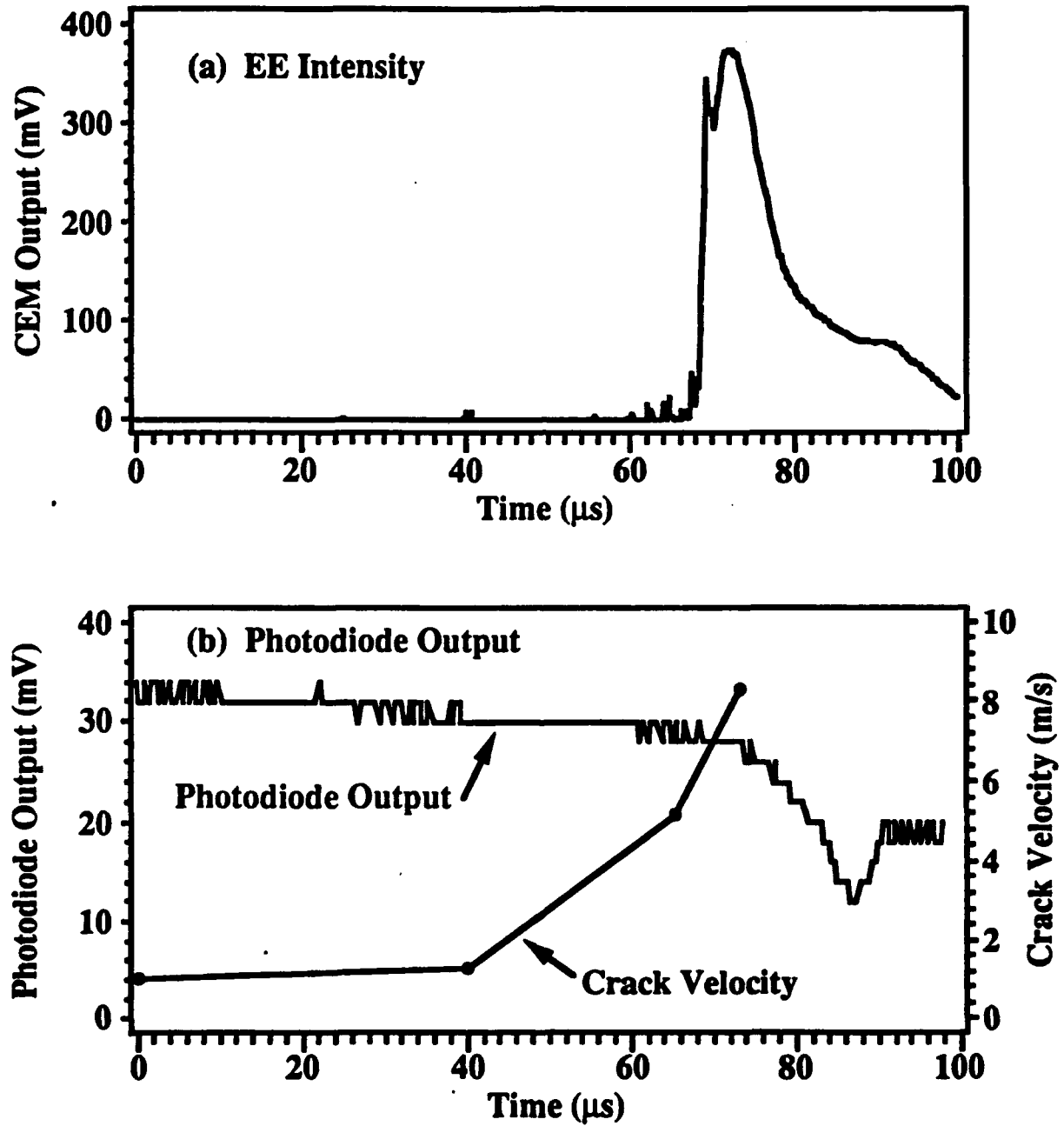
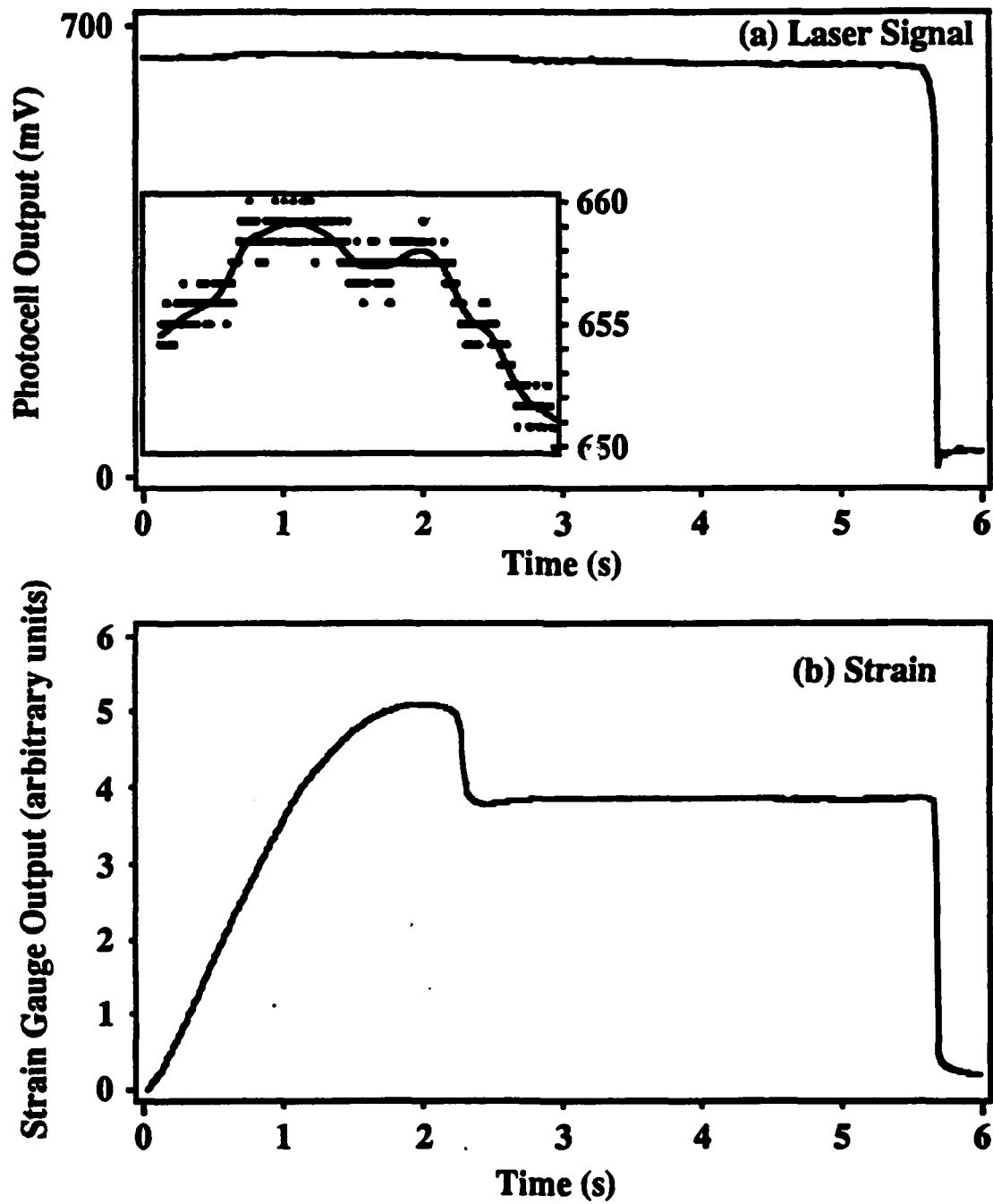


FIG. 10

**EE Intensity and Photodiode Output****FIG. 11**

**Transmitted HeNe Laser Signal and Strain Gauge Output  
During Elongation of Polycarbonate**



**FIG. 12**

# Transmitted HeNe Laser Signal and Strain Gauge Output In Region of Failure of Polycarbonate

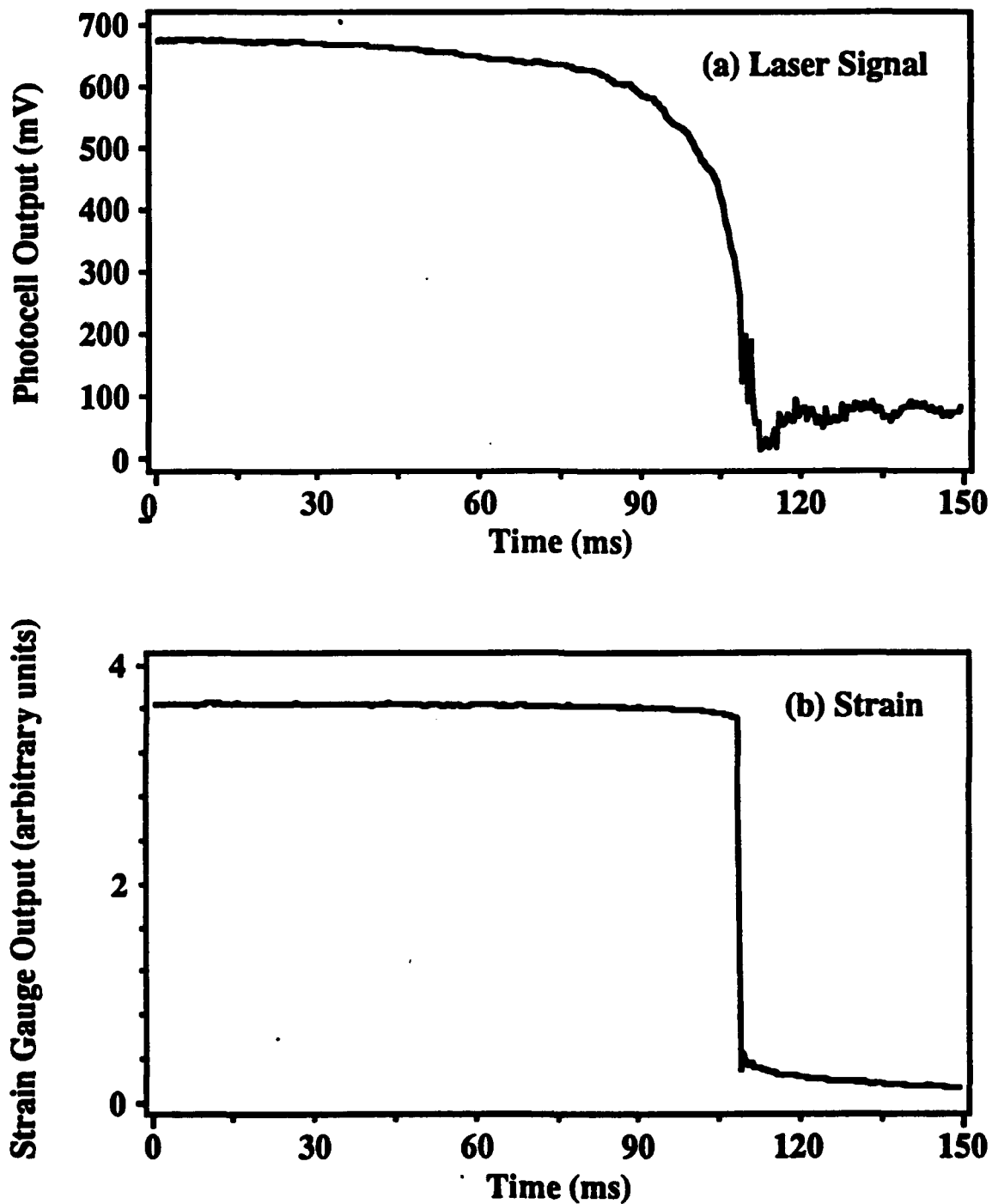
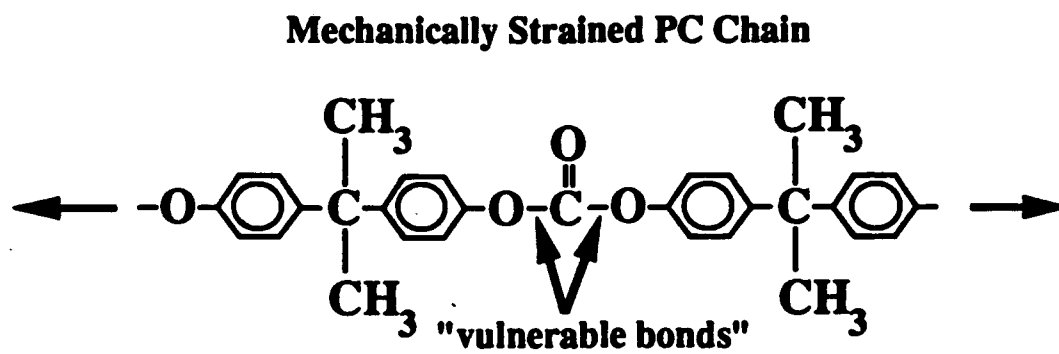


FIG. 13



**FIG. 14**

**V. Fracto-Emission from High Density Polyethylene:  
Bond Breaking vs Tribological Stimulation**

**J. T. Dickinson, L. C. Jensen  
Department of Physics  
Washington State University  
Pullman, WA 99164-2814**

**and**

**R. P. Dion  
The Dow Chemical Company  
Designed Thermoplastics Research  
Midland, MI 48667**

**ABSTRACT**

We re-examine the emission of electrons and positive ions from high density polyethylene (HDPE) during tensile deformation at strain rates on the order of  $30\% \text{ s}^{-1}$ . Earlier reports have suggested that electron emission due to bond scissions accompanying deformation of HDPE have been observed. Here we focus on the role of small frictional effects on the polymer at the edges of the clamps due to slippage during elongation. We show that when slippage is eliminated, the deformation-induced particle emission vanishes. Thus the pre-failure electron and positive ion emission is apparently not due to bond scissions as a result of tensile deformation of the polymer but to slippage of the polymer in the grips. We discuss the processes occurring during tribological loading which produce intense, longer lasting emission during and after stimulation. We present evidence that the emission due to tribological loading involves charge transfer upon contact between metal and polymer, mechanical separation of charge, and subsequent dynamic stimulation of the polymer surface due to energetic charge motion (surface flashover).

**Keywords:** fracto-emission, tribology, abrasion, contact electrification, polymers, interfaces.

## I. INTRODUCTION

Fracto-emission (FE) is the emission of particles (e.g., electrons, ions, neutral species, and photons) due to the deformation and failure of a material. A number of researchers have reported the observation of charged particle emission from tensile deformation of polymers. Polyakov and Krotova<sup>1</sup> first observed electron emission (EE) during the extension of gutta-percha. Zakrevskii and Pakhotin<sup>2,3</sup> observed pre-failure EE from elongation of polyethylene, polyethylene terephthalate, polyurethane rubber, and polycaprolactam. Kurov et al.<sup>4</sup> observed pre-failure EE from tensile deformation of notched, unfilled EPD epoxy. Fuhrmann et. al.<sup>5,6</sup> observed pre-failure EE and positive ion emission (PIE) from high density polyethylene. Most of these measurements were at relatively high strain rates ( 5-10 mm/s for initial sample lengths of ~ 20 mm). This pre-failure emission is sometimes referred to as mechano-emission.

An extremely important aspect of these results is the possible use of these emissions to measure the rate of bond breaking during the deformation process prior to failure. Measurements of unpaired spin densities as a function of deformation show indirectly that bond scissions are indeed occurring as the polymer is strained.<sup>7</sup> However, one must be very careful in determining the origin of the signals observed. In this paper, we re-examine the EE and PIE from the tensile deformation and fracture of high density polyethylene and find that the observed emissions are very sensitive to the type of clamps used to transfer the load to the sample. We show that for this particular material the origin of the pre-emission is due to frictional loading of the polymer due to small amounts of slippage in the clamps. When slipping is eliminated, a characteristic, highly reproducible rapid burst of emission is observed coincident with fracture, followed by a fairly rapid decay on the order of a few seconds in duration. We examine the tribological events necessary to produce these emissions and discuss the role of abrasion and contact electrification. A refined description of the mechanism for the charged particle (and photon emission) accompanying detachment between two dissimilar materials is presented

## II. EXPERIMENTAL

The high density polyethylene (HDPE) used in this study was a blown film of BASF Lupolen 6041. The film had a crystallinity of 86%, a density of  $0.960 \text{ g/cm}^3$ , and a thickness of 80-90  $\mu\text{m}$ . The samples were washed with methanol before use and straining was performed in the machine direction of the manufacturing process. The samples were cut to a width of 10 mm and placed in clamps with a length of 20 mm between the clamps. Unnotched samples of HDPE were strained at a constant rate until fracture at relatively high elongation rates of 6 mm/s or  $30\% \text{ s}^{-1}$  similar to the strain rates used in previous studies. Some of the tribological experiments employed HDPE (U.S. Industrial Chemicals LR 20175) supplied by Quantum Chemical Co.. This material had a density of  $0.95 \text{ g/cm}^3$ , a melt index of 0.1 g/10 min. (Condition E), and a thickness of 50  $\mu\text{m}$ .

Electron emission (EE) and positive ion emission (PIE) measurements were carried out during the deformation and fracture of the polymer samples. The charged particles were detected with two channeltron electron multipliers (CEMs) with the front cone biased at +300 V for collection of electrons and -2600 V for positive ions, respectively. The CEMs produced fast (10 ns) pulses with approximately 90% absolute detection efficiency for electrons and nearly 100% efficiency for positive ions. Standard data acquisition techniques were used to count and store the pulses in a multichannel scaler as a function of time (in 0.1 s time intervals). The background for the EE and PIE was typically 1 count/s. All experiments described here were performed in vacuum at  $10^{-5} \text{ Pa}$ .

Two different clamping systems were used for elongating the polymer samples. One system (A), shown in Fig. 1(a), used uncoated metal clamps which compressed the sample ends. As we were to discover, this system resulted in minute amounts of slipping, particularly at strain rates above a few percent/s. The other system (B), shown in Fig. 1(b), employed rectangles of fine sandpaper (#600) inserted between the HDPE and the metal clamps with the grit oriented towards the HDPE. This arrangement resulted in firm gripping of the HDPE

during the fast straining. The onset of elongation and the instant of fracture were determined by measuring the force applied to the sample. The force was measured with a load cell mounted in the load train inside the vacuum. The load cell output voltage was amplified and then recorded as a function of time with a digitizer. The timing of the start and end of abrasion for the blade experiments was determined by timing markers generated manually with a pulse generator. The uncertainty of determining the onset and completion of abrasion was  $\pm 0.2$  s.

Because we suspected that the differences in emission from samples clamped with and without sandpaper was due to tribological activity, we also measured EE and PIE during abrasion. In separate experiments, HDPE surfaces were abraded with either a stainless steel razor blade or a sharp glass blade. The experimental geometry is shown in Fig. 1(c). Further experiments were performed on bulk HDPE from Quantum Chemical Company in which a stainless steel wedge (radius of curvature  $\sim 100$   $\mu\text{m}$ ) was loaded with a known force and moved laterally across the surface. This arrangement allowed repeated abrasion at high loads.

### III RESULTS AND DISCUSSION

**Emission from Different Sample Clamps.** Figures 2(a) and 2(b) show typical EE and PIE curves (intensities are on logarithmic scales) from type A (metal) clamps, showing emission measured both during and following elongation. In both the EE and PIE, we observe considerable pre-failure emission as well as extensive post-failure emission. This post-failure emission has been shown to require substantial excitation of the polymer surface, very similar to stimulation by high energy electron bombardment, high energy photons, or electrical discharges.<sup>8</sup> The post-failure emission involves a relaxation of high lying trapped charge carriers which are mobile at room temperature and recombine at low lying recombination centers, similar to a number of thermally stimulated luminescence and electron emission phenomena.<sup>9</sup> The positive ion emission during fracture *may* be a direct emission accompanying bond breaking.<sup>10</sup> The emission occurring after fracture, however, as shown by a number of

studies in our laboratory, is best explained in terms of electron bombardment of the surface<sup>11,12,13,14</sup> generating what is known as electron stimulated ion desorption (ESD).<sup>15</sup> It is quite feasible that *all* of the positive ion emission, including that created during fracture is due to ESD.

Figures 3(a) and 3(b) are the same data as Fig. 2 on an expanded time scale to show in more detail the EE and PIE *during* deformation. Fig. 3(c) shows the corresponding force vs time curve plotted on the same time scale. Note that there is no evidence of any drop in force that correlates with the onset of the pre-failure emission. Nevertheless, visual inspection shows that a small amount of slipping is occurring and exposing HDPE which was originally in contact and under the metal clamp. When the HDPE under the clamps is marked with a felt-tip pen prior to clamping, we consistently observed the extension of the colored portion of the film 1-5 mm beyond the clamp edge during loading.

When steps are taken to prevent such slipping, the emissions are dramatically altered. Figures 4(a) and 4(b) show typical EE and PIE for type B (with sandpaper) clamps. First, compared with type A clamps, the total emission intensity is reduced considerably. Furthermore, the pre-failure emission is dramatically reduced; the major feature for type B clamps is the burst of emission at failure. The emission after fracture is also much weaker. Figure 5 shows the EE, PIE, and force vs time curves for the same test on an expanded time scale. The pre-emission is only a few counts above background (typically 1 count/s). Type B clamps yielded at most sub-millimeter pullout when marked with the felt-tip pen as described in the paragraph above.

Table I summarizes the emission results for nine samples for each of the two clamping systems. In Table I, the peak count is the number of charged particles in the 0.01 s time interval surrounding the fracture event, the pre-fracture count is the number of charged particles counted between the onset of straining and failure, and the post-fracture count is the number of charged particles counted in the first 10 seconds *after* fracture. One notices the significant decrease in the number of pre-fracture and post-fracture counts when type B (with sandpaper) clamps are

used instead of type A clamps. Although the scatter for each category is high, the differences between Type A and Type B clamping are dramatic and statistically significant. In the case of Type A clamps, the degree of damage due to slipping varied from sample to sample, which explains the widely varying emission intensities both during slipping and following fracture. Nevertheless, in comparing these clamping arrangements, we observe differences of over a factor of 100 in the pre-failure EE counts and almost a factor of 20 in the pre-failure PIE. Equally dramatic decreases in the EE and PIE post-failure emission are also observed when slipping is eliminated, suggesting that intense post-failure emission and slipping are correlated.

Pre-emission was also effectively suppressed in Type A clamps by wrapping aluminum foil around the ends of the sample to cover the region of the sample that would slip out of the clamps. Conversely, placing the detectors near one of the clamps enhanced the pre-failure emissions. The emissions were also sensitive to the pressure applied to the sample by Type A clamps. Light clamping usually produced *no* detectable emission despite substantial slipping. Heavy clamping often limited the amount of slipping considerably, and correspondingly displayed weak emissions. However, intermediate pressures generally displayed significantly stronger emissions. Post-failure examination of these samples showed that visible damage on the surfaces drawn from the clamps. Thus high emission intensities appear to be associated with surface damage produced by the clamps.

Thus, we conclude the following:

- Little (if any) of the pre-failure emission observed in Figs. 2 and 3 can be attributed to elongation and plastic yielding of the HDPE.
- The excitations produced by polymer fracture are insufficient to produce the long lasting post-failure emission.
- In the absence of surface damage produced by the clamps, fracture does yield reproducible bursts of EE and PIE; we propose that these signals are in fact a consequence of rapid bond breaking accompanying polymer failure.

- Tribological loading of the HDPE surface appears to be very effective in producing relatively intense EE and PIE both during and following relative motion of the surfaces.

To test further the concept that tribological loading (sliding and/or abrasion) was responsible for these observed differences in emission from HDPE, several abrasion experiments were done. Fig. 1(c) shows one arrangement of the surfaces we utilized. HDPE (1 cm wide, 80  $\mu$ m film) was strung across a sharp blade (similar to a bow of a violin pushing on a string) and translated at a speed of approximately 1 cm/s. Figures 6(a) and 6(b) show the EE due to the abrasion of HDPE by a stainless steel razor blade. Figures 7(a) and 7(b) show the EE caused by abrading HDPE with a sharp glass blade. (The glass blade was produced by fracture.) HDPE abraded with a sharp blade of either material yields intense EE during abrasion which continues for several minutes afterwards. The damage (scratches) produced by these blades was clearly visible with the naked eye. Although more intense, the emission during and following the abrasion of HDPE is very similar to the EE and PIE caused by straining HDPE gripped with metal (Type A) clamps.

**Mechanisms.** The origin of virtually all of the pre-failure emission in Figs. 2 and 3 is not due to deformation-related bond breaking, but rather tribological loading as the sample slips from the Type A clamps. This obviously leads to the question of the emission mechanism associated with tribological loading. The damage on the polymer surface due to abrasion is not insignificant, and one is tempted to attribute the emission to a bond breaking mechanism, i.e., broken bonds created by the microscopic abrasion process. At first glance, the fact that both metal and glass blades produce essentially identical emissions suggests that the degree of surface damage is the critical factor rather than the nature of material used to abrade the surface. Certainly the amount of damage is important, since a visual inspection showed that the samples with the most intense FE signals also had the most visible surface damage in the regions abraded by the clamps.

Nevertheless, it is well known that charge transfer between dissimilar material can play a very important role in the generation of fracto-emission. Many studies on the peeling of polymers



from a number of substrates have shown intense, long lasting fracto-emission signals (e.g., electrons<sup>16,17</sup> and photons<sup>15-25</sup>). In all of these cases, strong adhesion existed between the polymer and substrate and intimate contact was established between the two materials for several minutes to hours before detachment. Under these conditions, charge is readily transferred across the interface between the dissimilar materials (driven by differences in Fermi levels), resulting in "contact electrification."<sup>26</sup> Measurements with an electrostatic charge probe show that contact between HDPE with stainless steel results in a net negative charge transfer to the HDPE. Lowell and Rose-Innes<sup>26</sup> have discussed processes whereby charge carriers, usually electrons, can flow in *both* directions across a contact interface, with a net flow in one dominating direction. We propose that the polyethylene *loses* some electrons (creating positive ions), but accepts *many more* electrons which occupy high electron affinity sites (creating negative ions) and thus gains an overall negative charge. Although the charge in the metal is very mobile, electrons in the HDPE tends to be localized at high electron affinity sites, perhaps defect sites, or as positive ions and is thus relatively immobile.

In the first stages of separation, small displacements of the two surfaces tends to drive charge back to its original "owner", thus producing a *redistribution* of electrons between the two surfaces resulting in de-excitation events (e.g., electron-positive ion recombination) occurring in the polymer surface/near surface region, yielding EE via non-radiative transitions (possibly Auger transitions). Although not studied in this particular system, radiative transitions would be expected to yield photon emission with essentially the same kinetics.

As an additional experimental test of these concepts, we devised a friction experiment involving a grounded stainless steel abrader and a bulk HDPE sample where the compressive load between the metal and polymer could be controlled from outside the vacuum, repeated translations across the surface could be performed. In addition, the metal tool could be vertically lifted rapidly from the horizontal surface [see Fig 8(a)].

As in the previous abrasion experiments, at loads below creation of visible damage, very little emission was created by horizontal motion, whereas at high loads (30-50 N), where

noticeable "plowing" of the HDPE occurred, intense, long lasting emission resulted (a factor of 10 more intense than shown in Fig. 7). If the metal tool was first placed on the "virgin" surface and loaded with 50 N, left in contact for 5 minutes, then rapidly detached by lifting vertically, very little emission was observed. In contrast, when the surface was first abraded at 50 N load and the tool left in contact in the center of the wear track at 50 N load for 5 minutes, then lifted, a substantial burst of emission is observed which is followed by the classic decay following detachment [Fig. 8(b)]. The high background (extended by the dotted line) prior to detachment is the post-abrasion emission after 5 minutes of decay. Thus, intimate contact between the metal and "abraded" HDPE or by abrasion alone produces enhanced EE. In contrast, essentially no emission was detected from detachment following prolonged contact between the metal and an "as-received"(unabraded) HDPE surface. In situ charge density measurements showed that the damaged surfaces were charged negatively and the regions where sustained contact had been made showed ~40% more negative charge than the surrounding damaged region.

In terms of the contact results, the exact role of pre-damaging the surface is not clear. The overall nature of metal/polymer contact charging is known to be strongly influenced by the chemical nature of the contacting surfaces<sup>27,28</sup> which would be different for the "as received" vs freshly ploughed surface. Polyethylene is known to oxidize, and the branched polymer is measurably less stable than linear polyethylene.<sup>29</sup> Thus, the "as-received" surface could very well differ electronically from the bulk material, the latter becoming exposed by abrasion. Multiple contacts occurring during the slipping could also lead to much higher charge densities.<sup>30</sup> Metal-polymer contacts can produce separated charge densities of  $\sim 10^{-4}$  C/m<sup>2</sup> (measured *after* separation).<sup>31,32</sup> which yields electric fields of  $\sim 10^7$  V/m and therefore potential differences of several kV for sub-mm separations.

In addition, the electrostatic interaction of the newly formed charge on the damaged surface with the grounded metal tool could lead to changes in the polymer surface charge distribution. Accumulated surface charge on insulating surfaces can be highly unstable in the sense that micro-flashover events can occur. These events are evident by bursts of electrons of

high intensity and short duration. Using a digital oscilloscope (Lecroy 9450) we can obtain either single bursts or signal averaged bursts on a very fast time scale. Figure 9 shows an average of 100 bursts that are due to these flashover events; also shown on the same scale is a typical signal generated by an isolated, single electron striking the detector. The ratio of the areas indicates that we are detecting  $\sim 10^2 - 10^3$  electrons per burst. These bursts are most likely secondary electrons created and ejected from the surface when the flashover event occurs. Furthermore, accompanying bursts of positive ions are also seen, supporting the concept of energetic electrons moving across the surface, ricocheting off near surface polymer structures, producing ion bursts via electron stimulated desorption. In vacuum, these bursts can be seen to occur at extremely high rates during abrasion, and are followed by a slow decay of bursts amongst the slowly decaying single electron signal. We have observed bursts as long as 30 minutes after abrasion. Such long lasting electrical activity requires substantial charge separation. In the case of HDPE, these transient bursts are only evident when polymer damage has occurred and in vacuum where charge neutralization from the gas phase is blocked.

Finally, allowing the HDPE film to slip between stainless steel clamps (Type A) in room air, we have immediately dusted the exposed surface with a mixture of black photocopier toner (positive seeking) and fine white  $\text{TiO}_2$  powder (negative seeking). Whenever sufficient clamping pressure was used to cause abrasive damage to the film, we found toner images associated with mobile electron discharge tracks on the pullout surface. These tracks are revealed as black positive "trees" on large (white) patches of negative charge. This provides additional evidence for significant charge separation and charge motion along the polymer surface when abrasion and metal/polymer detachment has occurred during metal/HDPE tribological loading. We point out that with proper instrumentation, one can also make dynamic measurements of induced electrical transients produced during similar metal/polymer interfacial separation.<sup>32</sup> Recently, Horn and Smith<sup>33</sup> using an atomic force apparatus have measured substantial forces due to the electrostatic charge generated between mica and silica surfaces during detachment. They determined that the electrostatic component of the work of adhesion is

typically  $\sim 7 \text{ J/m}^2$ . Using the transient electrical currents produced during rapid debonding of a metal/epoxy interface we determined an electrostatic contribution to the work of adhesion of  $\sim 1 \text{ J/m}^2$ .

In summary, we propose that the dominant cause of charged particle emission accompanying tribological loading and interfacial failure between dissimilar materials results from the charge separation produced by contact electrification. Mobile charge carriers (in the case of stainless steel/HDPE, electrons are the most likely charge carrier) and recombination centers (+ ions) are created on the polymer surface during the detachment process. Acceleration of charge in the resulting E fields results in bombardment of the polymer surface causing additional excitations leading to EE and ESD-induced PIE emission. Instabilities in the charge patches (surface flashover) on the polymer surface lead to bursts of EE and PIE after detachment. As mentioned previously, very similar behavior in the photon emission is expected due to radiative recombination.<sup>25,34</sup> Although not investigated here, other interfacial detachment experiments often show gaseous discharges occurring, characterized by pH<sub>E</sub> consisting of characteristic line spectra of the gas (e.g., in air: N<sub>2</sub> lines).<sup>23</sup>

#### IV. CONCLUSION

When HDPE samples are held firmly and strained, pre-failure EE and PIE are very small and a burst of emission occurs at the instant of fracture; the post-failure emissions last for only a few seconds. However, when HDPE samples are not held firmly (particularly at high strain rates), and samples are held only with metal clamps, easily detected EE and PIE can occur during straining. This intense pre-failure emission is caused by small amounts of slipping of the samples from beneath the clamps causing fairly localized abrasion and accompanying excitation of the polymer. Abrasion experiments with two different materials (metal and glass) support the concept that abrasion is required for these intense signals. However, more detailed studies of the metal/polymer interaction indicates that the consequences of charge separation due

to the contact of metal with damaged polymer material is responsible for the accompanying intense, long lasting emission. In the case of HDPE, intimate contact between damaged (abraded) polymer and metal appear to be required to achieve efficient charge transfer; the surface species created by abrasion could be essential for the process. Dynamic motion of mobile charge experiencing very high accelerating potentials may be the major source of the excitations causing emission.

In the near future we hope to measure the neutral products created during abrasion of HDPE while simultaneously detecting the charged particle emission. Particular neutral species may be indicative of direct bond breaking (see, for example, Refs. 35 and 36 ) and could be correlated in time and intensity with the charged particle emission. This would probe what role bond breaking created by abrasion might have in producing the tribologically stimulated charged particle emission. We also plan to measure the photon emission to verify the role of recombination in the overall fracto-emission process accompanying abrasion.

Finally, concerning the small but reproducible fracto-emission signals seen accompanying fracture, correlations with specimen parameters which vary the number of bonds broken during failure could also prove useful. Eventual quantification of the signal intensity with bond breaking rates could provide information of use in the molecular design of polymers.

## ACKNOWLEDGMENTS

The authors wish to thank Steve Behler and Ed Donaldson for assistance in acquiring data and Professor J. Fuhrmann and Dr. Leo Nick, University of Clausthal, and Dan Hays and L. H. Lee, Xerox Corporation, Roger Horn and Douglas Smith, NIST, for helpful discussions. This work was supported by The Dow Chemical Company, AFOSR Contract F33615-91-C-0093, and the Washington Technology Center.

### Figure Captions

- Figure 1.** Schematic representation of sample arrangements showing (a) HDPE clamped between metal only (Type A) and (b) HDPE clamped between small pieces of fine grit sand paper and metal. The arrangement for abrading the HDPE by sharp blades of stainless steel or glass is shown in (c).
- Figure 2.** (a) EE and (b) PIE produced from the tensile deformation and fracture of HDPE using Type A clamps (metal only).
- Figure 3.** The same emission as Fig. 2 displayed on a faster time scale: (a) EE, (b) PIE, and (c) the applied force vs time.
- Figure 4.** (a) EE and (b) PIE produced from the tensile deformation and fracture of HDPE using Type B clamps (metal + sandpaper).
- Figure 5.** The same emission as Fig. 4 displayed on a faster time scale. (a) EE, (b) PIE, and (c) the applied force vs time. Note the lack of pre-failure emission.
- Figure 6.** (a) EE accompanying and following the abrasion of HDPE with a stainless steel blade, and (b) the same data on an expanded time scale showing electron emission during abrasion.
- Figure 7.** (a) EE accompanying and following the abrasion of HDPE with a sharp glass blade, and (b) the same data on an expanded time scale showing electron emission during abrasion.

**Figure 8.** (a) Schematic of the detachment experiment where the stainless steel tool can be loaded in compression onto the HDPE surface or lifted from the surface, as desired. Motion of the HDPE in the horizontal direction allows abrasion to be carried out. (b) the EE approximately 5 minutes after abrasion (left hand side) and the accompanying EE burst when the metal tool is lifted from the HDPE surface.

**Figure 9.** Signal averaged form of the fast bursts seen in the EE due to transient, energetic motion of charge on the abraded surface. the insert shows the typical size and shape of the signal generated by the detection of one electron. Note the relatively fast time scale.

Table I

**HDPE EE and PIE Counts from Two Different Sample Clamping Systems**

	EE Counts			PIE Counts		
	peak	pre-fracture	post-fracture	peak	pre-fracture	post-fracture
Type A	370	6640	54000	160	720	5500
Clamps	$\pm 130$	$\pm 1400$	$\pm 20000$	$\pm 90$	$\pm 400$	$\pm 2500$
Type B						
Clamps	640	65	250	290	40	40
(+Sand-paper)	$\pm 110$	$\pm 20$	$\pm 80$	$\pm 70$	$\pm 10$	$\pm 16$

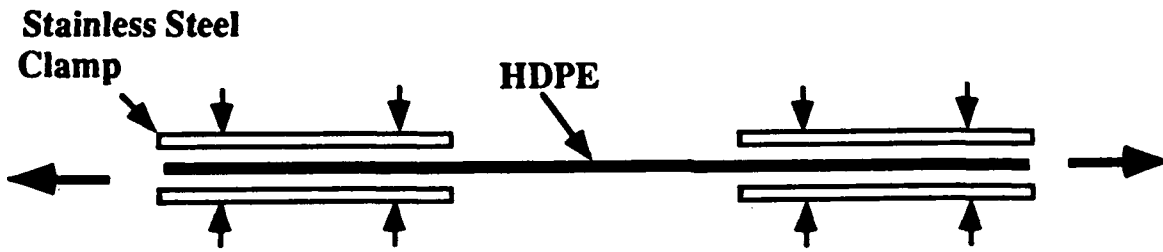


## References

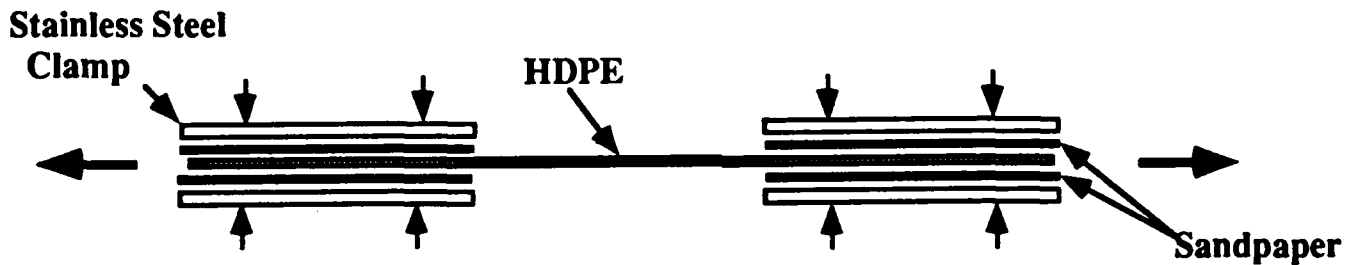
1. A. M. Polyakov and N. A. Krotova, *Dokl. Akad. Nauk. SSSR* **151**, 130 (1963).
2. V. A. Zakrevskii and V. A. Pakhotin, *Vysokomol. soyed.* **A17**, 568 (1975).
3. V. A. Zakrevskii and V. A. Pakhotin, *Sov. Phys. Solid State* **20**, 214 (1978).
4. I. E. Kurov, A. V. Movshovich, and V. P. Novozhilov, *Mekhanika Kompositnykh Materialov* **4**, 579 (1983).
5. J. Fuhrmann, G. H. Scherer, and R. Hofmann, *Polym. Commun.* **27**, 164 (1986).
6. J. Fuhrmann, G. H. Scherer, and L. Nick, *Makromol. Chem.* **188**, 2241 (1987).
7. H. H. Kausch, *Polymer Fracture*, 2nd Edition, Springer-Verlag, Berlin (1987) pp. 141-197.
8. J. T. Dickinson and L. C. Jensen, *J. Poly. Sci.: Poly. Phys. Ed.*, **23**, 873 (1985).
9. R. Chen and Y. Kirsh, *Analysis of Thermally Stimulated Processes*, Pergamon, Oxford, 1981, pp. 16-23.
10. S. C. Langford, J. T. Dickinson, and L. C. Jensen and L. R. Pederson, *J. Vac. Sci. Technol. A*, **7**, 1829 (1989).
11. J. T. Dickinson, L. C. Jensen, and M. K. Park, *Appl. Phys. Lett.* **41**, 443 (1982).
12. J. T. Dickinson, L. C. Jensen, and M. K. Park, *Appl. Phys. Letts.* **41**, 827 (1982).
13. J. T. Dickinson and L. C. Jensen, *J. Vac. Sci. Technol.* **A1**, 1160 (1983).
14. J. T. Dickinson and L. C. Jensen, *J. Poly. Sci.: Poly. Phys. Edition* **23**, 873 (1985).
15. G. Betz and P. Varga, eds., *Desorption Induced by Electronic Transitions: DIET IV*, Springer Verlag, Berlin (1990).
16. B. V. Deryagin, N. A. Krotova, and V. P. Smilga, *Adhesion of Solids*, Consultants Bureau, New York, 1978, pp. 95-100.
17. J. T. Dickinson, M. K. Park, E. E. Donaldson, and L. C. Jensen, *J. Vac. Sci. Technol.* **20**, 436 (1982).

18. K. Ohara and T. Hata, *J. Appl. Polym. Sci.* **14**, 2079 (1970).
19. B. V. Deryagin, B. V.; Tyurikova, L. A.; Krotova, N. A.; Toporov, Y. P.; *IEEE Indust. Appl. VI. IA-14*, 541 (1978).
20. V. A. Klyuev, et al., *Colloid Journal (Kolloidn Zh.)* **41**, 287 (1979).
21. E. E. Donaldson, J. T. Dickinson, and X. A. Shen, *J. Adhesion* **19**, 267 (1986).
22. J. T. Dickinson and E. E. Donaldson, *J. Adhesion*, **24**, 199 (1987).
23. Ma Zhenyi, Fan Jiawen, and J. T. Dickinson, *J. Adhesion* **25**, 63 (1988).
24. E. E. Donaldson and J. T. Dickinson, *J. Adhesion* **30**, 13 (1989).
25. J. T. Dickinson, "Fracto-emission from adhesive failure," Review, in *Adhesive Bonding*, L. H. Lee, ed., (Plenum Press, New York, 1991), pp. 395-423.
26. J. Lowell and A. C. Rose-Innes, *Contact Electrification*, *Adv. Phys.* **29**, 947 (1980).
27. D. A. Hays, *J. Chem. Phys.* **61**, 1455 (1974).
28. J. Lowell and A. Brown, *J. Electrostatics*, **21**, 69 (1988).
29. W. L. Hawkins, "Polymer Degradation and Stabilization," Springer Verlag, Berlin, 1984, pp. 13-16.
30. K. P. Homewood, J. Lowell, and A. C. Rose-Innes, *Inst. Phys. Conf. Ser. No. 66: Electrostatics 1983*, Oxford, (1983), pp. 225-230.
31. D. K. Davies, *J. Phys. D* **2**, 1533 (1969).
32. K. A. Zimmermann, S. C. Langford, and J. T. Dickinson, *J. Appl. Phys.* **70**, 4808 (1991).
33. R. G. Horn and D. T. Smith, "Contact Electrification and Adhesion Between Dissimilar Materials," *Science* **256**, 362 (1992).
34. Ma Zhen-Yi and J. T. Dickinson, *J. Appl. Phys.* **70**, 4797 (1991).
35. e.g., M. A. Grayson and C. J. Wolf, *J. Polym. Sci.: Polym. Phys. Ed.* **1985**, **23**, 1087.

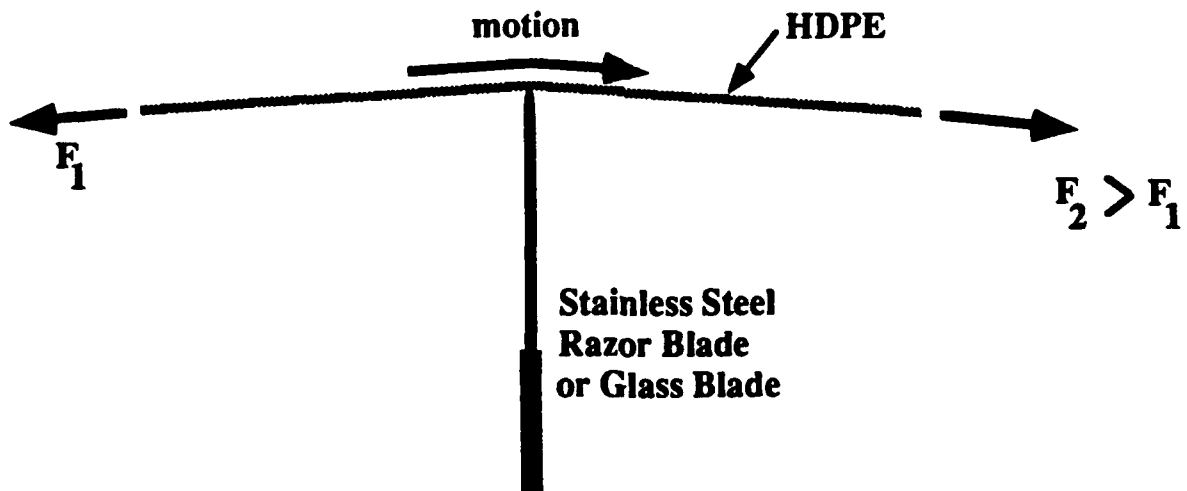
36. J. T. Dickinson, L. C. Jensen, S. C. Langford, and R. P. Dion, "CO emission accompanying fracture of polycarbonate: evidence for molecular cleavage", to be submitted.



a) Type A Sample Clamp



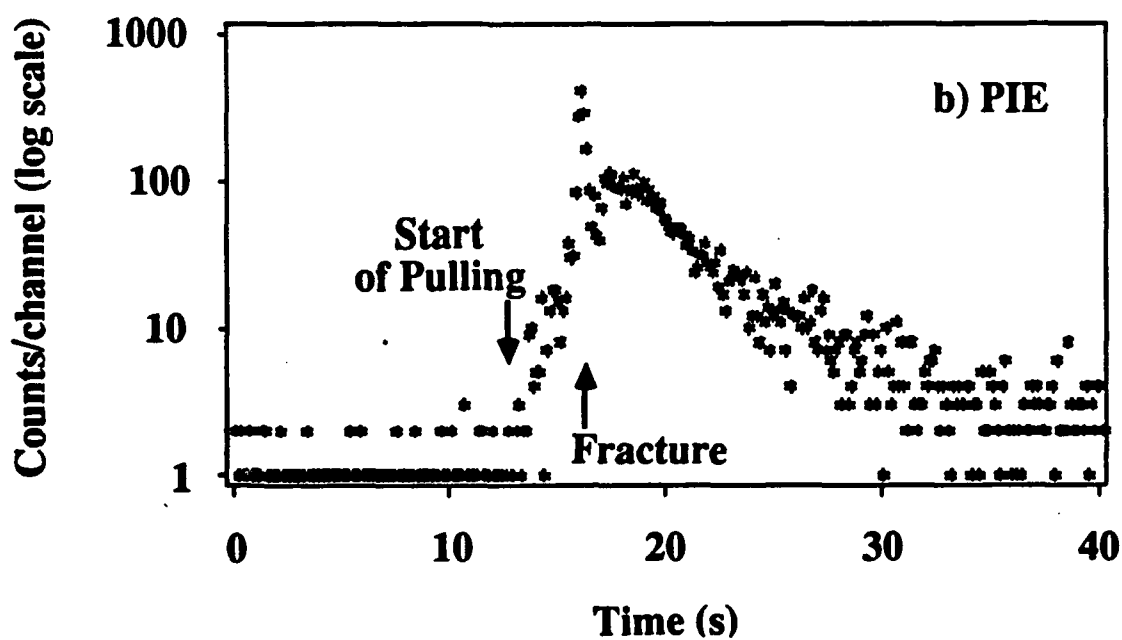
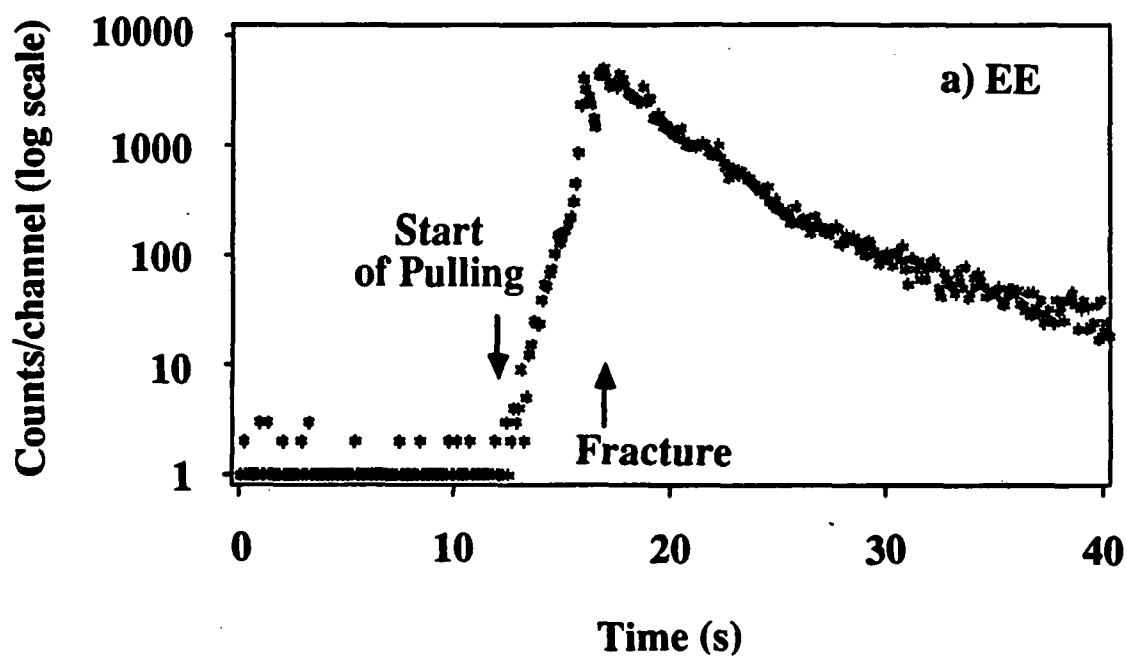
b) Type B Sample Clamp



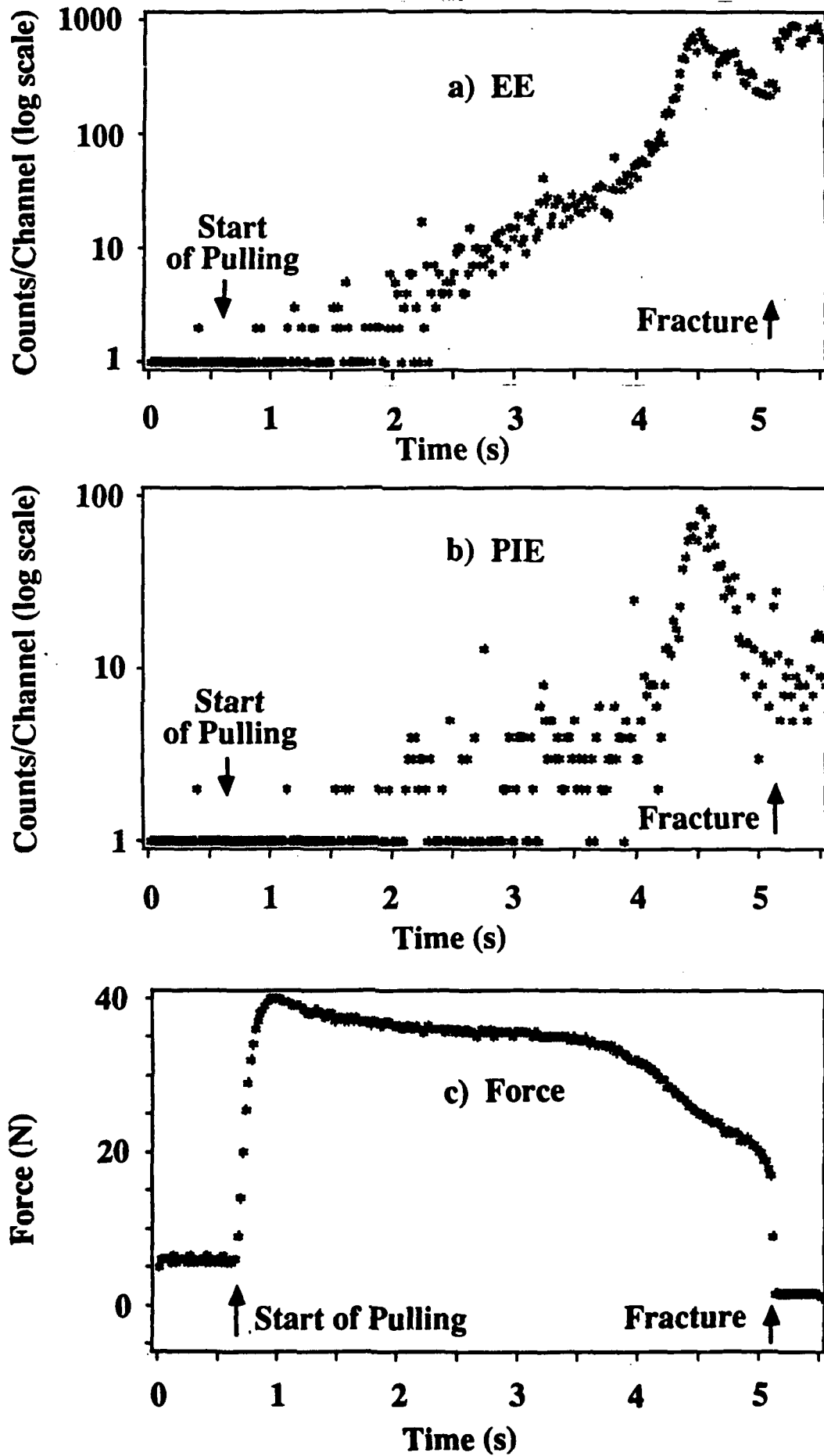
c) Direct Abrasion of HDPE

Fig. 1

**Electron and Positive Ion Emissions from HDPE :  
Type A Clamps**



# EE, PIE, and Applied Force vs Time During Elongation: Type A Clamps



**Electron and Positive Ion Emissions from HDPE :  
Type B Clamps**

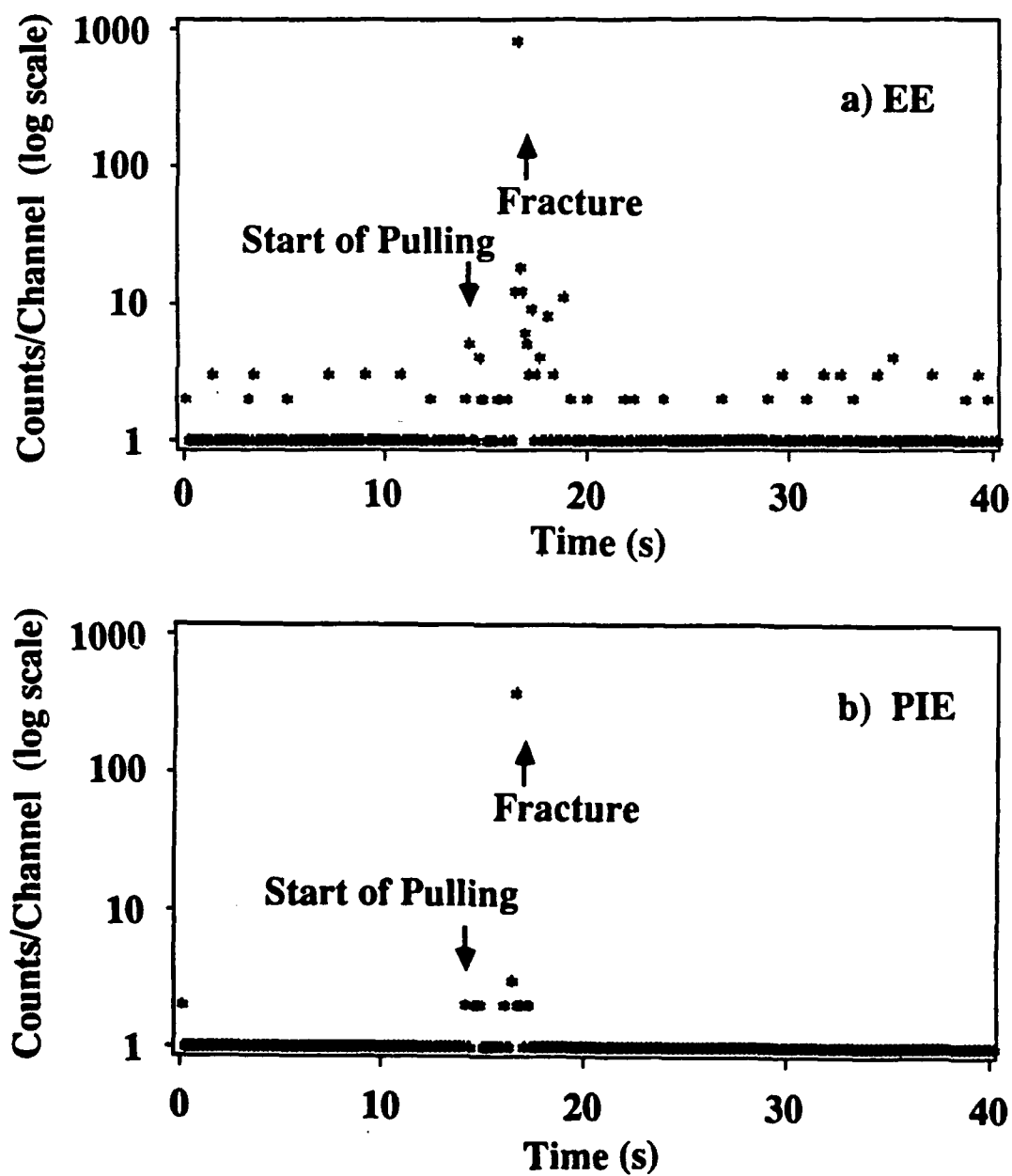


Fig. 4

# EE, PIE, and Applied Force vs Time During Elongation : Type B Clamps

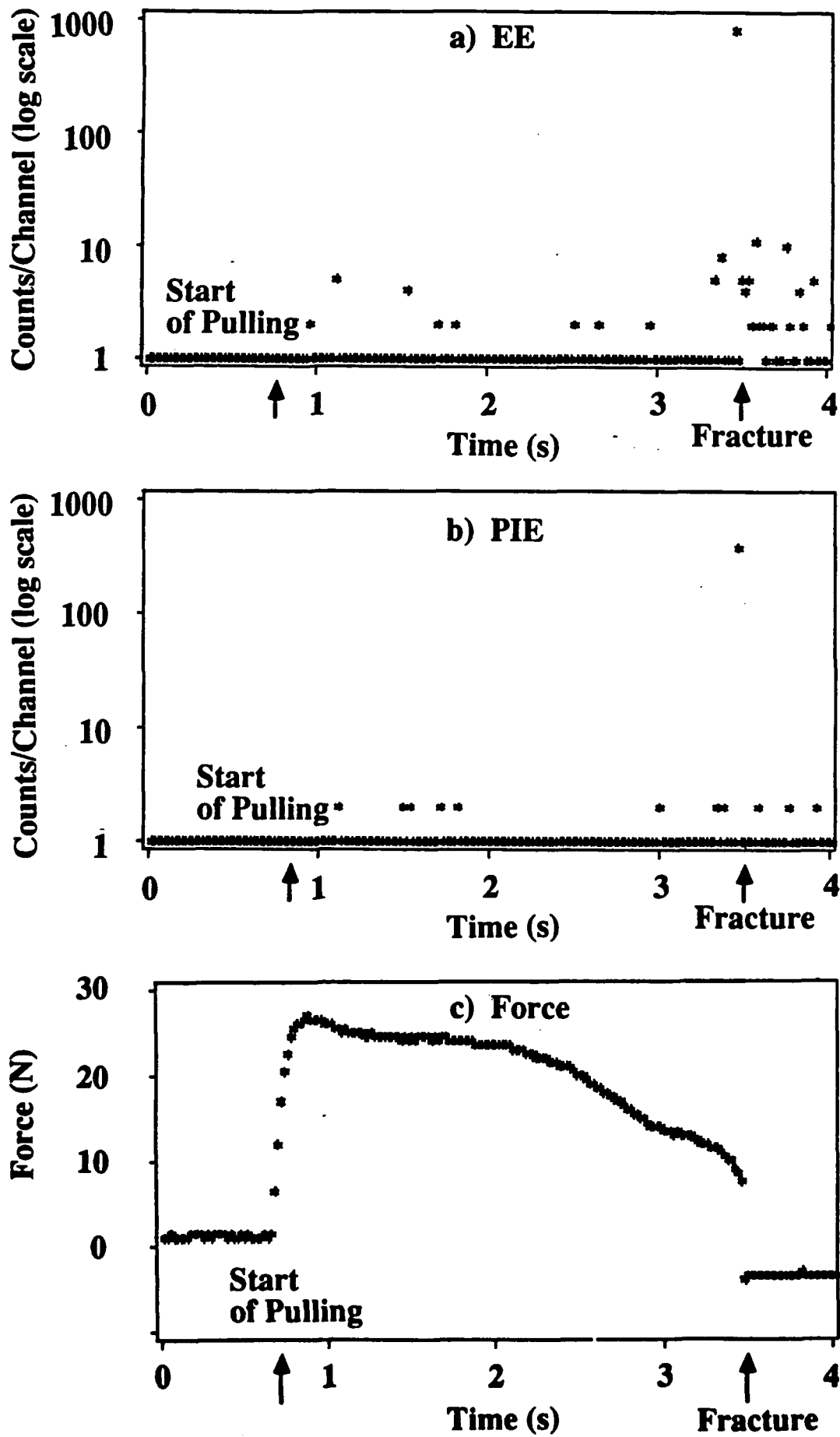
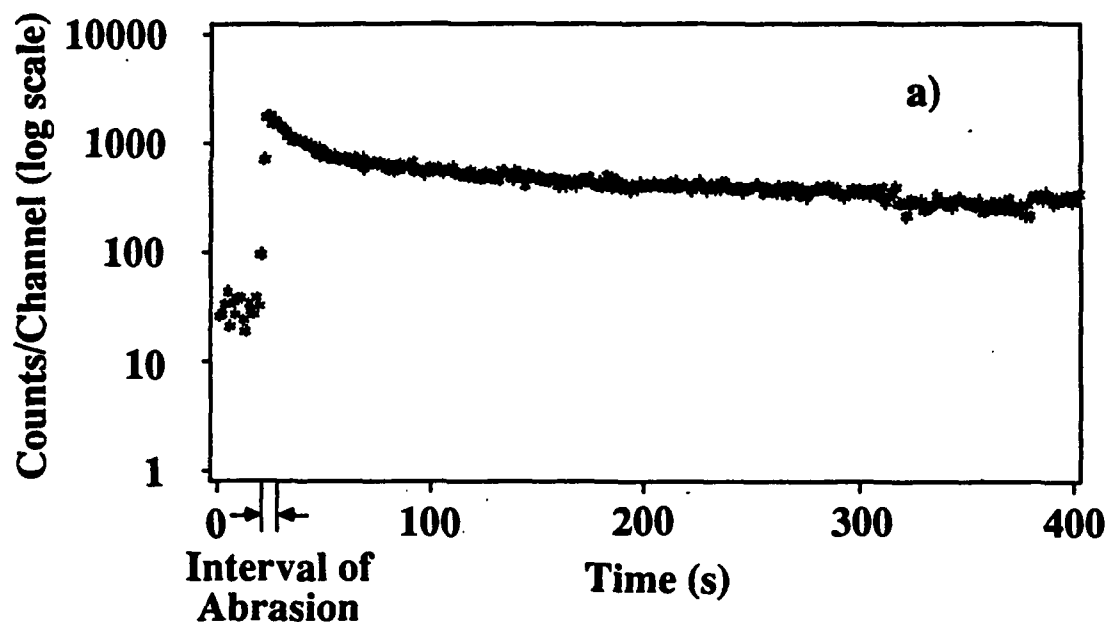


Fig. 5



### Electron Emission During and Following Abrasion of HDPE with a Stainless Steel Razor Blade



### Electron Emission During Abrasion of High Density Polyethylene with a Stainless Steel Razor Blade

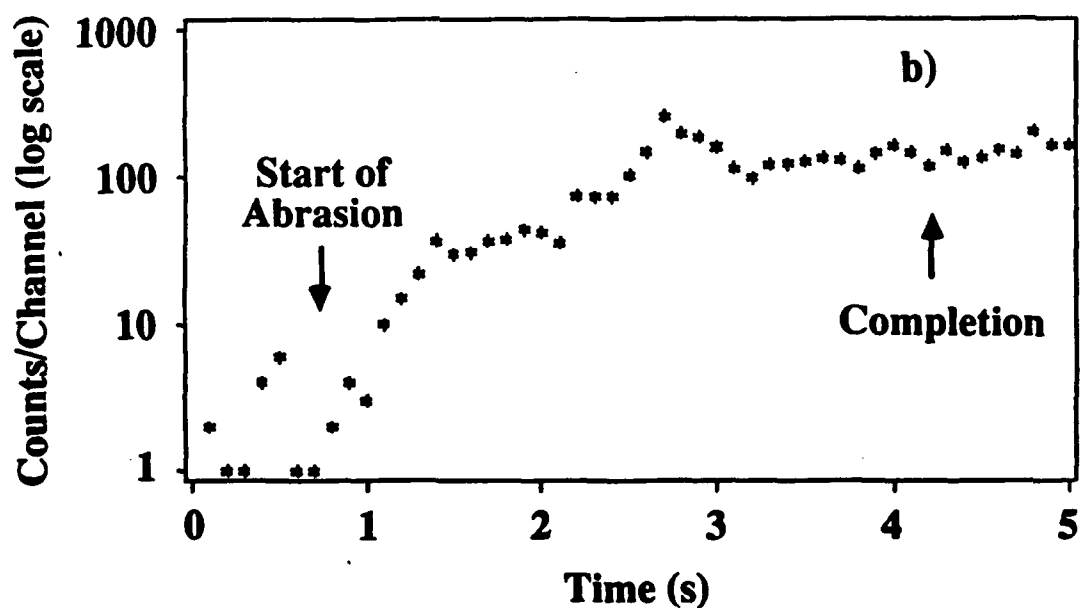
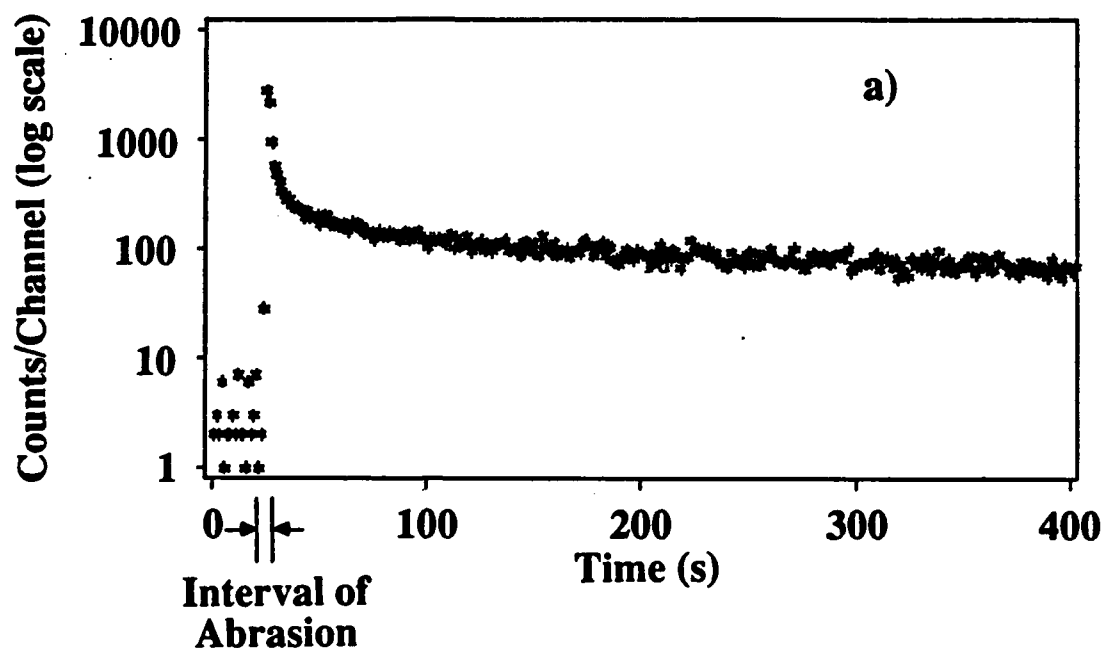
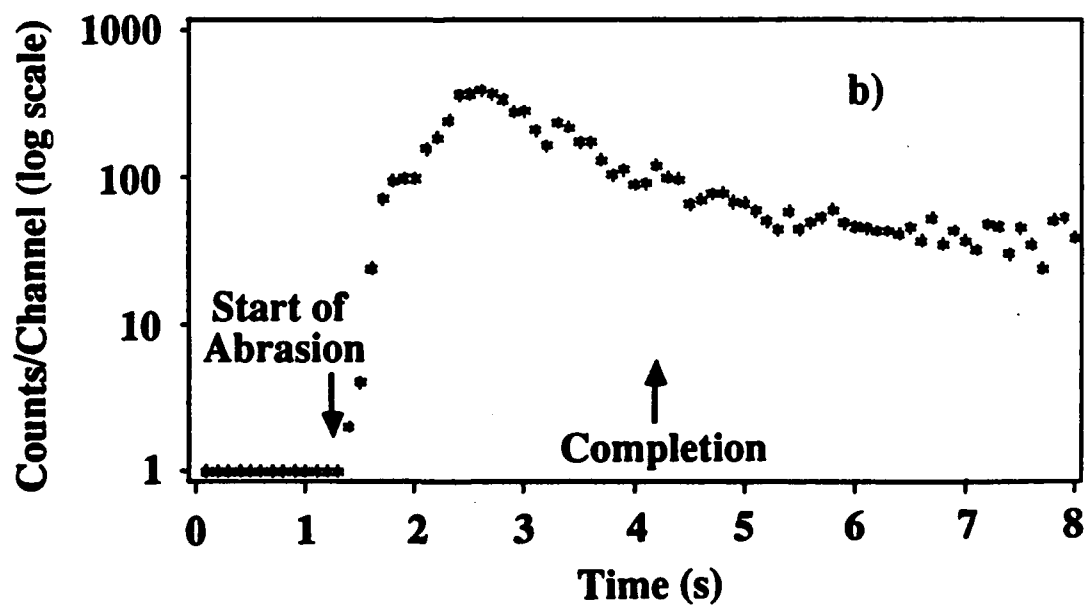


Fig. 6

### Electron Emission During and Following Abrasion of HDPE with a Sharp Glass Blade



### Electron Emission During Abrasion of High Density Polyethylene with a Sharp Glass Blade



# Metal/HDPE Detachment Experiment

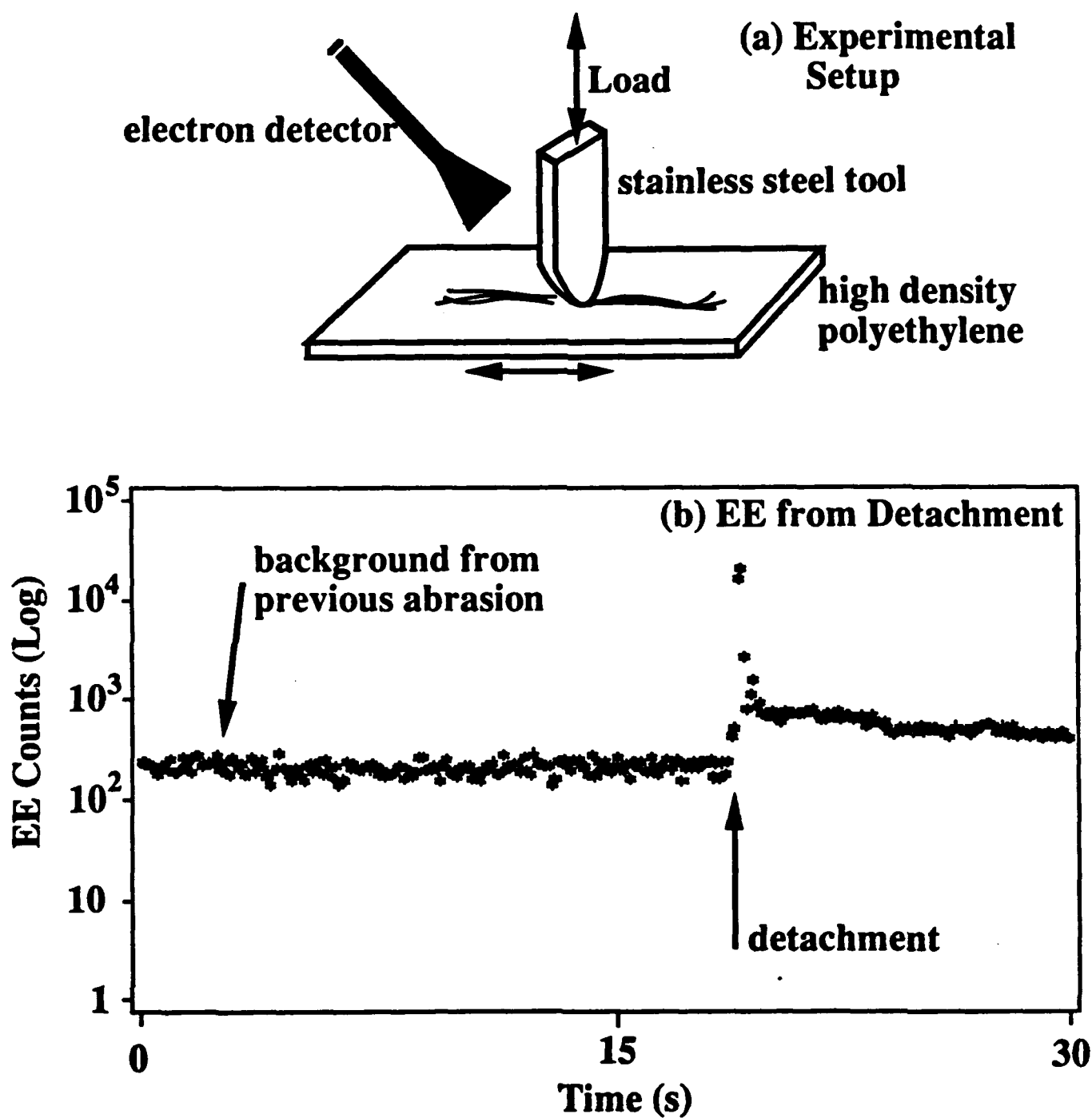
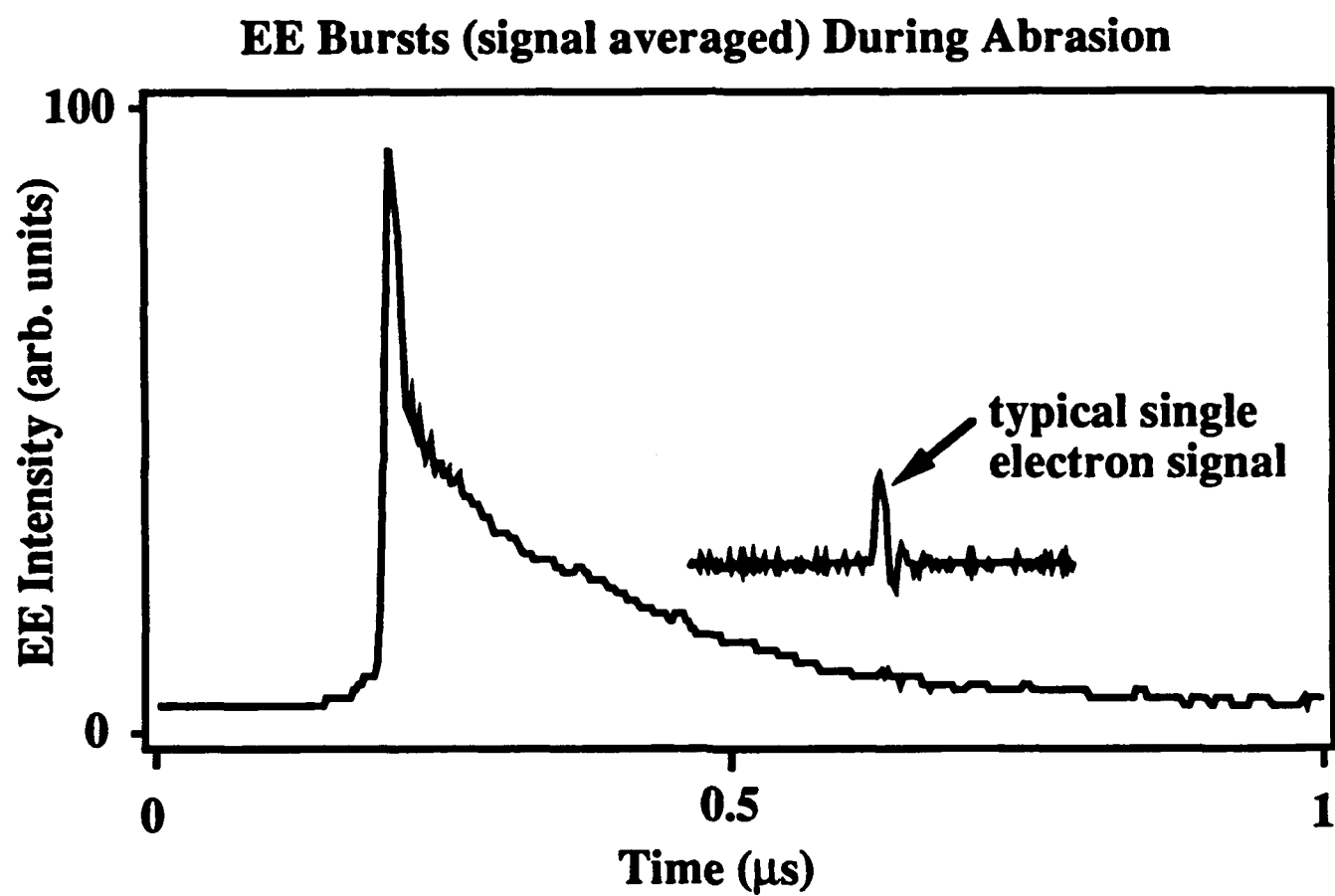


Fig. 8

**Fig. 9**

## VI. Recombination on fractal networks:

### Photon and electron emission following fracture of polymeric materials

J. T. Dickinson, L. C. Jensen, and S. C. Langford

Physics Department, Washington State University, Pullman, WA 99164-2814

#### Introduction

#### Numerical Analysis

In most cases the data were modeled by a difference equation of the form

$$\Delta A_{n+1} = \frac{A_0}{1 + k \cdot t_n^\beta} - \frac{A_0}{1 + k \cdot t_{n+1}^\beta} \quad (1)$$

which represents the number of decays due to particle reactions of the form  $A + B \rightarrow P$  taking place between times  $t_n$  and  $t_{n+1}$ . The rationale for this form is treated in separate discussion section below. This relation assumes that the initial concentration of reacting species are equal ( $A_0 = B_0$ ). The variable  $\beta$  allows for recombination involving random walks on various fractal lattices. The difference equation approach is more accurate immediately after fracture when the data are pulse counted.

A significant difficulty in the model is the choice of time  $t = 0$ , which is usually uncertain on time scales shorter than the counting interval. (In some cases, the duration of fracture can be longer than a counting interval, rendering the time of fracture fundamentally ambiguous.) This was treated by neglecting the first data point after fracture (which is undercounted because fracture occurs somewhere in the middle of the counting interval). The time of fracture was

polymer coiling can be probed by the diffusion of optical excitations along the polymer chain.<sup>4</sup> Most studies make use of specially introduced chromophores which are efficiently excited by optical means and whose decay is sufficiently slow to be influenced by transport on experimental time scales. In many cases, the effects of transport on the decay can only be studied in dilute solutions of the material of interest.

Long-lived excitations are produced during the fracture of many materials.<sup>5,6</sup> In vacuum, photon and electron emissions (two components of what is known as *fracto-emission*) are readily observed and we have examined on fast time scales fluctuations in these emissions as a measure of the erratic behavior of propagating cracks.<sup>7,8</sup> Following fracture, these emissions frequently have decay "tails" which last for many seconds, sometimes hours. As noted below, the relaxation kinetics of these excitations has much in common with the decay of excitations in restricted geometries. Admittedly, the physical interpretation of these signals can be more complex than the emissions from model systems employing dilute solutions and specially introduced chromophores. Nevertheless, fracture induced excitations are easily produced in a wide variety of solid materials without the introduction of chromophores, and are thus applicable to a wide range of materials which are perhaps not otherwise amenable to study. In scattering and fluorescence techniques internal absorption and multiple scattering can be problematic. The ability of fracture to localize excitations at the fracture surface, where geometry for detection is ideal, avoids many of these difficulties.

The photon and electron emissions from several materials could be measured on times scales of  $10^{-2}$  to  $10^3$  seconds following fracture. As these emissions are especially intense and long-lasting in composite materials,<sup>9</sup> filled materials were often employed. Although the details of the emission mechanisms are not known, a number of studies suggest that the dominate emission process involves the recombination of mobile electrons with immobile recombination centers.<sup>10,11</sup> In unfilled polymers, these excitations are consistent with species produced by bond breaking during fracture. However, in the filled materials, the overwhelming majority of excitations are produced by electron bombardment from surface discharges created during

separation of highly charged surfaces during fracture of the polymer-filler interface.<sup>12,13</sup> We present here analyses of these emission decays as (pseudo)unimolecular and bimolecular decays on fractal lattices as described by Zumofen, Blumen, and Klafter.<sup>1</sup>

## II. EXPERIMENT

The principle materials studied in this work include:

*Neat Epoxy.* Epon 828-Z (Shell Chemical Corporation), made from Epon 828, a condensation product of epichlorohydrin and bisphenol-A with no dilutants, cured with Hardener Z, a eutectic mixture of methylenedianiline, metaphenylenediamine, and phenylglycidyl ether. The material was cured for 4 hours at 55 °C and postcured for 16 hours at 95 °C. The samples were molded into dogbones with a gauge length of dimensions  $3.7 \times 13 \times 50 \text{ mm}^3$ .

*Kevlar-filled epoxy.* 250 10  $\mu\text{m}$  Kevlar strands were embedded into a thin epoxy strip 1mm in diameter. The epoxy was Dow DER 332, which is also a bisphenol-A based system.

*Glass-filled polybutadiene* These samples consisted of Diene 35 NFS (Firestone Tire and Rubber Company) mixed with 0.05% dicumyl peroxide, and filled with 34% by volume with 30-95  $\mu\text{m}$  untreated glass beads. The mixture was cured for 2 hours at 150 C.

*Glass-filled polycarbonate* Bisphenol-A-polycarbonate (Makrolon 2800<sup>TM</sup>, Bayer, Mobay) with 10 wt% of untreated E-glass fibers, with average fiber diameter of 10  $\mu\text{m}$  and average length of 100  $\mu\text{m}$ . The samples, provided by L. Nick, U. Clausthal, were extrusion molded dumbbells with nominal dimensions of  $40 \times 5 \times 2 \text{ mm}^3$ .

All samples were loaded in tension in a vacuum system maintained at a pressure of  $1 \times 10^{-5}$  Pa. Electron emission was detected by a Galileo Electrooptics Model 4821 Channeltron electron multiplier (CEM) mounted 2-3 cm from the center of the sample. Photon emission was detected with an EMI Gencom 9924QB photomultiplier tube (PMT), sensitive to wavelengths in the 180-600 nm range. The PMT was mounted opposite the CEM, 1-2 cm from the sample

surface. The output of the CEM and PMT were amplified, amplitude discriminated and counted over intervals from 10 ms to 1 s using a multichannel analyzer.

### III. NUMERICAL ANALYSIS

Photon and electron emission at times following fracture are due to recombination processes of the form



in which A and B are consumed in equal numbers. In the continuum limit, these processes are well described by rate equations of the form

$$F(dA,dt) = -k(t) A(t) B(t), \quad (1)$$

where  $A(t)$  and  $B(t)$  are the densities of species A and B, respectively, and  $k(t)$  is a potential time dependent rate constant. If A and B are consumed in equal numbers, their difference is constant. Letting  $A(t) - B(t) = \delta$ , the rate equation is readily solved by separation of variables. In particular, if  $k(t)$  is constant and  $A(t) \ll B(t) \approx \delta$ , the solution of Eq. 1 is in the form of the familiar unimolecular, exponential decay, which we refer to as (pseudo)unimolecular. If  $k(t)$  is constant and  $\delta = 0$ , the decay is bimolecular.

If recombination is rate limited by the diffusion of a mobile species (the "walker," A) via a random walk process, the rate "constant"  $k(t)$  is proportional to the average rate at which the walkers encounter new (previously unvisited) lattice sites in the material. It is convenient to express the solutions in terms of the integral of  $k(t)$ , here denoted by  $S(t)$ , which is the average number of distinct lattice sites visited by a walker in the time interval  $0 < \text{time} < t$ . Zumofen, Blumen, and Klafter<sup>1</sup> have generalized this treatment to recombination on lattices with non-



integral dimensions by allowing for a time dependent rate constant,  $k(t)$ , which yields  $S(t)$  of the form:

$$S(t) \sim a t^{D/2} \quad D < 2, \quad 2(a)$$

$$\sim a t \ln(b t) \quad D = 2, \quad 2(b)$$

$$\sim a t \quad D > 2, \quad 2(c)$$

where  $D$  is the dimension of the lattice on which the random walk takes place, and  $a$ ,  $b$ , and  $c$ , are constants. In the lattices of interest,  $D \neq 2$ , so that  $S(t) \sim t^\beta$ , where  $0 < \beta \leq 1$ . In case of  $D < 2$ , knowing  $S(t)$  immediately gives the dimension of the lattice:  $D = 2\beta$ . The interpretation of the parameter  $\beta$  depends somewhat on the physical system under study. Nevertheless, this formalism often describes the data well over broad ranges of time scales with a minimum number of adjustable parameters.

The time series defined by the counts per channel  $\{N_i\}$  in the pH and EE measurements were fitted to solutions of Eq. 1 assuming that the number of counts was proportional to the change in  $A(t)$  from the beginning of the counting interval to the end:

$$N_i \sim -\delta A_i = A_i - A_{i-1}, \quad (3)$$

To simplify the analysis, two obvious limiting forms of Eq. 1 were used. When  $A_0 = B_0$  ( $\delta = 0$ ), the decay follows bimolecular kinetics:

$$A_i = \frac{A_0}{1 + (A_0/N_0) S(t_i)} = \frac{A_0}{1 + a t^\beta} \quad (4)$$

Conversely, when  $A_0 \ll B_0$  ( $\delta \approx B_0$ ), the decay follows (pseudo)unimolecular kinetics:

$$A_i = A_0 e^{-\delta S(t_i)/N_0} = A_0 e^{-a t^\beta/N_0} \quad (5)$$

In the short time limit, bimolecular and (pseudo)unimolecular kinetics are indistinguishable. However, at long times bimolecular kinetics are well described by a power law ( $A \sim N_0 t^{-\beta}$ ), yielding linear behavior on a log-log plot. In contrast, a log-log plot of emission from a (pseudo)unimolecular decay is always concave downward at long times. Therefore, decays which showed power behavior at long times were modeled with bimolecular kinetics, while decays which did not were modeled with (pseudo)unimolecular kinetics.

Some decays were well described by a power law throughout the time scale of interest. Recombination follows power-law decay kinetics in the short time limits of both bimolecular and (pseudo)unimolecular kinetics, and in the long time limit of bimolecular decay. To avoid the numerical problems associated with fitting a three-parameter model to a decay which is well described by two parameters, these decays were fit with a power law expression of the form,

$$A_i = \frac{C}{t^\beta} \quad (6)$$

The curve fitting was performed by manually adjusting the parameters to minimize the sum of the squares until changes of  $\pm 1$  in the second decimal place yielded no improvement. The uncertainty in the parameter estimates is somewhat larger due to potential correlations among the parameters and to noise in the data. Fortunately, the optimum value of the exponent  $\beta$  is relatively insensitive to the values of the other parameters, suggesting that  $\beta$  is not highly correlated with the other parameters.

## IV. RESULTS

### A. Neat Epoxy

phE from neat epoxy persists for minutes after fracture. In the early stages of emission, bimolecular kinetics (Eq. 4) describe the emission quite well. Figure 1 shows the phE decay on

semilog and log-log scales. At longer times, ( $t > 1$  s), the pH<sub>E</sub> decay from epoxy shows a change in kinetics which deviates from the bimolecular kinetics of Eq. 4. The inflection at  $t \sim 3$  s, which is concave upward on a log-log scale, cannot be described by equations of the form of Eqs. 4-6. Nevertheless, this emission is significantly above background ( $\sim 3.4$  kHz is about three times the background level). The source of this change in decay kinetics is not clear, but may represent the effect of fractal or random fluctuations in the walker and recombination center densities [ $A_0(x) - B_0(x) = \delta(x) \neq \text{Constant}$ ]. In the early stages of decay, these fluctuations would be small relative to the total excitation densities ( $\delta/A$  and  $\delta/B \ll 1$ ). However, since A and B are consumed in equal quantities, the fluctuations can eventually control the recombination kinetics—generally resulting in slower decays over broad ranges of time scales.<sup>14</sup>

The first 1 s of emission following fracture is shown along with a model fit to bimolecular kinetics (Eq. 4). The best fit parameters were  $A_0 = 5.9 \times 10^5$ ,  $a = 1.8$ , and  $\beta = 0.83$ . Since  $\beta$  in Eq. 4 corresponds to the power of  $t$  in  $S(t)$  of Eq. 3, these results are consistent with recombination on a lattice with a fractal dimension  $D = 2 - \beta = 1.66$ . As noted below, this is consistent with the (mass) fractal dimension of the epoxy network early in the stages of curing, up until the gel point is reached.

The most likely cause of the apparent change in decay kinetics is the presence of deep electron traps which gradually remove walkers and small difference in the initial densities of walkers and recombination centers ( $A_0 - B_0 = \delta \neq 0$ ).<sup>15</sup> Providing that  $\delta$  is much less than  $A_0$  and  $B_0$ , the decay kinetics will initially follow bimolecular kinetics to a very good approximation. However, the recombination process will eventually reduce the smaller of A and B to values much less than  $\delta$ , and subsequent recombination will follow effectively (pseudo)unimolecular kinetics. presence of local (random or fractal) fluctuations in the initial density of recombination centers and walkers [ $A_0(x) - B_0(x) = \delta(x) \neq \text{Constant}$ ]. Except in the long-time limit of bimolecular kinetics, the effect of these fluctuations on the recombination kinetics is complex and not well described by analytic expressions; thus an analysis of this tail is not attempted here.

### B. Kevlar-filled epoxy

The emission intensities accompanying fracture are greatly enhanced when fracture involves interfacial failure. The higher emission intensities allow the fracto-emission decays to be probed on much longer time scales; different initial conditions may also apply. A log-log plot of EE from a Kevlar-filled epoxy is shown in Fig. 3. Aside from an initial transient ( $t < 10$  s), the entire decay is well described by bimolecular kinetics, with an exponent  $\beta \approx 0.79 \pm 0.01$ . This result is very similar to that obtained for the neat epoxy. The cause of the initial transient is not clear, but may be due a competing recombination process which proceeds to completion rather rapidly. Since this material is composite in nature, it is possible that both the epoxy and Kevlar components contribute significantly in the initial stages of decay, where the emission from one component decays rapidly and thereafter does not contribute.

### C. Glass-filled polybutadiene

The decay of EE and phE from glass-filled polybutadiene shows downward curvature on a log-log at times less than 1 s, as shown in Fig. 5. At later times, the decay tends to  $1/t$  behavior ( $\beta \approx 1$ ). Fitting the early portion of this data ( $t < 10$  s) to the modified second order decay (Eq. 3) yielded

	$A_0$	$a$	$\beta$
phE	$3.9 \times 10^6$	21	0.39
EE	$8.0 \times 10^5$	0.21	0.43

The two values of  $\beta$  agree quite well, indicating that over these time scales both emissions result from random walks on the same lattice with a corresponding dimension of  $D = 2\beta \approx 0.8$ . The case of  $D = 1$  would be consistent with transport along one-dimensional polymer chains. However, the difference from  $D = 1$  is significant.

The low EE background allows EE measurements for some hours after fracture. Figure 2 shows a log-log plot of pulse counted EE acquired at a counting interval of 1 s. On this time scale, a remarkably long decay is observed, which is quite linear on a log-log plot. The data is readily fit using the power law difference equation (Eq. 6), yielding  $C = 9.4 \pm 0.1 \times 10^5$  and  $\beta = 0.13 \pm 0.01$ .  $C$  is within a factor of 5 of the corresponding parameters in the short-term decay of Fig. 1 ( $C \rightarrow A_0/k = 4.8 \times 10^6$ ). Given that the data were collected from two different fracture events, this agreement is quite reasonable. However, the exponent in the power law expression is not consistent with the long-term limit of the short term decay above ( $\beta_{\text{long term}} = 0.13 \ll \beta_{\text{short term}} = 0.43$ ). This suggests different kinetics, are responsible for the emission in the long term ( $> 1\text{s}$ ) and short term ( $< 1\text{s}$ ) limits.

Note that power law decay fits the small curvature in the first few data points of Fig. 2 well; this small curvature is largely due to the finite differences involved in pulse counting an (initially) rapidly decaying signal.

The EE following the abrasion of glass-filled polybutadiene is even more long lasting than that accompanying a clean fracture event. This is evident in Fig. 6, which shows the emission on a log-log plot. At long times, the emission becomes almost "flat" on a log-log plot, remaining significantly above background. Other examples of similar behavior are discussed below.

#### D. Glass-filled polycarbonate

The long after-emission from glass fiber-filled polycarbonate has been reported by Fuhrmann et al.<sup>16</sup> Typical simultaneous pH<sub>E</sub> and EE decay curves from a similar sample are shown in log-log plots in Fig. 6. The pH<sub>E</sub> data shows a smooth decay which is well described by (pseudo)unimolecular decay over about two decades in time. In contrast, the EE decay shows a large number of spikes which are still observed thousands of seconds after fracture. The presence of these spikes renders this data unsuitable for analysis in terms of a continuous recombination process. We attribute these spikes to surface electrical breakdown events in the

regions of large gradients in charge density, e.g., exposed glass fibers emanating from the polycarbonate matrix. These fibers are highly charged because of the contact electrification between the glass and the polymer. The electric field enhancement at sharp points could promote the diffusion of charge to the ends of these short fibers, thus enhancing the probability of a breakdown event. These surface breakdowns tend to be "dark", in that there are not corresponding bursts in the visible photon emissions.

phE generated by peeling a polycarbonate film from a glass slide confirm that the phE is principally from the polymer and not the glass [we suspect that the observed EE is also from the polymer, although it has not been verified experimentally]. Fitting the phE data to a (pseudo)unimolecular decay yields  $\beta = 0.39 \pm 0.01$ , which is remarkably close to the value obtained for phE from the glass-filled polybutadiene. Both materials are composed of long polymer chains of considerably different chemical structure. The similar values of  $\beta$  for polycarbonate and polybutadiene suggests that the decay is totally determined by the dimension of the lattice.

### E. Single Crystal MgO

Although not a polymer, we wish to point out that the fracture-induced phE and EE from the fracture of single crystal MgO<sup>17</sup> (Fig. 7) is also well described by power law kinetics (Eq. 6) over substantial portions of its decay. This data had previously been modeled by second order, thermally stimulated recombination ( $\beta = 1$ );<sup>16</sup> but at long times, the decay appeared to be of "lower order." The exponent  $\alpha$  in the power law is about 0.1. This is consistent with bimolecular kinetics on a network of very low dimension,  $D \approx 0.2$ . To obtain such a low  $D$ , one might consider that walker motion is along the edges of surface steps where the step lengths are distributed in a fractal way (as in a Cantor set). Confinement of charge carriers at step edges is expected because of minima in conduction band energies at such structures.<sup>18</sup>

### F. Extra-extra slow decays

On some materials the emission intensities appear to "go flat" even on a log-log plot. For example, the phE following the peeling of 3M Magic Tape® from a Cu substrate<sup>9</sup> [Fig. 8(a)] shows power law kinetics over almost two orders of magnitude in time, but eventually flattens out. Likewise, the EE following the fracture of polycrystalline lead zirconate-titanate (PZT) shows similar behavior [Fig. 8(b)].<sup>19</sup> In both cases, the data at the end of the traces are well above any noise signals.

## V. DISCUSSION

The most obvious source of "fractal" behavior in the data presented here is the lattice upon which recombination takes place. A fractal lattice would in this case be associated with the pattern of crosslinks in the polymer network. In the case of the inorganic crystalline or polycrystalline materials, the fracture process is creating this underlying microstructure. Other sources of "fractal" behavior are possible. A fractal distribution of energy barriers in a tunneling process would produce similar decays.<sup>2</sup> An exponential distribution of trap depths or energy barriers can also lead to fractal-like behavior, in a manner describe by some in terms of "fractal time."<sup>20</sup>

The stretched exponential decay [ $\exp(-t^\beta)$ , with  $0 < \beta \leq 1$ ] describes a wide variety of relaxation phenomena in amorphous materials, probably because of its role as a probability limit distribution.<sup>21</sup> Assuming that the probability of a single excitation surviving until a time  $t$  in a lattice with one walker scales with  $[1 - aS(t)]$ , the survival probability in a lattice with  $N$  independent walkers scales with  $[1 - aS(t)]^N$ . In the limit of large  $N$  the survival probability is proportional to  $\exp[-aS(t)]$ , which yields a stretched exponential for  $S(t) \sim t^\beta$  when  $\beta < 1$ .

### A. Epoxy

Fractal dimension measurements on partially cured, branched epoxy structures have been made by dissolving partially cured material in a suitable solvent and studying the solution by small-angle X-ray scattering (SAXS)<sup>22</sup> or small-angle neutron scattering (SANS).<sup>23</sup> At least prior to the formation of a fully connected network, increasing the degree of cure does not affect the fractal dimension but increases the range of distance scales over which fractal behavior is observed. (The difficulty of dissolving cured material prevents similar measurements on fully cured material.) The observed fractal dimensions depend strongly on whether the rate controlling reaction is diffusion limited or kinetically limited; this in turn can be controlled somewhat by the choice of curing agent. The fractal character of the dilute epoxy network also involves a convolution between the fractal dimension of the individual clusters within the solvent and the (fractal) size distribution of the clusters themselves. Depending on the epoxy and the solvent, a different fractal dimension may be observed at small dimensions due to the coiling behavior of the polymer chain between entanglement points.<sup>24</sup>

SANS measurements have yielded values on the order of 1.6-1.7 when percolation conditions prevail during curing of partially cured epoxies.<sup>23</sup> The fractal behavior under percolation conditions is attributed largely to the distribution of cluster sizes in the curing epoxy. Although diffusion-limited conditions are more commonly obtained during curing, ( $D \approx 2.1$  over a broad range of distance scales), SAXS measurements at wavevectors  $1/30 \text{ \AA} \leq K \leq 1/4 \text{ \AA}$  (where coiling between entanglements is expected to dominate the scattering process) still show fractal behavior with a similar dimension ( $D \approx 1.67$ ).<sup>24</sup> The lower values are in good agreement with the fractal dimension inferred from the early stages of pH decay in the neat and Kevlar-filled epoxies ( $D_{\text{neat}} \approx 1.7$ ,  $D_{\text{Kevlar-filled}} \approx 1.6$ ). SAXS measurements made beyond the gelation threshold showed similar fractal behavior,<sup>24</sup> suggesting that the fractal character may persist in the solid material. If the observed pH and EE is produced by recombination on the epoxy lattice, the kinetics of the decay suggest that the process is rate limited by transport along the



short, coiled portions of the lattice network ( $D \approx 1.7$ ) rather than transport along the larger scale branches of the network ( $D \approx 2.1$ ).

As noted above, other effects may be important in the decay process. For instance, fractal distributions of walkers and/or recombination centers could have very interesting effects on the decay kinetics. Such a distribution may be associated with fractal fracture surfaces. The immobile recombination centers would be confined to this fractal surface, for instance. Fractal dimension measurements on Epon 828 fracture surfaces using the slit island technique yielded a dimension of  $2.6 \pm 0.1$ .<sup>7,8</sup> The fractional part of the dimension (fractal dimension increment) of the surface agrees well with the fractional part of the dimension inferred from the emission measurements.

Geometrically, the projection of a fractal object onto a space of lower dimension often yields a second fractal object with the same fractal dimension increment. For instance, the intersection of a plane ( $D = 2$ ) with a fractal surface of dimension  $D_s = 2.6$  yields a set of closed loops with a global fractal dimension of 1.6. Assuming that the excitations produced by fracture are confined to the fracture surface, the walkers would be confined to a lattice with a dimension given by the intersection of the epoxy network ( $D = 2.0$  in the classical Flory-Stockmayer model) with the epoxy surface ( $D_s = 2.6$ ). This would result in recombination on a lattice of dimension  $D = 2.6 - 1.0 = 1.6$ , similar to that inferred from the recombination kinetics. Walker confinement to the surface is not unreasonable, especially given the high density of (oppositely charged) recombination centers there. At this point we speculate that the fractal dimension of the surface produced during fracture is related to the fractal dimension of the small-scale lattice coiling noted above.

The similarity of the exponents obtained from the neat epoxy ( $\beta \approx 0.83$ ) and the Kevlar-filled epoxy ( $\beta \approx 0.79$ ) suggest that the presence of the Kevlar in the composite does not significantly affect the exponent after the decay of initial transients. In some systems, like the EE from glass-filled polycarbonate, electrical effects associated with second phase particles can yield complex signals. However, these effects appear to be minimal in the case of Kevlar-filled

epoxy and in many other materials. As the emissions from composite materials are much more intense, they are often much more convenient to study.

### **B. Glass-filled polybutadiene and polycarbonate**

The observation of similar decay kinetics ( $\beta \approx 0.4$ ) for both glass bead-filled polybutadiene and glass fiber-filled polycarbonate suggest that the decays are relatively insensitive to the chemical makeup of the polymer backbone. The much smaller exponent obtained for these materials vs the epoxies ( $\beta \approx 0.8$ ) is consistent with lower dimension of the lattice. Ideally, a chain-like polymer has a dimension  $D = 1$ , while a fully connected epoxy network should have a dimension  $D = 2.0$ . Since recombination on a linear polymer chain would yield  $\beta = 0.50$ , the observation of significantly smaller exponents (0.4) indicates that 1-D recombination does not adequately describe our observations. The simplest explanation is that the difference reflects the distribution of chain lengths (molecular weights) in these predominately linear materials. Fracture experiments with monodisperse materials, which have a very narrow distribution of molecular weights, should resolve this issue: recombination on monodisperse materials should yield  $\beta \approx 0.5$  if deviations from ideal behavior are due to dispersion in the molecular weights.

The very slow decay ( $\beta \approx 0.13$  for data taken on very long time scales) in the EE from glass-filled polybutadiene is more difficult to explain. There are two factors which would tend to slow down the decay on long time scales. Because of the filler particles, the distribution of walkers and recombination centers along any given chain is highly inhomogeneous. The density of walkers and recombination centers along a polymer chain are especially high where the polymer has been pulled away from a filler particle. Further, the density of walkers and recombination centers in these high density regions will not necessarily be equal ( $A_0 - B_0 = \delta \neq 0$ ). Since the polymer itself is globally electrically neutral, some regions along the polymer chain will have excess walkers ( $A > B$ ) and others will have excess recombination centers ( $A < B$ ). In the early states of the decay, recombination is dominated by recombination within small, highly

excited regions of the chain, where  $A \approx B \gg \delta$ , and the resulting kinetics are appropriately described by  $\beta \approx 0.4$ . At long times, however, the local exhaustion of the minority species can lead to distinctly slower recombination kinetics.

In the long time limit, we expect that the decay kinetics are dominated by recombination of walkers from patches where they are in the majority ( $A > B$ ) with recombination centers in different patches where they are in the majority ( $A < B$ ). Further, we expect that the distribution of these patches will be similar to the distribution of the filler particles, i.e., a random distribution in three dimensions. Walkers traveling from one patch to another will perform a random walk along a polymer chain, while the chain itself defines a highly coiled path from patch to patch. The length along the polymer chain traversed by such a walker in time  $t$ ,  $L(t)$ , scales as  $L \sim t^\beta$ , where  $\beta \approx 0.4$  as above. However, the distance in 3-D traveled by a walker traveling along the chain will scale as some power,  $\gamma$ , of  $L$ . The number of distinct patches visited by a walker will be proportional to the 3-D distance traveled and therefore scale as  $L^\gamma \sim (t^\beta)^\gamma$ . Modeling the chain coiling as a random walk yields  $\gamma = 0.5$ . A more accurate treatment, in which the chain performs a self-avoiding random walk, yields  $\gamma = 5/12 = 0.42$  (Flory relation).<sup>25</sup> This process would effectively lower  $\beta$  from the short-time value of about 0.4 to about  $0.4 \times 0.42 \approx 0.17$ , which is acceptably close to the observed value of 0.13.

Another factor which would slow the emission decay at very long times is related to the random distribution of excitation patches. The continuous time random walk description of recombination as formulated in Eqs. 1-6 assumes that the walkers and recombination centers are distributed uniformly throughout the lattice. In the limit of short times and high excitation densities, this assumption holds quite well. However, a random distribution of  $N$  particles is characterized by an uncertainty proportional to the square root of  $N$ , which locally sets a scale for  $\delta = A - B \sim N^{1/2}$ . This does not affect the decay kinetics until recombination produces local regions essentially devoid of either walkers or recombination centers.<sup>26</sup> Under these conditions, the decay of recombination centers and walkers is much slower because recombination is

essentially confined to the boundaries of A-rich regions and B-rich regions. The average density of surviving particles then scales as<sup>14</sup>

$$A(t) \sim t^{-D/4} \quad 0 < D < 4. \quad (7)$$

Comparing Eq. 7 with the long-time limit of the bimolecular decay in Eq. 4 [ $A(t) \sim t^{-D/2}$ ] shows that this effect essentially lowers the observed exponent by a factor of two. This effect alone is probably insufficient to explain the very slow EE decay in glass-filled polybutadiene, but may prove important in other emission decays.

The slower decay kinetics due to randomness in the densities of A and B apply only as long as the distance traveled by the average walker is less than the dimensions of the lattice (the size of the sample). Since the diffusion of walkers gradually destroys the fluctuations responsible for the slow decay, the faster decay of Eq. 4 [ $A(t) \sim t^{-D/2}$ ] is restored when the average distance traveled by a walker reaches the size of the system. Thus the emission may appear to "die" at long times. This is a good qualitative description of the behavior exhibited by EE from in some systems.

### C. Single Crystal MgO

Williams et al. have analyzed the luminescence decay from electron-irradiated MgO on ms time scales using a mixed tunneling-thermally stimulated recombination model.<sup>27</sup> Thermally stimulated charge transfer would tend to dominate at room temperature on the time-scales of the data shown above. The very low exponent obtained for the MgO is consistent with the presence of a fractal structure with a very low dimension. If the low fractal dimension is associated with a physical surface microstructure, it would be consistent with a random walk along linear structures with fractal distribution of lengths. For instance, walker motion along the edges of surface steps would yield a fractal dimension less than one if the step lengths were distributed in a fractal way (as in a Cantor set).

Fractal surface dimension measurements of  $\mu\text{m}$ -sized regions of the fracture surface of equivalent samples have been obtained from scanning tunneling microscope images.<sup>28</sup> The fractal behavior of the surfaces were found to be markedly inhomogeneous: some regions showed strong fractal character with  $2.3 \leq D \leq 2.6$ , while regions showed non-fractal character ( $D = 2$ ). This inhomogeneity could have profound effects in terms of its influence on rates of recombination.

#### D. Extra-slow decays

The slowest decays (as observed on a log-log plot) which can be described by recombination on fractal lattices occur in the short time limit of Eqs. 4 and 5. As noted above, bimolecular and (pseudo)unimolecular decays are indistinguishable in the limit of short times. Both are well described by a power law expression of the form  $dA/dt \sim t^{-\beta}$ . In the limit of small  $\beta$ , these decays can be extremely slow. However, the data of Fig. 9 indicate that the slow decays are established only at long times, after a considerable amount of recombination has taken place. The data suggests that a dramatic change in recombination kinetics takes place at long times, a change which ironically involves a transition to a short-time limit at relatively long times.

The most likely mechanism for such a transition involves local patches of excitations which are relatively isolated from one another, similar to those produced in the glass-filled polybutadiene by the filler particles. In some patches, the walkers slightly outnumber the recombination centers, while in others, the recombination centers are slightly in excess. The initial states of decay are dominated by recombination within patches of excitations, but eventually the minority species in each patch is completely exhausted. Subsequent recombination is controlled by transport between patches, which is typically slower than transport within patches. Again, transport between patches must be characterized by a low fractal dimension to explain the very long tails observed here. This could be accomplished by a fractal distribution of patches along the surface or a fractal interconnecting network along which the walkers move—either one of which could reasonably be characterized by very low

dimensions. Both  $\pm$ charge patches are readily observed on peeled adhesive tape by dusting the surface with toner particles, which (depending on the toner) are attracted to patches of either plus or minus charge.<sup>29</sup> This replica method of examining charge distributions always shows strong evidence of the surface breakdown (mentioned above for interfacial failure). Similarly, the individual piezoelectric grains in PZT may define charged patches after the initial stages of decay.

## VI. CONCLUSIONS

Fracto-emission from a number of materials often displays long-lived components which can be adequately modeled over long time scales by continuous time random walks on fractal lattices. This is especially true of composite materials, where interfacial failure accompanying fracture promotes especially intense, long-lasting emissions. In the random walk formalism, the exponent  $\beta$  describing the scaling behavior of the number of sites visited by a walker in time  $t$  [ $S(t) \sim t^\beta$ ] appears to reflect the dimension of the underlying lattice for dimensions  $D < 2$ . The similarity of the exponents from the two glass-filled polymers (polybutadiene and polycarbonate) indicates that this exponent reflects the structure of the underlying lattice, rather than the chemistry of the species making up the polymer backbone. Likewise, the similarity of the exponents determined from the neat epoxy and the Kevlar-filled epoxy suggests that the exponent is not sensitive to presence of a second phase after the decay of initial transients and may show a connection with the fractal dimension of the fracture surface. Even inorganic materials such as single crystal MgO and polycrystalline PZT show behavior consistent with recombination processes on a disordered lattice.

An advantage to recombination models based on fractal lattices in this regard is the relatively small number of parameters involved in the fitting process. A previously used thermally stimulated luminescence model of the emission decays from MgO involved 6 free parameters. A fractal description of the same process requires only 1-2 parameters, providing

useful dimensional information about the structure of the underlying lattice through the exponent  $\beta$  in  $S(t) \sim t^\beta$  in Eqs. 4-6.

The use of fracture as a means of excitation for the analysis of recombination kinetics has the advantage of providing relatively high energy excitations (several eV accompanying bond breaking, or the even higher energies produced by charge separation in filled systems) *localized in the near surface region.*, which minimizes the effects of scattering on the intensity of the observed emissions. This allows for the study of more opaque, dense materials in their solid form. The continuous time random walk description of these decays provides a simple, elegant description of this potentially very complex process.

#### ACKNOWLEDGMENTS

This work was supported by the Air Force Office of Scientific Research under Contract AFOSR-F49620-91-C-0093, the Ceramics and Electronic Materials Division of the National Science Foundation under Grant DMR 8912179, the 3M Co., and the Washington Technology Center. We thank Leo Nick, University of Clausthal, for providing the glass filled polycarbonate samples.

## REFERENCES

1. G. Zumofen, A. Blumen, and J. Klafter, *J. Chem. Phys.* **84**, 6679 (1985).
2. Several examples are cited in *Molecular Dynamics in Restricted Geometries*, edited by Joseph Klafter and J. M. Drake, (John Wiley, New York, 1989).
3. Raoul Kopelman, Jagdish Prasad, and S. J. Parus, in Klafter and Drake, *op. cit.*, pp. 145-164.
4. J. D. Byers, M. S. Friedrichs, R. A. Friesner, and S. E. Webber, in Klafter and Drake, *op. cit.* pp. 99-144.
5. J. T. Dickinson, in *Non-Destructive Testing of Fibre-Reinforced Plastics Composites*, Volume 2, edited by John Summerscales, (Elsevier, London, 1990), pp. 429-482.
6. J. T. Dickinson, in *Adhesive Bonding*, edited by Lieng-Huang Lee, (Plenum, New York, 1991), pp. 395-423.
7. S. C. Langford, Ma Zhenyi, and J. T. Dickinson, *J. Mater. Res.* **4**, 1272 (1989).
8. Ma Zhenyi, S. C. Langford, J. T. Dickinson, M. H. Engelhard, and D. R. Baer, *J. Mater. Res.* **6**, 183 (1991).
9. J. T. Dickinson, M. K. Park, E. E. Donaldson, and L. C. Jensen, *J. Vac. Sci. Technol.* **20**, 436 (1982).
10. J. T. Dickinson, in *Adhesive Chemistry*, L. H. Lee, ed., Plenum Pub. Corp, (1984), pp. 193-243.
11. J. T. Dickinson, "Fracto-Emission", Chap. 10 in *Non-Destructive Testing of Fibre-Reinforced Plastic Composites - II*, J. Summerscales, ed. Elsevier Applied Science, London (1990), pp. 429-482.
12. J. T. Dickinson, L. C. Jensen, and A. Jahan-Latibari, *J. Vac. Sci. Technol. A* **2**, 1112 (1984).



13. J. T. Dickinson, L. C. Jensen, and R. P. Dion, "Fracto-Emission from High Density Polyethylene: Bond Breaking vs Tribological Stimulation", to appear in J. Appl. Phys.
14. Doug Toussaint and Frank Wilczek, J. Chem. Phys. 78, 2642 (1983).
15. H. Schnörrer, V. Kuzovkov, and A. Blumen, J. Chem. Phys. 93, 7148 (1990).
16. J. Fuhrmann, L. Nick, J. T. Dickinson, and L. C. Jensen, "Photon Emission during deformation of glass-fiber reinforced bisphenol-A- Polycarbonate," to appear in J. Applied Polym. Sci.
17. S. C. Langford, J. T. Dickinson, and L. C. Jensen, J. Appl. Phys. 62, 1437 (1987).
18. C. Satoko, M. Tsukada, and H. Adachi, J. Phys. Soc. Jpn. 45, 1333 (1978).
19. J. T. Dickinson, L. C. Jensen, and W. D. Williams, J. Am. Ceram. Soc. 68, 235 (1985).
20. M. F. Shlesinger, Ann. Rev. Phys. Chem. 39, 269 (1988).
21. H. Scher, M. F. Shlesinger, and J. T. Bendler, Phys. Today 44, 26 (1991).
22. Benjamin Chu, Chi Wu, D.-Q. Wu, and J. C. Phillips, Macromolecules 20, 2642 (1987).
23. W.-L. Wu, B. J. Bauer, and W.-J. Su, Polymer 30, 1384 (1989).
24. Benjamin Chu and Chi Wu, Macromol. 21, 1729 (1988).
25. Hagen Kleinert, *Path Integrals in Quantum Mechanics, Statistics, and Polymer Physics*, (World Scientific, Singapore, 1990), p. 480.
26. P. Meakin and H. E. Stanley, "Novel dimension-independent behavior for diffusive annihilation on percolation fractals," J. Phys. A 17, L173 (1984).
27. R. T. Williams, J. W. Williams, T. J. Turner, and K. H. Lee, Phys. Rev. B 20, 1687 (1979).
28. S. C. Langford, Ma Zhenyi, L. C. Jensen, and J. T. Dickinson, J. Vac. Sci. Technol. A 8, 3470 (1990).
29. Jearl Walker, Amateur Scientist, *Scientific American* 258(4) 114 (1988).

**FIGURE CAPTIONS**

- FIG. 1. phE following fracture of a neat epoxy: (a) entire emission curve on a semi-log plot (background not subtracted); (b) the decay portion of the curve plotted on a log-log plot with background subtracted.
- FIG. 2. phE from the early stages of Fig. 1(b) with a fit of the decay to bimolecular kinetics.
- FIG. 3. EE following fracture of a Kevlar-filled epoxy composite. A fit of the decay to bimolecular kinetics is shown as a dotted line.
- FIG. 4. (a) EE, (b) phE following fracture of glass-filled polybutadiene. Fits of the decays to bimolecular kinetics are shown as dotted lines.
- FIG. 5. EE following fracture of glass-filled polybutadiene. This data was pulse-counted at 1 s/channel for a much longer time.
- FIG. 6. EE following abrasion of glass-filled polybutadiene.
- FIG. 7. (a) phE and (b) EE following fracture of glass-fiber-filled polycarbonate. A fit of the phE data is shown as a dotted line in (a).
- FIG. 8. (a) EE and (b) phE following fracture of MgO on a log-log scale.
- FIG. 9. EE following (a) rapid peel of a pressure sensitive adhesive (Magic Tape®) from copper, and (b) following fracture of lead-zirconia-titanate (PZT).

# Pulse Counted phE Following Fracture of Epon 828

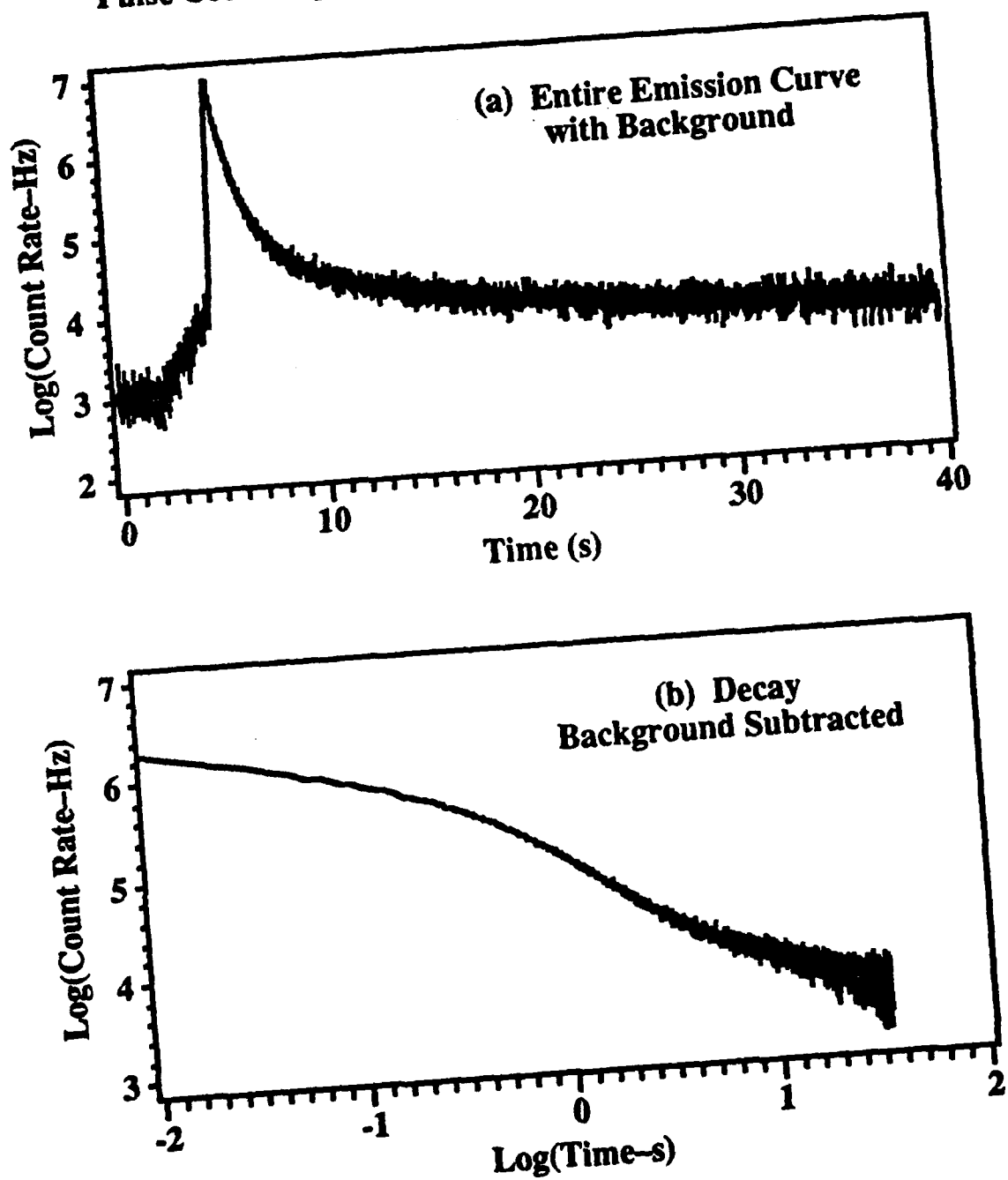
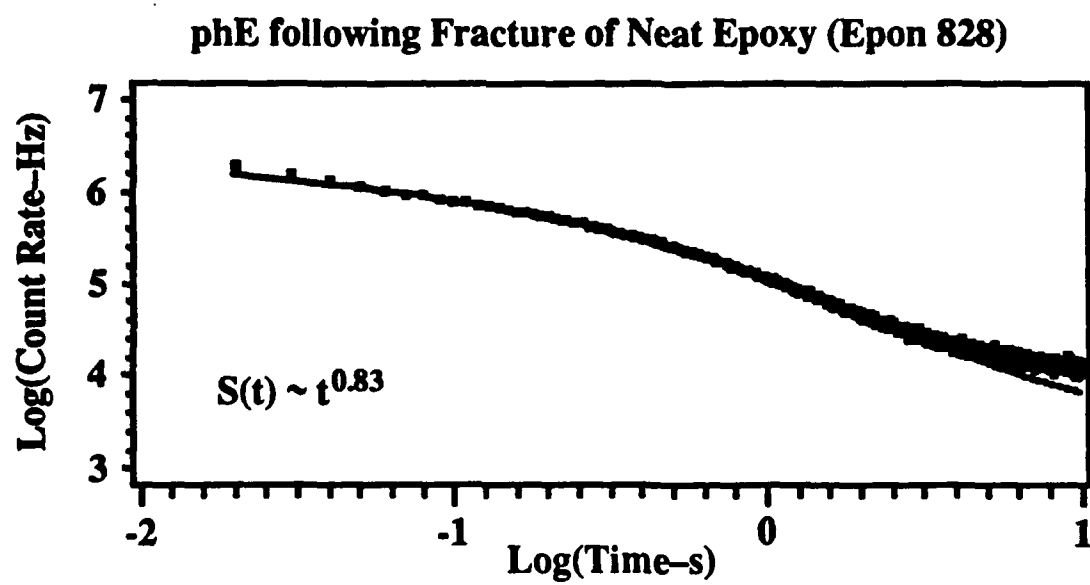
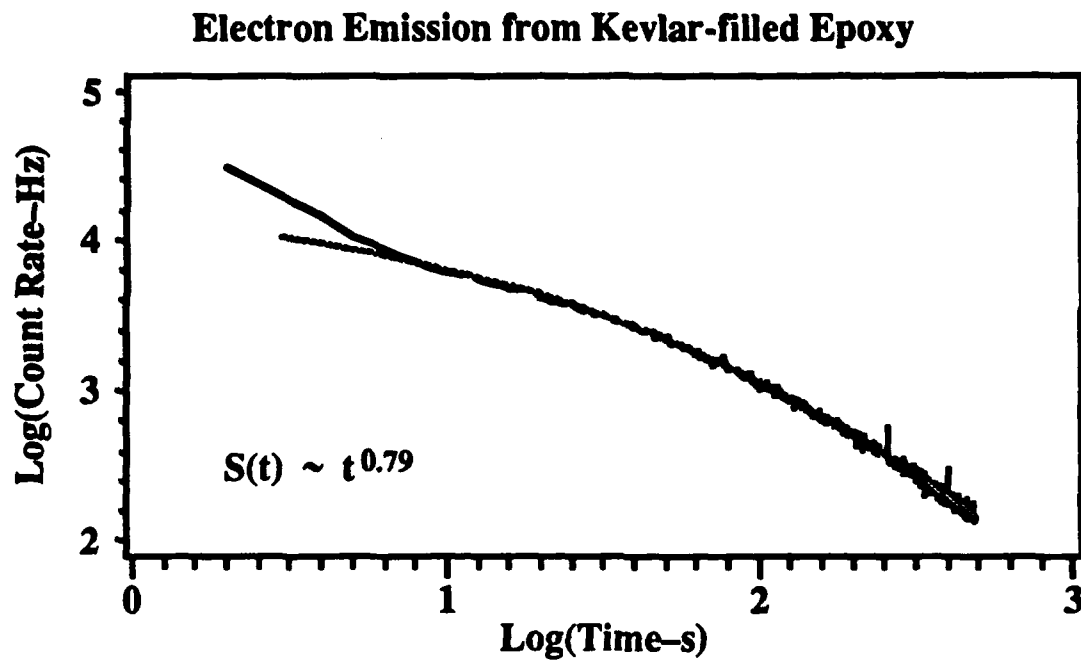
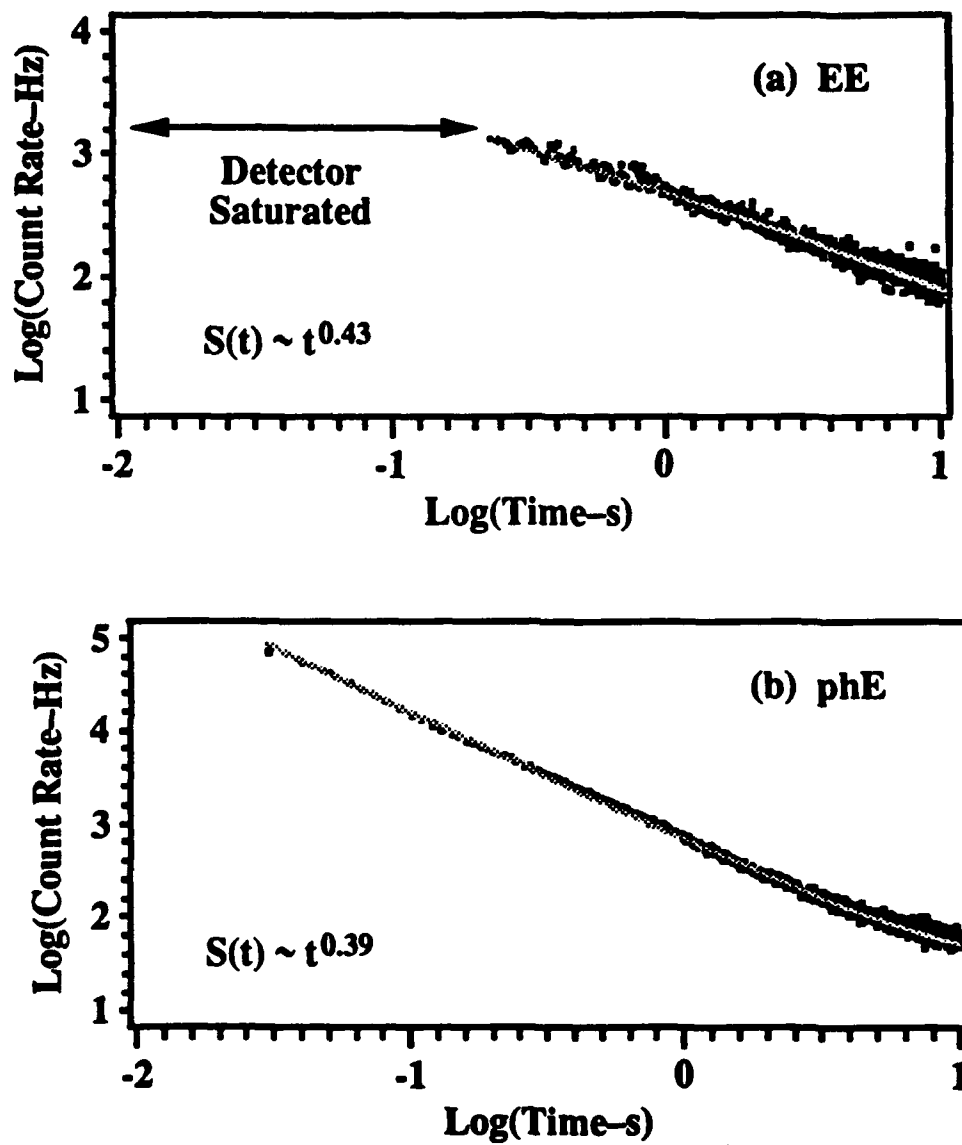


FIG. 1

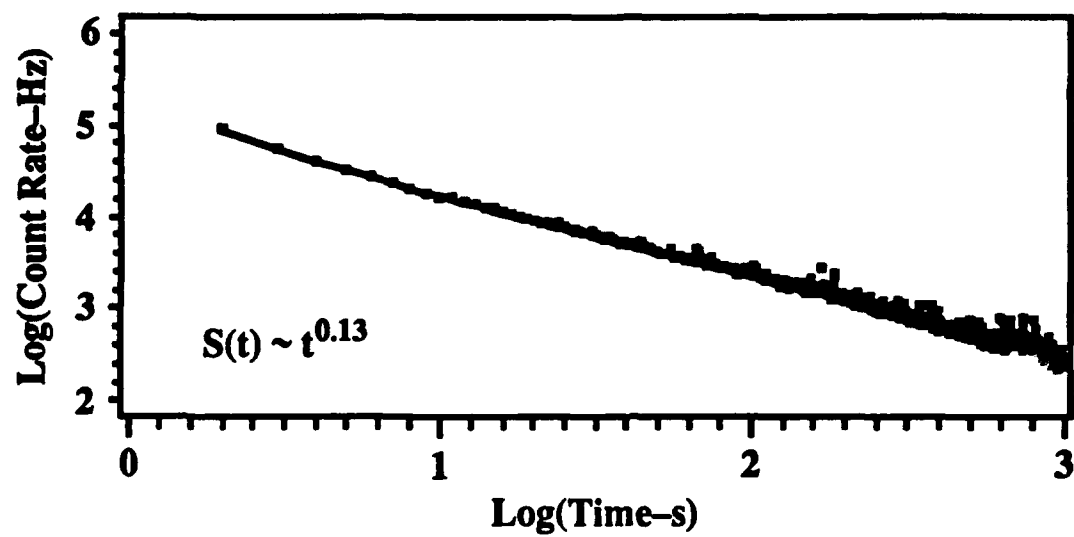
**FIG. 2**

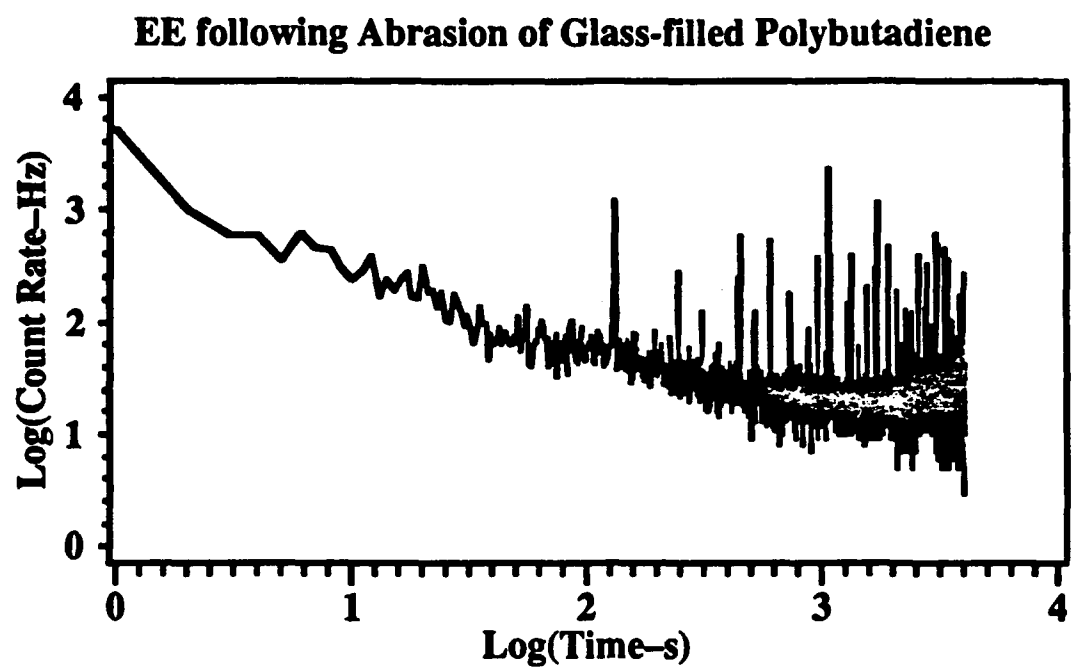
**FIG. 3**

**EE and phE following Fracture of Glass-filled  
Polybutadiene (10 s)**

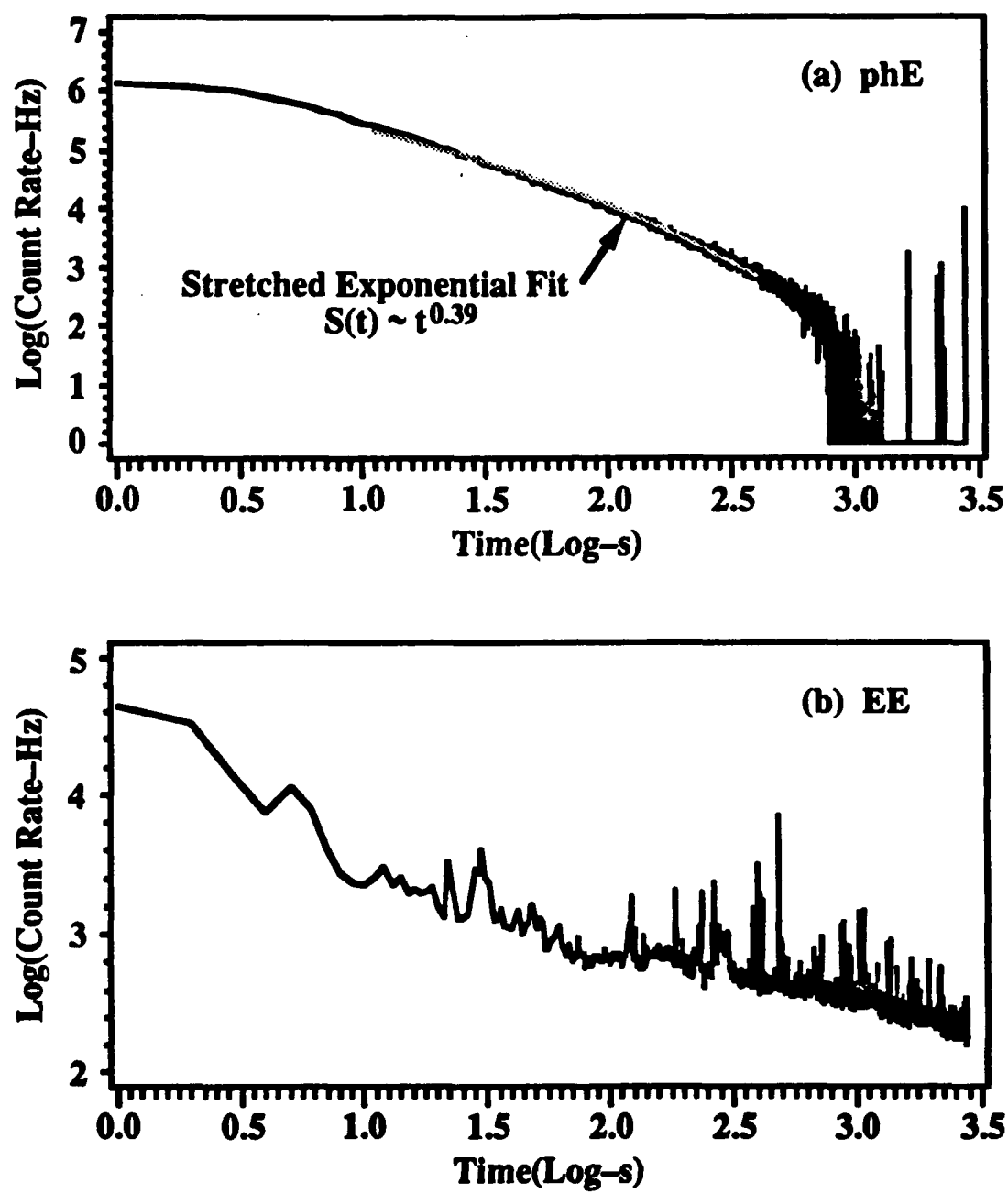


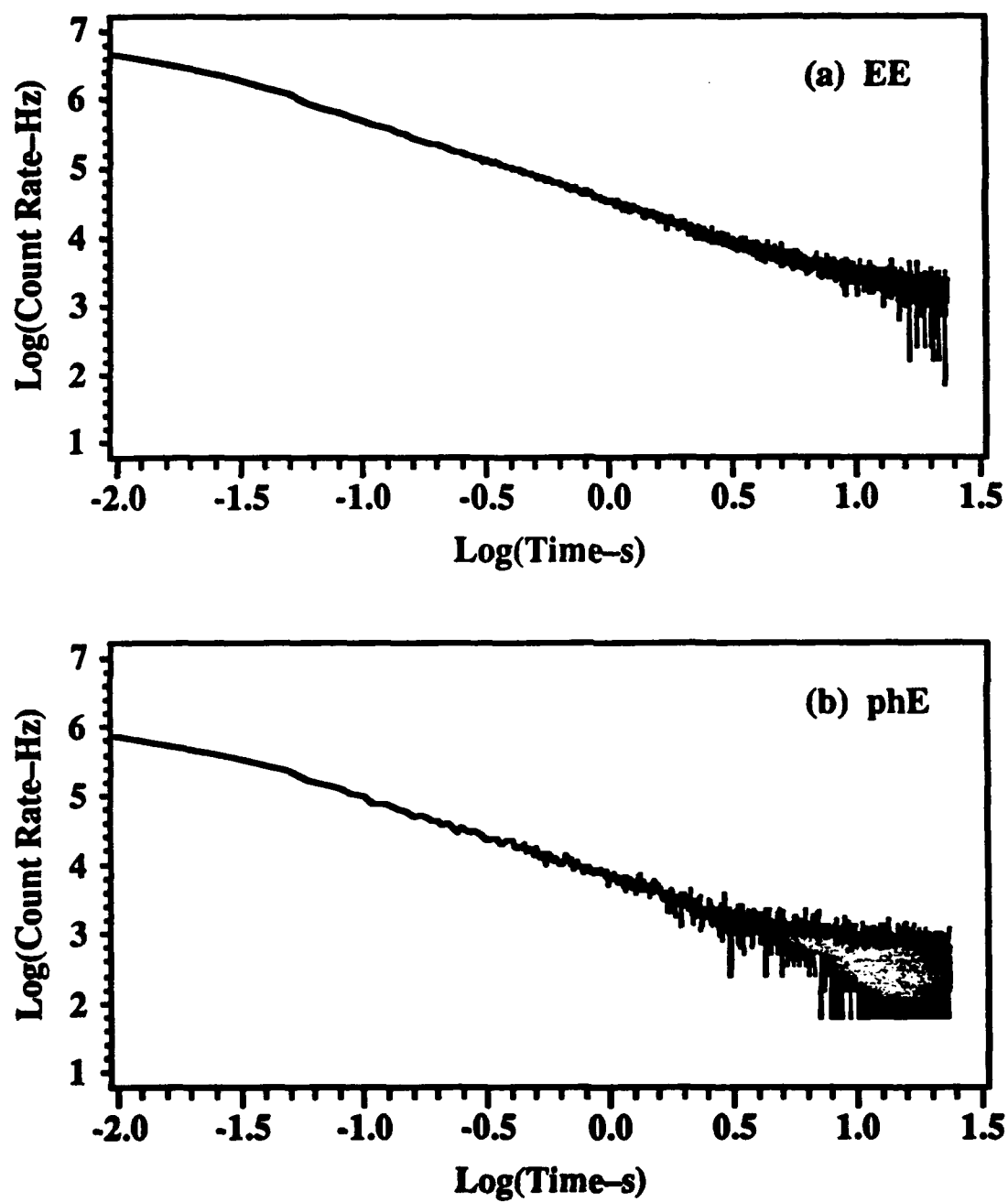
**FIG. 4**

**EE following Fracture of Glass-filled Polybutadiene (1000 s)****FIG. 5**

**FIG. 6**



**phE and EE following Fracture of Glass-filled Polycarbonate****FIG. 7**

**phE and EE Following Fracture of Single-Crystal MgO****FIG. 8**

**phE Following Rapid Peel of Magic Tape® from Copper  
and EE Following Fracture of PZT**

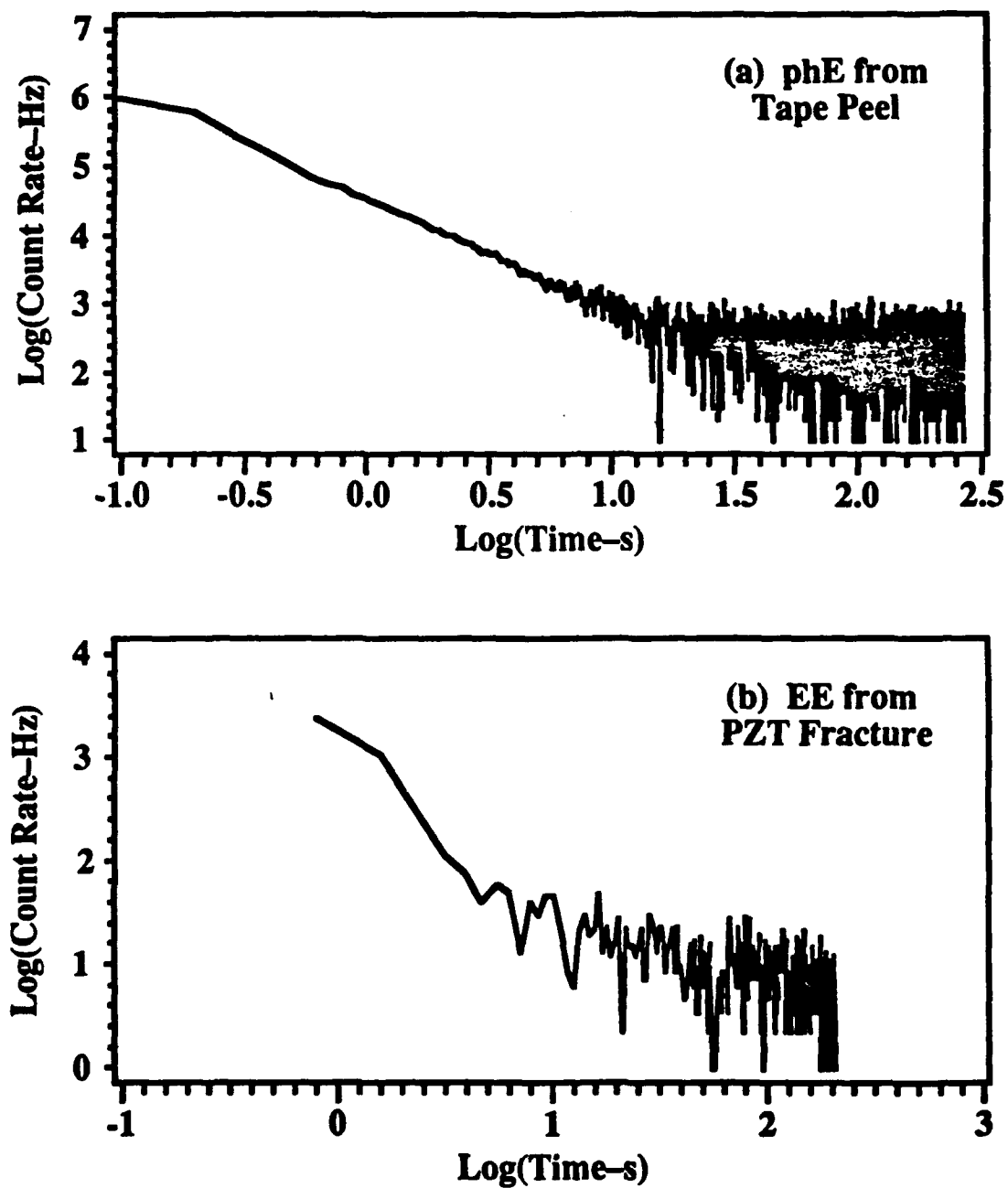


**FIG. 9**

## **VII. Ar atom emission as a probe of craze formation and craze growth in polystyrene**

J. T. Dickinson, L. C. Jensen, S. C. Langford,

Physics Department, Washington State University, Pullman, WA 99164-2814

and

R. P. Dion,

The Dow Chemical Company, Designed Thermoplastics Research, Midland, MI 48667

We report measurements of Ar emission during the loading of polystyrene and high impact polystyrene in vacuum. Argon was introduced into the material prior to the experiment by storing the samples in an Ar atmosphere. The development of crazes during loading was monitored by videotaped visual observations and scattered light measurements. Increased Ar emission is observed at the onset of crazing, provided that the crazes intersect the surface. The strength of the Ar signal depends upon the extent of crazing; especially intense signals are observed from samples which display significant crazing prior to fracture. High impact polystyrene shows intense emissions at yield which soon decay due to the depletion of Ar from the near surface material. The emission intensity rises again prior to fracture, when surface crazes become connected to crazes in the bulk. Thus the emission of volatile species during deformation reflects the growth of crazes intersecting the surface, as well as changes in the "connectivity" of the craze network.

## I. INTRODUCTION

Crazing as a deformation mechanism is unique to glassy polymers and has important consequences with regard to impact strength and durability. Although crazes themselves often display considerable tensile strength and consume energy in their formation, they also serve as stress concentrators, promoting further craze growth and ultimately leading to failure. In high impact polystyrene, crazing is nucleated by small rubber particles which also serve to limit the growth of the individual crazes; the large number of small crazes allows for considerable energy dissipation while minimizing the ability of individual crazes to initiate fracture. Nevertheless, craze thickening and rubber particle failure eventually produce connected craze networks of sufficient size to initiate catastrophic failure. Although several techniques are available to monitor the total craze volume in such samples (e.g., dilatation measurements and small angle x-ray and neutron scattering), it is difficult to assess the development of connectivity in the craze network growth with these techniques.

The growth of crazes which communicate with the polymer surface may be detected by the enhanced diffusion of volatile atoms or molecules from the interior to the surface. In vacuum, this enhanced diffusion is readily observed with a nearby mass spectrometer tuned to the mass of interest. For this purpose we have "loaded" several polystyrene samples with Ar by storing them in an Ar atmosphere. The diffusion of Ar from polymeric materials is readily detected in vacuum, and the resulting signal is free of interference from extraneous sources. In this paper, we show that the signal due to Ar is a sensitive indicator of the onset of crazing in polystyrene, providing that the crazes communicate with the surface. Further, we show that the deformation of high impact polystyrene is accompanied by two major peaks in Ar emission, one at tensile yield and one prior to failure. We attribute the first peak to the development of short, surface crazes which rapidly deplete the near surface region of occluded Ar. The second peak is attributed to the development of connectivity between near-surface crazes and crazes in the

interior. Volatile emission in vacuum appears to reflect the development of connectivity among surface and bulk crazes, which ultimately leads to failure.

## II. EXPERIMENT

The polystyrene used in this study was Styron 680® provided by The Dow Chemical Company. Two types of samples were employed: injection molded dogbone samples and dogbone samples machined from compression molded bars. The gauge length of the machined samples was 6.3 cm long, with a cross section of  $3.2 \times 3.2 \text{ mm}^2$ , while that of the injection molded samples was 7.6 cm long with a cross section of  $13 \times 3.2 \text{ mm}^2$ . Since the progress of crazing can be substantially affected by molecular orientation introduced by the process of injection molding, some injection molded samples were annealed at 85 °C in a Teflon tube for twelve hours to remove this orientation. Argon gas was introduced into all samples by storing the samples under one atmosphere of Ar for a minimum of two weeks, assuring saturation [from known Ar-polystyrene diffusion and solubility data, the predicted time to attain saturation was 2 days].

The samples were mounted in a tensile loading apparatus inside a high vacuum system and pumped overnight. The base pressure of the vacuum system immediately prior to the experiment was from  $10^{-5}$ - $10^{-7}$  Pa, depending on the elapsed time of pumpout prior to testing. The Ar emission was monitored with a UTI 100C quadrupole mass spectrometer mounted about 3 cm away from the gauge length of the sample. In several experiments, the progress of crazing was illuminated and observed through windows in the vacuum system and recorded with a video camera, allowing correlations between the onset and growth of crazes and the onset and growth of the Ar signal. In other experiments, the progress of crazing was monitored by photocell measurements of the light intensity scattered from the developing craze.

### III. RESULTS

**Machined samples.** The machined polystyrene samples displayed two contrasting fracture modes. Some samples developed a large number of parallel, closely spaced crazes prior to fracture which extended across the entire thickness of the sample. Subsequent crack growth in these "heavily crazed" samples was largely confined to crazes formed during loading.<sup>1</sup> The resulting fracture surfaces were composed of smooth, flat regions bounded by abrupt steps, where crack growth "jumped" from one craze to another. Most samples, however, showed little crazing prior to fracture. The crazes which were observed were small, and did not extend far into the bulk of the sample. Aside from the initial stages of crack growth, the crack in these "lightly crazed" samples generated its own craze, forming characteristic bands (a mackerel pattern) via repeated cycles of crack arrest, extensive craze branching, and subsequent crack growth.<sup>2</sup> [For an extensive discussion of the morphology of polystyrene fracture surfaces, see Ref. 3.] SEM micrographs of representative samples of both types appear in Fig. 1. In each case, crazes were generally nucleated at surface defects induced by machining. In those samples which crazed extensively prior to fracture, crazes were nucleated rather uniformly over a large area, while in those samples which failed after minimal crazing, craze nucleation was confined to just a few of the larger defects.

Prior to deformation, a small but easily detectable mass 40 signal was detected from all Ar filled samples due to steady outgassing (diffusion + desorption) of the sample. Models of outgassing of volatile gases into vacuum<sup>4</sup> show that starting from an initially uniform concentration distribution, the concentration is smallest at the sample surface and largest in the center. Thus, if any defect opens a pathway to material below the surface, one expects an increase in the gas phase component. Depending on the extent of crazing, all samples showed a detectable increase in the Ar signal when strained, with a extremely large pulse of Ar at fracture followed by a substantial decaying tail. The fracture induced emissions are due to the interior surface being suddenly exposed to the vacuum; these emissions are enhanced by the transient

heating accompanying fracture due to rapid, localized plastic deformation. [In experiments to be reported elsewhere<sup>5</sup> we have measured the temperature of the emitted gases by time-of-flight techniques. These temperatures (~650 K) indicate significant surface heating.]

Heavily crazed samples displayed intense Ar emissions during the course of crazing. The mass 40 emission from a heavily crazed, machined sample loaded at a strain rate of  $1 \times 10^{-3} \text{ s}^{-1}$  appears in Fig. 2. In this case, crazing resulted in a small load drop prior to fracture. Craze formation provides crack-like openings which extend from the Ar-rich interior of the sample to the surface, raising the Ar signal above background. Although the relationship between the load and the Ar signal is not simple, the Ar signal clearly correlates with the deviation from elastic behavior apparent in the load; i.e., the greater the curvature in the load signal, the stronger the Ar signal. The mass 40 signal rises sharply at the shoulder in the load, where the rate of craze growth increases markedly.

Figure 3 compares typical mass 40 signals on somewhat faster time scales from fracture events accompanied by moderate crazing (~20-40 visible crazes, many extending through the sample thickness) and light crazing [typically 5-10 small (<1 mm) crazes]. Both samples were loaded at a strain rate of  $1 \times 10^{-3} \text{ s}^{-1}$ . Ar emission prior to fracture from the lightly crazed sample is almost two orders of magnitude less than that from the moderately crazed sample, consistent with minimal crazing prior to fracture. In contrast, the *peak* mass 40 emission from moderately crazed samples is often smaller than that from lightly crazed samples, as in Fig. 3. The weak emission *during* crack growth in the moderately crazed material is reduced because of depletion during of Ar during loading from crazes formed in the region where fracture eventually occurs. The exposure of Ar-depleted material by subsequent fracture along the craze yields less emission than fracture through previously uncrazed material. It is also possible that the temperature increase during crack growth is greater for the lightly crazed sample due to higher crack tip stresses producing more rapid, localized deformation.

**Injection-molded samples.** The emission of occluded gases during crazing requires that crazes intersect the surface to provide an escape route for gases released from the bulk into the



craze. Substantial crazing can occur in the interior of injection-molded polystyrene samples before any crazes reach the surface; crazing in the near-surface region is hindered by the relatively high degree of molecular orientation in this region produced by the molding process. Figure 4 shows the Ar emission from an injection molded sample immediately prior to failure; post-fracture examination of the sample confirmed that the crazes did not intersect the sample surface. The duration of the data record in this experiment was limited in order to examine the emission immediately prior to fracture in more detail. At this sensitivity, no increase in Ar emission was observed until some tens of  $\mu\text{s}$  prior to fracture.

In general, samples which displayed few crazes and little Ar emission showed smoothing rising, almost linear load curves until ultimate failure. [The uneven rise in stress in Fig. 4(b) is due to variations in the loading rate, and not to material properties. Unlike the other samples in this report, this sample was loaded manually.] In contrast, samples which displayed dense crazing along the gauge length and intense Ar emission prior to failure generally showed a flattening of the load curve prior to failure. Figure 2(b) shows an extreme case of flattening in the load curve prior to failure. The stress at failure for both heavily crazed and lightly crazed injection-molded samples ranged from 30 MPa to 60 MPa. The craze density in the heavily crazed samples often exceeded 100 crazes/mm throughout the gauge portion of the sample, which is enough to account for the flattening of the load curve.

The molecular orientation which hinders crazing near the surface can be removed by annealing. In the absence of molecular orientation, crazing is expected to nucleate the surface, so that virtually all crazes should contribute to the mass 40 signal. Visual inspection of annealed samples after failure confirmed that the crazes intersect the surface. The sensitivity of the technique may be illustrated by comparing videotaped observations of the crazing process with the mass 40 signal from annealed, injection-molded samples. The VCR frame number and the Ar signal were synchronized within 1/30 s (time/single frame). White light was directed towards the sample to reflect specularly from the newly formed craze surfaces towards the camera lens.

Simultaneously acquired videotaped observations of and mass 40 signals from fracture of an annealed, injection molded sample loaded at a strain rate of  $3.3 \times 10^{-3} \text{ s}^{-1}$  appear in Fig. 5. Although lighting conditions vary somewhat throughout loading, the transparency of the uncrazed sample is clearly evident in Fig. 5(b)(1). The sample was illuminated from behind, through the window appearing to the left in the background. Crazes generally appeared as bright spots or lines in the images due to light scattered from the individual crazes. However, very heavily crazed regions of the sample often appeared as dark lines.

The first VCR image to show signs of crazing appeared 53 frames prior to fracture, at the point labeled (1) in Fig. 5(a). At low QMS sensitivity, the onset of Ar emission leads the first visual sign of crazing by 80 ms ( $> 2$  frames). The two spots of light on the bottom edge of the right side of the sample in Fig. 5(b)(1) are less than 1 mm long. These two crazes comprise the majority of the craze area at point (1); therefore, the Ar emission grows to significant levels before the total craze area is less than  $6 \text{ mm}^2$ . Fourteen frames later, at point (2), extensive crazing is noted along the right side of the sample. The mass 40 signal is quite strong and rising rapidly at this point. Somewhat later (at point 3), the craze density has increased to the point where the individual crazes are no longer individually resolved in the videotaped images, and the mass 40 signal is approaching its maximum value. The intensity of the scattered light due to crazing after fracture [image (4)] is impressive, especially when compared to the image at the onset of crazing [image (1)]. Post-fracture examination of the sample showed dense crazing throughout the gauge length of the sample, with exceptionally dense crazing along a strip 2-3 mm wide adjacent to the fracture surface on both fragments. This exceptionally high craze density accounts for the darker regions along the fracture surfaces in Fig. 5(b)(4).

Employing more QMS sensitivity allows emissions to be observed much earlier in the loading process. Figure 6(a) shows the mass 40 signal during the loading of another annealed, injection-molded sample. The initial sensitivity of the quadrupole was  $100\times$  that employed above. Twice during loading, the quadrupole sensitivity was lowered by a factor of ten so as to keep the observed emission "on scale." In this experiment, crazing was monitored by measuring

the intensity of light scattered from a collimated light beam directed through the sample. The intensity of the scattered light was monitored with a photocell and used to study the growth of the developing crazes.

At the highest quadrupole sensitivity employed, the mass 40 signal begins to increase immediately at the onset of loading in a steadily increasing fashion, as indicated in the inset of Fig. 6(a). Fig. 6(b) is the increase in scattered light from crazing detected by a photocell and Fig. 6(c) is the applied load. The origin of this small, gradual increase in Ar emission shown in Fig. 6(a) is discussed below. The much more intense Ar signals which follow are attributed to short periods of relatively rapid craze growth involving a large number of small crazes. (The sharp spike in the mass 40 signal 5 s after the onset of loading is probably due to a micro-fracture event.) Similar signals would be expected when previously nucleated crazes in the interior of the sample intersect the surface; however, crazing in annealed samples generally nucleates at the surface. Note that these broad shoulders occur long before the major rise in the scattered light signal. The major rise in the scattered light signal coincides with the last major rise in the mass 40 signal immediately prior to fracture. Both signals reflect the rapid growth of a large number of crazes immediately prior to failure. Post-fracture examination of the sample showed dense crazing through about half the gauge length of the sample. Thus, the mass 40 signal is sensitive to the growth of crazes while they are still quite small, undetectable by scattered light.

The small, gradual increase in mass 40 signal in the earliest stages of loading is not due to crazing, which is expected at higher loads. Prior to the onset of visible crazing, the mass 40 signal is a fairly reversible function of load. Figure 7 shows the mass 40 signal when a rapid, transient strain was applied to an annealed, injection molded sample. The rapid rise in the mass 40 emission with loading and the equally rapid decay following loading shows that the Ar emission here is associated with an elastic deformation of the sample, rather than the growth of new craze. Experiments with Ar loaded bisphenol-A polycarbonate, which does not craze at room temperature, shows very similar Ar emissions prior to the onset of yielding.<sup>6</sup> Thus, for both polycarbonate and polystyrene, we attribute these early signals to an increase in free volume

which accompanies tensile loading that enhances the diffusion of Ar to the surface of the sample. This would account for the observed emissions in the absence of crazing of the polystyrene. The intensity of the observed emissions decreases with subsequent loading cycles, due to the depletion of Ar in the near-surface region.

**HIPS.** The deformation behavior of HIPS samples contrasts markedly with that of neat polystyrene, leading to striking differences in the emission behavior. Several experiments were performed on machined HIPS samples, where crazing is localized to very small regions along the gauge length. This results in premature failure. Typical emissions from a machined HIPS sample loaded at a strain rate of  $3.3 \times 10^{-3} \text{ s}^{-1}$  appear in Fig. 8. The gradually accelerating load drop prior to failure and the absence of a pronounced mass 40 peak are consistent with relatively slow crack growth through one of the crazed regions. The Ar signal during the early stages of loading is shown on an expanded scale. At this level of sensitivity, the onset of emission was noted at about 1% strain. As noted below, on more sensitive quadrupole scales the onset of emission coincides with the onset of loading. (At high sensitivities, the Ar peak at fracture would invariably go off scale.)

Injection molded HIPS samples showed a great deal more deformation before failure than the machined samples. Emissions from an injection molded sample loaded at a strain rate of  $3.3 \times 10^{-3} \text{ s}^{-1}$  appear in Fig. 9. The two Ar emission peaks are characteristic of emission from this material. The mass 40 signal begins to rise immediately on the onset of loading, which is marked by an arrow in Figs. 9(a) and 9(b). The mass 40 signal rises sharply at the upper yield point and continues to rise for the next 30 s (peak  $\sim 10\%$  strain). The Ar emission subsequently drops to rather low levels, indicating that near-surface crazes are being depleted of Ar faster than new surface crazes are being produced. This suggests that the principle deformation mechanism at this point is the thickening of pre-existing crazes rather than the development of new crazes. About 50 s prior to fracture, corresponding to  $\sim 25\%$  strain, the mass 40 signal rises slowly to form a broad, flat peak. Aside from a narrow spike at fracture ( $\sim 35\%$  strain), fracture results in a sharp drop in the emission intensity. The stress relief upon fracture produces fibril contraction

in the crazes, which narrows the crazes and hinders further diffusion of Ar from the sample interior.

We therefore attribute the first peak to the rapid growth of new crazes subsequent to yield, and the second peak to craze thickening or rubber particle failure, which eventually provides continuous paths from interior crazes to surface crazes. Initially, the surface crazes do not communicate with crazes deep in the bulk and are soon depleted of Ar. Thus the Ar emission intensity soon peaks and drops to a low level. Subsequent thickening of the near-surface crazes yields little emission until this process opens up direct paths between crazes in the interior and crazes at the surface, allowing Ar from crazes in the interior to desorb into crazes which communicate with the surface. The development of connectivity among the crazes naturally leads to the formation of large flaws, one of which ultimately precipitates failure of the entire sample in a localized fashion. This portion of the Ar emission signal therefore serves as a measure of the final breakdown of the material.

As in the case of neat polystyrene, the onset of Ar emission from HIPS virtually coincides with the onset of loading. The onset of Ar emission evident in Fig. 9(a), where the emission in the early stages of loading was monitored with a higher quadrupole sensitivity. The time of the onset of loading is marked with an arrow. When viewed with higher sensitivity, we find no time delay between the onset of loading and the onset of emission. As in the case of neat polystyrene, Ar emission in the earliest stages of loading probably reflects the enhanced diffusion of Ar through the bulk material. When the load becomes sufficient to promote crazing, the mass 40 signal rises sharply.

#### IV. DISCUSSION AND CONCLUSION

The emission of occluded Ar is a sensitive indicator of the onset and growth of crazes in polystyrene provided that the crazes reach the surface. Even at modest instrument sensitivities, the production of visible crazes produces readily measured increases in the mass 40 signal.

Measurements at high instrument sensitivities show measurable increases in emission intensities long before the onset of visible crazing. In neat polystyrene, the signals associated with crazing do not necessarily grow smoothly, suggesting that craze growth can be sporadic in the early stages of loading. Intense emissions accompany fracture, and require less sensitive quadrupole scales. The dynamic range of the quadrupole mass spectrometer is several orders of magnitude, allowing for considerable flexibility, depending on the process of interest. For species like Ar, where the background signals are quite low, high quadrupole sensitivities are readily employed to study the weak emissions early in the stages of loading.

Although Ar provides a readily measured signal, other volatiles could easily serve this purpose. For instance, substantial amounts  $N_2$  and water are entrained in most polymers by virtue of constant exposure to the atmosphere. The emission of water from polystyrene is readily detected in vacuum, for instance, and shows many of the same behavior as the mass 40 emission from Ar-soaked samples. However, the relatively high background signals at mass 18 ( $H_2O$ ) and 28 ( $CO$ ) from the walls of the vacuum system limits the maximum sensitivity of measurements at these masses. In other studies, we have used exposure to  $D_2O$  as a way to circumvent this problem. Also, the use of volatiles introduced by processing is possible. For instance, the styrene monomer, dimer, and trimer are present in most commercial materials in significant concentrations. These are readily detected at fracture, and provide potentially useful signals during loading as well.

The time resolution of these measurements is limited largely by the time required for the diffusion of gases into and along the craze. Estimates of this time suggest that considerable time resolution is possible, especially along short crazes. For instance, distance between fibrils in a typical polystyrene craze is about 20 nm.<sup>7</sup> Assuming that the diffusion of gas along the craze is limited by collisions with fibrils, the diffusion process can be modeled as a random walk through a rectangular array of craze fibrils. The time  $\tau$  required for the average particle to travel a distance  $d$  in such an array is roughly

$$\tau = \frac{d^2}{lv} \quad (1)$$

where  $l$  is distance between fibrils and  $v$  is the thermal velocity of the diffusing molecule. Assuming a molecular velocity of 300 m/s, a gas molecule can travel the length of a typical craze in HIPS (10  $\mu\text{m}$ ) in about  $\tau = 25 \mu\text{s}$ . Special amplifiers can be used for detecting changes in ion current on such a time scale so that the potential time resolution appears to be adequate for tensile experiments at strain rates some orders of magnitude greater than those employed in this study.

Craze development has been studied by numerous techniques, of which few are suitable for the study of crazing at high rates of deformation. For instance, total craze volume measurements by small angle X-ray scattering can be made with a time resolution of perhaps 10 ms using intense synchrotron X-ray sources.<sup>8</sup> Although the enhanced diffusion and desorption of occluded volatiles from crazed material does not directly indicate the total craze volume, it does yield information on the connectivity of the craze network which is otherwise difficult to study in real-time. The sensitivity of the technique to the onset of crazing at the surface is also high, which may prove useful in studying the effect of surface preparation as well as bulk properties on the onset of crazing.

## ACKNOWLEDGMENTS

This work was supported by The Air Force Office of Scientific Research Contract AFOSR-F49620-91-C-0093, The Dow Chemical Company, and the Washington Technology Center.

## REFERENCES

1. J. Hoare and D. Hull, *J. Mater. Sci.* **10**, 1861 (1975).
2. D. Hull, *J. Mater. Sci.* **5**, 357 (1970).
3. D. M. Kulawansa, S. C. Langford, and J. T. Dickinson, *J. Mater. Res.* **7**, 1292 (1992).
4. P. A. Redhead, J. P. Hobson, and E. V. Kornelsen, *The Physical Basis of Ultrahigh Vacuum*, (Chapman and Hall, London, 1968), Section 2.5.
5. J. T. Dickinson, L. C. Jensen, S. C. Langford, and R. P. Dion, "Temperature measurements of the gaseous emission of occluded volatiles during the fracture of polystyrene," in preparation.
6. J. T. Dickinson, L. C. Jensen, S. C. Langford, and R. P. Dion, "Emission of occluded volatiles during deformation of polycarbonate", in preparation.
7. A. C.-M. Yang, and E. J. Kramer, *J. Polym. Sci. Polym. Phys. Ed.* **23**, 1353 (1985).
8. R. A. Bubeck, J. A. Blazy, E. J. Kramer, D. J. Buckley, and H. R. Brown, *Polym. Commun.* **27**, 357 (1986).



## FIGURE CAPTIONS

- FIG. 1.** SEM micrographs of two polystyrene fracture surfaces. The sample of (a) showed extensive crazing prior to fracture, while that of (b) showed little if any visible crazing prior to failure.
- FIG. 2.** (a) Mass 40 and (b) load signals accompanying the fracture of machined polystyrene in tension. An SEM micrograph of this sample appears in Fig. 1(a). Arrows mark the time of fracture, which occurred at about 0.74% strain.
- FIG. 3.** Comparison of mass 40 signals from machined polystyrene samples showing (a) extensive crazing prior to failure, and (b) minimal crazing prior to failure. An SEM micrograph of the sample yielding the emissions in (b) appears in Fig. 1(b).
- FIG. 4.** (a) Mass 40 and (b) load signals accompanying the loading of injection molded polystyrene. Inspection of the sample after failure indicated that few, if any, of the crazes reached the surface. Arrows mark the time of fracture. The fluctuations in the load are due to variations in the strain rate accompanying loading.
- FIG. 5** (a) Mass 40 signal and (b) photographs of videotaped images made during loading of an annealed, impact-molded polystyrene sample. The arrows in (a) mark the times at which the four images in (b) were recorded. The scale bar refers only to objects in the plane of the sample. Due to foreshortening, more distant objects are not scaled accurately.
- FIG. 6.** (a) Mass 40 signal, (b) photocell output (sensing scattered light), and (c) load accompanying tensile loading of annealed, injection molded samples. The sensitivity of the quadrupole mass spectrometer was changed at two points during loading, and is indicated along the horizontal axis in (a). The inset in (a) shows the mass 40 signal at the onset of loading on a ( $\times 10$ ) expanded vertical scale.

**FIG. 7.** (a) Mass 40 signal and (b) load accompanying the application of a step function load to an annealed, injection molded sample. Vertical dotted lines indicate the onset and end of the loading cycle.

**FIG. 8.** (a) Mass 40 signal and (b) load signals accompanying the fracture of machined HIPS sample. Arrows mark the time of fracture, which occurred at about 3% strain, and the apparent onset of mass 40 emission. The mass 40 signal is (a) is shown on an expanded vertical scale; however, the quadrupole sensitivity employed was constant throughout the experiment.

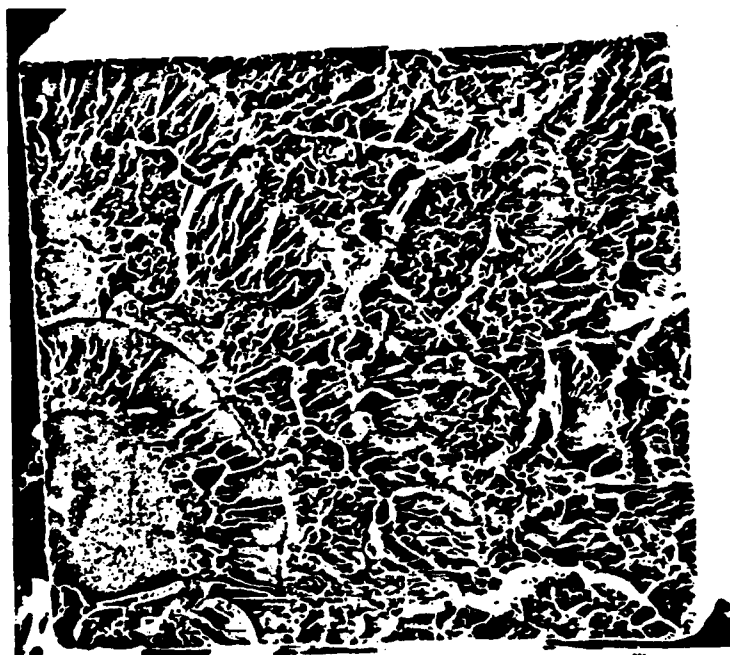
**FIG. 9.** (a) Mass 40 and (b) load signals accompanying the fracture of injection molded HIPS. Arrows mark the time of fracture (at about 35% strain) and the onset of loading. The mass 40 signal in the early portions of (a) were measured with increased quadrupole sensitivity, as indicated along the top of the diagram.



(a) Heavily Crazed



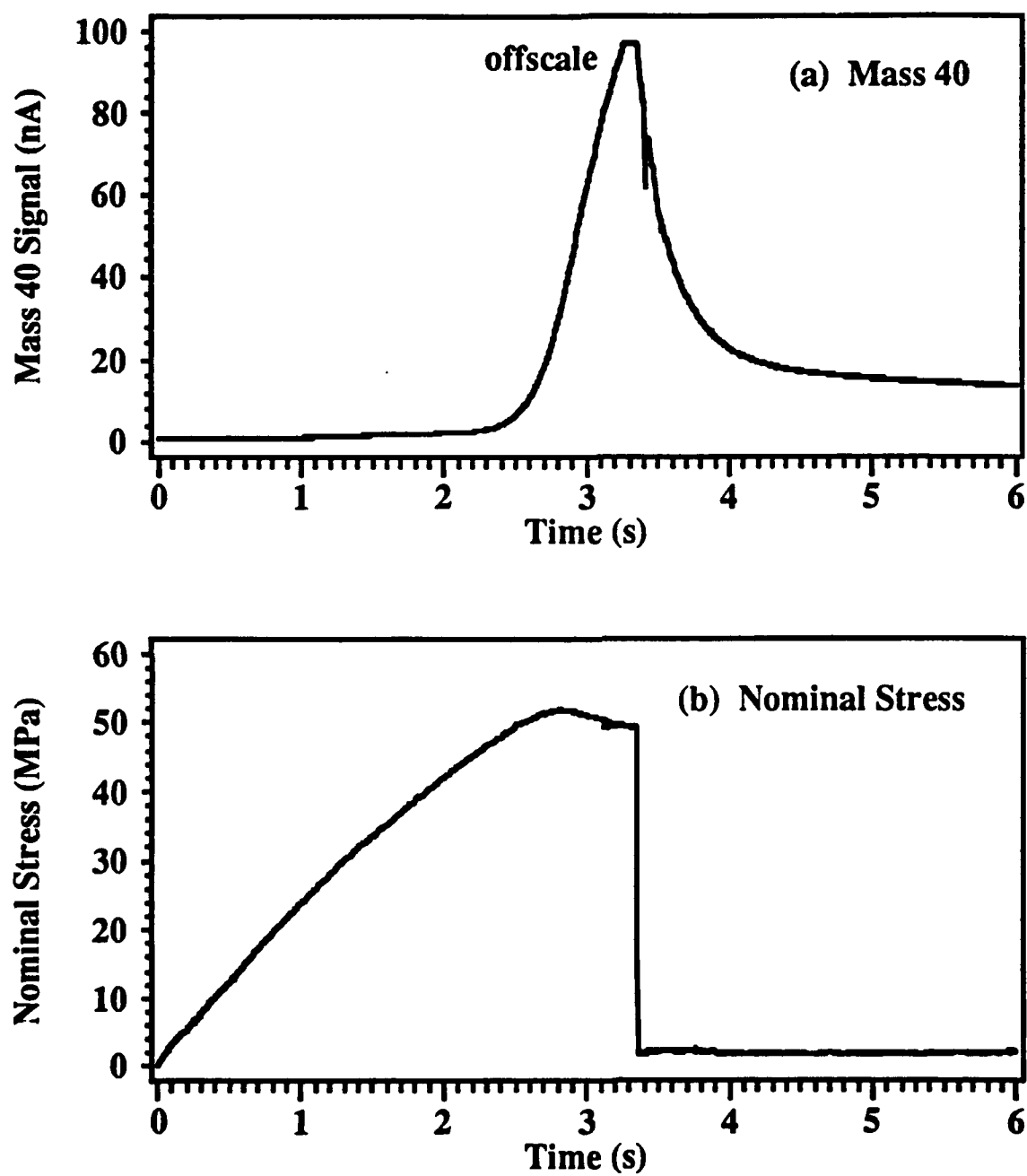
1 mm



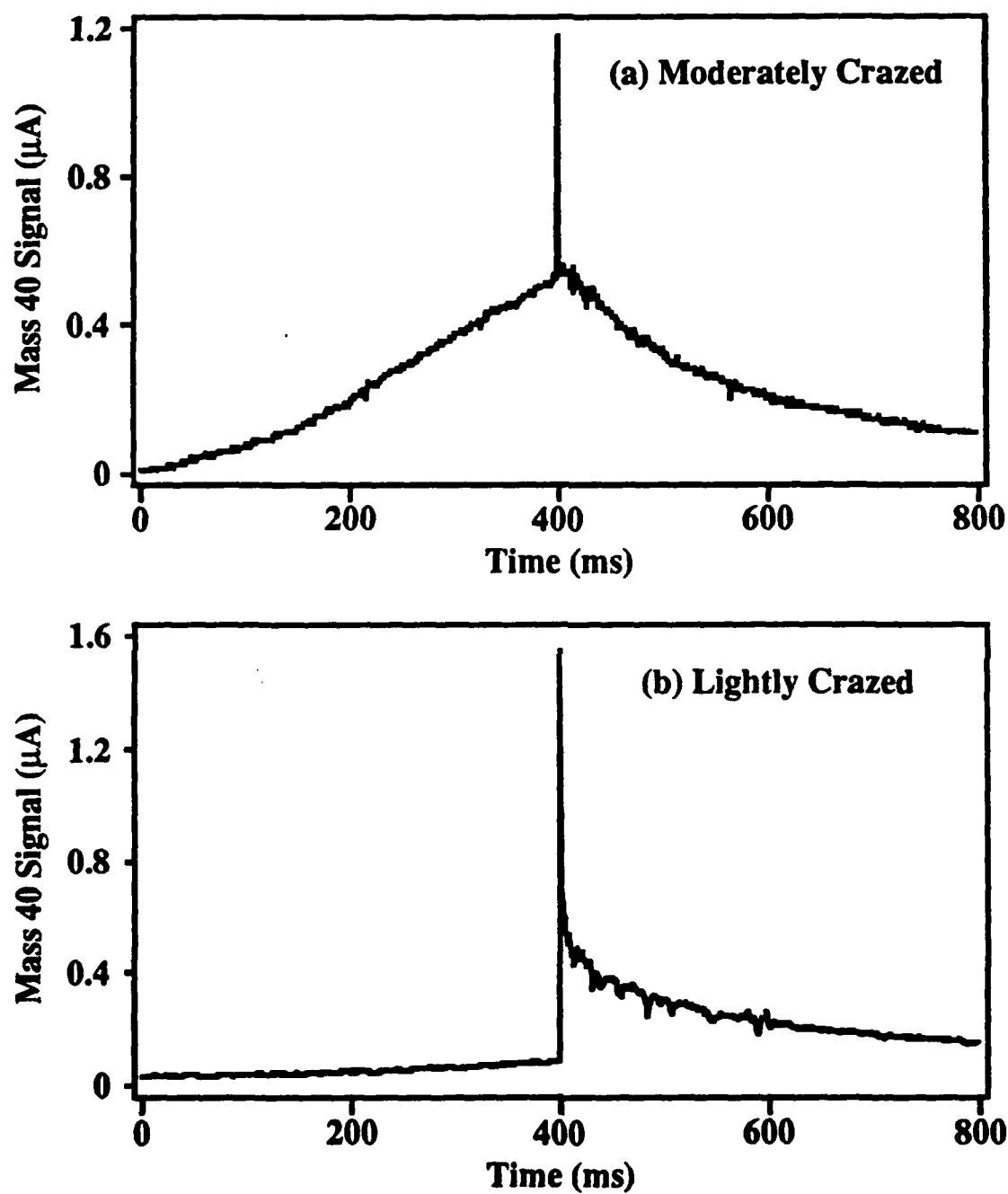
(b) Lightly Crazed



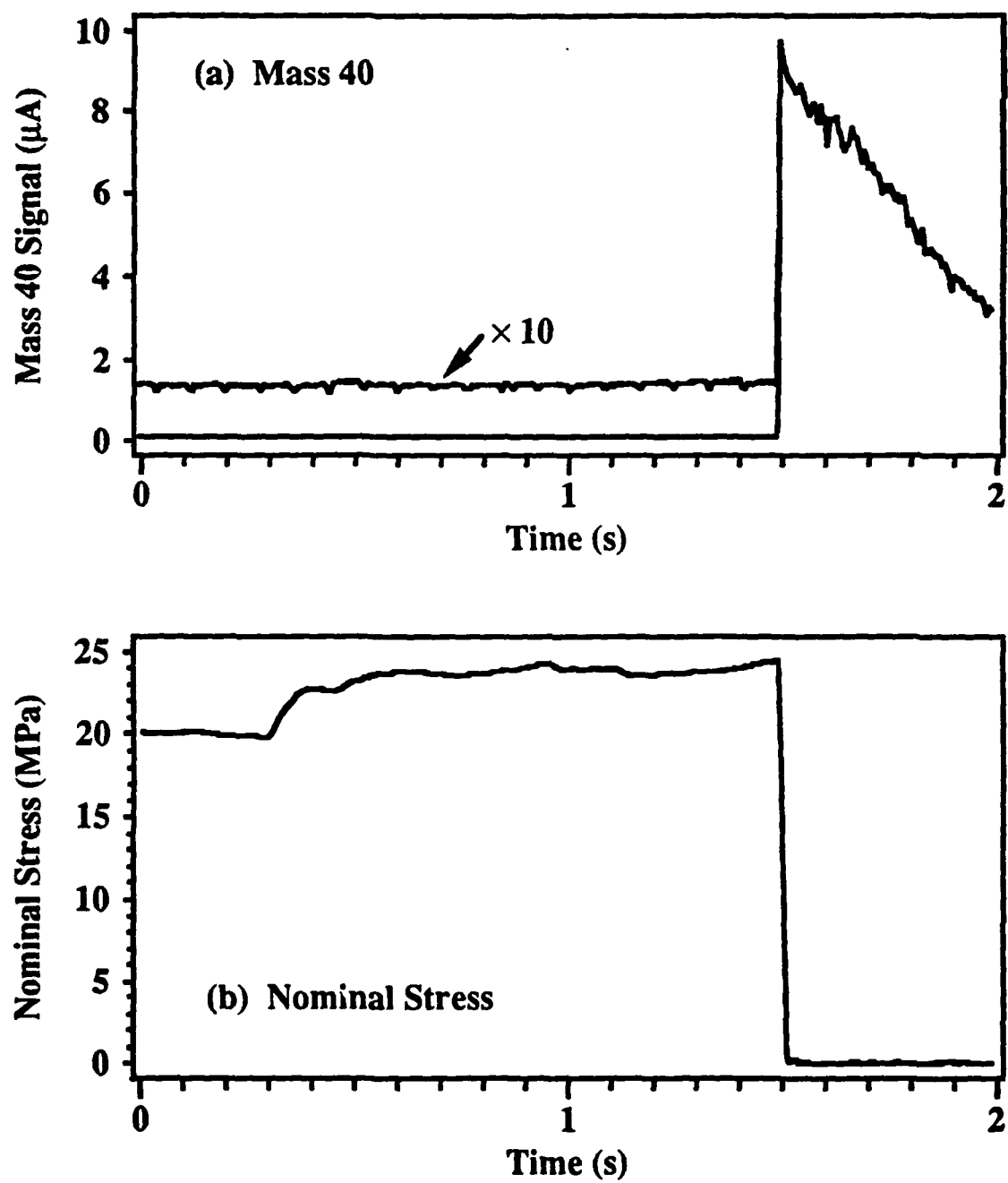
FIG. 1

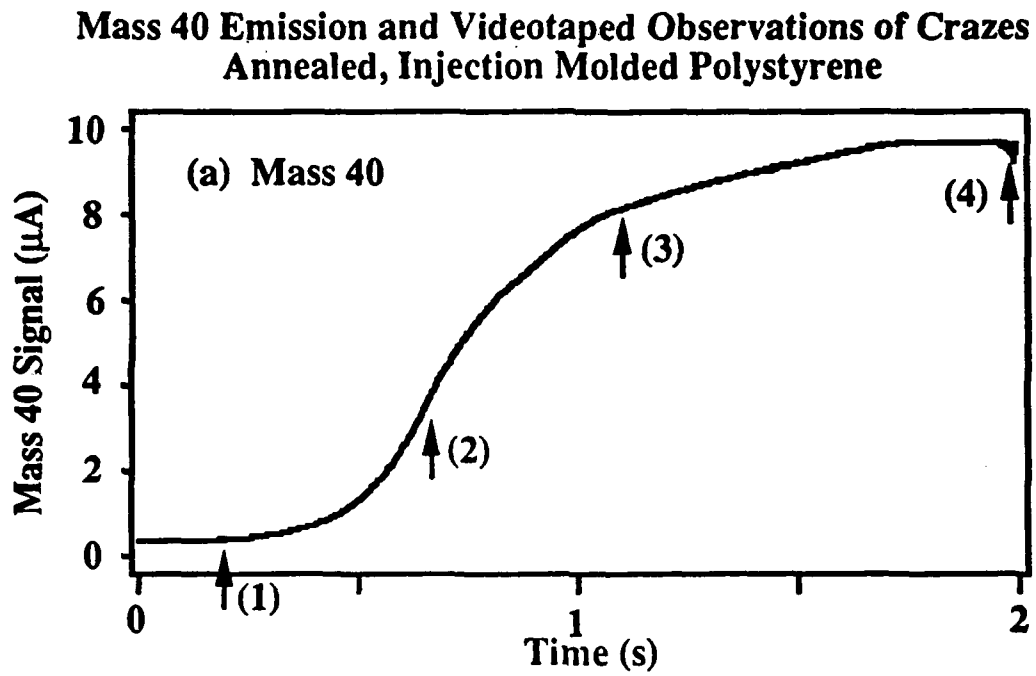
**Mass 40 Emission and Stress: Machined Polystyrene****FIG. 2**

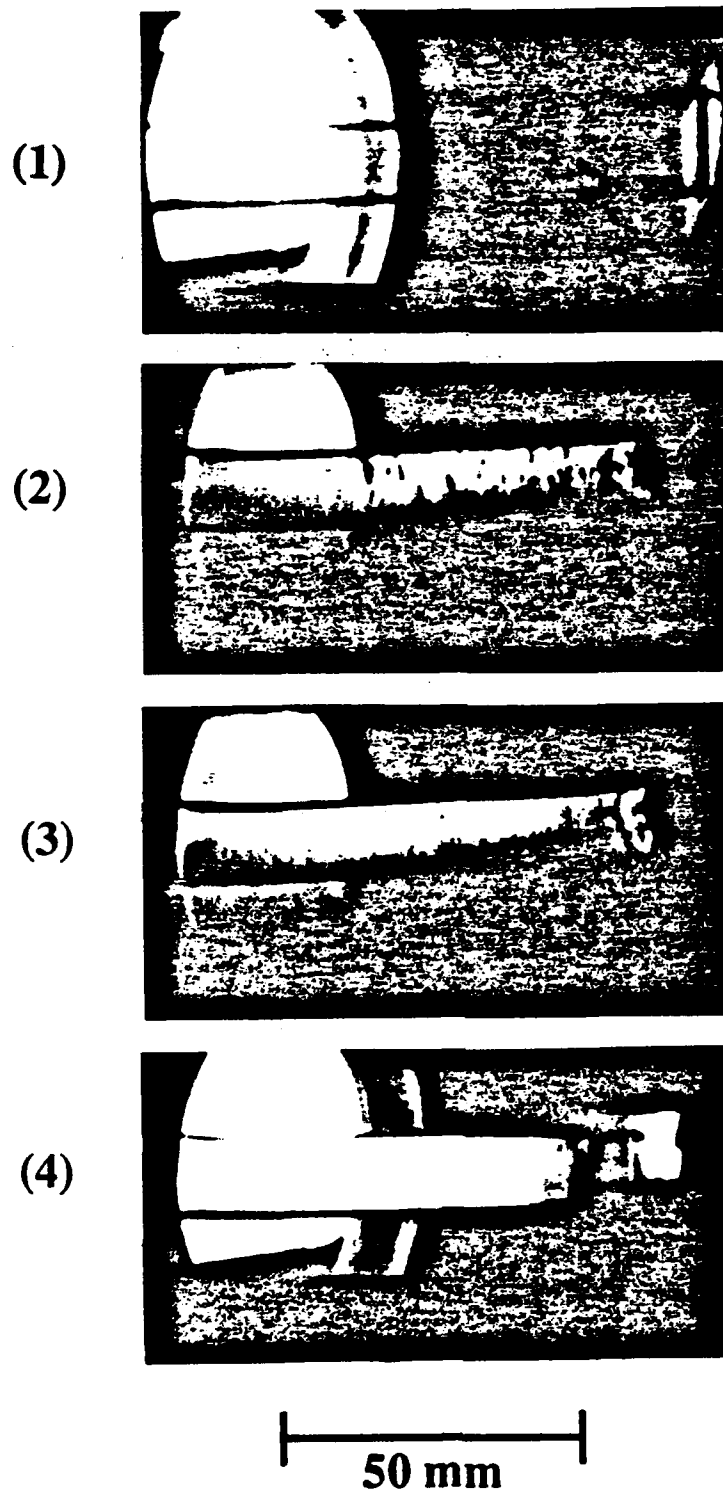
### Mass 40 Emission from Machined Polystyrene



**FIG. 3**

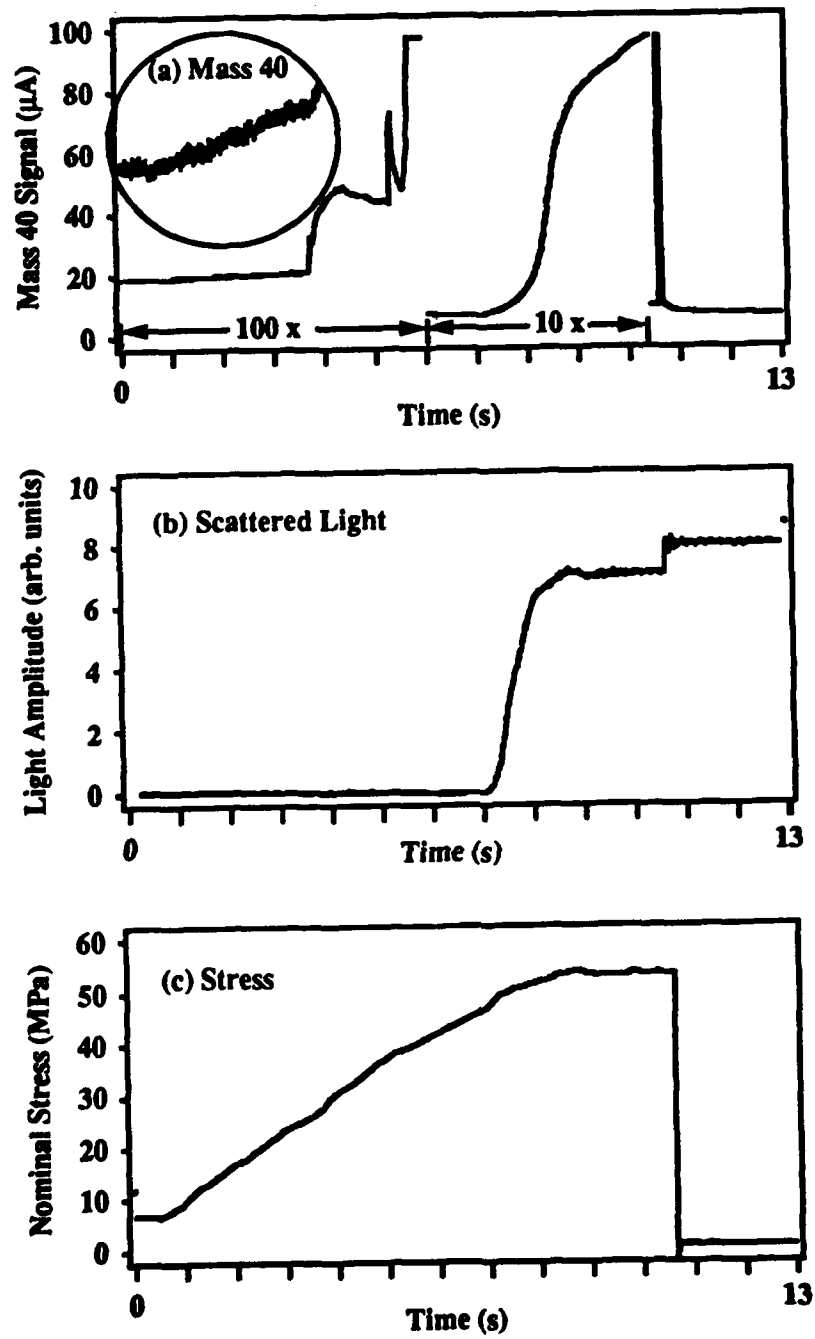
**Mass 40 Emission and Stress: Injection Molded Polystyrene****FIG. 4**

**FIG. 5(a)**

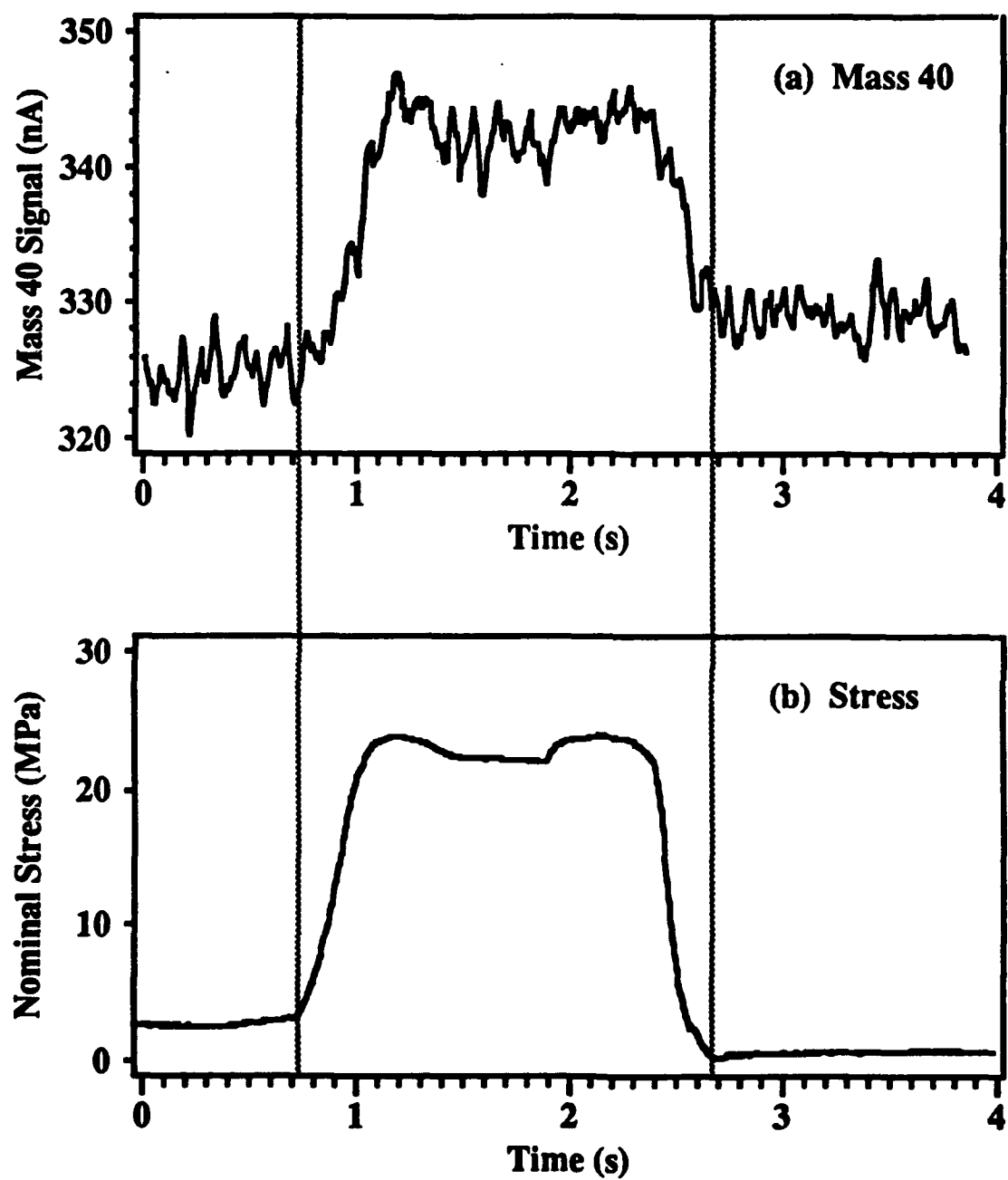
**(b) VCR Observations****FIG. 5(b)**

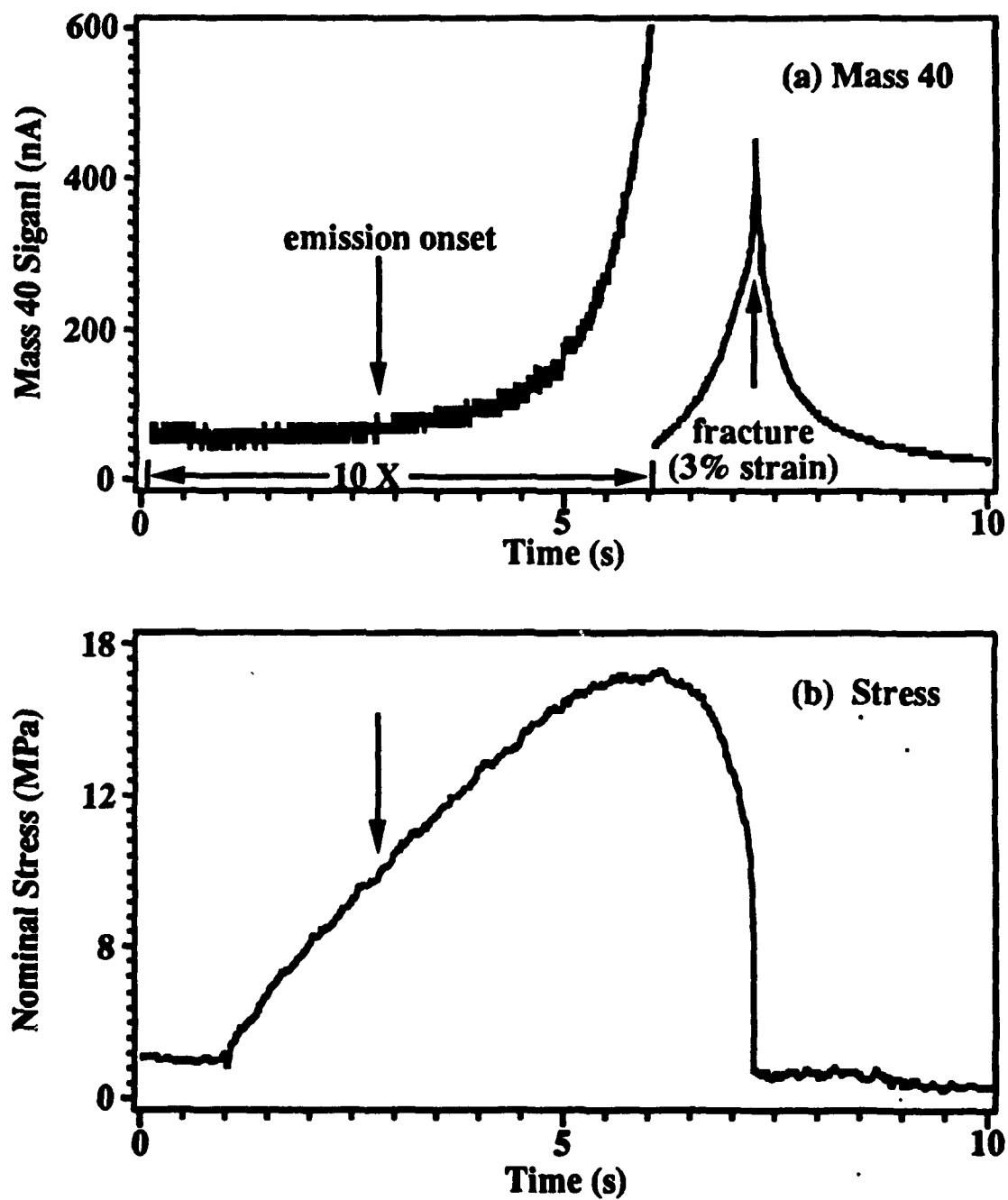


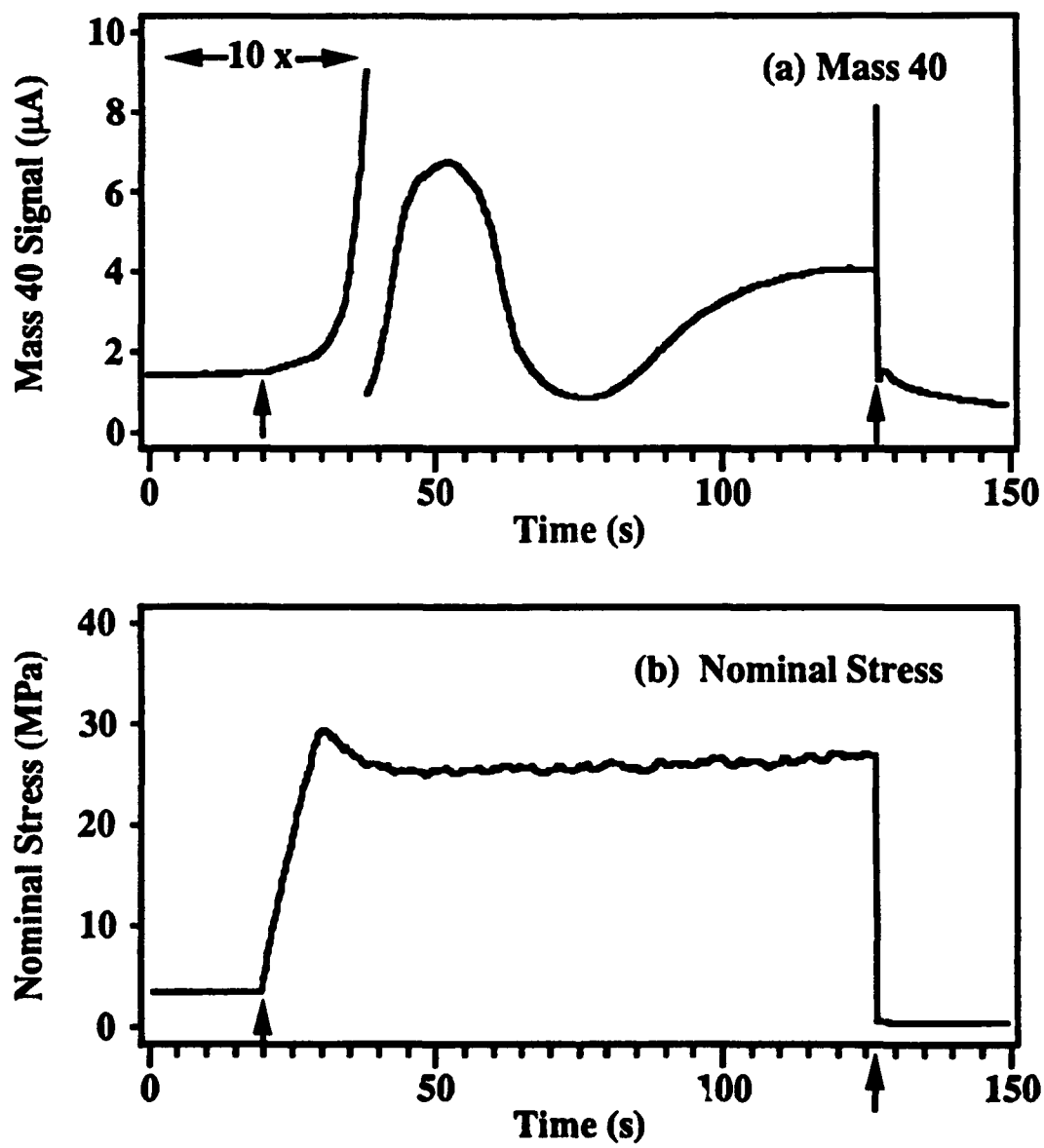
**Mass 40, Scattered Light, and Stress:  
Annealed, Injection Molded Polystyrene**



**FIG. 6**

**Mass 40 and Stress: Annealed, Injection Molded Polystyrene****FIG. 7**

**Mass 40 Signal and Stress: Machined HIPS****FIG. 8**

**Mass 40 Emission and Stress: High Impact Polystyrene****FIG. 9**

## **VIII. Electrical transients generated by the peel of a pressure sensitive adhesive from a copper substrate. Part I: Initial Observations.**

Sunkyo Lee, L. C. Jensen, S. C. Langford, and J. T. Dickinson

Physics Department, Washington State University, Pullman, WA 99164-2814

It is well known that the formation of adhesive bonds is generally accompanied by contact electrification. Thus, it is not too surprising that when a pressure sensitive adhesive (PSA) is peeled from a metal substrate, transient electrical signals are observed, related to the charge separation during detachment. We present detailed measurements of the currents generated by peeling a PSA from a electropolished Cu substrate in air and in vacuum. Correlations with peel force, photon emission, and optical microscopy provide details of the current generating mechanisms as well as connections with the micromechanics of the peel process. These electrical measurements are a potentially new way to obtain in a time-resolved fashion insight into the micromechanical processes accompanying peeling.

### **1. INTRODUCTION**

The peeling of a pressure sensitive adhesive is often accompanied by intense photon emission and long-wavelength electromagnetic signals.<sup>1-3</sup> In air, the photon emission (phE) can be sufficiently intense to expose photographic film, producing "autographs" of the peel process.<sup>4</sup> This intense phE has been attributed to gaseous discharges due to charge separation during the removal of the adhesive from the substrate. In an earlier paper we have examined the electrical transients accompanying propagation of a delamination crack between a metal rod and a brittle polymer matrix.<sup>5</sup> These electrical transients were shown to arise from separation of charge across

the opening crack, where contact electrification was the original source of such charge. In this work, we show that peeling a commercial pressure sensitive adhesive from a metal substrate also yields readily detectable currents. These currents reflect a number of details of the peeling process in a time-resolved fashion including specific microstructural events.

Adhesive failure in a peel geometry can be quite complex, owing to the extremely nonlinear, viscous behavior of the adhesive phase. Cavitation, viscous fingering, fibril formation and drawout in the adhesive phase contribute substantially to the energy dissipated in the peel process, and thus are of considerable practical importance. The complex nonlinear behavior of these materials suggests the possibility of chaotic behavior, which is of intense theoretical interest as well. In Part I of this work we examine the close relation between the electrical currents during peeling and the micromechanical events which produce them, showing that these measurements can provide important information about the peel process. In part II, we explore methods of enhancing the current fluctuations and additional correlations of these fluctuations with micromechanical phenomena.

## 2. EXPERIMENT

Fig. 1 shows schematically the typical experimental arrangements. This work employed 3M Scotch Brand Magic Tape [No. 810] 1/2 inch (12.7 mm) which consists of a cellulose acetate backing coated with a long-side-chain alkyl acrylate adhesive. Most peel experiments employed a rectangular copper block ( $13 \times 13 \times 19 \text{ mm}^3$ ) as a substrate. In order to obtain a reproducible, clean substrate, the copper block was electropolished in  $\text{H}_2\text{PO}_4$  solution for 20 seconds at 6 volts, then rinsed with acetone and distilled water prior to each experiment.

A schematic of the current measurements is shown in Fig. 1(a). Care was taken to ensure that the adhesive surface was electrically neutral during the formation of the adhesive bond. After the adhesive was removed from its role, it was electrically neutralized near the burning flame of a propane torch (avoiding significant heating) which provides a copious supply of ions of both

charges. The electrical neutrality of the tape was verified with a charge probe prior to applying the adhesive to the substrate; the residual charge was  $< 10^{-12}$  C/mm<sup>2</sup>—orders of magnitude less than the charge on the tape after peeling from the copper. The tape was attached to the electropolished copper block by gently rubbing a Q-tip on the tape backing. As this rubbing imparted a small negative charge to the tape, the tape backing was subsequently reneutralized near a propane flame.

The tape was loaded in a 90° peel geometry using an Applied Test Systems Universal Testing Machine. One end of the tape was attached to the grip of the testing machine, and the other end to the copper block supported on a ceramic block electrically insulated from ground. The current signals were monitored by connecting the copper block to ground through a picoammeter (Keithley 416). In some experiments, the load applied to the tape backing was measured with a sensitive load cell (maximum load 43 N). The outputs of the picoammeter and load transducer were digitized at intervals ranging from a few  $\mu$ s to a few ms, depending on the peel speed. The peel speed ranged from less than 0.01 mm/s to 8 mm/s. To minimize electrical noise and pH background, the testing machine was enclosed in a light-tight, grounded aluminum box.

Photon emission measurements were made with an EMI Gencom 9816QB photomultiplier tube (PMT) with bialkali phosphor and a quartz window (sensitive to wavelengths in the 180-600 nm range) and mounted about 1 cm from the detachment region. The PMT was cooled to -40° C, which reduced the PMT dark count rate to less than 10 Hz (10 counts per second). The PMT output was amplified, discriminated, and pulse counted with a multichannel scaler using standard nuclear physics instrumentation. Fast time scale pH measurements during photon bursts were occasionally made by digitizing the amplified pH signal directly at rates up to 200 MHz.

The schematic diagram of the arrangement for taking optical spectra is shown in Fig. 1(b). Spectroscopy of the pH utilized a T-peel geometry for the peel. The peel zone is stationary in this geometry, simplifying the optics and allowing long duration peels. To permit measurements in vacuum and in controlled atmospheres, these experiments were performed in a stainless steel vacuum system. The adhesive was applied to a thin, electropolished copper strip (20  $\times$  250 mm<sup>2</sup>). Peeling was performed with a set of rollers positioned in front of photomultiplier tube and a silica

optical fiber bundle, all of which were mounted in the vacuum system. The rollers were turned by a variable speed motor. Structural limitations made it difficult to maintain a precisely uniform peel speed, which modified the emissions as noted below. The output of the optical fiber bundle was directed into the input aperture of a Thermo Jarrel Ash Monospec-18 spectrometer (grating 600 lines/mm) with a EG&G Model 1421 position sensitive detector, sensitive to wavelengths in the 200-830 nm range. Time-integrated spectra were acquired utilizing an EG&G OMA-III system. Much of the pH<sub>E</sub> accompanying peel occurs in isolated,  $\mu$ s bursts. Thus the spectral measurements represent an average spectrum of the light emitted before, during, and following isolated bursts.

To facilitate the correlation of micromechanical events with fluctuations in the current signal, experiments were also performed with narrow (1 mm wide) strips of adhesive. The small dimensions of the adhesive strip ensured that individual mechanical events were well separated in time from other similar events, therefore minimizing interference from events elsewhere in the peel zone. The entire peel zone of the narrow strips was readily observed with an optical microscope; synchronized videotaped observations allowed correlation between visual observations and the current signals.

As a means of analysis, power spectra of the current fluctuations were formed by summing the squares of the components of the Fourier sine and cosine transforms of the data.

## 2. QUALITATIVE DESCRIPTION OF THE PEEL ZONE

A schematic representation of the more frequently observed micromechanical events that occur during peeling appears in Fig. 2. As the backing is withdrawn from the substrate, voids form in the adhesive to produce long sheet-like fibrils joining the backing with the substrate. In the copper-Magic tape system, ultimate failure occurs principally along the copper-adhesive interface, leaving no observable residue on the copper surface. (One expects low molecular weight residues on the Cu, detectable by XPS or AES.) Fibril formation is a consequence of a dynamic instability within the adhesive.<sup>6,7</sup> A similar process is responsible for crazing in glassy polymers.<sup>8</sup> These



fibrils display a relatively high degree of molecular orientation and thus considerable tensile strength along the direction of drawing.

Visual observation of the nominal peel front in a stereomicroscope show a great deal of fibril motion associated with the intersection of the peel front with voids produced ahead of the nominal peel front. Although direct observation of the void formation is difficult due to the opacity of the copper substrate, observations of peeling through a transparent glass substrate show similar voids which are clearly initiated at the interface. The difficulty of forming voids within the interior of fluid-like material also argues for interfacial void formation. When the peel front encounters a void, the fibril structure is strongly disrupted, resulting in rapid retraction of material along the fibril, as indicated in Fig. 2(c). Providing that the peel speed is low enough to allow for void growth and molecular orientation before the void encounters the nominal peel front, these interfacial cavities produce depressions in the adhesive layer on the backing after peel, as shown in Fig. 2(d). Fibril and cavity formation were the dominant microstructural processes observed during peeling from clean, smooth copper surfaces.

The size and distribution of the cavities or depressions remaining on the detached adhesive surface was a strong function of peel speed. Especially large numbers of depressions were found whenever the course of peeling was interrupted, e.g., at the arrow in the optical micrograph in Fig. 3(a). At peel speeds between 0.02 and 4 mm/s, the size and density of these depressions decreases as the peel speed increases. The right hand portion of Fig. 3(a) shows a relatively large number of large depressions formed during peeling at 0.02 mm/s; the depressions are typically 50-100  $\mu\text{m}$  in diameter in the micrograph. Figure 3(b) is an optical micrograph of a typical detached adhesive surface formed during peel at 2 mm/s peel speed; this surface displays a few large depressions and a few small ones ( $< 50 \mu\text{m}$  in diameter). At very slow peel speeds ( $< 0.01 \text{ mm/s}$ ), the adhesive surface is almost entirely covered with large depressions. In all cases, the size of the interfacial cavities responsible for the depressions was much larger than the resulting depressions due to the relaxation of the adhesive during and after peeling. In addition, other instabilities were observed in

the course of peeling which were likely associated with spatial variations in the adhesion; these also lead to detectable fluctuations in the current and are discussed below.

### 3. RESULTS

**Current Generation.** The current generated during peeling ranged from pA to nA in magnitude depending on sample dimensions and peel speed. Appendix I presents a model to illustrate the physics of the current-generating mechanism based on charge separation. Intuitively, if a patch of charge is quickly lifted away from the metal, a current fluctuation will result. Figure 4 shows simultaneously acquired load and current measurements during peel of a thin (1 mm wide) strip of adhesive at a speed of 0.1 mm/s. Current peaks were strongly correlated with periods of decreasing load. Periods of decreasing load were typically associated with brief periods of relatively rapid motion of the peel zone. Due to the constant peel speed imposed on the adhesive system, acceleration of the peel zone relaxes the stresses in the flexed backing, thus decreasing the measured load. Both the magnitude and duration of the drop in load are reflected in the current signal: large decreases in load tend to be associated with big current peaks, and sharp decreases in load tend to be associated with sharp current peaks. Figure 4 shows a strong periodicity in both current and load signals, with a major component at a frequency of about 1.1 Hz ( $9 \text{ mm}^{-1}$ ).

The net current from the copper block is positive. Faraday cup measurements indicate that the net charge of the adhesive after peeling is negative. Prior to detachment, the negative charge on the adhesive is balanced by a net positive charge on the copper block. During peeling, the adhesive removes negative charge from the region of the interface, resulting in a flow of positive charge from the copper to ground (see Appendix I). However, several negative current spikes are also observed in this data which will be described in more detail below. This single data set shows that the current potentially contains a wealth of information about the dynamics of interfacial failure.

The relation between the current signal and the applied load for a wider strip and over a longer time interval is illustrated in Fig. 5. In this experiment, the tape was not under tension at the

onset of loading, and loading was continued until the end of the tape was removed from the copper. No current is observed at the onset of loading (Point A), as the tension in the tape is slowly increased because no detachment has occurred; when actual peeling begins, (Point B) the current is seen to rise. Both the load and current signals increase sharply between Points B and C, during fibril formation. "Steady state" peeling starts soon after Point C, where the load signal decreases to a steady level. During "steady state" peeling, the average current (between the negative current spikes) reflects the average load: both the load and current signals gradually rise until detachment. When the end of the tape is detached from the copper block, at Point D, the charged adhesive material rapidly accelerates away from the copper block, yielding a strong positive current signal which remains off scale for some time due to electrometer saturation.

**Photon Emission.** Photon emission (phE) accompanying the peeling of pressure sensitive adhesives in air has been shown to be primarily due to gaseous discharges.<sup>1-4</sup> Thus, simultaneous measurements of both phE and the current may shed light on the origin of some of the current signals. Typical phE and current signals accompanying peel in air at a low peel speed (0.02 mm/s) are shown in Fig. 6. In order to minimize transient signals at the onset and end of peel, tension was applied to the tape prior to the onset of data collection and peeling was stopped before the tape was completely detached from the copper surface. As seen here, the onset of phE above background coincides with the onset of current. As peeling continues, a positive current is observed which gradually increases and eventually attains some positive average value. In addition, many strong negative current spikes are observed, which are discussed below. Both phE and current flow continue briefly after the loading apparatus is turned off, reflecting the continuation of peeling as the substrate-adhesive-backing system relaxes.

The phE and current signals accompanying peel at a speed of 4 mm/s are shown in Fig. 7. The average (positive) current between the negative spikes is two orders of magnitude higher in Fig. 7 than in Fig. 6. The magnitude of the average current taken at halfway through the peel, denoted by  $I_{CS}$ , is closely related to the average peel speed.  $I_{CS}$  is nearly proportional to the peel speed over more than three order of magnitudes of peel speed, as shown in Fig. 8. This indicates

that the average amount of charge removed per unit length of tape peel is independent of peel speed. The slow rise seen in the positive current (Figures 6-8) is a consequence of the geometry of the experiment and is qualitatively in agreement with the calculation presented in Appendix I.

**Current spikes and Current Fluctuations.** The negative current spikes appear at irregular intervals, although the average number of spikes per mm is fairly reproducible and characteristic of peel speed. The measured spike width is limited by the 30 ms time response of the electrometer. In terms of charge transfer, negative current results from negative charge suddenly returning from the detached adhesive back to the Cu substrate. This can occur either in the gas phase or along the polymer surface. Comparing Figs. 6(b) and 7(b), it is apparent that many more spikes are observed at low peel speeds than at high peel speeds. As the peel speed varied from 0.01 mm/s to 8 mm/s, the number of negative spikes per unit time was nearly constant—about three per second. The spike amplitudes were roughly proportional to peel speed.

At low peel speeds, pH E bursts and negative current spikes virtually always appear in coincidence, but at high peel speeds ( $> 1$  mm/s) the pH E bursts greatly outnumber the current spikes. Gaseous discharge events generally yield intense pH E bursts with distinctive spectra corresponding to atomic and molecular lines of the ambient gas; spectral measurements presented below show that peeling in air yields strong  $N_2$  lines characteristic of electrical breakdown in air. Therefore, the strong correlation between the negative current spikes and pH E bursts at modest peel speeds strongly suggests that the negative current spikes accompany gaseous discharge events from the adhesive to the copper.

The small number of negative current spikes at high peel speeds is probably a consequence of the short time available for conduction of charge along the adhesive surface to asperities, where they become available for discharge events involving the copper substrate. The photon bursts observed at high peel speeds are generally not associated with discharge to the copper substrate. For example, gaseous discharges between charged patches on the detached adhesive surface would produce pH E bursts without significantly affecting the observed current signal because the charge

does not reach the metal. These types of discharges would create pH bursts without corresponding negative current spikes.

Direct evidence for the correlation between negative current spikes and peel mechanics is provided by simultaneous visual observations and current measurements at low peel speeds. Large negative current spikes are produced when portions of the adhesive are rapidly drawn away from the copper surface. This effect is especially dramatic when a patch of unpeeled adhesive remains after the passage of the nominal peel front; fibrils joining such patches to the backing often become greatly extended and snap with great force to the backing when the patch is completely peeled. Negative current spikes also accompany the rapid fibril movement produced when the nominal peel front encounters a cavity which has formed ahead of the peel front. At low and modest peel speeds, these cavities produce the depressions in the detached adhesive discussed above. At low peel speeds, the numbers of negative current spikes and depressions are too large for accurate comparison. However, at modest peel speeds, the number of large depressions along the detached adhesive correlated well with the number of negative current spikes observed during peeling. At the highest peel speeds, where few large depressions and current spikes were observed, a one-to-one correspondence between current spikes and depressions could often be established.

**Current Fluctuations.** Figure 9(a) shows a small portion (0.5 s) of the current signal observed at a peel speed of 1 mm/s. To facilitate the analysis of the slower fluctuations, we "removed" the spikes by replacing those data, replacing the affected data by extrapolating from nearby values. (This method is commonly used by astronomers to handle signals containing unavoidable eclipses of a light source and for "cleaning up" the music from old, scratched records.) A number of frequencies are clearly present with no obvious periodicity. The Fourier transform (derived from the finite sine and cosine series representations of the data) is shown in Fig. 9(b). The spectrum is very broadband, with the majority of the power ranging from 0-100 Hz. The individual peaks in the transform (aside from the peak at 60 Hz due to pickup from the laboratory electrical system) are not significant, being a result of the finite size of the data set used

in the analysis. However, the broad groups of peaks observed at 5-40 Hz, 40-55 Hz, as well as 65-90 Hz are quite significant. These broad bands in the spectrum of the current signal reflect the "tap-dance" of adhesive detachment. From video taped microscope observations, the 5-40 Hz components appear to correspond to the motion of the major fibrils. Although the time resolution of these images is insufficient to resolve faster motion in the smaller structures, the 40-55 Hz signals probably correspond to the detachment of the next order of fibril bifurcation. More details concerning these fluctuations and the micromechanics of the peel will be presented in Part II of this paper.

**Peeling in Other Atmospheres.** To sort out the role of the surrounding atmosphere on the detected current and corresponding photon emissions, we explored in a preliminary fashion these signals in vacuum and SF<sub>6</sub> for comparison with air. We examine the resulting spectra as well as the time dependence of current and total pHE generated during peel.

Previous work indicates that the light from peeling pressure sensitive adhesives in air is due to electrostatic discharges alone.<sup>2</sup> The time integrated spectrum when 3M Magic Tape is peeled in air is shown in Fig. 10(a). Each spectral line is due to N<sub>2</sub>. When the tape is peeled at greater speeds, the amplitudes of these lines increase, but no new lines are observed. Peeling in high vacuum ( $< 10^{-4}$  Pa) yields a much different spectrum, as shown in Fig. 10(b). N<sub>2</sub> lines, when observed, are much reduced in intensity. The N<sub>2</sub> lines in Fig. 10(b) are believed to be due to occluded N<sub>2</sub> in the adhesive. The spectral lines at wavelengths greater than 370 nm can be attributed to CH, C<sub>2</sub>, H, H<sub>2</sub>, which are plausible adhesive decomposition products. The dominant feature in the emission spectrum in vacuum is band at about 290 nm. A very similar feature is produced by electron beam and uv (248 nm) irradiation of the adhesive surface in vacuum. This band is consistent with the bulk phase luminescence spectra of a polymer containing aromatic rings. We therefore conclude that in vacuum the excitation mechanism that dominates involves electrical discharge events that occur *along* the adhesive surface, i.e., surface flashover,<sup>9</sup> which excites the polymer and forms dissociative fragments, also in excited states.

Spectral measurements during peel in 1 atm SF<sub>6</sub> show no evidence of spectral lines, provided that great care is exercised to exclude N<sub>2</sub> from the ambient atmosphere and the adhesive-copper interface. To exclude N<sub>2</sub> from the adhesive-copper interface, the tape was degassed in vacuum prior to forming the adhesive joint. As shown in Fig. 10(c), peeling under these conditions yield no spectral lines at this level of sensitivity. However, when the adhesive is attached to the copper in air and peeled in SF<sub>6</sub>, the intensities of the N<sub>2</sub> lines are similar to those measured in air. Therefore, the small amount of N<sub>2</sub> entrained along the adhesive-copper interface during attachment in air is sufficient to yield strong gaseous breakdown events.

The pH<sub>E</sub> and current signals produced in the T-peel geometry and acquired simultaneously with the spectrum taken in air are shown in Fig. 11. Both signals are similar to those obtained at carefully controlled peel speeds in the 90° peel geometry, except for a slow modulation of the current signal due to the nonuniform peel speed in the T-peel apparatus. (The peel speed of the testing machine used in the 90° peel tests was much more uniform.) At a peel speed of 1 mm/s, the number of photon bursts was about  $3 \times 10^3$  counts/mm<sup>2</sup>.

The current signals accompanying peel in vacuum contrast dramatically with those acquired in air, as shown in Fig. 12. Instead of the strong negative spikes observed in air, very strong but similar *positive* current spikes are observed. These spikes are at least three orders of magnitude more intense than the *negative* spikes observed in air at comparable peel speeds. Nevertheless, the continuum component of current,  $I_{CS}$ , is essentially unchanged. The continuum component in Fig. 12(b) is about 56 pA, quite comparable to the average current observed in air at the same peel speed. (See Fig. 5.) [This current is not apparent in Fig. 12(b) due to the less sensitive scale employed to show the positive current spikes.] The number of photon bursts in vacuum was about  $5 \times 10^5$  bursts/mm<sup>2</sup>, more than one hundred times that in the air. We attribute the positive current spikes observed in vacuum to the emission of large numbers of secondary electrons due to the electrical discharge events discussed above. In vacuum, electron bombardment during a discharge can result in intense electron emission from the substrate, sufficient to produce a net positive current from the surface. This requires that the number of emitted electrons be greater than the

number of electron striking the substrate. The emitted (secondary) electrons are probably created at the oxidized copper surface, which has a secondary electron coefficient greater than one (i.e., more electrons are emitted than strike the surface) for incident energies above about 100 eV.<sup>10</sup> In air, collisions between primary electrons and air molecules reduce their energy and essentially eliminate the emission of secondary electrons from the region of the copper substrate. However, in vacuum, the secondary electrons will escape, resulting in the net removal of negative charge from the copper-tape system and thus producing a positive current spike.

The size and number of current spikes in vacuum is much greater than in air. This is presumably due to lower leakage currents (which would lead to higher charge densities) and the higher potentials required for breakdown in vacuum. Both of these factors would lead to more energetic and perhaps more frequent breakdown.

Significantly, many negative current spikes are observed in SF<sub>6</sub> despite the absence of spectral lines in the measured spectra. Typical pH<sub>E</sub> and current signals accompanying peel in SF<sub>6</sub> at 1 mm/s are shown in Fig. 13. (Attachment was performed in a SF<sub>6</sub>-filled glove box.) The presence of negative currents spikes is consistent with gaseous discharge events. The number of pH<sub>E</sub> bursts observed in this experiment correspond to about  $1.5 \times 10^3$  bursts/mm<sup>2</sup>, roughly half the number in air.

**Insulating Substrates.** Finally, it should be noted that current measurements accompany peel from insulating substrates are readily made by applying thin films of the substrate material on a copper sheet. Figure 14(a) shows current measurements made in vacuum accompanying the peel of 3M Magic Tape from its own backing. Measurements in vacuum allow for the detection of other emissions, e.g., electrons and positive ions. Simultaneous measurements of electron emission (EE) accompanying peel are shown in Fig. 14(b). Strong positive current spikes are observed during peel from the adhesive backing in vacuum, similar to those observed to accompany peel from copper in vacuum. A number of EE bursts (marked with vertical dotted lines) are in coincidence with the current bursts (in number, the EE bursts exceed the detectable current bursts). Interestingly, the EE often shows a gradual build up and then falls dramatically as



the current spikes, suggesting that we are time-resolving the initiation of breakdown. The detection of these electron bursts support our interpretation that the breakdown events release electrons from the overall sample, thus yielding positive current spikes.

## 6. DISCUSSION

The complex energy level structure in the adhesive phase suggests that the net negative charge observed on freshly peeled adhesive represents the difference between electrons donated by the copper to the adhesive and electrons donated to the copper by the adhesive.<sup>11</sup> Although the charge in the copper is quite mobile, the charge in the adhesive (insulator) occupies high electron affinity sites and is far less mobile. As the adhesive is removed from the copper, much of the bound charge in the adhesive will remain with the adhesive. The loss of this (net negative) charge from the interface will be accompanied by a flow of (positive) current from the copper to ground. Very similar currents are observed during the debonding failure metal-epoxy joints,<sup>5</sup> which yield readily observable signals despite the small ( $\mu\text{m}$ -scale) displacements that accompany debonding.

The continuum component of the current from the copper ( $I_{\text{CS}}$ ) is positive, as expected for removal of negatively charged adhesive, and is of the appropriate magnitude. Measurements of the charge density on the detached tape after peel in the  $90^\circ$  geometry at a speed of 0.02 mm/s yielded values of  $\lambda = -1.5 \times 10^{-10} \text{ C/mm}$  ( $-1.2 \times 10^{-9} \text{ C/cm}^2$ ), which corresponds to a current of 3 pA. This is acceptably close to the observed steady-state current from the copper block ( $I_{\text{CS}} \sim 2 \text{ pA}$ ). The steady state current was observed to be very nearly proportional to the peel speed, indicating that the average net charge per unit area removed from the adhesive-copper interface does not depend significantly on the peel speed over the range of speeds studied here.

Fluctuations in the current signal correlate well with micromechanical events during peel over a wide range of time/size scales. Variations in the peel speed show up clearly in the observed current. Slow oscillations in the rate of adhesive removal due to successive relaxation and tension along the peel zone are also clearly observed in the accompanying current. More rapid current

fluctuations appear to involve more localized events, in which small portions of adhesive are rapidly transported along highly strained fibrils. Some of these events are sufficient to trigger electrical breakdown between the adhesive and the copper. The rapid transport of negative charge to the copper through the channel formed by ionized gases results in a strong negative charge spike.

Rapid motion of charged portions of adhesive can result in very high (but transient) currents. Assuming that the charge density along adhesive-copper interface is uniform, the instantaneous current level will be proportional to the rate at which detached adhesive is removed from the substrate (see Appendix I). Adhesive motion along the fibrils is normally rather slow—probably much slower than the rate at which the “roof” of a cavity along the adhesive-copper interface moves away from the substrate in the initial stages of cavity growth.

Surprisingly, the average spike frequency (in time) is nearly independent of peel speed over a wide range of peel speeds. The close association the depressions observed on the detached adhesive and the negative current spikes suggest the electrical discharges are associated with cavity formation ahead of the nominal peel front. Rapid motion of the cavity roof away from the copper substrate should yield a strong, positive current spike in the absence of electrical breakdown. This is consistent with the extremely strong positive current spikes observed during peel in vacuum; the intensity of these spikes is probably enhanced by the rapid movement of adhesive along nearby fibrils when the cavity intersects the nominal peel front. Presumably high vacuum prevents normal gaseous discharges, allowing for electrical fields much higher than can be obtained at atmospheric pressure. These higher fields produce the “surface breakdown” and accompanying electroluminescence spectra observed during peel in vacuum.

During peel at atmospheric pressure, the pressure inside newly formed cavities is still probably quite low. This is evident during peels from a transparent glass substrate, where the forming cavities are readily observed; when the tension on the backing is relieved, cavities which have not intersected the nominal peel front disappear entirely. Providing that the initial cavity pressure is sufficiently low, very strong electric fields across the cavity may be readily maintained.

The subsequent rise in pressure when the cavity intersects the nominal peel front can greatly reduce the electric field required for breakdown and could precipitate gaseous breakdown. The required electric field would be higher in  $\text{SF}_6$  than in air, due to the high ionization potential of  $\text{SF}_6$ . (The ionization potential of  $\text{SF}_6$  is 19.3 eV,<sup>12</sup> while that of  $\text{N}_2$  and  $\text{O}_2$  are 15.6 and 12.1 eV, respectively.) This would account for the relatively low number of photon bursts observed during peel in  $\text{SF}_6$ . As noted above, electrical breakdown results in the rapid transfer of electrons from the adhesive to the copper, yielding strong negative current spikes.

The high luminous efficiency of  $\text{N}_2$  under electrical breakdown results in strong  $\text{N}_2$  lines in the presence of  $\text{N}_2$ . Even small amounts of  $\text{N}_2$  entrained at the adhesive copper interface or introduced into the vacuum system by small leaks is sufficient to produce significant  $\text{N}_2$  line spectra. This is not surprising because the luminescence efficiency of  $\text{SF}_6$  is much lower.

As a strictly parenthetical note, we remark that under carefully controlled laboratory conditions, the potentials generated by the peel event can reach  $10^6$  volts/m and are sufficient to detonate a gaseous  $\text{CH}_4\text{-O}_2$  mixture.<sup>13</sup>

## 7. CONCLUSIONS

Peeling a pressure sensitive adhesive from a metal substrate results in processes on a wide variety of distance and time scales. These include oscillations along the peel front, which leads to fibril formation and to occasional interfacial void formation behind the nominal peel front. The morphology of these bifurcation processes depend on peel speed which also influences the time dependence of the fluctuations in detachment of adhesive from the copper, which in turn produce fluctuations in the current measured from the copper block. Sudden, localized detachment of small patches of adhesive can lead to very strong current spikes. In the presence of gases such as  $\text{N}_2$  this can lead to gaseous breakdown between the adhesive and substrate. In vacuum, densities of separated charge appear to be higher and result in surface breakdown as well as secondary electron emission causing a complete reversal in sign of the observed current bursts.

The peel zone of a pressure sensitive adhesive shows a remarkable degree of electrical activity. Simultaneous microscope observations of the peel zone and current measurements indicate that fluctuations in the progress of the peel zone are strongly correlated with fluctuations in the measured current signal. Therefore, these current fluctuations yield information on the dynamics of the peel process. Time series analysis of these current fluctuations is the subject of Part II of this work.

## **ACKNOWLEDGMENTS**

This work was supported by 3M Company, the Air Force Office of Scientific Research under Contract AFOSR-F49620-91-C-0093, and the Washington Technology Center. We wish to thank Louis Scuderio and Ed Donaldson, WSU, for their help in acquiring part of the experimental data.

## APPENDIX I.

### A Model for the Origin of the Current

The origin of the current generated during peeling is a result of the finite size of the substrate plane. For an infinitely large Cu surface, no current would result due to the fact that to maintain the Cu block at zero potential, the induced charge on the Cu surface is equal in magnitude to any charge located above the surface. The simplest geometry to represent a finite Cu sample, although somewhat different from our samples studied here, is a sphere of radius  $R$ , shown in Fig. 15. [This model is like "assuming a spherical horse"]. Assume all of the charge due to contact electrification is concentrated in two parallel patches at the sphere surface symmetric to the azimuthal axis, denoted by  $\pm Q_0$ . Since each -charge on the tape (the top patch) is matched by a +charge on the Cu immediately below it, the system is in equilibrium and there is no difficulty seeing that no current flow is needed to keep the Cu at ground potential.

To simplify the calculation further, we now simulate the peeling process by removing a linear "string" of -charge of linear density  $-\lambda$  [C/mm], directly along the  $z$  axis. If no charge transfer could occur [through the picoammeter to ground], this would cause the sphere to change its potential. For lifting the string a distance  $L$ , the total charge lifted is  $-\lambda \cdot L$ ; thus, before charge transfer there is a corresponding +charge of  $+\lambda \cdot L$  on the sphere which originally matched the -charge removed. Using the method of image charges for a point charge  $q$  at a distance  $z$  from the center of the sphere of radius  $R$  ( $z > R$ ), one can show that the *correct* +charge,  $q'$  on the surface of the sphere to maintain the sphere at 0 volts potential is given by:<sup>14</sup>

$$q' = \frac{R}{z} q \quad (1)$$

[Note that for  $z > R$ ,  $q' < q$ ]. Therefore, treating the "string" of charge as a sum of  $q'$  distributed from  $z=R$  to  $z=R+L$ , we obtain the following +charge,  $Q'$ , which should remain on the sphere to match the removed -charge:

$$Q' = \int_R^{R+L} \frac{R\lambda dz}{z} = R\lambda \cdot \ln\left(1 + \frac{L}{R}\right) \quad (2)$$

Thus, the +charge which should be removed from the sphere,  $\Delta Q'$  [through the picoammeter] to keep the sphere at 0 volts is:

$$\Delta Q' = \lambda(L - R \cdot \ln(1 + \frac{L}{R})) \quad (3)$$

[Note that as  $R \rightarrow \infty$ ,  $\Delta Q' \rightarrow 0$ ]. When differentiated with respect to time, the predicted current vs time is given by:

$$i = \lambda \cdot \frac{dL}{dt} \left\{ 1 - \frac{R}{[R + \frac{dL}{dt} t]} \right\} \quad (4)$$

Note that for large  $R$ , the current is approximately proportional to peel speed ( $dL/dt$ ). A plot of this equation for typical values of  $\lambda$ ,  $dL/dt$ , and  $R$  ( $1 \times 10^{-9}$  C/mm, 5 mm/s, and 15 mm, respectively) is shown in Fig. 15(b). For different geometries one would expect the current signal to evolve somewhat differently.

If a patch of -charge suddenly returns from the string to the sphere, to readjust to ground potential, negative charge must flow from the sphere to ground. This causes a rapid burst of negative current. Since current =  $dQ/dt$ , rapid motion of charge can lead to very large currents due to a very short "dt".

## REFERENCES

1. E. E. Donaldson, J. T. Dickinson, and X. A. Shen, *J. Adhesion* **19**, 267 (1986).
2. Ma Zhenyi, Fan Jiawen, and J. T. Dickinson, *J. Adhesion* **25**, 63 (1988).
3. J. T. Dickinson, in *Adhesive Bonding*, edited by L. H. Lee (Plenum Press, New York, 1991), pp. 395-423.
4. J. T. Dickinson and E. E. Donaldson, *J. Adhesion* **24**, 199 (1987).

5. K. A. Zimmerman, S. C. Langford, and J. T. Dickinson, *J. Appl. Phys.* **70**, 4808 (1991).
6. A. D. McEwan and G. I. Taylor, *J. Fluid Mech.* **26**, 1 (1966).
7. R. J. Fields and M. F. Ashby, *Philos. Mag.* **33**, 33 (1976).
8. A. M. Donald and E. J. Kramer, *Philos. Mag. A* **43**, 857 (1981).
9. H. Craig Miller, *Trans. Electrical Insulation* **24**, 765 (1989).
10. Walter H. Kohl, *Handbook of Materials and Techniques for Vacuum Devices*, (Reinhold Publishing, New York, 1967), pp. 564-568.
11. J. Lowell and A. C. Rose-Innes, *Contact Electrification*, *Adv. Phys.* **29**, 947 (1980)
12. V. I. Vedeneyev, L. V. Gurvich, V. N. Kondrat'yev, V. A. Medvedev, and Ye. L. Frankevich, *Bond Energies Ionization Potentials and Electron Affinities*, (St. Martin's Press, New York, 1966), p. 183.
13. J. T. Dickinson, private communication.
14. Any undergraduate electricity and magnetism text, e.g., V. D. Barger and M. G. Olsson, *Classical Electricity and Magnetism*, (Allyn and Bacon, Newton, MA, 1987), pp.123-124.

## FIGURE CAPTIONS

FIG. 1. Diagram of apparatus used in (a) current measurements in the 90° peel geometry and (b) spectra measurements in the T-peel geometry.

FIG. 2. Schematic diagram of cavitation and fibril formation during peeling. (a) Cavity formation ahead of the nominal peel front; (b) cavity growth; (c) rapid fibril retraction when the cavity intersects the peel front; (d) the formation of depressions or holes in the peeled adhesive at points where large cavities have formed. Shaded lines indicate the position of fibrils and cavities in the background. The arrow in (a) indicates the position of the nominal peel front.

FIG. 3. Adhesive remaining on the backing after the peeling of pressure sensitive adhesive at a speed of (a) 0.02 mm/s and (b) 2 mm/s, showing depressions caused by cavity formation. (Due to the ambiguity of interpreting the shadows in the micrograph, the depressions look like droplets on the surface.)

FIG. 4. (a) Load and (b) current signals accompanying peel of a 1 mm wide adhesive strip from copper. The vertical dotted lines note positions of maxima in the current signal, which correlated well with periods of decreasing load.

FIG. 5. (a) Applied load and (b) current signal accompanying peel at a speed of 0.5 mm/s.

FIG. 6. (a) pH<sub>E</sub> counts and (b) digitized current accompanying the peel at a speed of 0.02 mm/s. The inset in (b) shows the onset of current flow on an expanded vertical scale.

FIG. 7. (a) pH<sub>E</sub> counts and (b) digitized current accompanying the peel at a speed of 4 mm/s.

FIG. 8. Average magnitude of current in between spikes as a function of peel speed.

FIG. 9. (a) Typical current signal between negative spikes during peel at a speed of 1 mm/s. (b) Power spectrum of the current over a 3 s time interval.

FIG. 10. Time integrated spectrum of pH<sub>E</sub> accompanying peel a speed of 1 mm/s in the T-peel geometry: (a) in air, (b) in vacuum, and (c) in 1 atm of SF<sub>6</sub>. [Integration time 40 s]

FIG. 11. (a) pH<sub>E</sub> counts and (b) current signal accompanying peel in air.

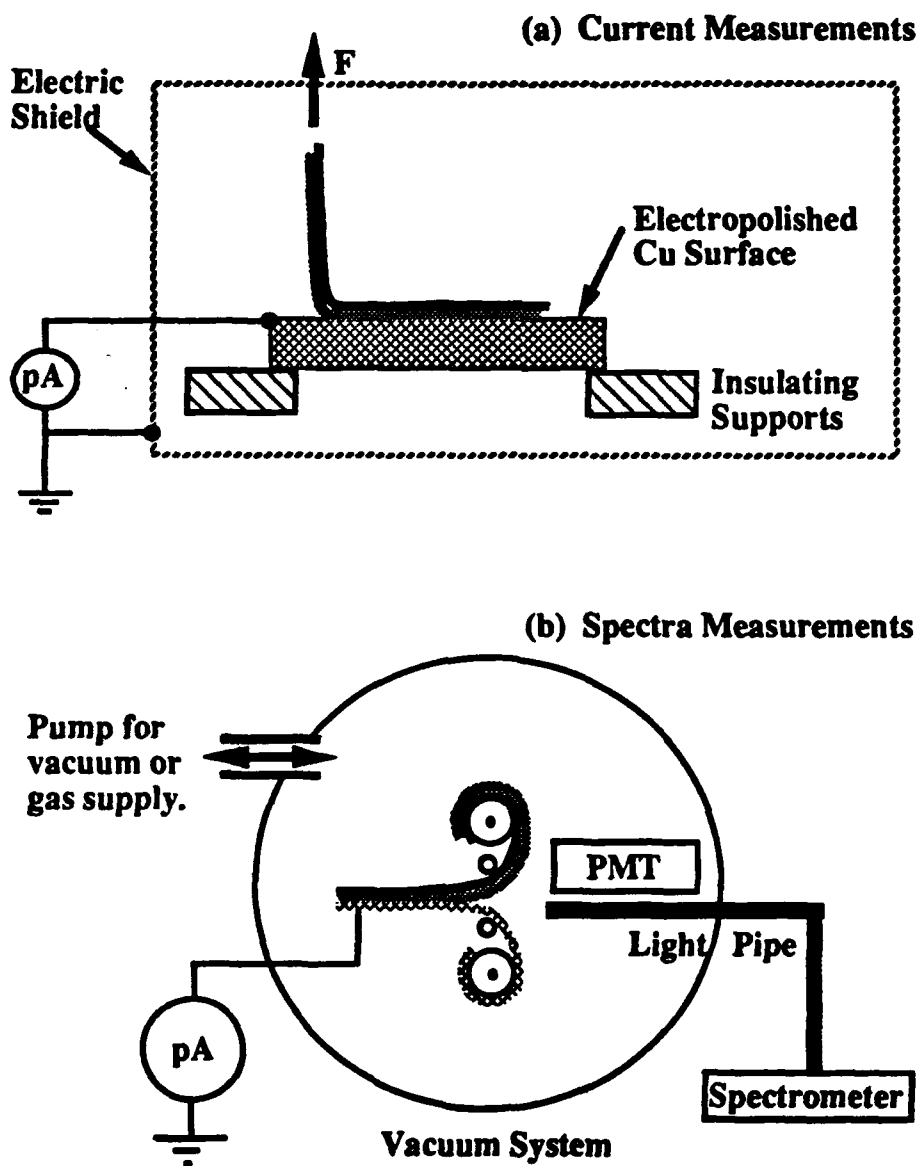


**FIG. 12.** (a) pH<sub>E</sub> counts and (b) current signal accompanying peel in vacuum.

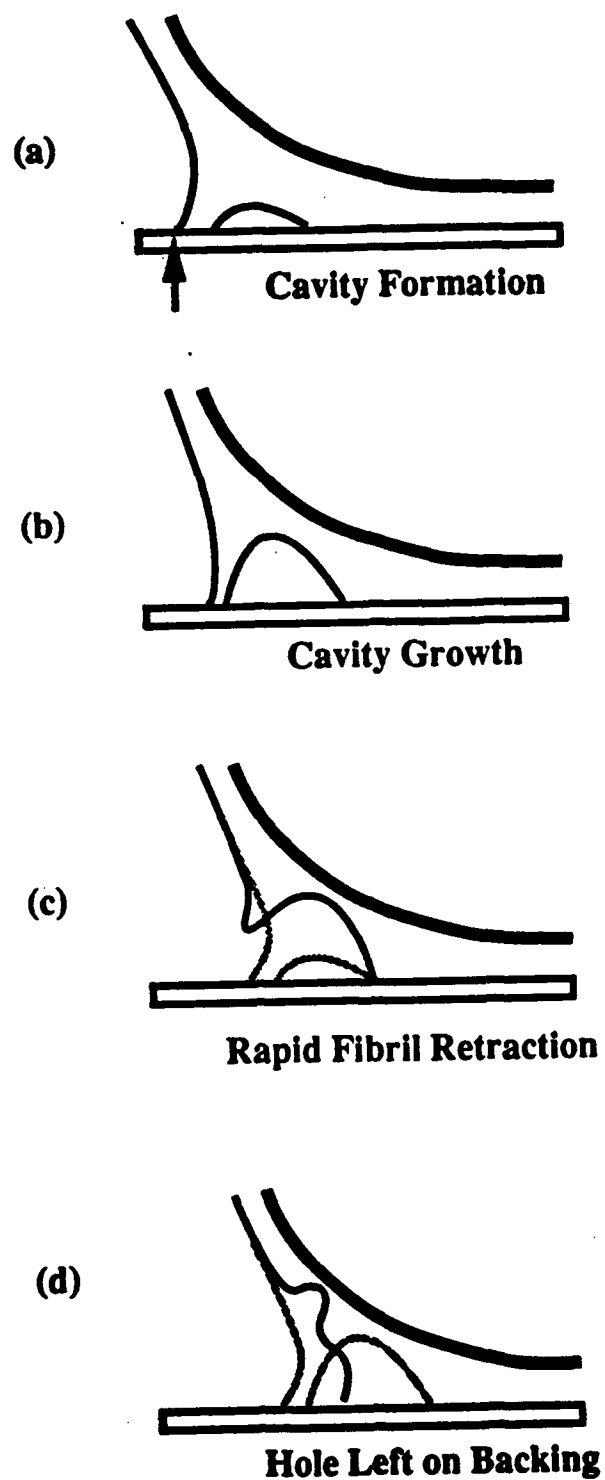
**FIG. 13.** (a) pH<sub>E</sub> counts and (b) current signal accompanying peel event in 1 atm SF<sub>6</sub>.

**FIG. 14.** Current and electron emission from peel in vacuum of Magic Tape from backing.

**FIG. 15.** (a) A schematic diagram of the mechanism for current generation during the peel of a pressure sensitive adhesive. (b) Simulated Current vs time accompanying steady "peel".

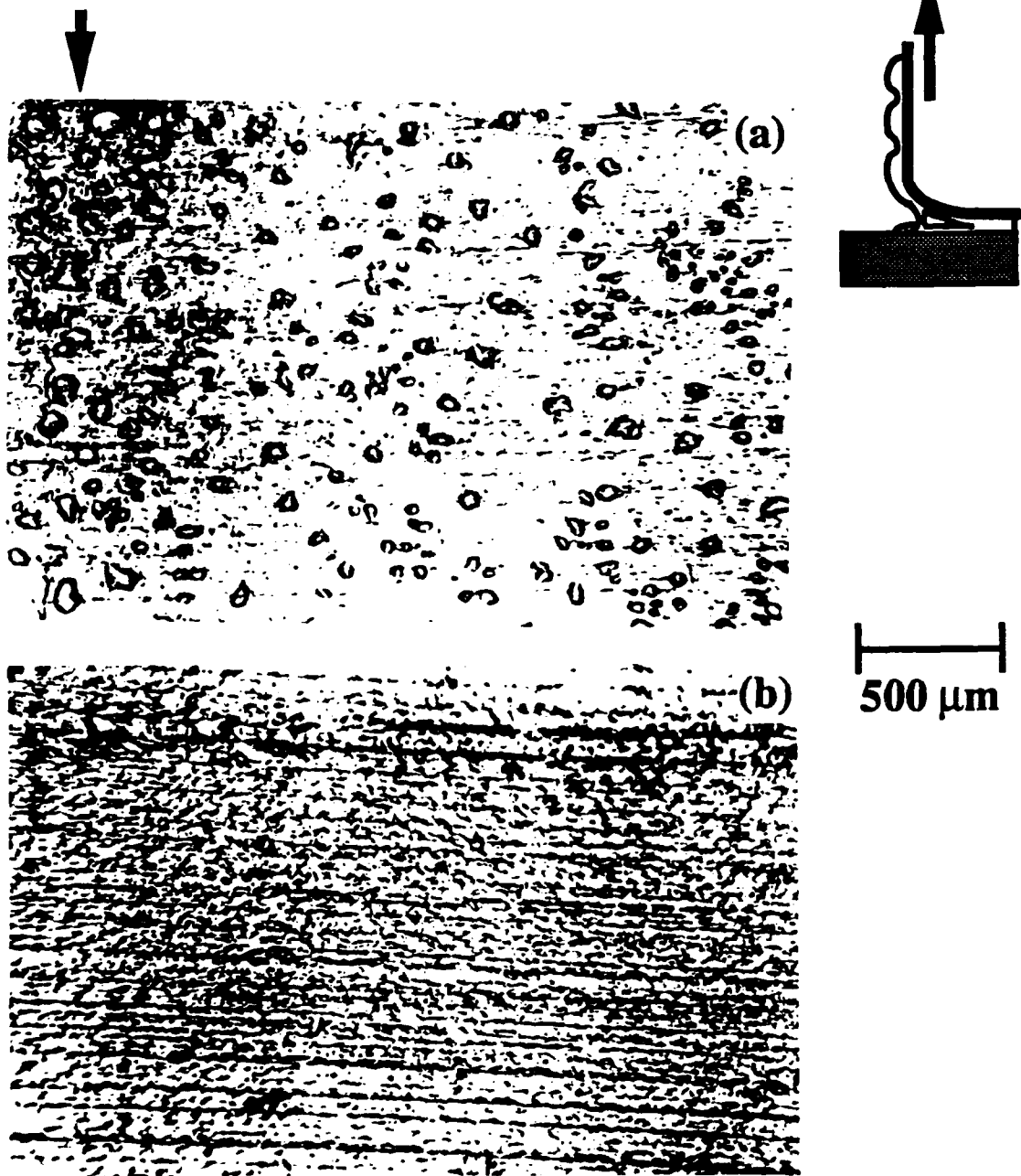
**Diagram of Apparatus Employed for Current and Spectra Measurements****FIG. 1**

## Schematic of Peeling Process



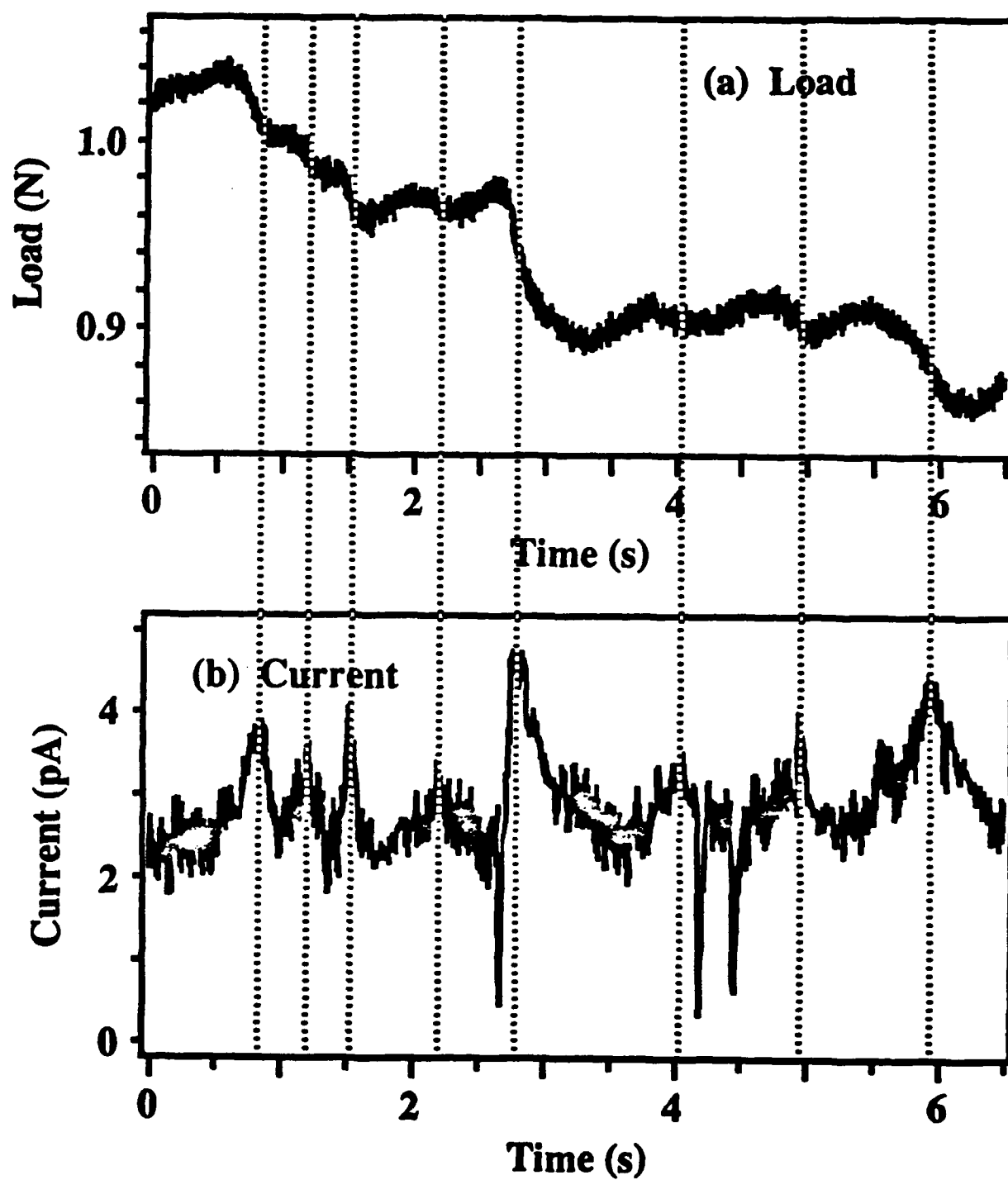
**FIG. 2**

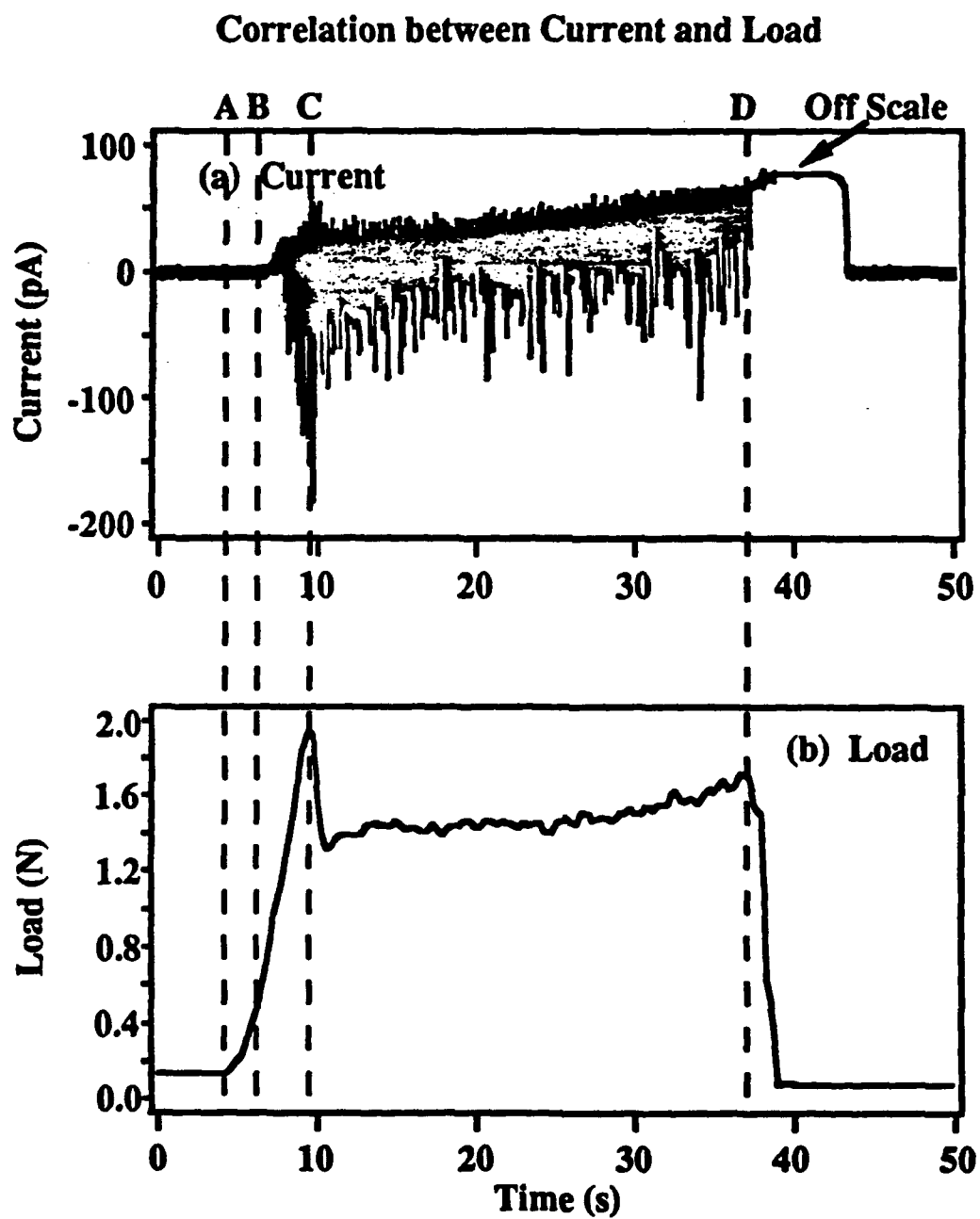
### Depressions Formed at Different Speeds

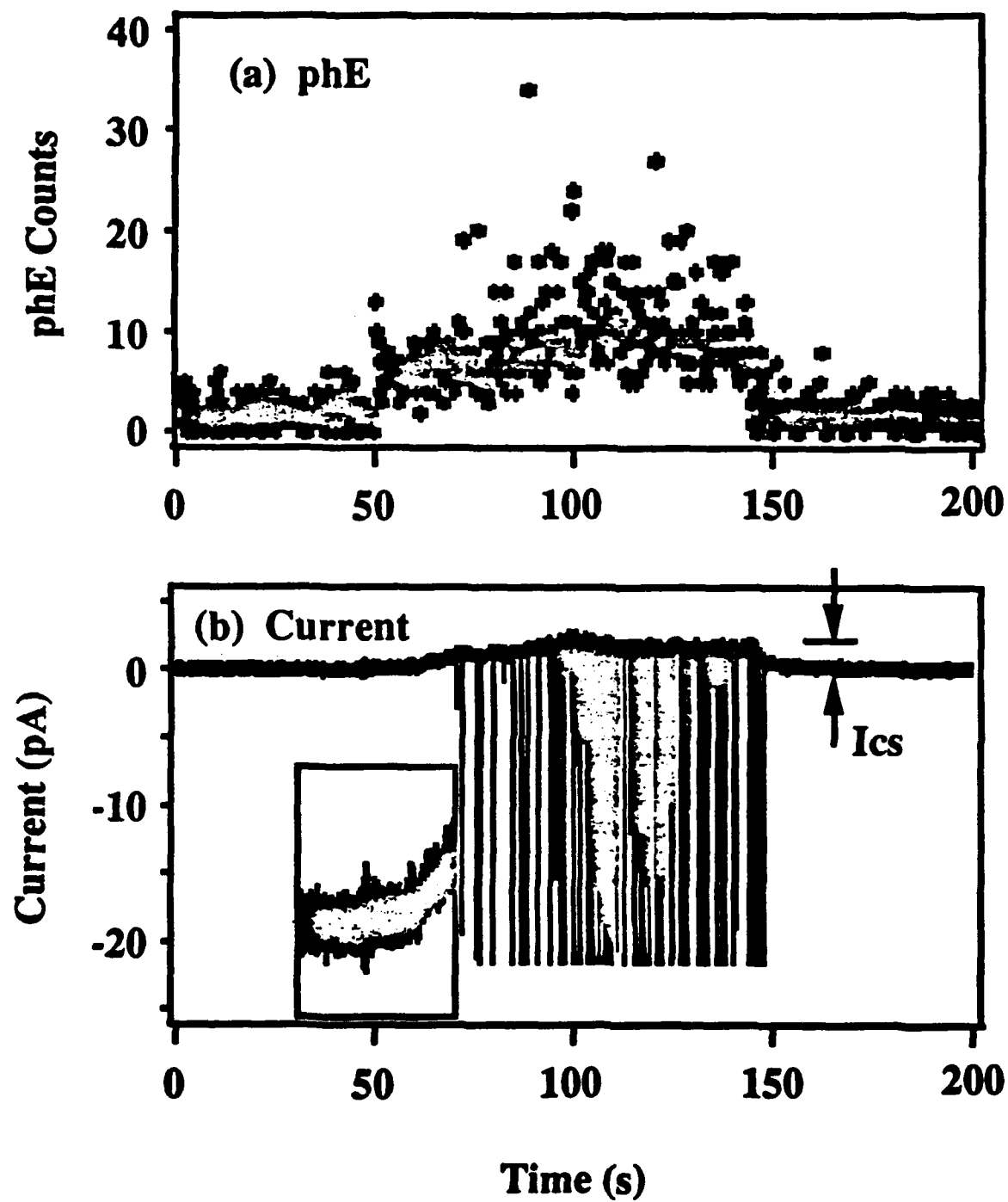


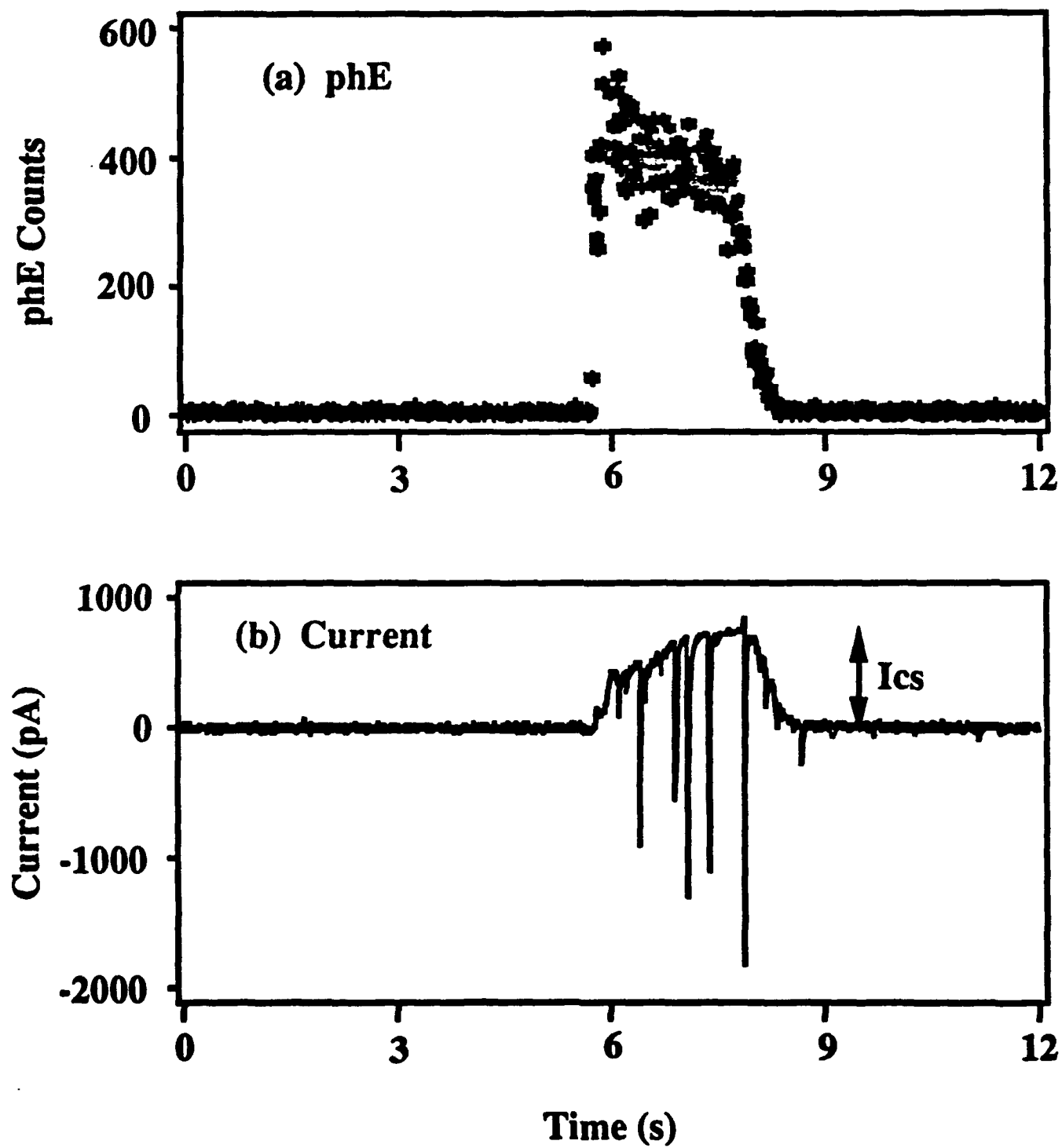
**FIG. 3**

### Load and Current at Peel Speed of 0.1 mm/s

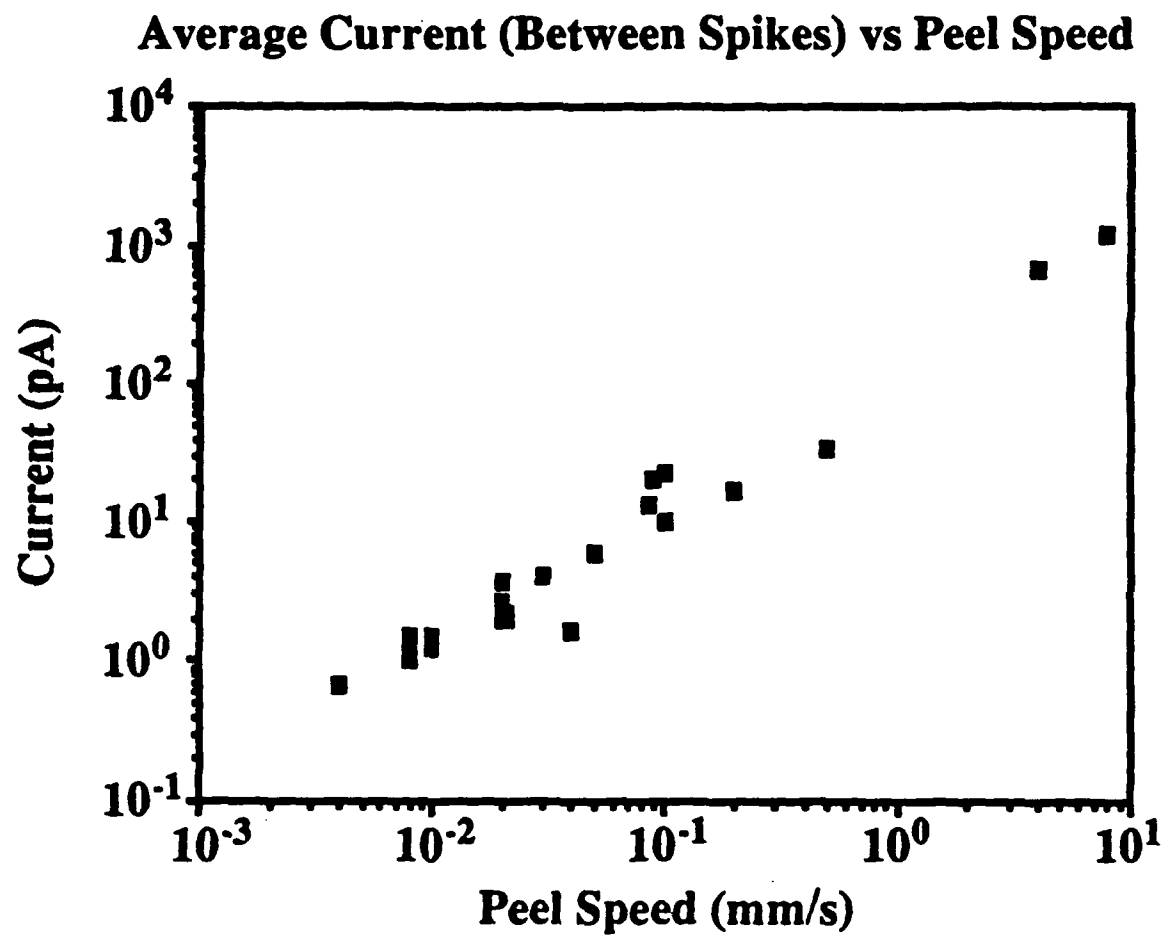
**FIG. 4**

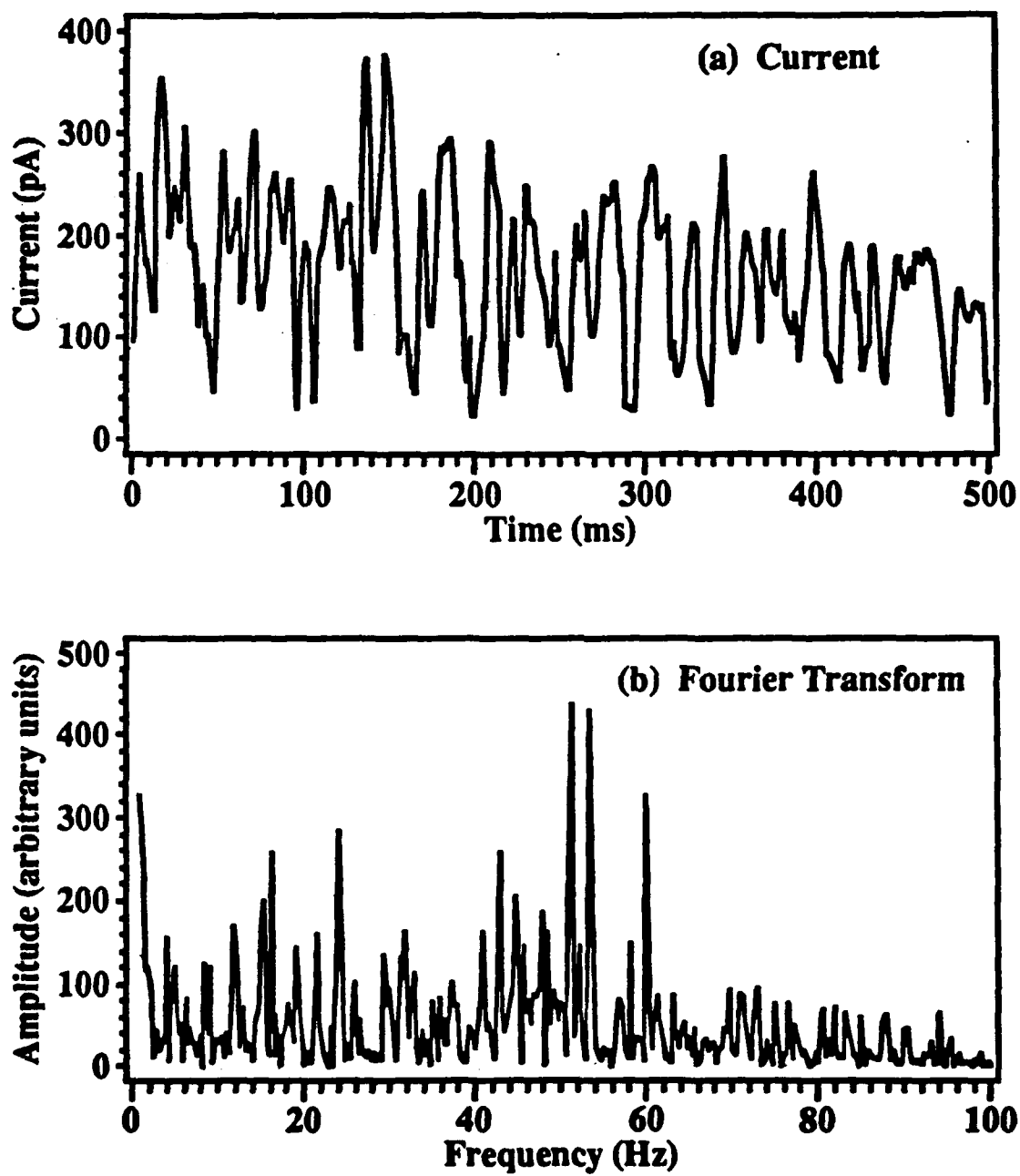
**FIG. 5**

**phE and Current at a Peel Speed of 0.02 mm/s****FIG. 6**

**phE and Current at a Peel Speed of 4mm/s****FIG. 7**



**FIG. 8**

**Current and Fourier Transform of Current****FIG. 9**

## Spectra of pHE During Peel in Different Atmospheres

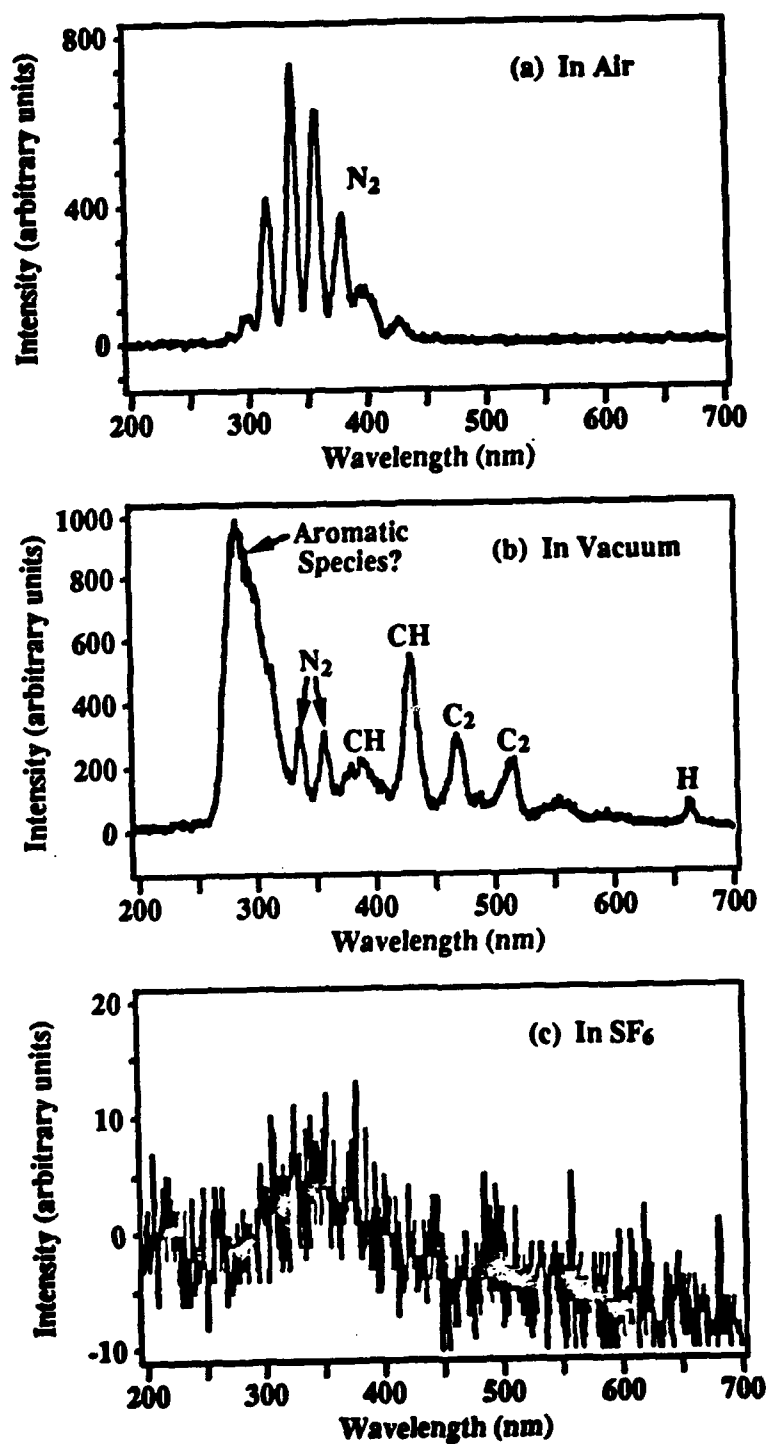
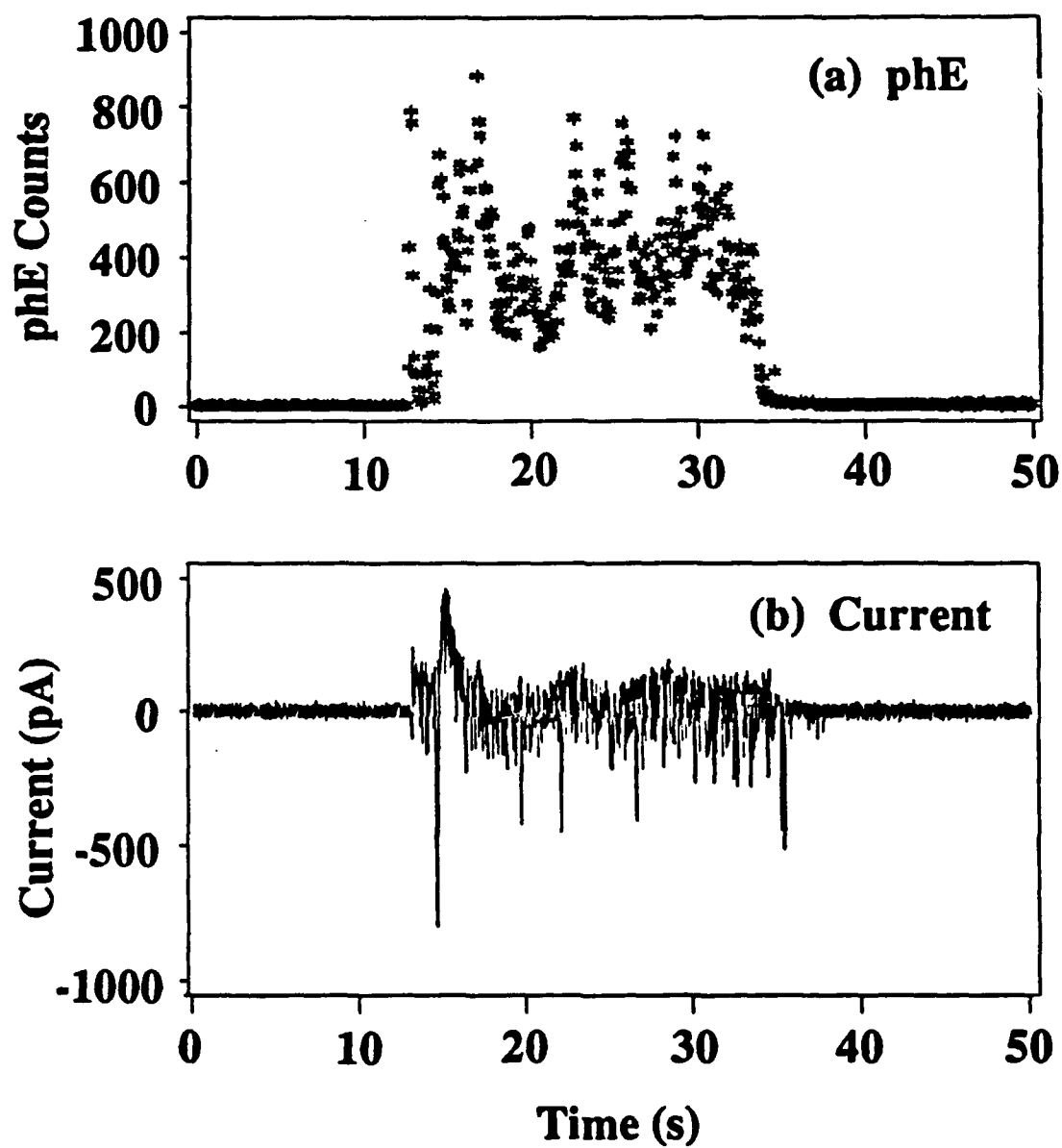
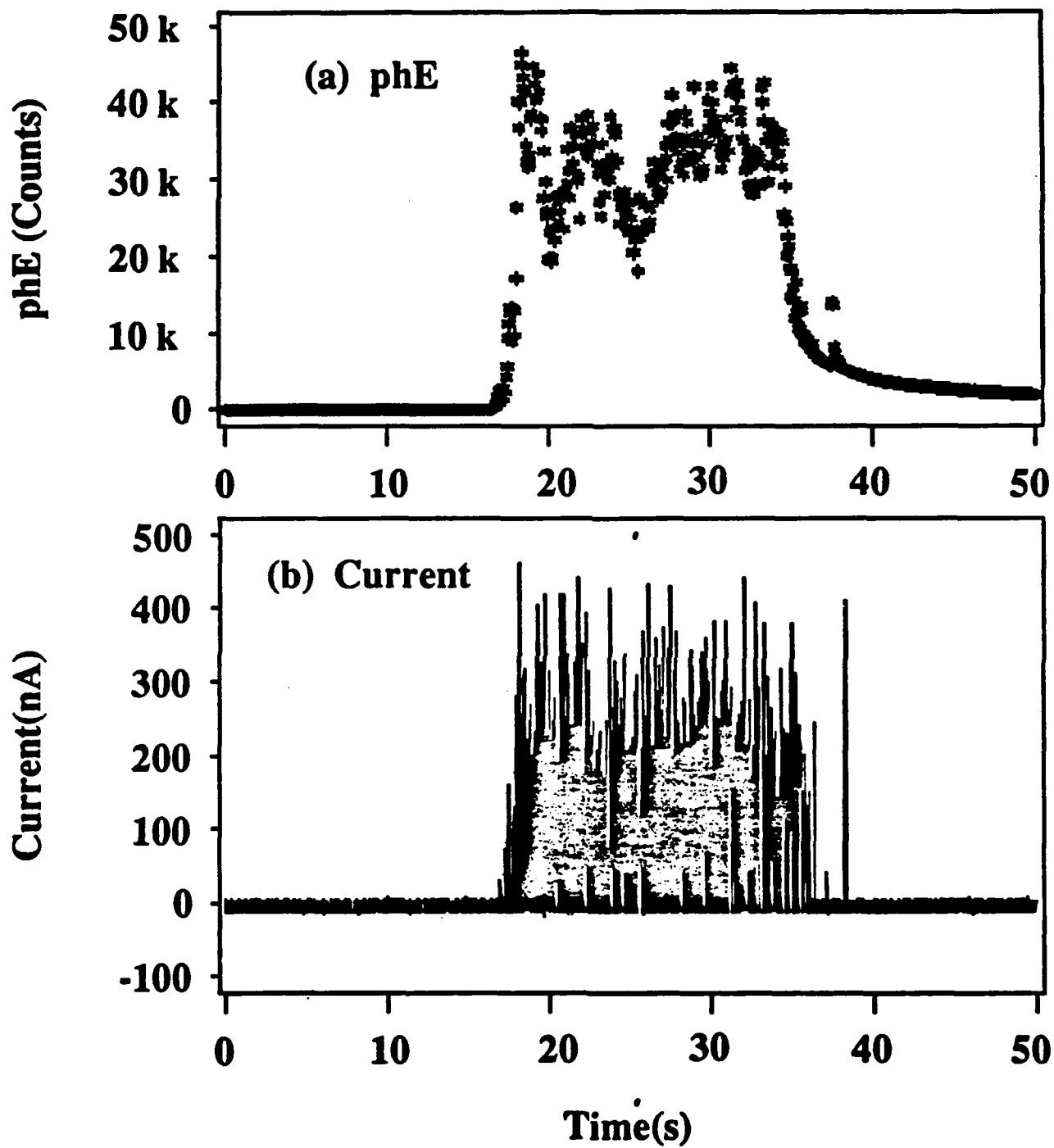
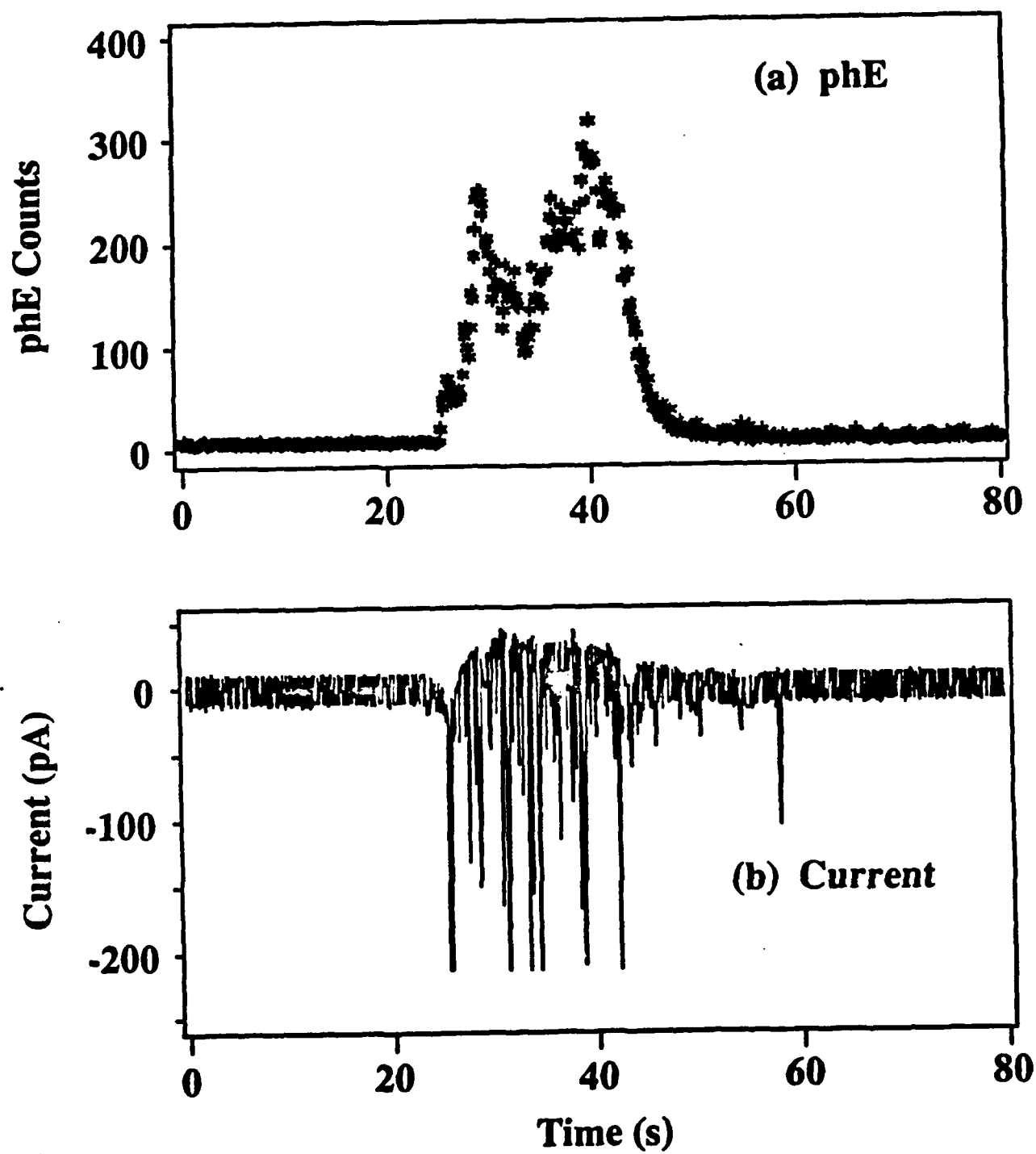


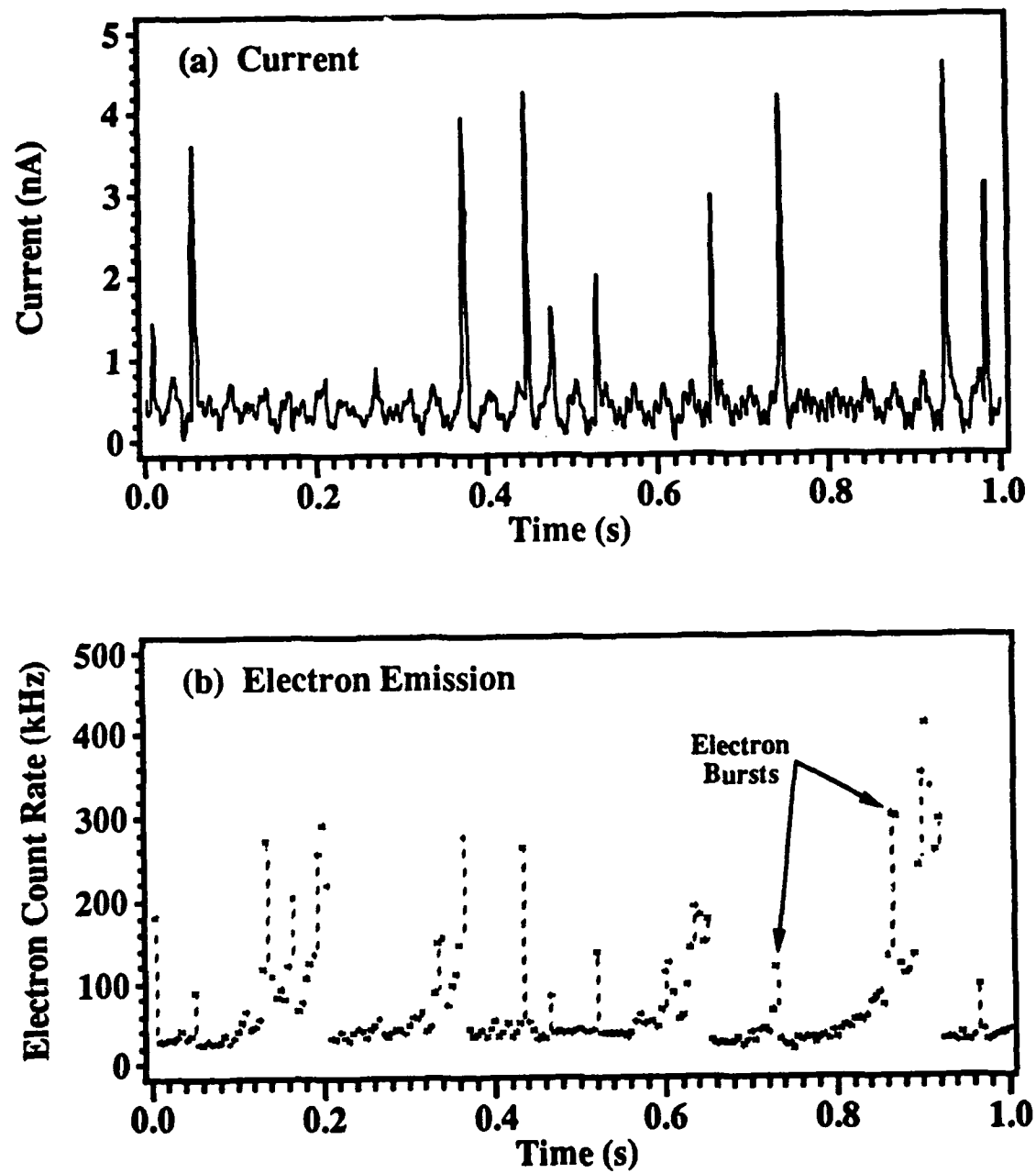
FIG. 10

### phE Counts and Current in Air

**FIG. 11**

**phE and Current in Vacuum****FIG. 12**

**phE Counts and Current in SF<sub>6</sub>****FIG. 13**

**Current and Electron Emission Accompanying Peel at 0.6 mm/s****FIG. 14**

## (a) Schematic of Current Generation Model

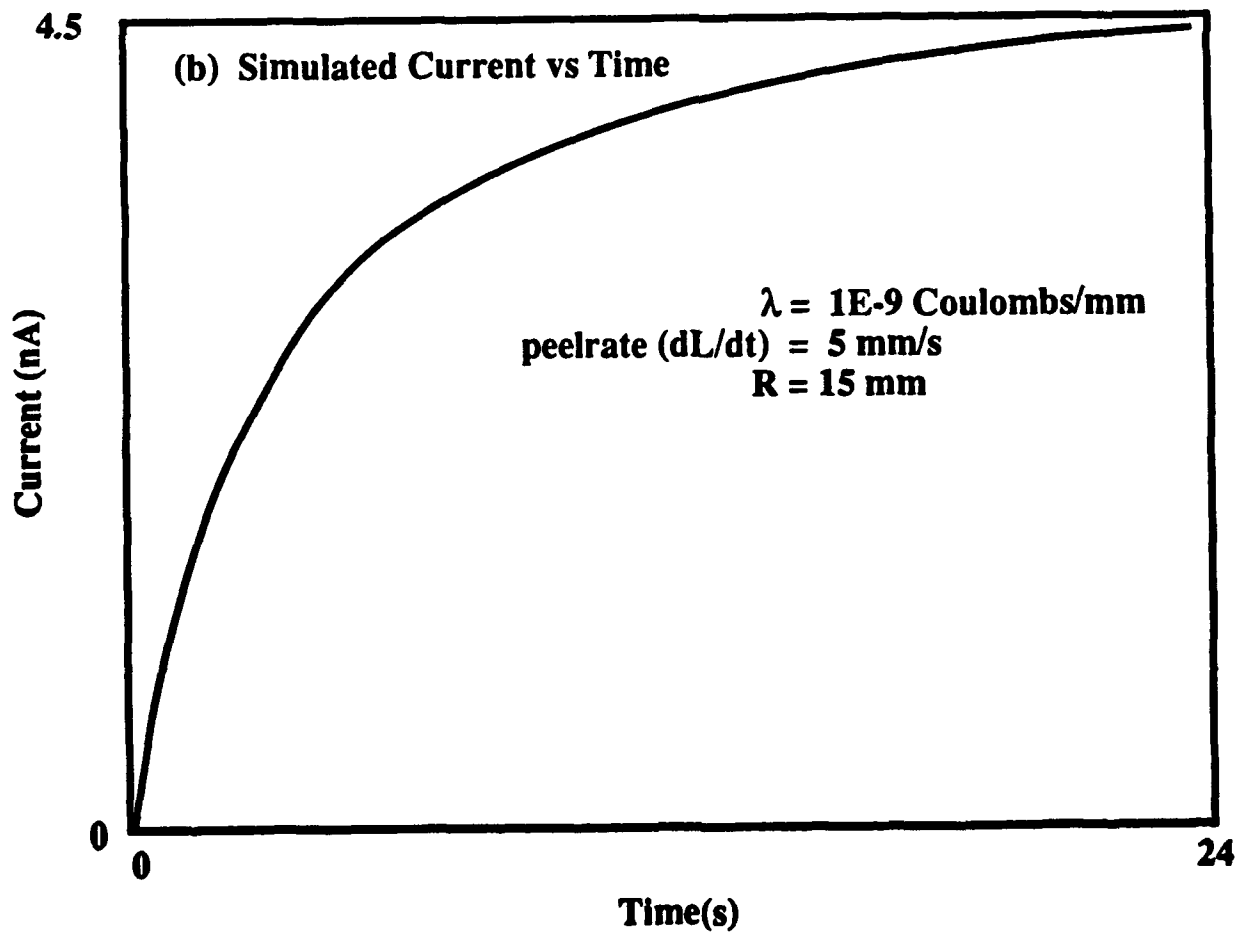
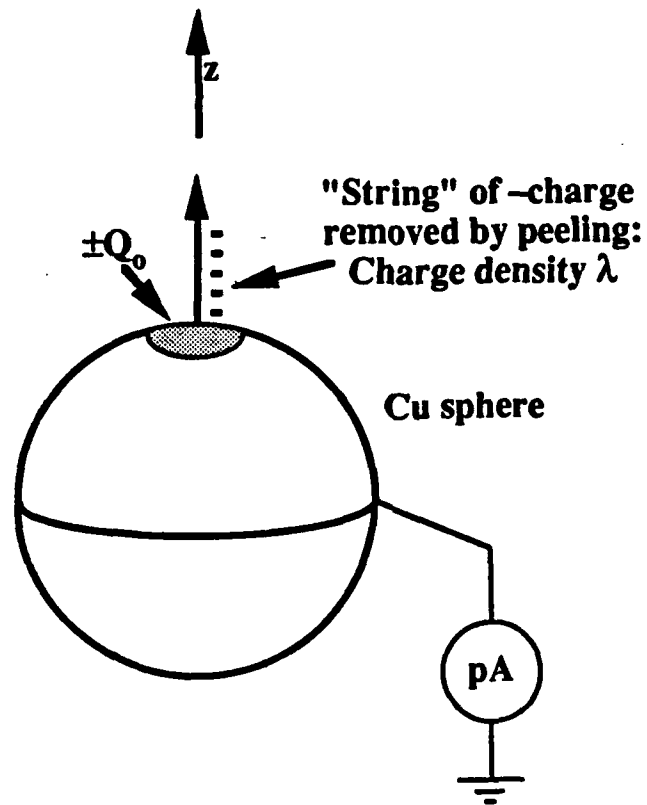


Fig. 15



## **IX. Scanning Tunneling Microscope Observations of Metallic Glass Fracture Surfaces**

D. M. Kulawansa, J. T. Dickinson, and S. C. Langford

Physics Department, Washington State University, Pullman, WA 99164-2814 USA

and

Yoshihisa Watanabe,

Department of Materials Science and Engineering, National Defense Academy, Hashirimizu,  
Yokosuka, Kanagawa 239, JAPAN

We report scanning tunneling microscope observations of fracture surfaces formed during catastrophic crack growth in three metallic glasses:  $\text{Ni}_{56}\text{Cr}_{18}\text{Si}_{22}\text{B}_4$ ,  $\text{Co}_{69}\text{Fe}_4\text{Ni}_1\text{Mo}_2\text{B}_{12}\text{Si}_{12}$ , and  $\text{Fe}_{78}\text{B}_{13}\text{Si}_9$ . Macroscopically, the first two glasses fail along a slip band formed during loading and display a characteristic,  $\mu\text{m}$ -scale pattern of vein-like ridges; in contrast,  $\text{Fe}_{78}\text{B}_{13}\text{Si}_9$  displays little slip prior to fracture and its fracture surface shows a  $\mu\text{m}$ -scale chevron pattern of steps. STM observations of fracture surfaces of all three materials show nm-scale grooves. The grooves in  $\text{Co}_{69}\text{Fe}_4\text{Ni}_1\text{Mo}_2\text{B}_{12}\text{Si}_{12}$  are especially prominent and display stepped edges which we attribute to the intersection of shear bands with the surface. STM observations of the vein-like features on  $\text{Ni}_{56}\text{Cr}_{18}\text{Si}_{22}\text{B}_4$  show also stepped edges. We attribute the vein features to the interaction of adjacent crack fingers in which the material between adjacent fingers fails in plane stress. The origin of the grooves is less certain, but may be due to shear instabilities in the material immediately behind the crack tip. In plane strain, this material experiences strong lateral stresses which can be partially relieved by groove formation.

## I. INTRODUCTION

Metallic glasses are amorphous alloys produced by extremely rapid quenching from the molten state. First produced by Klement *et al.*<sup>1</sup> in 1960, their unique properties facilitate several important applications. Their amorphous structure and metallic character are associated with unique behavior during deformation and fracture. In particular, deformation by slip in these materials tends to be highly localized in shear bands on the order of 5 nm thick.<sup>2</sup> Fracture properties of amorphous alloys have been widely studied and fractography of amorphous metals are reviewed thoroughly in the literature.<sup>3,4</sup> Observations of fracture surface topography (fractography) have long played an important role in studies of fracture behavior,<sup>5</sup> especially on the  $\mu\text{m}$ -distance scales accessible by scanning electron microscopy (SEM). However, nm-scale observations of metallic glass fracture surfaces are desirable, especially in view of the extremely localized nature of slip in these materials.

Although metallic glasses are typically brittle on macroscopic scales, microscopically they can be extremely ductile. Many metallic glasses display extensive slip prior to failure at room temperature; crack growth in these materials generally proceeds along one of the slip bands formed during loading. The resulting surface generally displays a characteristic veined morphology. Metallic glasses in which slip bands do not form prior to fracture generally display dimpled surfaces, often associated with a chevron pattern of steps. Except at temperatures well below room temperature, virtually all metallic glasses display fracture features associated with localized plastic deformation.

Due to the extreme localization of slip, its role in fracture can be difficult to assess. The amorphous structure of metallic glasses does not allow for contrast mechanisms suitable for the observation of individual dislocation-like structures. Transmission electron microscope (TEM) studies of slip generally rely on the contrast provided by thickness variations or surface steps produced by slip.<sup>2</sup> The difficulty of sample preparation for TEM has apparently precluded extensive use of thinning or replica techniques. The size of the step structures on a ribbon fracture

surface can easily be too small for observation by SEM. In contrast, scanning tunneling microscopy (STM) of metallic glass surfaces can be performed with relative ease and sufficient resolution for the observation of small surface ( $< 10$  nm) steps produced by slip activity. As noted below, STM readily reveals the slip activity responsible for the formation of the veined morphology when fracture occurs along a preexisting slip band. Although indirect arguments require slip activity for vein formation,<sup>3,6</sup> the direct observation of step structures provides direct confirmation of this mechanism.

Although atomic resolution has been achieved with STM on smooth, conducting and semiconducting surfaces, this resolution has not been attained on the surfaces of amorphous materials. Nevertheless, even nm-scale resolution is often a substantial improvement over conventional fractographic techniques.<sup>7,8</sup> Previous STM (and AFM—atomic force microscopy) observations of metallic glass surfaces<sup>9-13</sup> have generally focused on atomic clusters and crystallites formed on ribbon surfaces during annealing. These observations are often complicated by the formation of an insulating oxide layer. To avoid problems due to prolonged exposure to air, the samples in this work were examined immediately after fracture.

## II. EXPERIMENT

This study involves three metallic glass materials:  $\text{Ni}_{56}\text{Cr}_{18}\text{Si}_{22}\text{B}_4$  (METGLAS® MBF-20),  $\text{Co}_{69}\text{Fe}_4\text{Ni}_1\text{Mo}_2\text{B}_{12}\text{Si}_{12}$  (METGLAS® 2705M), and  $\text{Fe}_{78}\text{B}_{13}\text{Si}_9$  (METGLAS® 2605S-2), provided by Allied Signal Metglas Products in the form of 50  $\mu\text{m}$  thick ribbon. The ribbon was cut into dogbones with gauge dimensions of  $6 \times 35$  mm<sup>2</sup> and loaded in tension until fracture in an Applied Test Systems testing machine. Except as noted below, the samples were drawn at a rate of 420 nm/s ( $1.2 \times 10^{-5}$  s<sup>-1</sup>). The resulting fracture surfaces were immediately investigated in air by STM using chemically etched tungsten tips in a double tube instrument.<sup>14</sup> Each of the STM images presented below were taken at some distance from the origin of crack growth and thus

reflect conditions of rapid, catastrophic crack growth. A large number of scans were performed to ensure that the observed features were representative and free of obvious artifacts.

Some samples were subsequently examined by scanning electron microscopy (SEM) using a JOEL-6400 to confirm the mode of fracture and to facilitate correlations between  $\mu\text{m}$ -scale features observed by SEM and nm-scale features observed by STM. The fracture surface of the  $\text{Ni}_{56}\text{Cr}_{18}\text{Si}_{22}\text{B}_4$  material was also examined by energy dispersive spectroscopy with a Si(Li) X-ray detector to determine the composition of particle-like structures on the fracture surface.

The interpretation of STM images is often complicated by distortions resulting from the non-negligible size of the probe tip. Reiss et al. have addressed these distortions.<sup>15,16</sup> In particular, angular surface features tend to be smoothed by convolution with the rounded surface of the tip. Thus, if anything, the topographs tend to underestimate the sharpness and depth of surface features. Although artifacts are occasionally observed, these are in most cases significantly smaller than the features described below.

Variations in the electronic or chemical state of the surface can also complicate the interpretation of STM images. Pampillo and Chen have shown that slip bands in metallic glasses are preferentially attacked by acids, suggesting that the chemical potential of the surface region is altered by the presence of a slip band.<sup>17</sup> Variations in chemical potential could produce apparent changes in elevation in STM images, giving the appearance of grooves or ridges along the intersection of the slip band with the surface. In the work reported below, surface steps are frequently observed whose size and spacing are consistent with slip bands. However, their step-like nature is consistent with the surface topography at the intersection of a slip band with the surface and inconsistent with the expected change in surface potential. Conversely, the vein-like and groove-like features described below are much larger than slip bands and may be confidently attributed to topographic surface features. Thus it is not likely that local potential differences at slip bands are reflected in our images. The absence of features related to changes in surface potential in this study is probably related to the nm-scale resolution of the images and the particular potential difference employed between the tunneling tip and sample.

Preliminary AFM observations of the smooth region of  $\text{Fe}_{78}\text{B}_{13}\text{Si}_9$  fracture surfaces near the origin of crack growth were made with a Digital Instruments Nanoscope II.<sup>®</sup> Near the origin of crack growth, the fracture surface is generally much smoother than the regions imaged by STM, which were some distance from the fracture origin.

### III. RESULTS

$\text{Ni}_{56}\text{Cr}_{18}\text{Si}_{22}\text{B}_4$  displays extensive slip prior to failure and shows the characteristic veined morphology discussed above. This morphology is evident in the SEM micrograph in the Fig. 1. The veins are believed to form along the intersection of adjacent "fingers" of growing crack. The minimum distance between parallel veins indicates the typical scale of crack fingering, which is about 400 nm on this fracture surface. Fracture proceeds along the fine veins to the heavy veins, indicating that fracture in Fig. 1 was nucleated locally near the center of the photograph. Several particle-like features are also seen on the fracture surface, as well as two cavities consistent with the removal of partially embedded particles. Such particles are of interest as potential crack nuclei.<sup>3</sup> X-ray dispersion analysis of the larger particles show compositions very similar to the bulk, suggesting that the particles are crystallized portions of the glass. This impression is further supported by the growth of particle-like features in AFM studies of  $\text{Fe}_{78}\text{B}_{13}\text{Si}_9$  heated to 773 K,<sup>12-13</sup> which are attributed to crystalline material formed at elevated temperatures. The particles in Fig. 1 are not produced during manufacture and are apparently formed during tensile loading of the glass. SEM observations of samples broken in flexure showed no such particles, indicating that their creation depends strongly on the stress state producing slip. Similar particle formation accompanies the tensile loading and fracture of  $\text{Fe}_5\text{Co}_{70}\text{Si}_{15}\text{B}_{10}$ , where TEM observations of the fracture surface show microcrystalline regions along slip bands near the fracture surface.<sup>18</sup>

Figure 2 shows an STM image of a particle-like feature on a  $\text{Ni}_{56}\text{Cr}_{18}\text{Si}_{22}\text{B}_4$  fracture surface. This feature is 225 nm long, 131 nm wide and 65 nm high. The area surrounding this feature is fairly smooth, with no evidence of inter-phase decohesion. (Decohesion cracks less than

about 0.5 nm wide would be obscured by the finite radius of the STM tip.) The absence of extensive decohesion suggests that this particle, at least, did not serve as a local origin or nucleus of crack growth. The rounded surface of this particle shows some structure suggestive of slip-related deformation, consistent with deformation produced as the particle was pulled free from the mating fracture surface.

Several vein features were also imaged by STM. Figure 3(a) shows an STM image of a vein feature on  $\text{Ni}_{56}\text{Cr}_{18}\text{Si}_{22}\text{B}_4$  glass. The size of this feature is consistent with the veins observed in Fig. 1, about 100 nm across and 100 nm high. Although the ridges in the three dimensional image appear smooth, examination of individual scans across the vein show distinct steps, as shown in Fig. 3(b). We attribute these steps to slip bands formed in the material between adjacent "fingers" of the growing crack. The material between adjacent crack fingers necks down to form matching veins on the two mating fracture surfaces. The extensive deformation required for this necking is for the most part localized to the slip bands, forming distinct steps along the veins.

The vein features occupy only a small portion of the fracture surface. In the broad regions between the veins, grooved surfaces were generally observed. A representative  $\text{Ni}_{56}\text{Cr}_{18}\text{Si}_{22}\text{B}_4$  surface is shown in Fig. 4. These grooves are typically 10–40 nm deep, with parallel grooves separated by about 200 nm. As noted below, the edges of the grooves show distinct step-like features which are attributed to localized deformation along slip bands.

Similar vein and groove features were observed on  $\text{Co}_{69}\text{Fe}_4\text{Ni}_1\text{Mo}_2\text{B}_{12}\text{Si}_{12}$  fracture surfaces. This material shows more extensive (microscopic) deformation prior to failure than  $\text{Ni}_{56}\text{Cr}_{18}\text{Si}_{22}\text{B}_4$  and thus displays relatively large surface features. Figure 5 shows what appears to be the origin or tip end of a vein. The vein, indicated by the arrow on the left, appears to originate on the right, from a cavity at its tip. As discussed below, material constraints along the intersection of the crack fingers apparently hinder the formation of the slip geometry required for vein formation; these constraints can be relaxed by cavity formation. The surfaces on either side of the vein (in the foreground and background, respectively) differ in elevation by 40–50 nm,

reflecting small differences in the elevation and inclination of the crack fingers meeting to form the vein.

The grooves on  $\text{Co}_{69}\text{Fe}_4\text{Ni}_1\text{Mo}_2\text{B}_{12}\text{Si}_{12}$  fracture surfaces are especially prominent, as seen in Fig. 6(a). The edge of one of these grooves is shown on an expanded scale in Fig. 6(b). In the expanded view, the sides of the grooves are clearly stepped, much like the veins of Fig. 3. Again, we attribute the steps to the intersection of slip bands with the surface. Slip along these bands appears to be responsible for groove formation. Assuming that the relatively flat surfaces on either side of the grooves are formed by the advance of adjacent crack fingers, groove formation can be explained in a manner analogous to vein formation. As discussed below, we propose that the state of stress (plane stress vs plane strain) of the material between the adjacent crack fingers determines whether grooves or veins are produced.

Although grooves are also observed on the fracture surfaces of  $\text{Ni}_{56}\text{Cr}_{18}\text{Si}_{22}\text{B}_4$  and  $\text{Fe}_{78}\text{B}_{13}\text{Si}_9$ , the small size of these grooves make the identification of step-like features less conclusive. This is presumably due to distortions introduced by the finite size of the STM tip when imaging narrow grooves. The grooves on the  $\text{Co}_{69}\text{Fe}_4\text{Ni}_1\text{Mo}_2\text{B}_{12}\text{Si}_{12}$  surface are sufficiently wide and deep to avoid these distortions.

Figure 7 shows an intriguing STM image of a  $\text{Ni}_{56}\text{Cr}_{18}\text{Si}_{22}\text{B}_4$  surface formed during rapid loading. The sample was loaded at a rate of  $8.4 \mu\text{m/s}$  ( $2.4 \times 10^{-4} \text{ s}^{-1}$ ) and displayed higher fracture stress (1.7 GPa) than samples loaded at lower rates. This fracture surface shows two sets of interpenetrating steps intersecting at right angles. These interpenetrating steps appear to be associated with intersecting shear bands. The higher stress at fracture of this sample may have played an important role in the formation of these structures.

In contrast to  $\text{Ni}_{56}\text{Cr}_{18}\text{Si}_{22}\text{B}_4$  and  $\text{Co}_{69}\text{Fe}_4\text{Ni}_1\text{Mo}_2\text{B}_{12}\text{Si}_{12}$ ,  $\text{Fe}_{78}\text{B}_{13}\text{Si}_9$ , displays little slip activity prior to fracture. An SEM micrograph of a typical fracture surface appears in Fig. 8. This sample shows the characteristic chevron pattern of fracture steps, apparently formed by crack fingering.<sup>19</sup> Most of the surface is covered with dimpled structures similar to those formed by void nucleation in the ductile fracture of polycrystalline metals. The nm-scale roughness of the

dimpled surfaces most likely exceeds the vertical range of our STM, rendering these regions difficult to image. However, the smooth ledges or steps formed between the dimpled regions should be readily imaged. As we have little control of the STM tip position across the width of the sample (beyond the 3  $\mu\text{m}$  travel of the tip positioning piezoelectric tubes), several approaches were generally required in order to find a region which could be imaged by our instrument. This is consistent with the fraction of the surface occupied by the smooth ledges.

The STM images obtained from  $\text{Fe}_{78}\text{B}_{13}\text{Si}_9$  are distinctly different from the more "ductile" metallic glasses, as seen in Fig. 9. The grooves on the  $\text{Fe}_{78}\text{B}_{13}\text{Si}_9$  surface are much more closely spaced, typically 15–30 nm apart. (The orientation of the displayed surface in Fig. 9(b) reveals the groove-like nature of these features more clearly.) The pattern of grooves is also more connected in  $\text{Fe}_{78}\text{B}_{13}\text{Si}_9$ , lending a patchwork appearance to the surface. The average patch area is about  $0.004 \mu\text{m}^2$ . Unlike the other two materials, the surfaces between the grooves in  $\text{Fe}_{78}\text{B}_{13}\text{Si}_9$  are often inclined to the nominal fracture surface, as in Fig. 9(a). (The surfaces between the grooves in Fig. 9(b) are more parallel to the nominal plane of the fracture surface.) Crack growth in  $\text{Fe}_{78}\text{B}_{13}\text{Si}_9$  is not strongly confined to the nominal fracture plane, which is consistent with the absence of a well defined slip plane prior to crack growth. Similar deviations from the nominal fracture plane commonly appear when growing crack fingers experience small changes in the direction of the maximum principle stress.<sup>20,21</sup>

Comparing the SEM image of Fig. 8 and the STM images of Figs. 9, one observes remarkably similar patterns, despite the  $100\times$  larger scale of the SEM micrograph. This suggests that the features are at least approximately scale invariant (or fractal) over this range of dimensions.

Near the origin of crack growth,  $\text{Fe}_{78}\text{B}_{13}\text{Si}_9$  fracture surfaces are much smoother than the regions imaged above. Nevertheless, substantial nm-scale steps are observed even here. Preliminary AFM observations taken in the "initiation zone" of a  $\text{Fe}_{78}\text{B}_{13}\text{Si}_9$  fracture surface show long, parallel steps, as shown in Fig. 10. Like the STM images of surfaces formed later in the course of fracture, the material between the steps is often inclined to the nominal fracture surface. However, the spacing of the steps in the initiation zone appears to be less regular and somewhat



greater than the spacing between grooves formed later. We attribute the smoothness of the parallel steps in Fig. 10 to the relatively low stress intensities characteristic of this stage of crack growth. In the early stages of crack growth, the stress intensity at the crack tip rises rapidly. As the stress intensity increases, crack growth becomes more energetic and chaotic, yielding the more broken pattern of grooves shown in Fig. 9. Similar trends are observed in STM observations of initiation zones in silicate glasses,<sup>22</sup> although in silicate glasses the roughest portions of the fracture surface are often confined to a semicircular ring about the fracture origin.

We note in passing that the local orientation of the fracture surface is readily obtained from STM images which have not been "background subtracted." Normally the images are processed to remove the average slope of the imaged area, which renders the smaller surface features more visible. By way of comparison, the image of Fig. 4 ( $\text{Ni}_{56}\text{Cr}_{18}\text{Si}_{22}\text{B}_4$ ) is replotted in Fig. 11 without the background subtraction. The sample has been mounted with the tensile axis along the vertical axis of Fig. 11, and with the narrow dimension of the ribbon (ribbon thickness) running from the foreground into the background. The inclination of the surface relative to the tensile axis and the narrow dimension of the sample is quite clear. The angle between the average (nominal) fracture surface and the tensile axis is estimated to be  $50^\circ \pm 5^\circ$  to the tensile axis, consistent with fracture along the plane of maximum shear (as opposed to tensile) stress. The principal source of uncertainty in this measurement is sample misalignment in the sample holder.

#### IV. DISCUSSION

The distinctive vein features on the fracture surfaces of many metallic glasses, including  $\text{Ni}_{56}\text{Cr}_{18}\text{Si}_{22}\text{B}_4$  and  $\text{Co}_{69}\text{Fe}_4\text{Ni}_1\text{Mo}_2\text{B}_{12}\text{Si}_{12}$ , appear much like those formed by the failure of viscous fluid. For instance, a similar pattern of veins can be produced by wedging apart two microscope slides which have been stuck together by a uniform layer of vacuum grease or fresh (not dry) rubber cement, known as a variable Hele-Shaw cell (VHSC).<sup>23</sup> La Roche et al.<sup>24</sup> have an extended diffusion limited aggregation model which they show generates similar patterns and

suggest a tie to metallic glasses in terms of mechanism for formation of fingers. This similarity led some early workers to suggest that a fluid-like material is actually formed at the crack tip. Fluid-like behavior was variously attributed to localized adiabatic heating created by plastic flow<sup>25</sup> or to free volume effects due to the extreme hydrostatic tension at the crack tip.<sup>26</sup> However, estimates of the temperature rise at the crack tip due to plastic deformation rule out significant adiabatic heating.<sup>3</sup> Later work suggested that the veins are formed by necking of the material along the intersection of two coalescing crack fingers.<sup>6</sup>

This impression is strongly confirmed by the present work, in which the individual slip bands responsible for this necking are clearly discerned. Thus inhomogeneous slip, rather than fluid-like shear, is responsible for the vein features.

Meniscus instabilities along the crack front can have important implications in the mechanical and fracture behavior of nominally brittle materials. The phenomenon of crazing in many polymers is an example.<sup>27</sup> The formation of a meniscus instability requires a negative pressure gradient in the material ahead of the crack tip, so that the tensile stress at some distance in front of the crack tip is greater than the tensile stress at the tip itself. These negative pressure gradients typically arise from nonlinear or plastic responses to stress. Linear crack fronts are unstable in the presence of a negative pressure gradient, and therefore develop oscillations whose wavelength is governed by the balance between the energy released as the fingers grow in to regions of higher tensile stress and the energy consumed in forming the additional crack length. Crack fingers are more closely spaced in materials which have low surface energies (requiring little energy to lengthen the crack front) and high resistance to plastic flow (resulting in high negative pressure gradients). Assuming a constitutive relation of the form  $\sigma = \eta (\dot{\epsilon} / \dot{\epsilon}_0)^n$ , materials with high  $n$  tend to have high finger spacings; i.e. strong nonlinearities tend to increase the energy cost of fingering. These considerations have been quantified for conditions appropriate to metallic glasses by Argon and Salama to yield:<sup>28</sup>

$$\lambda = 12\pi^2 A(n) \left( \frac{\chi}{\tau} \right), \quad (1)$$

where  $\lambda$  is the finger spacing (the wavelength of the fastest growing instability),  $\chi$  is the surface energy,  $\tau$  is the plastic resistance in shear, and  $A(n)$  is a monotonically increasing function of  $n$ , the exponent in the constitutive relation. Although the values of these quantities are not well known for most metallic glasses, relative values based on reasonable expectations allow for qualitative comparisons.

All three metallic glasses show extensive groove formation, allowing for qualitative comparisons of crack fingering behavior based on typical groove spacings. These grooves are all formed in plane strain and would appear to be equivalent in most other respects as well. The much smaller groove spacings observed in  $\text{Fe}_{78}\text{B}_{13}\text{Si}_9$  are consistent with the difficulty of shear in this material, which is readily inferred from the lack of extensive shear prior to failure. This increases the energy available to drive the fingering process and yields narrowly spaced fingers and grooves. Conversely, the fracture geometry of  $\text{Ni}_{56}\text{Cr}_{18}\text{Si}_{22}\text{B}_4$  and  $\text{Co}_{69}\text{Fe}_4\text{Ni}_1\text{Mo}_2\text{B}_{12}\text{Si}_{12}$  suggests that shear is much easier in these materials, consistent with lower energy available to drive crack fingering and more widely spaced fingers and grooves. The grooves in  $\text{Co}_{69}\text{Fe}_4\text{Ni}_1\text{Mo}_2\text{B}_{12}\text{Si}_{12}$  tend to be deeper and more closely spaced than the grooves in  $\text{Ni}_{56}\text{Cr}_{18}\text{Si}_{22}\text{B}_4$ . Deeper grooves imply a larger plastic zone radius and thus a lower resistance to shear deformation. The closely spaced fingers in  $\text{Co}_{69}\text{Fe}_4\text{Ni}_1\text{Mo}_2\text{B}_{12}\text{Si}_{12}$  suggests that the lower resistance to shear is more than compensated by a lower energy for surface formation (from Eq. 1) in determining the wavelength of the most stable oscillations along the crack front. (A lower exponent  $n$  in the constitutive relation would have a similar effect.)

The oscillations along a crack front associated with a meniscus instability are seldom stationary. Only under carefully controlled conditions, such as the flow of a viscous liquid under a rotating cylinder, do meniscus instabilities yield quite stable "crack fronts." Crack fingers are constantly branching and arresting, in response to small changes in the local stress. The arrest of crack fingers yields the characteristic vein features observed in the failure of viscous fluids and

presumably yields the similar features on the fracture surfaces of  $\text{Ni}_{56}\text{Cr}_{18}\text{Si}_{22}\text{B}_4$  and  $\text{Co}_{69}\text{Fe}_4\text{Ni}_1\text{Mo}_2\text{B}_{12}\text{Si}_{12}$ .

The fracture geometry involved in vein formation (along a preexisting slip band) is shown schematically in Fig. 12. Slip during loading forms the smooth, featureless surfaces along line segments AB (on the lower fracture surface) and CD (on the upper fracture surface) in Fig. 12(a). Fracture through the remaining material initiates along one edge of the slip band, labeled B, and proceeds through the thin dimension of the sample. The veins are formed as the crack proceeds from B to C in Figs. 12(a) and 12(b). As the crack approaches the opposite edge of the sample, C, secondary failure is initiated along edge C as well; the intersection of the main crack from edge B and the secondary crack from edge C produces a long vein along the line of intersection, E. Since the crack front is roughly parallel to the long edge of the ribbon, it can be several hundreds of  $\mu\text{m}$  long even in a thin (thickness 50  $\mu\text{m}$ ) ribbon. The great length of the crack has important implications with regard to the state of stress at the crack tip, i.e., crack growth under these conditions occurs in plane strain rather than plane stress.

The state of stress at the crack tip depends principally on the length of the crack front relative to the characteristic radius of plastically deformed material at the crack tip. If the radius of the plastic zone is much shorter than the crack front, deformation at the crack tip is largely restricted to the direction of the applied stress, i.e., the material is in plane strain. In plane strain, the slip bands are characteristically oriented as shown in Fig. 13(a) to produce strong dilatational stresses ahead of the crack tip. These dilatational stresses favor void nucleation and growth ahead of the crack tip. Plane strain conditions are thus conducive to the formation of grooves, which are essentially long voids. Conversely, when the radius of the plastic zone is much longer than the crack length, the material along the crack tip readily deforms in all directions. This deformation tends to relieve the tensile components stress perpendicular to the applied stress, producing plane stress conditions. In plane stress, slip at the crack tip is characteristically oriented as shown in Fig. 13(b). Material is drawn in from the free surfaces, reducing the sample thickness in front of the

crack. Thus plane stress conditions are conducive to the formation of veins, which are essentially long ridges formed by the cold drawing of material between adjacent crack fingers.

The pattern of deformation associated with crack fingering when plane stress conditions prevail between adjacent crack fingers is quite different from the pattern associated with plane stress. In plane stress, the pattern of deformation should be similar to that shown in Fig. 14(a). As adjacent crack fingers approach each other, the material between adjacent crack fingers necks down to produce features very much like veins. Conversely, under plane strain conditions, the strong dilatational stresses in the unfractured material between them can open up long thin voids which appear as grooves on each of the mating fracture surfaces, as shown in Fig. 14(b). The arrows in Fig. 14 show the local direction of crack growth through the material between crack fingers, which is along the direction of global crack growth in plane stress and perpendicular to the direction of global crack growth in plane strain. Thus crack growth in plane stress yields vein features between the fingers and crack growth in plane strain yields grooves.

As suggested in Fig. 12, the crack front during vein formation can be very long (hundreds of  $\mu\text{m}$ ), much longer than typical plastic zone radii in metallic glasses (a few  $\mu\text{m}$ ). Thus plane strain conditions along the crack front in the initial stages of fracture. Consequently, we expect that vein formation is accompanied by a transition to plane stress conditions. Once established in the material between adjacent crack fingers, plane stress conditions would propagate stably because the characteristic spacing of crack fingers (a few hundred nm) is generally much less than a characteristic plastic zone radius (a few  $\mu\text{m}$ ). However, the transition from plane strain to plane stress is geometrically hindered by the incompatibility of the deformation patterns. In plane strain [Fig. 14(a)], slip bands from the adjacent crack fingers intersect above and below the nominal fracture plane, while in plane stress [Fig. 14(b)] they intersect within the nominal fracture plane. The geometric incompatibility of plane stress and plane strain can be circumvented if the plane strain crack front were to be locally deflected out of the nominal fracture plane, allowing a number of slip bands to intersect in the (nominal) fracture plane. The deep cavity observed at the origin of the vein in Fig. 5 probably serves this purpose. Once plane stress deformation patterns are

established, the deflected portion of the crack front can return to the nominal fracture plane with plane stress deformation patterns in place. Subsequent necking on the plane stress slip bands would yield the observed veins.

Similar geometrical considerations apply to the coalescence of the veins and grooves. The displacement of material along the slip bands in adjacent veins or grooves is along different directions, hindering the coalescence of parallel, coplanar features. In the case of adjacent veins, this incompatibility can be circumvented by lifting the restraint of coplanarity. If one of the adjacent crack fingers is deflected out of the nominal fracture plane, two nearly parallel veins may approach and coalesce in a characteristically "vein-like" manner. In contrast, the incompatibility of the displacements responsible for groove formation requires that the constraint of parallelness be lifted. Two adjacent grooves can merge if they both turn  $90^\circ$  toward each other and meet head on. This accounts for the strong tendency of adjacent grooves to merge by forming closed loops seen in Fig. 4.

If both vein and groove spacings are created by deformation between adjacent crack fingers, one would expect that the characteristic groove and vein spacings to both equal the characteristic spacing of crack fingers. However, in  $\text{Ni}_{56}\text{Cr}_{18}\text{Si}_{22}\text{B}_4$  the characteristic minimum vein spacing ( $\sim 400$  nm) is about twice that of the characteristic groove ( $\sim 200$  nm). The vein features tend to coalesce as fracture proceeds, and the larger, more visible veins that result are more widely spaced than the smaller features formed soon after the onset of crack growth. Conversely, the increasing stress concentration at the crack tip early in the course of fracture provides increasingly greater stress gradients at the crack tip, decreasing the wavelength of the meniscus instability and thus decreasing the spacing of crack fingers. Presumably, the majority of the observed grooves were produced later in fracture and thus are more closely spaced.

In contrast to  $\text{Ni}_{56}\text{Cr}_{18}\text{Si}_{22}\text{B}_4$  and  $\text{Co}_{69}\text{Fe}_4\text{Ni}_1\text{Mo}_2\text{B}_{12}\text{Si}_{12}$ ,  $\text{Fe}_{78}\text{B}_{13}\text{Si}_9$ , does not exhibit extensive slip prior to fracture. As a consequence, fracture occurs (nominally) in the plane of maximum tensile stress. Further, the direction of crack growth is typically along the length of the ribbon, with the crack front passing through the thin dimension of the ribbon. The characteristic

plastic zone radius in  $\text{Fe}_{78}\text{B}_{13}\text{Si}_9$  is apparently greater than the ribbon thickness (i.e., the length of the crack front), so that plane strain conditions prevail.<sup>19</sup> Plane strain conditions yield strong dilatational stresses in front of the crack, which promote the nucleation and coalescence of voids ahead of the crack tip and explains the dimpled appearance of much of the fracture surface in SEM observations of  $\text{Fe}_{78}\text{B}_{13}\text{Si}_9$  fracture surfaces.

The development of the  $\mu\text{m}$ -scale chevron pattern is readily explained in terms of crack fingering in the absence of a well developed slip band. Under these conditions, the crack fingers are free to rotate about the direction of crack growth due to small variations in the direction of the maximum tensile stress during fracture. Similar variations in the maximum tensile stress are not able to reorient the crack fingers in  $\text{Ni}_{56}\text{Cr}_{18}\text{Si}_{22}\text{B}_4$  and  $\text{Co}_{69}\text{Fe}_4\text{Ni}_1\text{Mo}_2\text{B}_{12}\text{Si}_{12}$ , where crack growth is largely confined to a preexisting slip band. If the fingering mechanism for groove formation applies to  $\text{Fe}_{78}\text{B}_{13}\text{Si}_9$ , then crack fingering in this material occurs on two contrasting length scales: the  $\mu\text{m}$  scale fingering responsible for the chevron pattern (spacing  $\sim 1 \mu\text{m}$ ) and the nm scale finger responsible for the groove pattern (spacing 30-40 nm). [Compare the SEM and STM micrographs of  $\text{Fe}_{78}\text{B}_{13}\text{Si}_9$  in Figs. 8 and 9.] Similar evidence for crack fingering on contrasting length scales has been provided by Robertson and Mindroiu by SEM of epoxy fracture surfaces.<sup>20</sup>

The process of crack fingering and rotation has been described by Robertson and Mindroiu,<sup>20,21</sup> and is briefly summarized in Fig. 15. During finger growth, small changes in the direction of the maximum tensile stress cause a local reorientation of the planes of the fingers. As a consequence, these fingers are no longer coplanar with each other nor with the nominal fracture plane. During fracture, these crack fingers are constantly coalescing and dividing, as suggested by the pattern of steps observed under the SEM. As illustrated in Fig. 15(b), this process produces a set of roughly parallel surfaces which are often undercut. Final failure requires the fracture of the material between the fingers, but the local stresses are not well oriented to promote this failure. Thus the material between crack fingers tends to bend rather than break. Extensive plastic deformation of material between crack fingers is observed in macroscopically brittle  $\text{LiF}$ ,<sup>29</sup> for

instance. The smooth appearance of the steps between the fingers in Fig. 8 (SEM) is consistent with failure along a  $\mu\text{m}$ -scale slip band formed between adjacent crack fingers. However, since the nm-scale crack fingers in this region are not strongly confined to the nominal fracture plane [as in Fig. 9(a)], the presence of a slip band along the path of fracture is doubtful. In  $\text{Ni}_{56}\text{Cr}_{18}\text{Si}_{22}\text{B}_4$  and  $\text{Co}_{69}\text{Fe}_4\text{Ni}_1\text{Mo}_2\text{B}_{12}\text{Si}_{12}$ , the corresponding nm-scale crack fingers appear to be confined to the nominal plane of fracture.

## VI. CONCLUSION

STM scans of the vein-like features of a nickel-based metallic glass ( $\text{Ni}_{56}\text{Cr}_{18}\text{Si}_{22}\text{B}_4$ ) show a pattern of steps which we attribute to the intersection of shear bands with the fracture surface. These steps are inconsistent with a fluid stage in the development of these features, but provide strong evidence for extensive shear deformation which would mimic fluid-like behavior. The pattern of deformation required is consistent with necking of the material between adjacent crack fingers under conditions of plane stress. Previous models of crack fingering due to meniscus instabilities in metallic glasses appear to account for the required crack fingering.

We attribute the grooves observed in  $\text{Ni}_{56}\text{Cr}_{18}\text{Si}_{22}\text{B}_4$  and  $\text{Co}_{69}\text{Fe}_4\text{Ni}_1\text{Mo}_2\text{B}_{12}\text{Si}_{12}$  to void nucleation and growth along the intersection of adjacent crack fingers under conditions of plane strain. Steps are observed on the edges of these grooves which are again consistent with the intersection of shear bands with the fracture surface. Meniscus instability models of crack fingering in metallic glasses qualitatively account for the spacing between the veins in  $\text{Ni}_{56}\text{Cr}_{18}\text{Si}_{22}\text{B}_4$  and the grooves in the same material, as well as the small spacing between grooves in  $\text{Fe}_{78}\text{B}_{13}\text{Si}_9$ .

STM observations of metallic glass fracture surfaces reflect the nm-scale mechanics of crack growth in these materials. These mechanics can be strongly affected by the transition from local plane strain to plane stress in the material between adjacent crack fingers in  $\text{Ni}_{56}\text{Cr}_{18}\text{Si}_{22}\text{B}_4$  and  $\text{Co}_{69}\text{Fe}_4\text{Ni}_1\text{Mo}_2\text{B}_{12}\text{Si}_{12}$ . The vein-like features observed on the fracture surfaces of these and



similar metallic glasses are produced by deformation of the material between crack fingers in plane stress. Conversely, nm-scale grooves are produced when the material between crack fingers fails in plane strain. The processes of vein and groove formation are a consequence of the extremely localized nature of deformation in the metallic glasses. Our observations imply the existence of highly localized slip *systems* between propagating crack fingers during catastrophic crack growth—an extreme example of microscopically ductile behavior in these macroscopically brittle materials.

Although the horizontal resolution of STM on amorphous materials like metallic glasses is less than atomic, the vertical resolution is still significantly better than can be obtained by competing microscopies (SEM, TEM replica) on unthinned samples. The combination of good vertical and horizontal resolution in a 3-D representation clearly shows the nature of the groove features. Previous observations of similar features in other materials by SEM have not clearly indicated their nature. Thus, the STM should serve as a useful fractographic tool for examining a number of different materials.

## 6. ACKNOWLEDGMENTS

This particular work was inspired by a lecture delivered several years ago at WSU by John Gilman, Lawrence-Berkeley Laboratory, where he discussed possible plastic deformation processes in metallic glasses. The authors wish to thank Les Jensen, WSU, for his assistance in developing the STM hardware. Support for this work was provided by the Air Force Office of Scientific Research under Contract AFOSR-F49620-91-C-0093, the Ceramics and Electronics Materials Division of the National Science Foundation under Grant DMR-8912179, and the Washington Technology Center.

## REFERENCES

1. W. Klement, Jr., R. H. Willens, and P. Duwez, *Nature* **187**, 869 (1960).
2. V. K. Sethi, R. Gibala, and A. H. Heuer, *Scripta Metall.* **12**, 207 (1978).
3. C. A. Pampillo, *J. Mater. Sci.* **10**, 1194 (1975).
4. J. J. Gilman, *J. Appl. Phys.* **46**, 1625 (1975).
5. R. W. Rice, in *Fractography of Glasses and Ceramics*, edited by J. R. Varner and V. D. Frechette, (American Ceramic Society, Westerville, OH, 1988), pp. 3-56.
6. L. A. Davis, in *Metallic Glasses*, (America Society for Metals, Metals Park, OH, 1978), pp. 190 .
7. S. C. Langford, Ma Zhenyi, L. C. Jensen and J. T. Dickinson, *J. Vac. Sci. Technol. A* **8**, 3470 (1990).
8. D. M. Kulawansa, S. C. Langford, and J. T. Dickinson, *J. Mater. Res.* **7**, 1292 (1992).
9. K. Habib and A. Abdullah, *J. Mater. Sci. Letters* **2**, 1055 (1990).
10. R. Wiesendanger, M. Ringger, L. Rosenthaler, H. R. Hidber, P. Oelhafen, H. Rudin and H.-J. Güntherodt, *Surf. Sci.* **181**, 46 (1987).
11. Y. Watanabe, J. T. Dickinson, D. M. Kulawansa, and S. C. Langford, *Memoirs of the National Defense Academy, Japan* **31**, 53 (1992).
12. Y. Watanabe, T. Kubozoe, and Y. Nakamura, *J. Mater. Res.* **7**, 1396 (1992).
13. Y. Watanabe and Y. Nakamura, *J. Mater. Sci. Lett.*, in press.
14. J. W. Lyding, S. Skala, J. S. Hubacek, R. Brockenbrough, and G. Gammie, *Rev. Sci. Instrum.* **59**, 1897 (1988).
15. G. Reiss, J. Vancea, H. Wittmann, J. Zweck, and H. Hoffmann, *J. Appl. Phys.* **67**, 1156 (1990).
16. G. Reiss, F. Schneider, J. Vancea, and H. Hoffmann, *Appl. Phys. Lett.* **57**, 867 (1990).
17. C. A. Pampillo and H. S. Chen, *Mater. Sci. Engin.* **13**, 181 (1974).
18. N. I. Noskova, N. F. Vildanova, Yu. I. Filippov, and A. P. Potapov, *Phys. Stat. Solidi (a)* **87**, 549 (1985).

19. Pavel Diko, Vaclav Ocelik, Vladimir Hajko Jr., Jozef Miskuf, and Kornel Csach, *Kovove Materialy* **25**, 523 (1987).
20. R. E. Robertson and V. E. Mindriou, *Polym. Engin. Sci.* **27**, 55 (1987).
21. R. E. Robertson and V. E. Mindriou, *J. Mater. Sci.* **20**, 2801 (1985).
22. D. M. Kulawansa, J. T. Dickinson, S. C. Langford, and Yoshihisa Watanabe, "Scanning tunneling microscope observations of the mirror region of silicate glass fracture surfaces," manuscript to be submitted.
23. E. Ben-Jacob, R. Godbey, N. D. Goldenfeld, J. Koplik, H. Levine, T. Mueller, and L. M. Sander, *Phys. Rev. Lett.* **55**, 1315 (1985).
24. H. La Roche, J. F. Fernandez, M. Octavio, A. G. Loeser, and C. J. Lobb, "Diffusion-Limited aggregation model for Poisson growth," *Phys. Rev. A* **44**, R6185 (1991).
25. H. J. Leamy, H. S. Chen, and T. T. Wang, *Metall. Trans.* **3**, 699 (1972).
26. F. Spaepen and D. Turnbull, *Scripta Metall.* **8**, 563 (1974).
27. A. S. Argon and M. M. Salama, *Philos. Mag.* **36**, 1217 (1977).
28. A. S. Argon and M. M. Salama, *Mater. Sci. Engin.* **23**, 219 (1976).
29. M. V. Swain, B. R. Lawn, and S. J. Burns, *J. Mater. Sci.* **9**, 175 (1974).

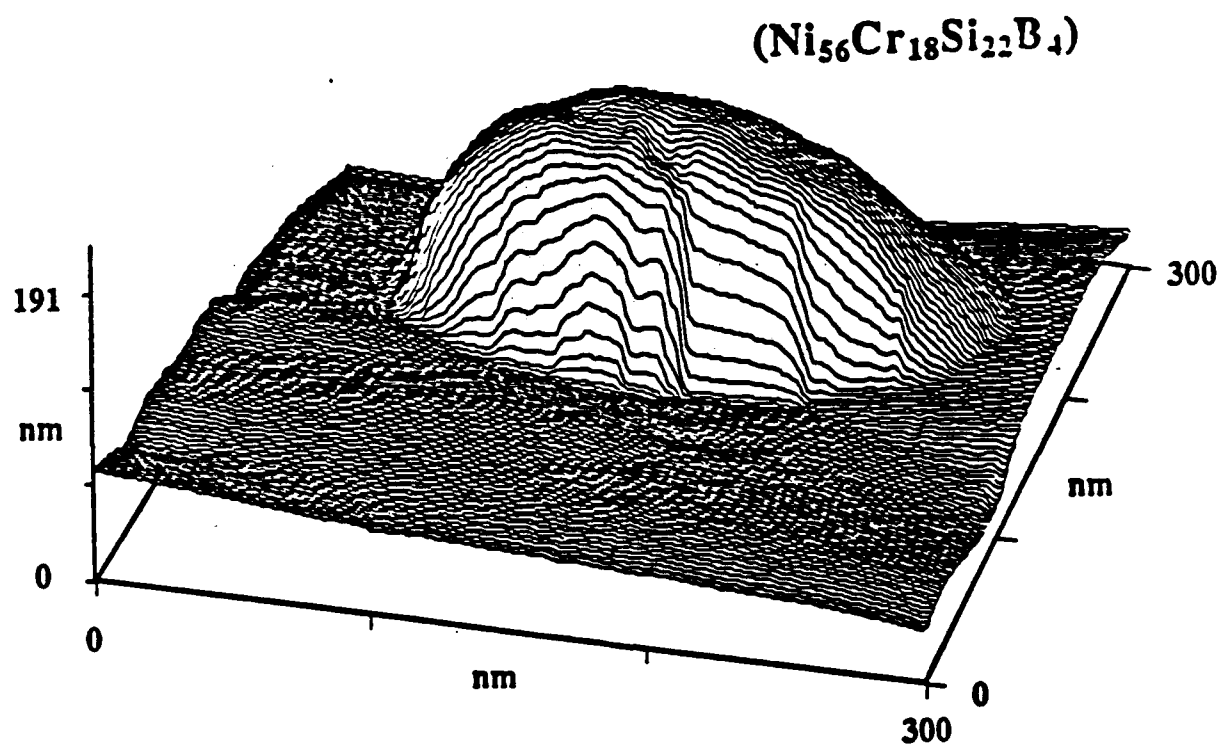
**FIGURE CAPTIONS**

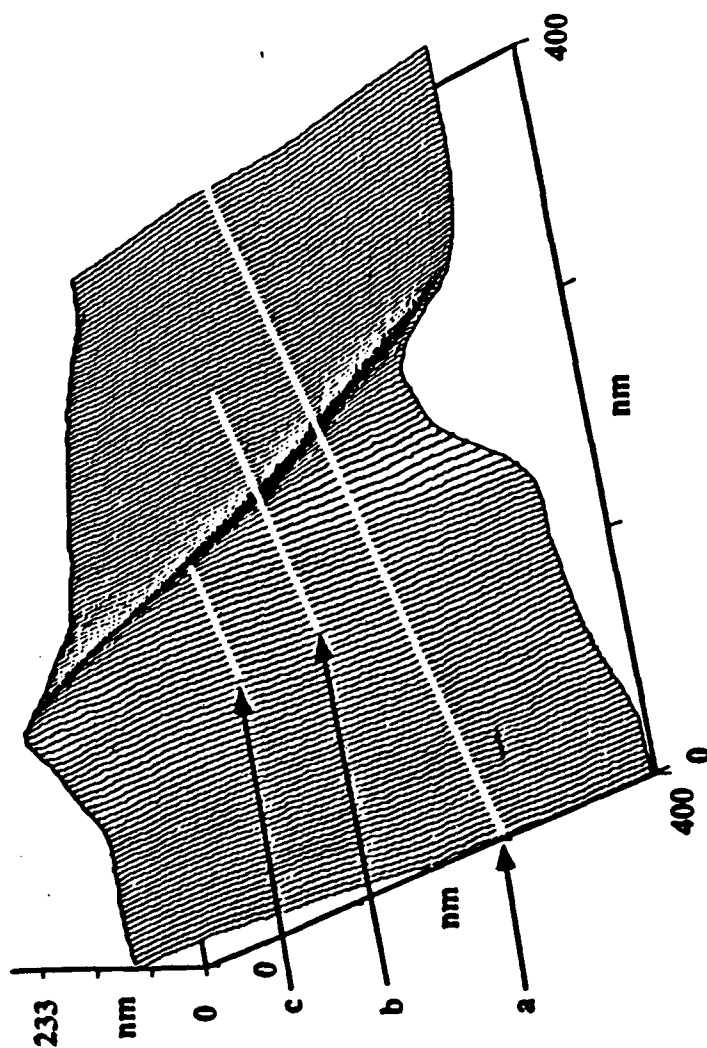
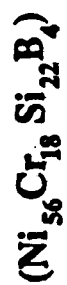
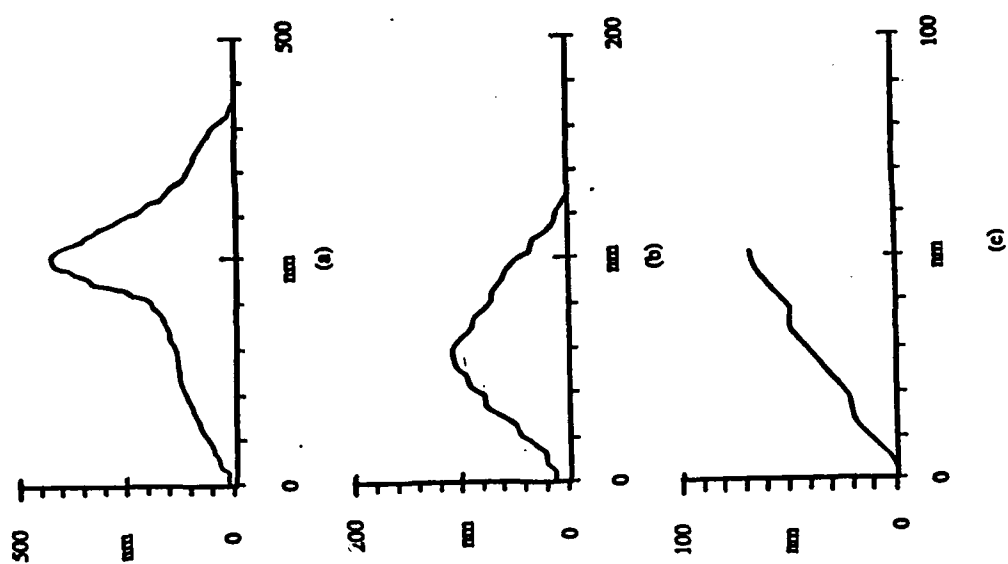
- FIG. 1.** SEM micrograph of a  $\text{Ni}_{56}\text{Cr}_{18}\text{Si}_{22}\text{B}_4$  fracture surface showing the characteristic vein pattern as well as several large particle-like features.
- FIG. 2.** STM image of the sample of Fig. 1 showing a small particle-like feature.
- FIG. 3.** (a) STM image of a  $\text{Ni}_{56}\text{Cr}_{18}\text{Si}_{22}\text{B}_4$  fracture surface showing a ridge which we identify with a vein on the fracture surface. (b) Cross-sections of the above ridge along the lines indicated in white in (a). Note the steps in each cross section.
- FIG. 4.** STM image of a  $\text{Ni}_{56}\text{Cr}_{18}\text{Si}_{22}\text{B}_4$  fracture surface showing a typical pattern of grooves.
- FIG. 5.** STM image of a  $\text{Co}_{69}\text{Fe}_4\text{Ni}_1\text{Mo}_2\text{B}_{12}\text{Si}_{12}$  fracture surface showing what appears to be the origin of a vein.
- FIG. 6.** STM image of a  $\text{Co}_{69}\text{Fe}_4\text{Ni}_1\text{Mo}_2\text{B}_{12}\text{Si}_{12}$  fracture surface showing (a) two typical grooves and (b) steps or ridges along the side of a groove.
- FIG. 7.** STM image of a  $\text{Ni}_{56}\text{Cr}_{18}\text{Si}_{22}\text{B}_4$  fracture surface formed by fracture at high loading rates, showing a two sets of intersecting fracture steps.
- FIG. 8.** SEM image showing the characteristic chevron features on a  $\text{Fe}_{78}\text{B}_{13}\text{Si}_9$  fracture surface formed in tension.
- FIG. 9.** Two STM images of a  $\text{Fe}_{78}\text{B}_{13}\text{Si}_9$  fracture surface formed in tension showing nm-scale grooves. The tilt of the image in (b) clearly shows the groove-like nature of the structures between the crack fingers.
- FIG. 10.** AFM image taken in the initiation zone of a  $\text{Fe}_{78}\text{B}_{13}\text{Si}_9$  fracture surface. In contrast to the STM images of Fig. 9, this portion of the fracture surface was formed in the early stages of crack growth.
- FIG. 11.** STM image of Fig. 4 ( $\text{Ni}_{56}\text{Cr}_{18}\text{Si}_{22}\text{B}_4$ ) without the subtraction of background slope.
- FIG. 12.** Schematic diagram of the formation of a vein pattern. (a) Shear deformation prior to fracture; (b) fracture along the shear band; and (c), the resulting vein pattern.

- FIG. 13.** Pattern of deformation at a crack tip in (a) plane stress and (b) plane strain, indicating the orientation of planes along which shear deformation occurs.
- FIG. 14.** Pattern of deformation along crack fingers in the case of (a) plane stress and (b) plane strain.
- FIG. 15.** The formation of steps between crack fingers. (a) The rotation of crack fingers under the influence of local changes in the direction of the maximum principal (tensile) stress. (b) The orientation of adjacent crack fingers when viewed along the direction of crack growth: (top) with the maximum principal stress *normal to the nominal fracture plane*; (middle) after a small change in the direction of the maximum principal stress; and (bottom) the resulting pattern of fracture steps. The arrows indicate the instantaneous direction of the maximum principle (tensile) stress during crack growth.



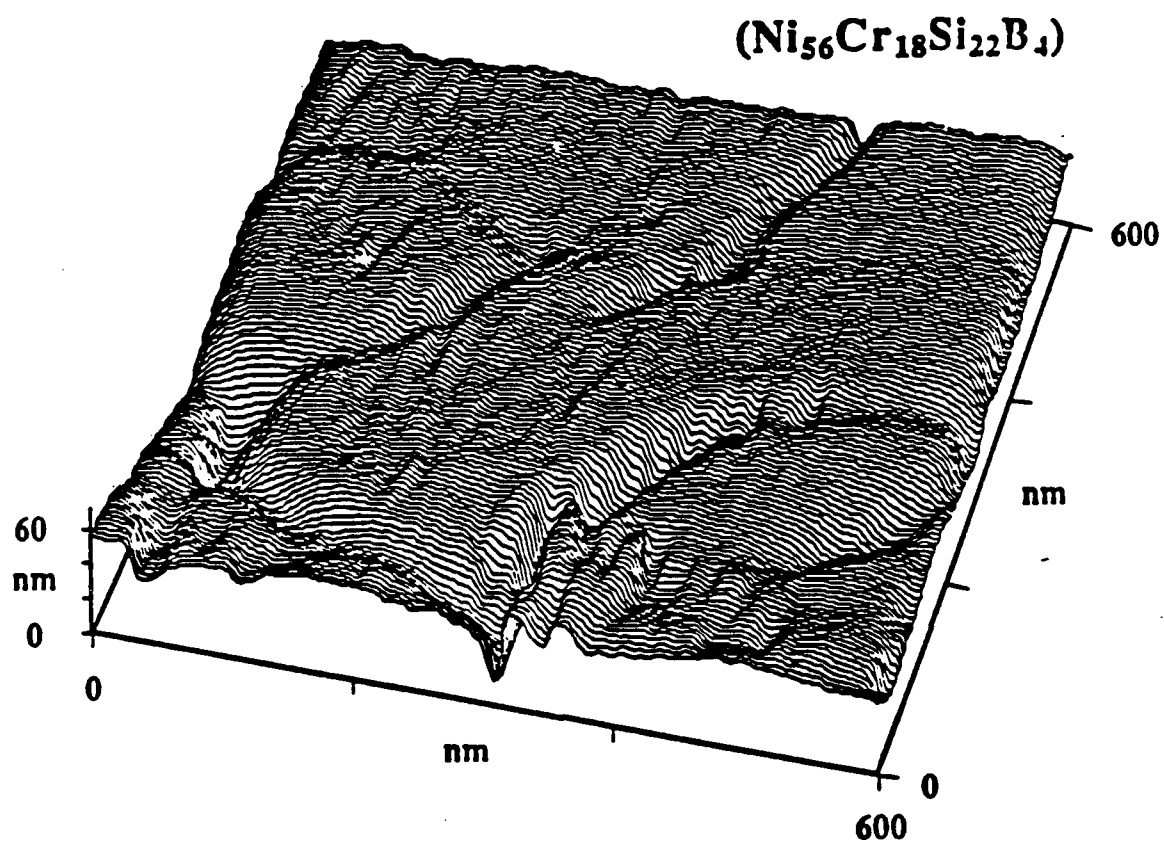
**Fig. 1**

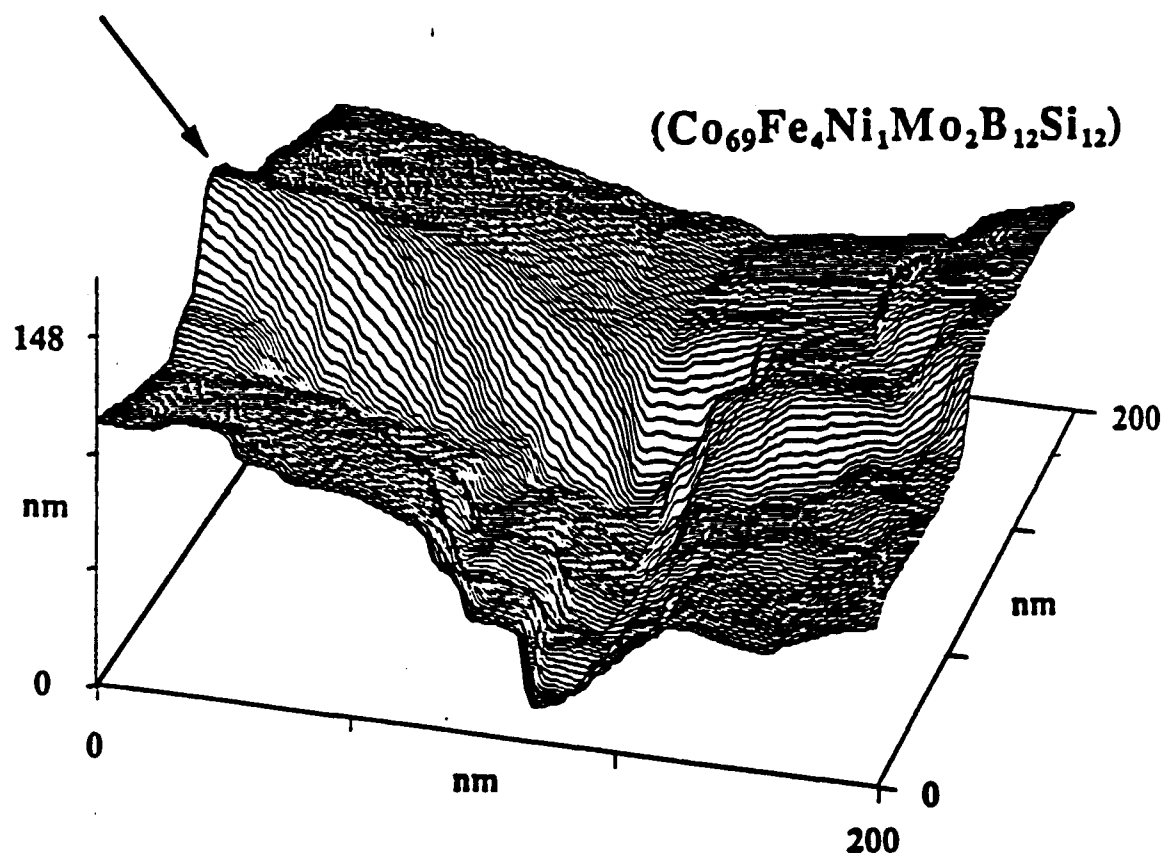
**Fig. 2**

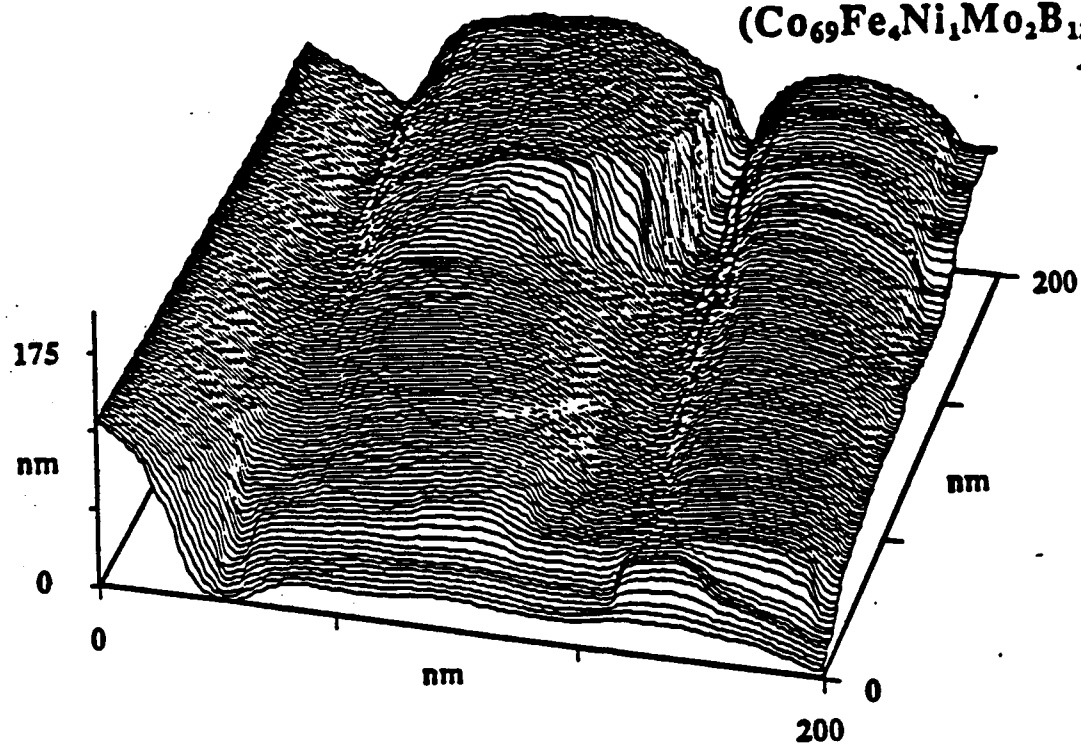


**Fig. 3**

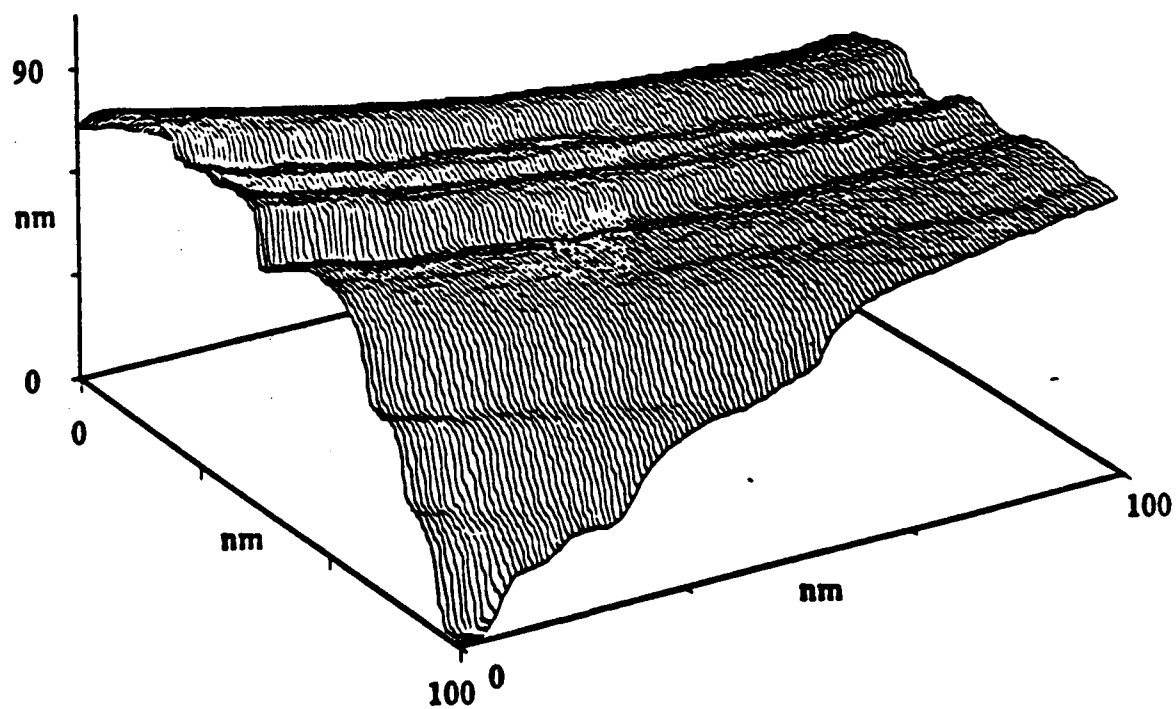


**Fig. 4**

**Fig. 5**

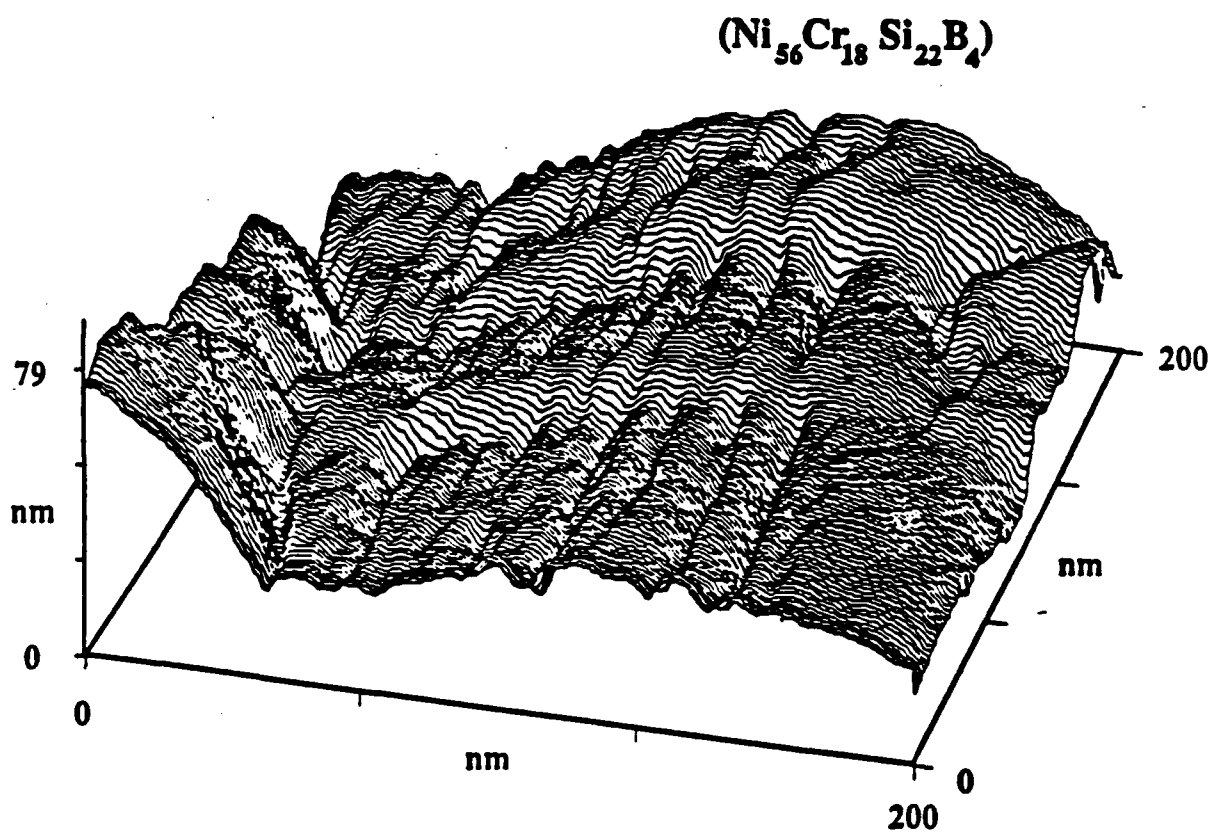


(a)



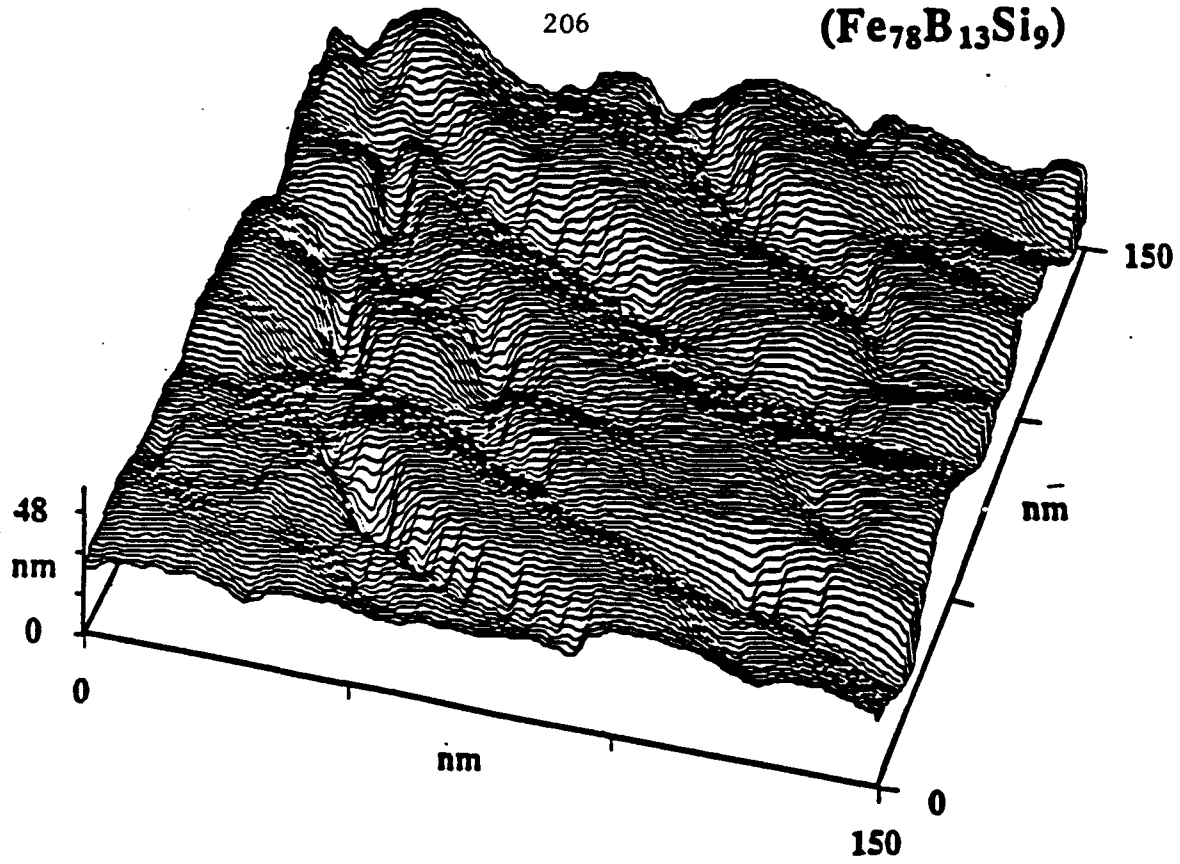
(b)

**Fig. 6**

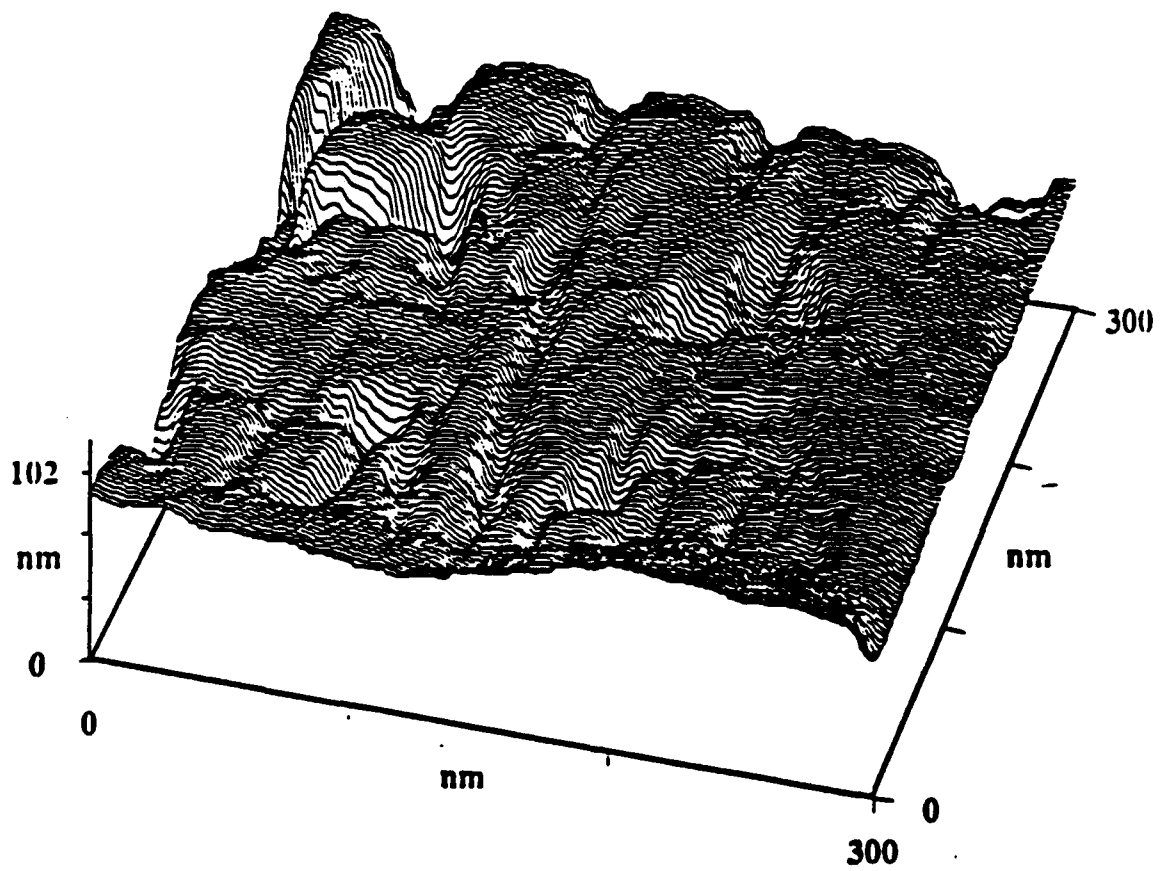
**Fig. 7**



**Fig. 8**

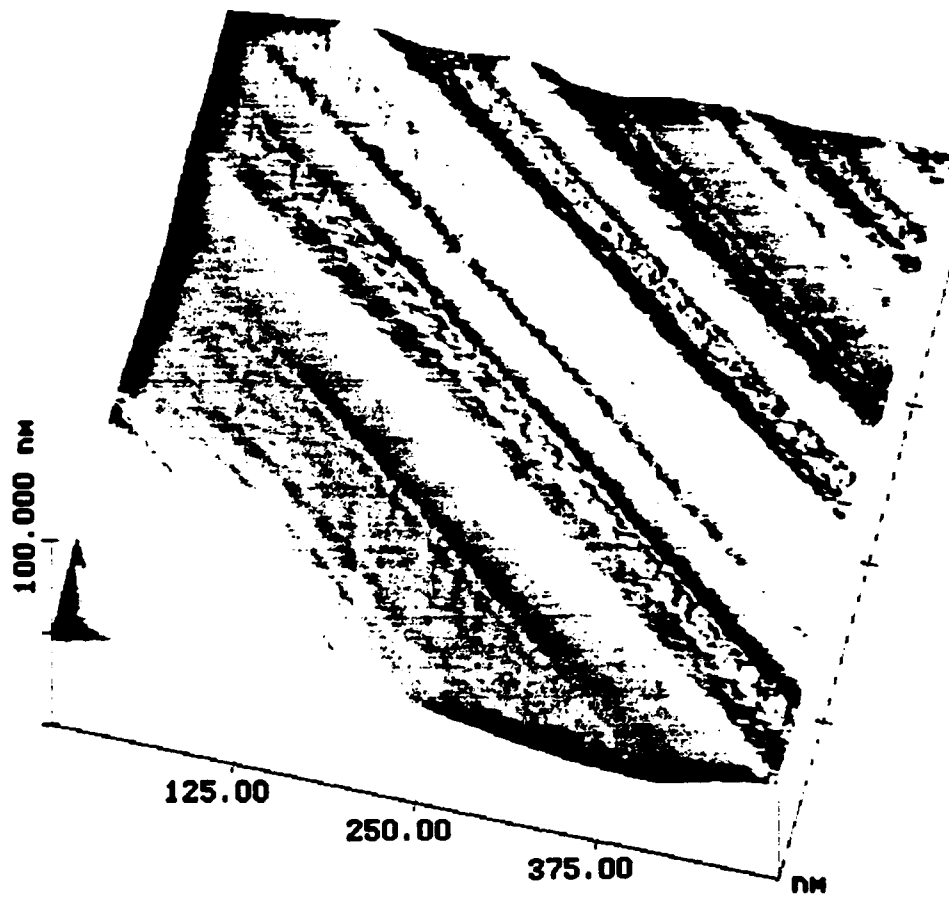


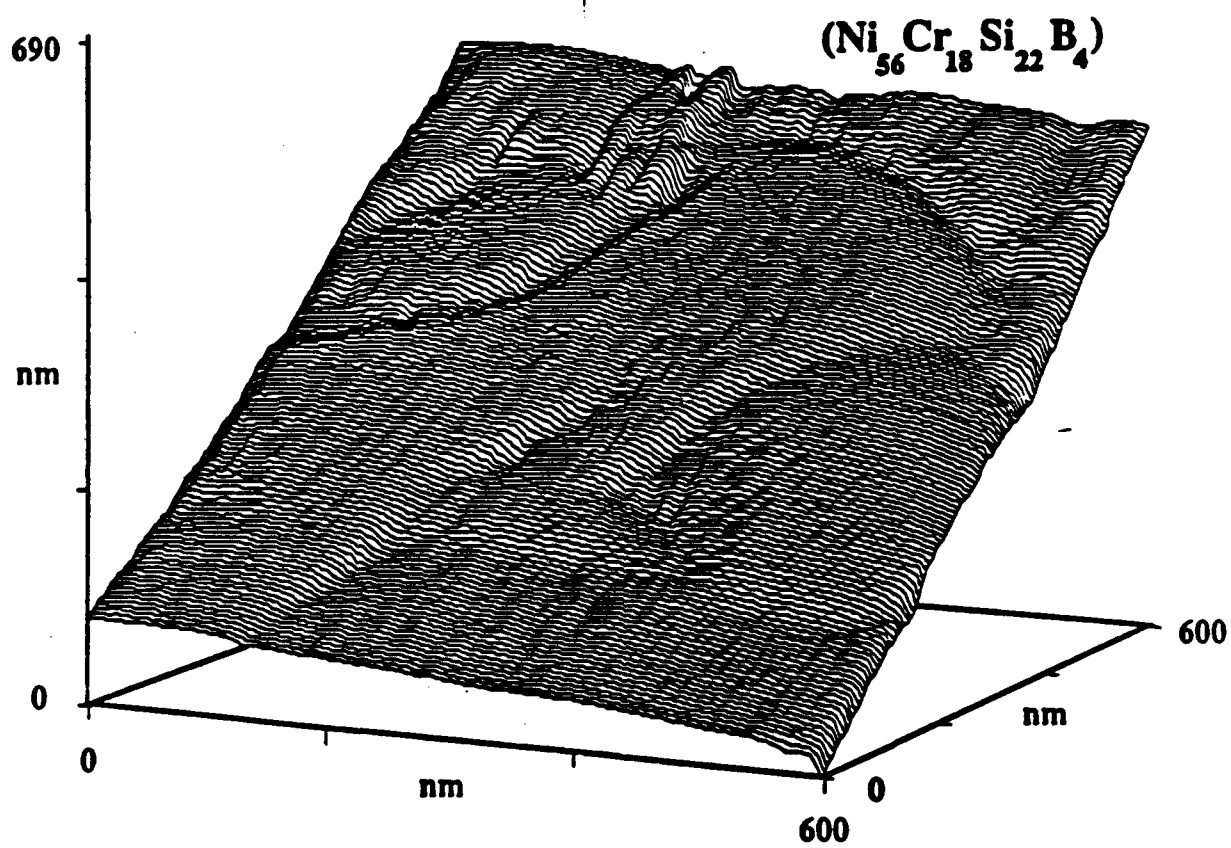
(a)



(b)

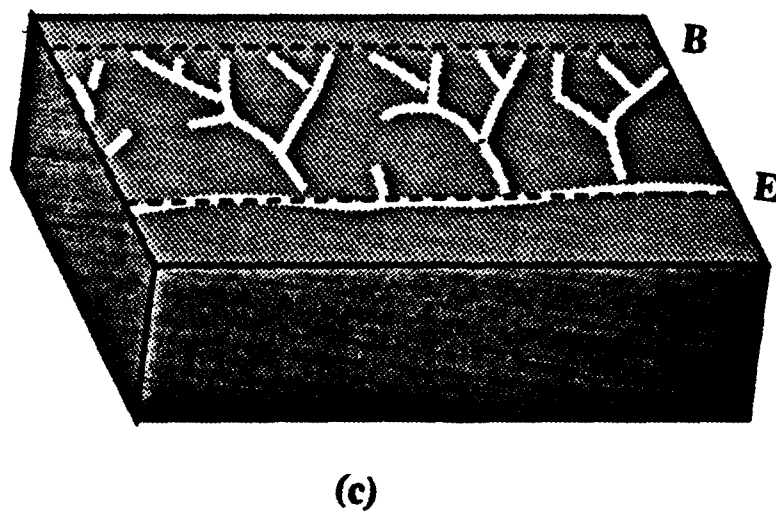
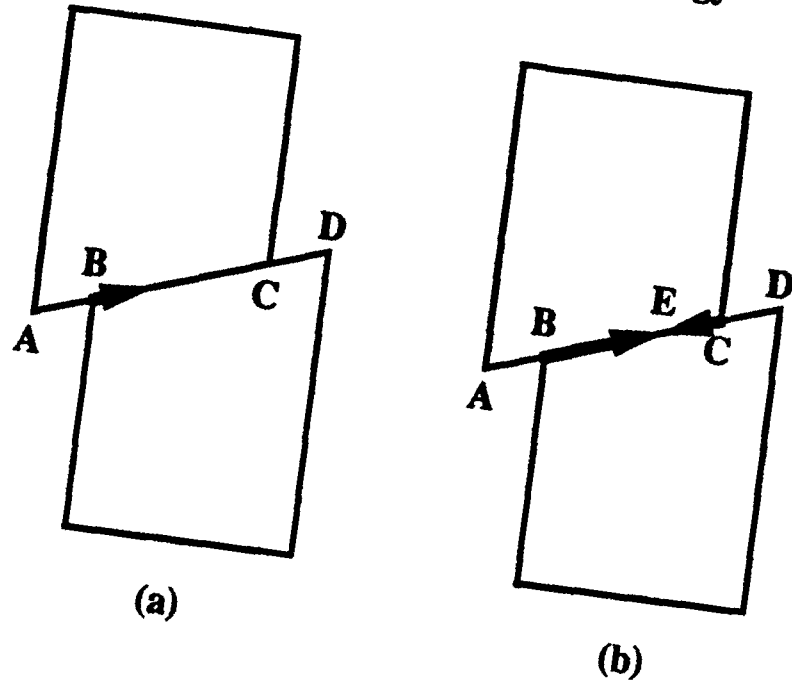
Fig. 9

**Fig. 10**

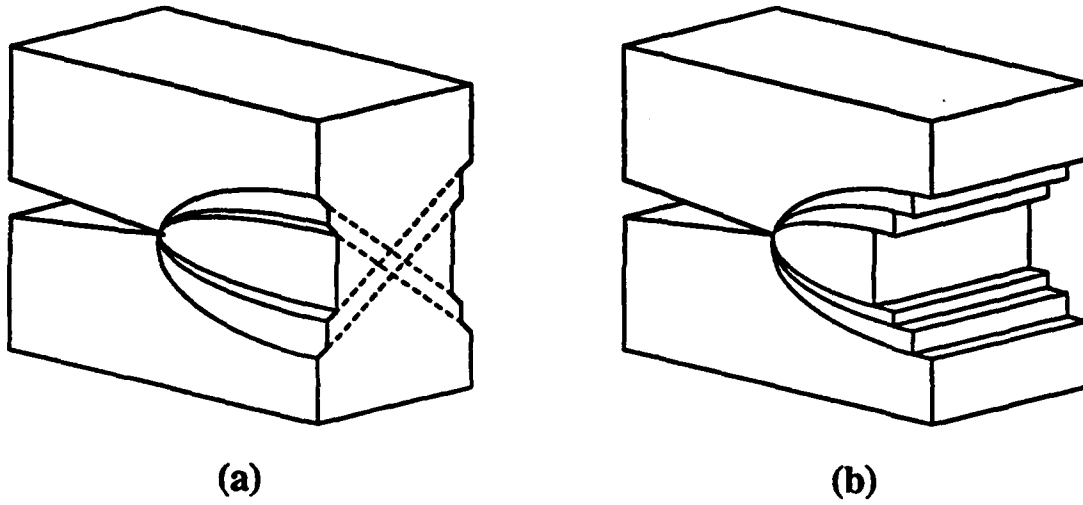
**Fig. 11**

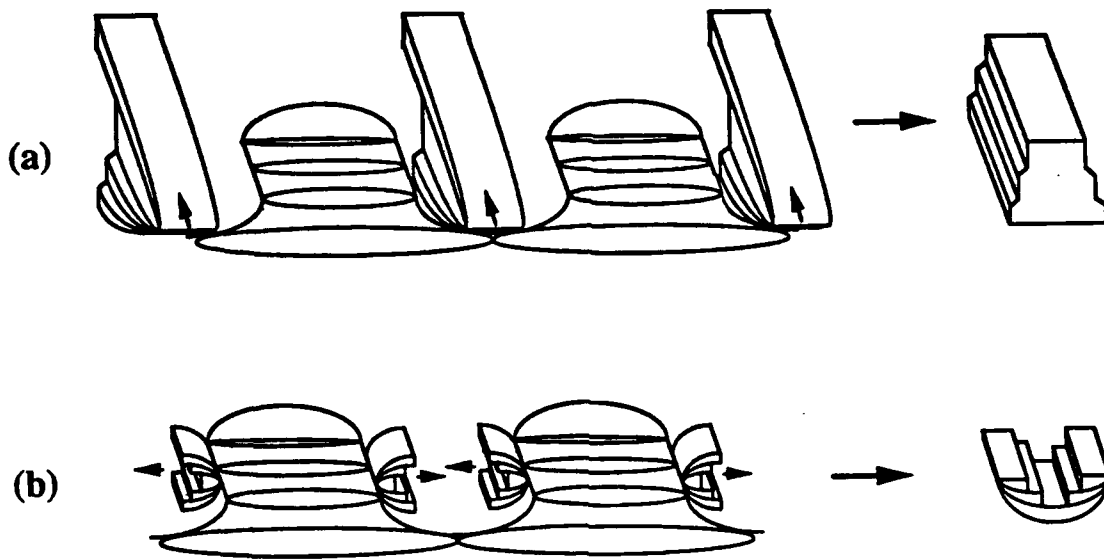


### Formation of Veined Morphology



**Fig. 12**

**Deformation at Crack Tips in Plane Stress and Plane Strain****Fig. 13**

**Formation of Vein and Groove Features****Fig. 14**

### Cleavage Step Formation by Crack Finger Rotation

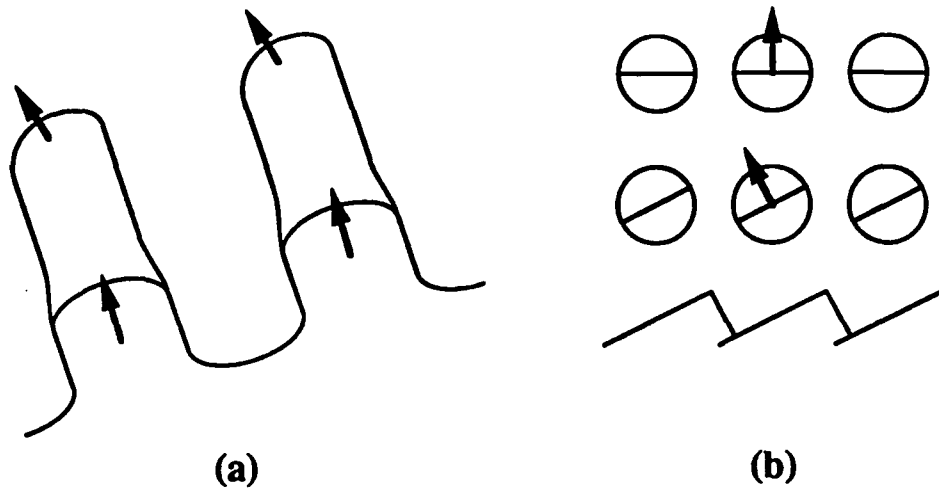


**Fig. 15**

**X. XENON EMISSION ACCOMPANYING FRACTURE OF  
XENON-IMPLANTED CUBIC ZIRCONIA**

**M. Grant Norton\*<sup>1</sup>, Wenbiao Jiang<sup>1</sup>, J. Thomas Dickinson\*<sup>2</sup>,  
Leslie C. Jensen<sup>2</sup>, and Stephen C. Langford\*<sup>2</sup>**

***1. Department of Mechanical and Materials Engineering  
2. Department of Physics  
Washington State University, Pullman, WA 99164***

**Elizabeth L. Fleischer and James W. Mayer**

***Department of Materials Science and Engineering  
Cornell University, Ithaca, NY 14853***

submitted to

**Journal of the American Ceramic Society**

November 23rd, 1992

**\* Member of the American Ceramic Society.**

**Work supported by the Ceramics and Electronic Materials Division of the National Science Foundation under Grant DMR 8912179, the Air Force Office of Scientific Research under Contract AFOSR-F49620-91-C-0093, and the Washington Technology Center.**

### Abstract

The emission of xenon following the fracture of xenon-implanted cubic zirconia has been studied by mass spectrometry. All samples showed intense Xe bursts at failure. Order of magnitude estimates of the amount of Xe released suggest that  $\mu\text{m}$ -scale regions of the tensile surface on either side of the fracture surface must be substantially depleted in Xe. SEM micrographs of the tensile surface of these samples do not show sufficient damage to account for this emission. However, SEM micrographs of the fracture surface show evidence for extensive microcracking immediately adjacent to the tensile surface. It is believed that these microcracks are formed when the advancing crack encounters the tensile stresses immediately below the Xe-implanted surface layer and disrupt the Xe inclusions produced by implantation. Some samples also show Xe bursts prior to failure; SEM observations of these samples show shallow cone cracks on the tensile surface which appear to form during loading and would account for the release of Xe prior to failure.

[Key words: ion-implantation, fracto-emission, zirconia, xenon, microcracking, fracture].

## 1. Introduction

Ion implantation of ceramic materials has been investigated by a number of researchers, primarily because of the resultant improvements in hardness that can be achieved [e.g., references 1 and 2]. The implanted ions have included metals such as Cr, Ni, Y, Ti, and Al and gases such as N and Xe.<sup>3</sup> The implantation of noble-gas ions is of particular interest in studying some of the fundamental aspects of the ion-implantation process. These ions are immiscible with the matrix and therefore chemical effects resulting from ion implantation, such as intermixing, are unlikely. The microstructure of single crystal MgO and yttria-stabilized cubic zirconia (YSZ) implanted with Xe has been examined by Rutherford backscattering spectrometry (RBS) and transmission electron microscopy (TEM).<sup>4,5,6</sup> Of particular interest in these previous studies was the physical state of the implanted noble gas. Energy dispersive spectroscopy (EDS) in the TEM and RBS confirmed that Xe was retained in the sample following implantation. Electron diffraction studies clearly demonstrated that the Xe was in two forms—solid and fluid. In the case of the solid inclusions it was determined<sup>5</sup> that their average diameter was typically 10 nm with confinement pressures of  $\sim 0.6$  GPa. The diameter of the fluid inclusions was typically 50 nm.

The mechanical properties—wear resistance and hardness—have been determined for YSZ implanted with Xe over a range of fluences.<sup>7</sup> These mechanical properties were correlated to both the fluence and the resulting microstructural disorder due to heavy particle bombardment. The role of the noble-gas inclusions in influencing the mechanical behavior has been postulated<sup>6</sup> but direct correlations have not yet been experimentally determined. In the present study, fracture events in the near-surface region, associated with the presence of the solid and fluid inclusions in the near surface layer, were monitored by measuring the Xe emission during fracture.

The fracture of many materials is accompanied by various emissions, which may include electrons, ions, neutral molecules, and photons; collectively, these emissions are

called 'fracto-emission' [e.g., refs. 8-11]. In particular, the neutral emission intensities are strongly material dependent.<sup>12-15</sup> Under the appropriate conditions, the neutral emission signal can reflect the temperature of the newly formed fracture surface,<sup>16</sup> the amount of bond-breaking during fracture,<sup>17</sup> and/or the presence of a number of pre-failure processes, including crazing and deformation in polymers.<sup>18,19</sup> In this study, the emission of Xe before, during, and after fracture was determined as a function of time for samples loaded in 3-point bend. The tensile surface was chosen to be the Xe-implanted surface.

## 2. Experimental

Single-crystal, fully stabilized (9.4 mol%  $\text{Y}_2\text{O}_3$ ) cubic zirconia obtained from Ceres Corporation was oriented to within  $1^\circ$  of a  $\langle 100 \rangle$  axis and cut into  $1\text{ cm} \times 1\text{ cm} \times 1\text{ mm}$  samples and polished to a mirror finish.

Monoenergetic  $\text{Xe}^+$  ions were implanted into the zirconia at room temperature using an accelerating voltage of 240 kV. The energy was selected to obtain a shallow implant with a range of approximately 50 nm from the irradiated surface. The ion fluence was between  $3\text{--}7 \times 10^{16} \text{ Xe}^+/\text{cm}^2$ . Previously reported TEM studies indicate that both solid and fluid Xe inclusions are produced by irradiation under these conditions.<sup>6</sup> At higher fluences, the measured Xe concentration reaches a limiting value; probably due to concurrent sputtering. All the samples were examined by RBS following implantation to determine the location and concentration of Xe in the ceramic matrix.

The implanted samples were cut in half using a diamond saw to obtain pieces  $0.5\text{ cm} \times 1\text{ cm} \times 1\text{ mm}$ . The rough edges of the samples, produced by cutting, were removed using silicon carbide paper. The samples were then cleaned in ethanol, dried, and loaded into a sample carousel, which was in turn mounted in an ultra-high vacuum chamber. Rotation of the sample carousel positioned each sample, in turn, between a loading manipulator and the detector. Each sample was loaded in three point bend with the implanted surface (in tension) facing the mass spectrometer. The Xe emission intensity



was monitored with a UTI 100C quadrupole mass spectrometer (QMS). Xenon ionized by electron bombardment at the entrance aperture of the QMS was directed into the instrument. The spectrometer was tuned to pass ions with a mass to charge ratio corresponding to  $131.5 \pm 1$  amu. This setting allowed the detection of the abundant Xe isotopes at 131 and 132 amu (these two isotopes account for 48% of naturally occurring Xe). The samples were fractured in a three-point bending mode. The force applied to the loading apparatus was monitored with a Kistler Model 211B2 piezoelectric force transducer. Following fracture the specimens were removed from the sample carousel and examined by light optical microscopy and by SEM using a JSM 6400.

An important point is the sequence of fracture events for the type of loading used in this experiment. For flexural loading, the fracture typically initiates at an edge flaw on the tensile side and first propagates along this front tensile side (for details, see references 20 and 21). Following completion of this event, the crack moves directly back (starting approximately at the neutral plane) to complete separation of the sample. For the samples used in this study, the significant event is the intersection of a moving crack tip with its accompanying high stress intensity and the shallow implanted region. As shown below, this results in intense Xe emission due to extended damage in the implanted region.

### 3. Results.

A total of 12 samples were fractured in vacuum. Prior to loading, no evidence of a background at mass 131-132 was observed. Intense Xe emission was characteristically observed to accompany fracture of all the specimens. In addition, however, some samples showed weak Xe signals prior to fracture. The Xe signal intensity and the measured load accompanying fracture of a typical sample which yielded no detectable Xe prior to fracture are shown in Fig. 1. At the point of failure of the ceramic a large peak in the Xe intensity versus time curve is observed. Other samples produced Xe emissions during the application of the load, as illustrated in Fig. 2. These emissions were not continuous but

appeared as discrete bursts. Further increase in the applied load produced a much larger burst of Xe associated with complete failure of the ceramic.

Specimens which showed the two types of emission behavior could be clearly distinguished using SEM. Fig. 3a shows a typical secondary electron image of the tensile surface of a fractured zirconia sample which showed no pre-emission. The tensile surface of this sample appears quite smooth. This type of surface was characteristic of all the specimens where no pre-emission was observed. Fig. 3b shows a typical secondary electron image of part of the tensile surface of a sample which showed pre-emission. Small cone cracks were observed on the tensile surface adjacent to the main crack. All specimens which showed pre-emission of Xe during fracture had similar cone cracks along the tensile surface. The fracture surface, like the cone cracks, had a conchoidal appearance, which is common in cubic zirconia.<sup>22</sup> In some cases, cone cracks had formed in the tensile surface without spallation, as illustrated in Fig. 4.

EDS analysis was performed on a number of samples showing both the pre-emission and no pre-emission. A common feature of the EDS analysis was that in regions of the tensile surface, up to a few microns from the fracture surface, Xe was still detected at a level consistent with the bulk concentration. For cone cracks which spalled, the remaining cavity was totally depleted of Xe, as expected. For cone cracks which did not spall, significant Xe depletion was also observed. In the region undercut by the cone crack, e.g., area A in Fig. 4, EDS analysis revealed significant depletion of the implanted Xe, as illustrated in Fig. 5(a). EDS analysis of areas outside the cone crack, e.g., area B in Fig. 4, showed Xe concentrations typical of regions far from the fracture surface, as shown in Fig. 5(b).

An order of magnitude estimate of the amount of Xe emitted during fracture,  $N_{Xe}$ , can be deduced from the area of the emission peak (the total detected charge),  $Q_d$ .

$$N_{Xe} \sim \frac{Q_d}{S_{Xe} \tau \eta_g}, \quad (3)$$

where  $S_{Xe}$  is the quadrupole detection efficiency for Xe,  $\tau$  is the average time required for a neutral Xe atom to pass through the ionizer (i.e., the time in which it may be potentially ionized and detected), and  $\eta_g$  is the geometric collection efficiency of the ionizer, accounting for the solid angle it subtends as viewed from the sample. Fig. 6 shows the Xe emission signal of Fig. 1 on an expanded time scale; in this instance, the total detected charge is about 840 pC.  $S_{Xe}$  was estimated to be  $4 \times 10^{-19}$  A/atom (i.e., amperes per atom inside the quadrupole ionizer);  $\tau \sim 120 \mu\text{s}$  (assuming thermal velocities at 300 K), and  $\eta_g \sim 0.20$ . Thus, to within an order of magnitude,  $10^{14}$  Xe atoms were emitted during or soon after fracture.

A planar fracture surface intersecting the tensile surface at right angles will intersect only those Xe inclusions within one inclusion radius of the fracture surface. However, it is likely that somewhat more distant inclusions will also be disrupted. Assuming a uniform distribution of Xe inclusions in a thin layer adjacent to the tensile surface, it is estimated that at most  $10^{12}$  Xe atoms will be released by this process. In this estimation it was assumed that all the inclusions within 50 nm of the fracture surface were disrupted. The observed emission intensities would indicate that disruption of Xe inclusions at distances on the order of microns from the fracture surface occurred.

One potential source for this emission is roughening of the fracture surface adjacent to the tensile surface. Figure 7 shows an SEM image of the same sample imaged in Fig. 3(a). However, in Fig. 7, the specimen was remounted and tilted to enable observation of both the fracture and tensile surfaces. Considerable roughness is clearly visible along the fracture surface adjacent to the tensile side. This roughening, which extends along the entire length of the fracture surface, is not typical of unimplanted crystalline and amorphous materials fractured in 3-point bend, e.g., MgO<sup>20,21</sup>, and is probably produced when the crack front encounters the large stresses produced by the implanted Xe near the tensile surface.

The fracture of stronger samples yielded even more intense Xe emission as illustrated in Fig. 2—about ten times greater than that shown in Fig. 1, i.e., approximately  $10^{15}$  Xe atoms. Considerable macroscopic crack branching was observed in these samples as well as cone cracks on the tensile surface.

#### 4. Discussion.

In all the samples fractured in this study, the amount of Xe detected by the mass spectrometer was approximately two orders of magnitude larger than the amount of Xe implanted in regions adjacent to the nominal fracture surface. The smooth appearance of the tensile surface in samples which did not show pre-emission belies the extensive microcracking along the fracture surface adjacent to the tensile side. The large emissions accompanying fracture appear to be due to branching as the crack approaches the tensile surface, as illustrated schematically in Fig. 8. The high compressive stresses in the implanted layer are balanced by tensile stresses in the underlying material. As the crack approaches the tensile surface, the tensile stresses in the zirconia promote crack branching. It is not clear from the SEM image in Fig. 7 whether all these crack branches actually reach the tensile surface; the strong compressive stresses in the implanted region may be sufficient to arrest many of the branch cracks. This explanation would account for the apparent smoothness of the tensile surface shown in Fig. 3(a). However, it is reasonable to assume that these branch cracks could disrupt many of the Xe inclusions within a few microns of the nominal fracture surface, and would thus explain the intensity of the Xe emissions accompanying fracture.

The sharp transition between compression in the Xe-implanted layer and tension in the material immediately below is conducive to spalling of the surface layer,<sup>23</sup> although this is not always observed. Spalling is probably responsible for the cone cracking in samples yielding the bursts of emission prior to failure. Since some of the strongest samples showed no evidence of cone cracking prior to failure, spalling probably requires the

presence of an initiating defect, such as machining damage. The resulting cone cracks may serve as initiation sites for catastrophic failure. The fact that the cone cracks form in the region between the compressive Xe-rich layer and the tensile region of the zirconia below this layer is supported by evidence obtained in the SEM. The micrograph in Fig. 4 shows a cone crack in which the undercut zirconia was not ejected from the sample but remained in place. Microcracks under this cone crack are visible in the secondary electron image. The escape depth of the secondary electrons is quite small,<sup>24</sup> typically on the order of 50 nm. Thus the features visible in Fig. 4 under the cone crack may be ~50 nm below the surface, which corresponds closely to the projected depth for the implanted Xe.

The low diffusion coefficients for atomic Xe and for nanometer-sized Xe inclusions ( $D_{\text{Xe}} \approx 10^{-16} \text{ cm}^2\text{s}^{-1}$  for Xe atoms and  $D_{\text{Xe}} \approx 10^{-24} \text{ cm}^2\text{s}^{-1}$  for Xe clusters in an aluminum matrix at room temperature<sup>25</sup>) indicate that diffusion of Xe from the implanted region to the fracture surface is unlikely, especially given the short time scales of the Xe burst at fracture.

## 5. Conclusions.

The introduction of noble gases into a ceramic matrix by ion implantation produces a unique nanostructure in the near-surface region and modifies the mechanical properties of the ceramic. The resulting inclusions remain stable for long periods of time due to the constraint of the matrix, and produce compressive surface stresses which provide considerable resistance to the growth of shallow surface flaws. When the implanted layer is breached, shallow cone cracks are often formed; these cracks are not strong stress concentrators and do not appear to nucleate failure except at the highest applied loads. The present results suggest that the tensile stresses underlying the implanted Xe can result in microcracking along the tensile side of the fracture surface during catastrophic crack growth. This branching greatly increases the intensity of the Xe emissions accompanying failure. Although the energy required for crack branching is small in terms of the total

energy dissipated at fracture, the local rate of energy dissipation must be quite high. The implanted Xe also promotes the formation of cone cracks on the tensile surface during loading, which yield intense bursts of Xe prior to failure. Xe emission during the loading and failure of Xe-implanted zirconia appears to reflect the timing and degree of fracture along the tensile surface during loading and along the tensile side of the fracture surface during catastrophic failure. The stress gradients associated with Xe implantation not only hinder the growth of shallow surface flaws, but also strongly affect the course of crack growth along the implanted surface during catastrophic failure.

## References

1. C.J. McHargue, "The mechanical properties of implanted ceramics—a review," *Defects and Diffusion Forum* **57/58**, 359-380 (1988).
2. P.J. Burnett and T.F. Page, "Criteria for mechanical property modifications of ceramic surfaces by ion implantation," *Radiation Eff.* **97**, 283-296 (1986).
3. C.W. White, C.J. McHargue, P.S. Sklad, L.A. Boatner, and G.C. Farlow, "Ion implantation and annealing of crystalline oxides," *Mater. Sci. Rep.* **4**, 41-146 (1989).
4. M.G. Norton, E.L. Fleischer, W. Hertl, C.B. Carter, and J.W. Mayer, "Transmission-electron microscopy study of ion-beam implanted single-crystal ceramics," *Nucl. Instr. and Meth.* **B59/60**, 1215-1218 (1991).
5. M.G. Norton, E.L. Fleischer, W. Hertl, C.B. Carter, J.W. Mayer, and E. Johnson, "Occurrence of solid noble-gas inclusions in ion-beam-implanted magnesium oxide," *Phys. Rev. B* **43**, 9291-9294 (1991).
6. E.L. Fleischer, M.G. Norton, M.A. Zaleski, W. Hertl, C.B. Carter, and J.W. Mayer, "Microstructure of hardened and softened zirconia after xenon implantation," *J. Mater. Res.* **6**, 1905-1912 (1991).
7. E.L. Fleischer, PhD thesis, Cornell University (1991).

8. L.A. K'Singam, J.T. Dickinson, and L.C. Jensen, "Fractoemission from failure of metal/glass interfaces," *J. Am. Ceram. Soc.* **68**, 510-514 (1985).
9. J.T. Dickinson, L.C. Jensen, and W.D. Williams, "Fractoemission from lead zirconate-titanate," *J. Am. Ceram. Soc.* **68**, 235-240 (1985).
10. J.T. Dickinson, L.C. Jensen, S.C. Langford, and J.P. Hirth, "Atomic and molecular emission following fracture of alkali halides: A dislocation driven process," *J. Mater. Res.* **6**, 112-125 (1991)
11. J.T. Dickinson, L.C. Jensen, and S.C. Langford, "Atomic and molecular emission accompanying fracture of single-crystal Ge: A dislocation-driven process," *Phys. Rev. Lett.* **66**, 2120-2123 (1991).
12. J.T. Dickinson, L.C. Jensen, M.R. McKay, and F. Freund, "The emission of atoms and molecules accompanying fracture of single-crystal MgO," *J. Vac. Sci. Technol. A* **4**, 1648-1652 (1986).
13. J.T. Dickinson, L.C. Jensen, and M.R. McKay, "Neutral molecule emission from the fracture of crystalline MgO," *J. Vac. Sci. Technol. A* **5**, 1162-1168 (1987).
14. J.T. Dickinson, S.C. Langford, L.C. Jensen, G.L. McVay, J.F. Kelso, and C.G. Pantano, "Fracto-emission from fused silica and sodium silicate glasses," *J. Vac. Sci. Technol. A* **6**, 1084-1089 (1988).
15. S.C. Langford, L.C. Jensen, J.T. Dickinson, and L.R. Pederson, "Alkali emission accompanying fracture of sodium silicate glasses," *J. Mater. Res.* **6**, 1358-1368 (1991).
16. J.T. Dickinson, "Fracto-emission," in *Non-Destructive Testing of Fibre-Reinforced Plastics Composites*, edited by John Summerscales, Elsevier Applied Science, London, 1990, pp. 249-282.

17. J.T. Dickinson, L.C. Jensen, S.C. Langford, R.P. Dion, and L. Nick, "CO emission accompanying fracture of polycarbonate: evidence for molecular cleavage," manuscript in preparation.
18. J.T. Dickinson, L.C. Jensen, S.C. Langford, and R.P. Dion, "Emission of occluded volatiles accompanying the crazing of polystyrene and high impact polystyrene," manuscript in preparation.
19. J.T. Dickinson, L.C. Jensen, S.C. Langford, and R.P. Dion, "Emission of occluded volatiles during deformation of polycarbonate," submitted to J. Poly. Phys. Part B: Polym. Phys. Ed.
20. S. C. Langford, J. T. Dickinson, and L. C. Jensen, "Simultaneous Measurements of the Electron and Photon Emission Accompanying Fracture of Single Crystal MgO," J. Appl. Phys. 62, 1437-1449 (1987).
21. S. C. Langford, L. C. Jensen, Ma Zhenyi, and J. T. Dickinson, "Scanning Tunneling Microscopy Analysis of MgO Fracture Surfaces," J. Vac. Sci. Technol. A 8, 3470-3478 (1990).
22. K. Nassau, "Cubic zirconia: an update," Lapidary J. 35, 1194-1200 (1981).
23. I. W. Donald, "Review: Methods for improving the mechanical properties of oxide glasses," J. Mater. Sci. 24, 4177-4208 (1989).
24. J.I. Goldstein, D.E. Newbury, P. Echlin, D.C. Joy, C. Fiori, and E. Lifshin, *Scanning Electron Microscopy and X-Ray Microanalysis*, Plenum Press New York (1981).
25. C. Templier, H. Garem, J.P. Riviere, and J. Delafond, "Solid and fluid xenon in Xe implanted aluminum," Nucl. Instrum. Methods B 18, 24-33 (1986).

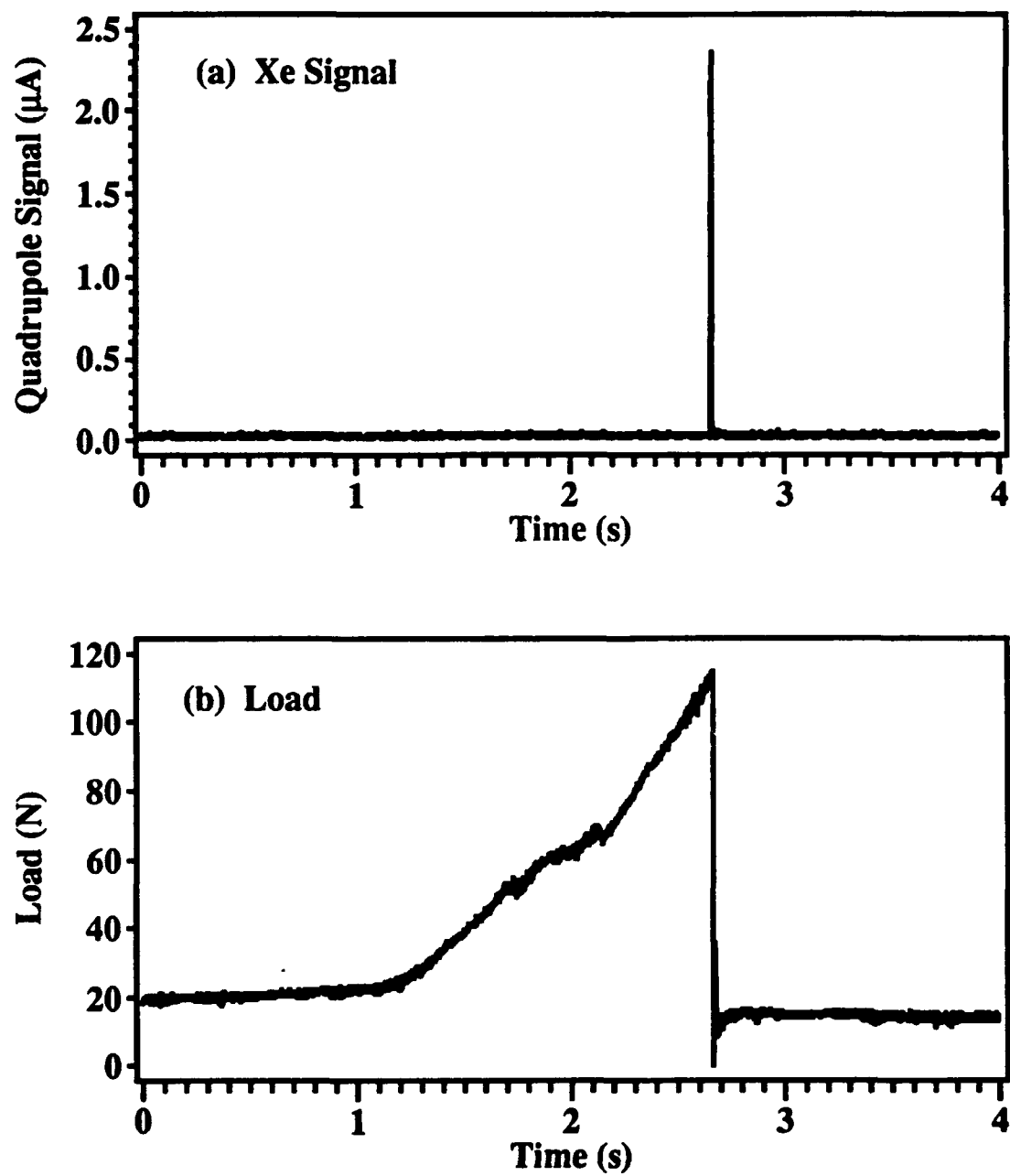


## Figure Captions

- Fig. 1.** Xenon emission and load signals from Xe-implanted zirconia. This sample showed no pre-emission of Xe during application of the load.
- Fig. 2.** Xenon emission and load signals from Xe-implanted zirconia. This sample showed pre-emission of Xe during application of the load.
- Fig. 3a.** SEM image showing part of the tensile surface, near the fracture surface, of a zirconia specimen which showed no pre-emission.
- Fig. 3b.** SEM image showing a cone crack in part of the tensile surface of a zirconia specimen adjacent to the fracture surface. This sample showed pre-emission during loading.
- Fig. 4.** SEM image showing a cone crack in part of the tensile surface of a zirconia specimen adjacent to the fracture surface. In this region the piece of zirconia bound by the crack has not been ejected. EDS analysis was performed on regions inside the crack (e.g., position A) and outside the crack (e.g., position B).
- Fig. 5.** EDS plots from regions A and B in Fig. 5.
- Fig. 6.** Enlarged region of Fig. 2, showing the Xe emission during and just after fracture. The arrow indicates the position of fracture.

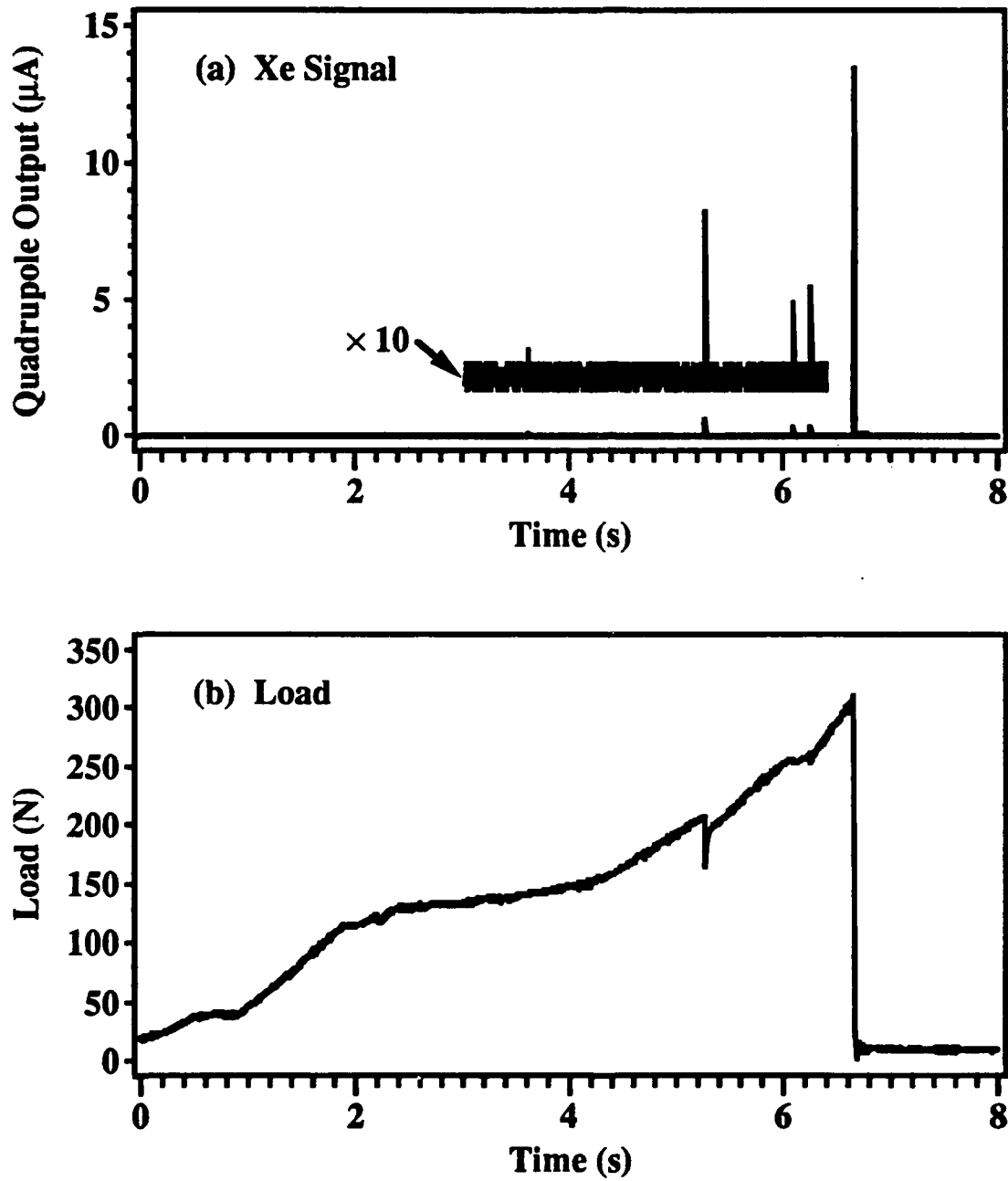
- Fig. 7.** SEM image showing the interface between the tensile and fracture surfaces for a sample which showed no pre-emission.
- Fig. 8.** Schematic representation of cone crack formation and associated Xe emission. (a) The implanted Xe forms inclusions just beneath the surface. The resulting compression near the surface is balanced by tensile stresses further in the interior. (b) These subsurface tensile stresses promote crack branching roughly parallel to the tensile surface during catastrophic failure. These crack branches apparently disrupt many Xe inclusions on either side of the nominal fracture surface, greatly increasing the intensity of the observed Xe emissions.

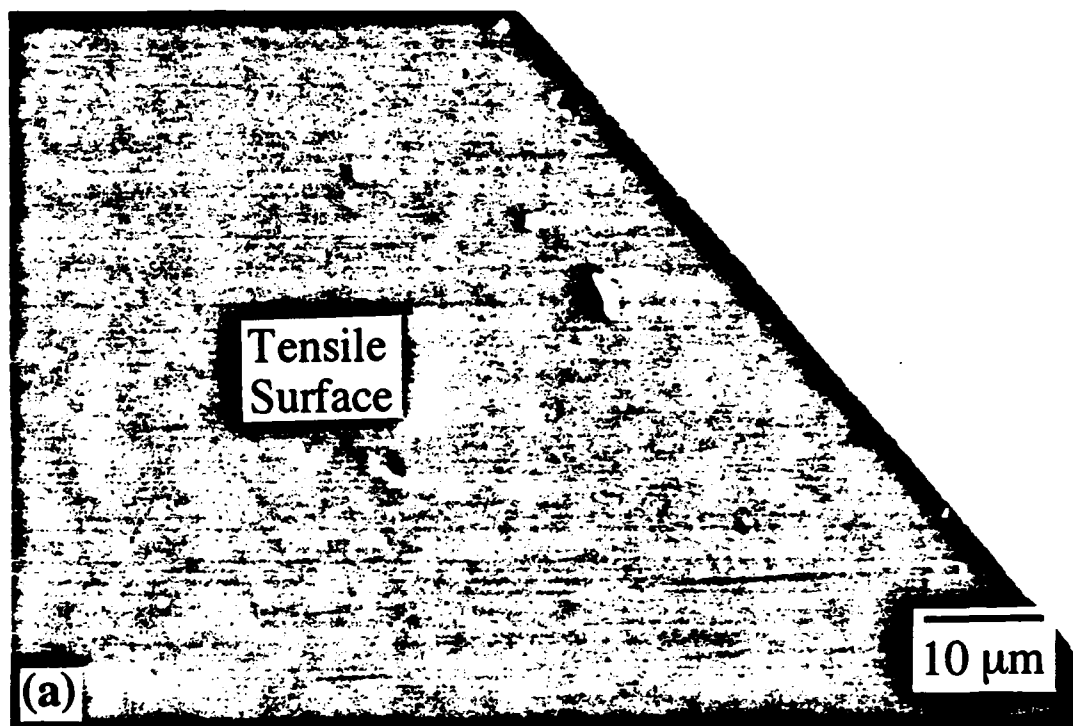
### Xe and Load Signals from Xe-Implanted Zirconia



**FIG. 1**

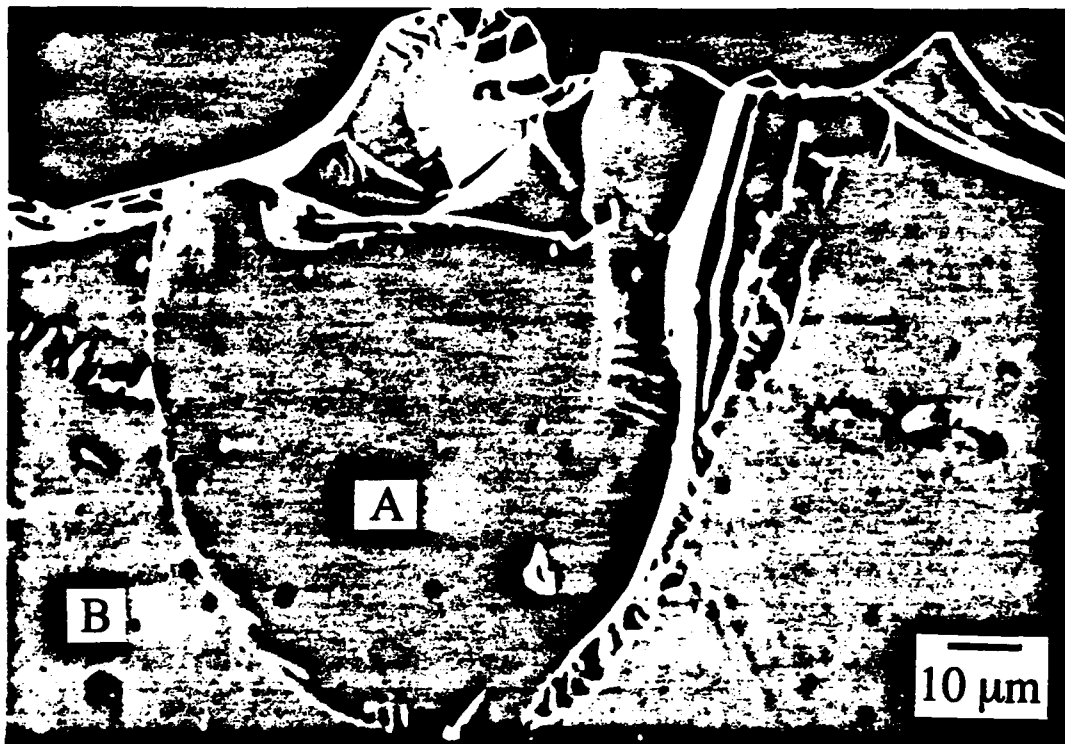
### Xe and Load Signals from Xe-Implanted Zirconia

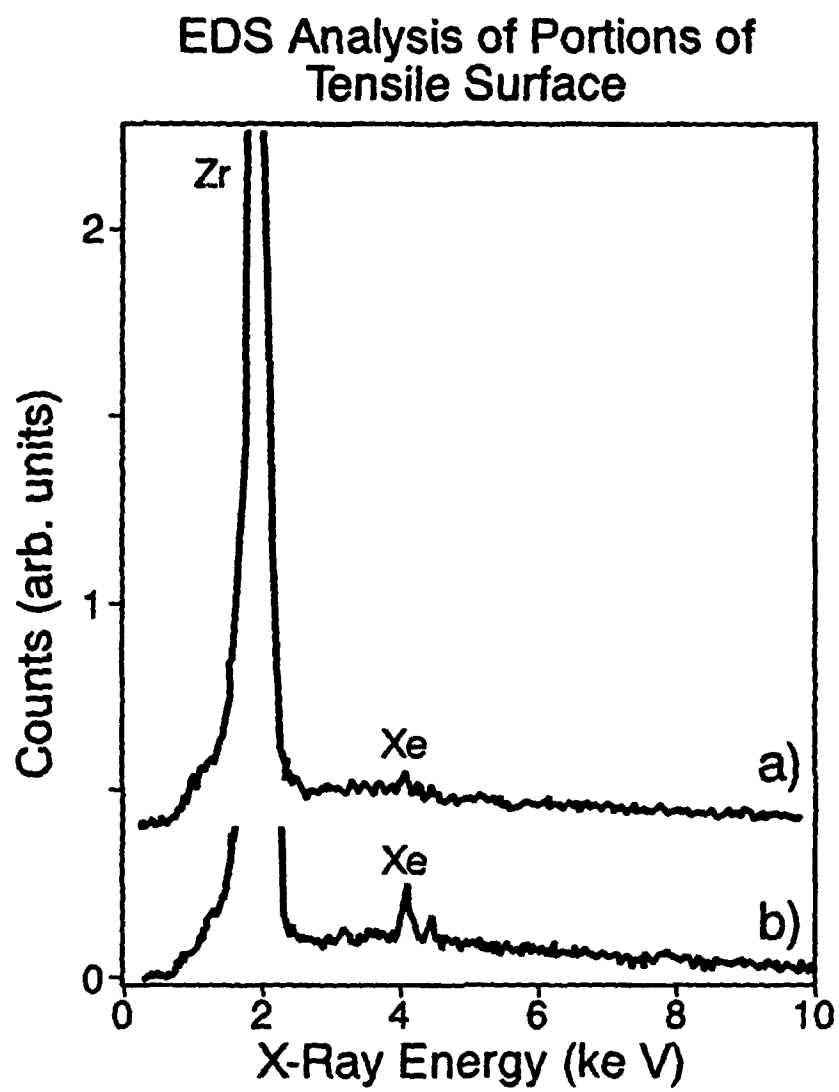
**FIG. 2**

**FIG. 3(a)**



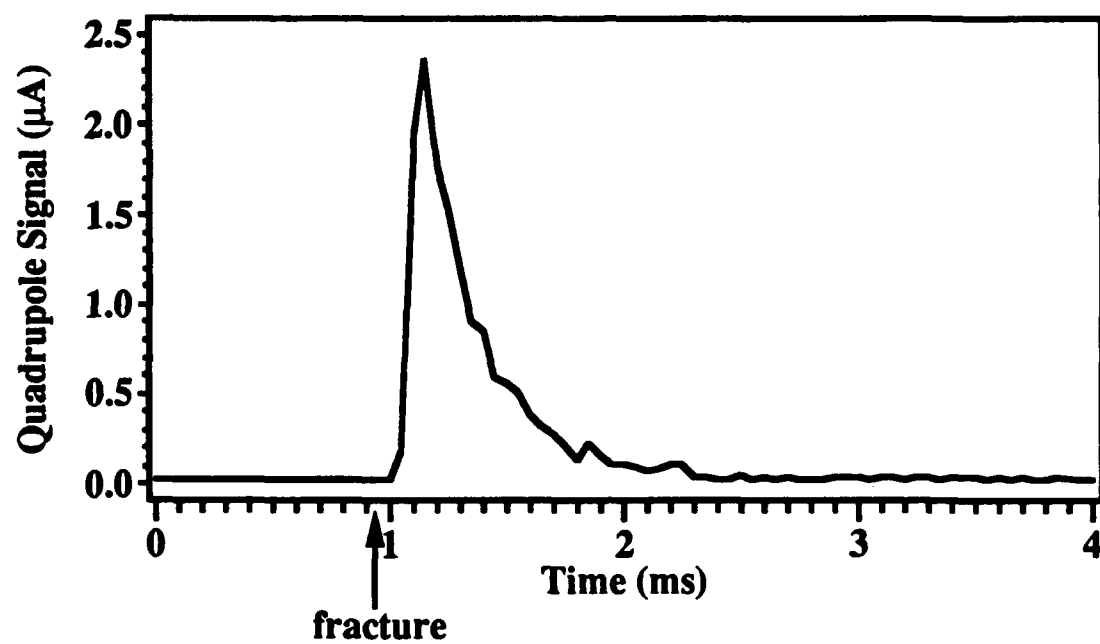
**FIG. 3(b)**

**FIG. 4**

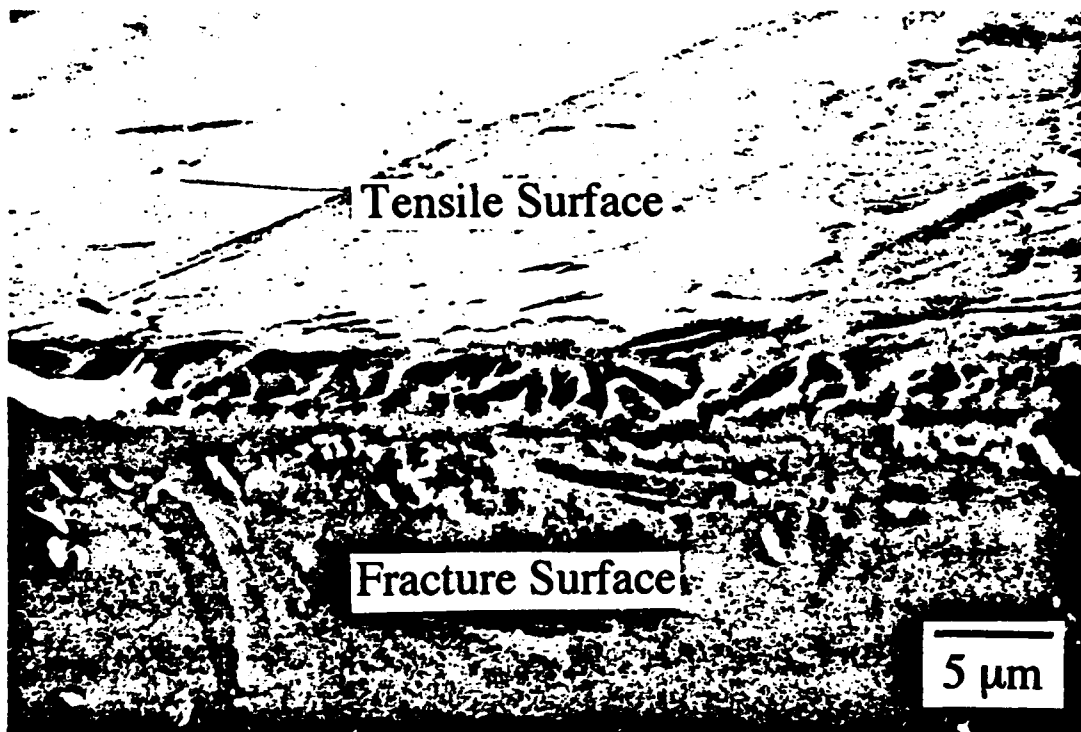
**FIG. 5**

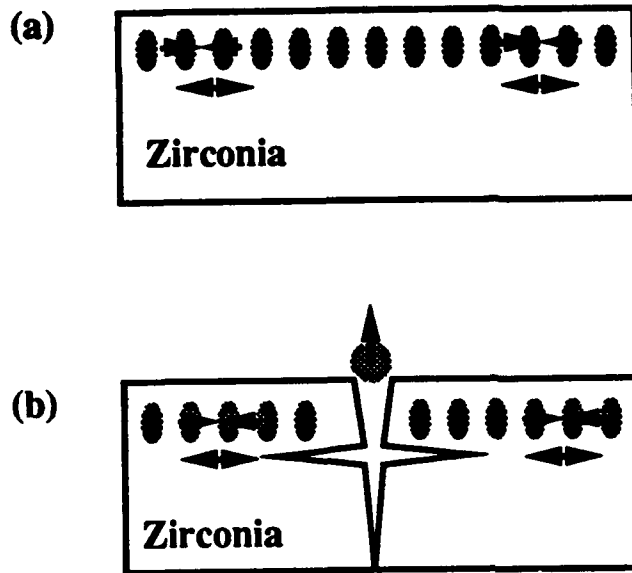


### Xe Emission from Xe-Implanted Zirconia



**FIG. 6**

**FIG. 7**

**FIG. 8**

## XI. WORK IN PROGRESS

### Emission of occluded volatiles during deformation of polycarbonate

The diffusion of volatile gasses through polymers is significantly affected by the ambient temperature and pressure, as well as the mechanical/thermal history of the polymer.<sup>1</sup> These effects are commonly attributed to changes in the size and density of small voids,<sup>2</sup> which together constitute the "free volume" of the polymer structure. In particular, the effect of pressure on the diffusion of polymers suggests that uniaxial strain will have similar effects on the diffusion process. Stress induced changes in the permeability of thin films have previously been demonstrated in polystyrene,<sup>3</sup> polyethylene, and polypropylene.<sup>4</sup> We show that the diffusion of Ar and D<sub>2</sub>O from the near-surface region of polycarbonate samples in vacuum is affected strongly by the applied uniaxial strain. Transient applications of load allow measurements to be made on time scales of a few second or less. The nearly complete reversibility of the changes in the diffusion constant in transient experiments suggests that the associated changes in free volume are also largely reversible.

Polymeric materials typically contain substantial amounts of entrained volatiles, including water, atmospheric gases, and products of incomplete polymerization.<sup>1-3</sup> Significant quantities of these volatiles can remain in the interior of reasonably thick samples even after days in vacuum conditions, as may be verified by mass spectroscopy of the volatiles diffusing to the surface of the sample and desorbing into vacuum. Any transient changes in the diffusion constant of these volatiles will make a corresponding change in the signal detected by the mass spectrometer. To enhance the signal to noise ratio of the detected signals, polycarbonate samples were "loaded" with selected volatiles whose masses are well removed from common vacuum system contaminants. Some samples were store under one atmosphere of Ar at room temperature for periods of days to weeks to provide a strong Ar signal at 40 amu. Others were

soaked in heavy water at room temperature for somewhat shorter periods to provide a strong  $D_2O$  signal at 20 amu.

**Experiment.** The polycarbonate used in this work was Calibre® 300-10 provided by The Dow Chemical Company. Dogbone shaped samples were milled from 3.2 mm injection molded sheet to produce a gauge section 1.5 cm long and  $3.2 \times 3.2 \text{ mm}^2$  in cross section. Some experiments were undertaken with larger, injection molded dogbone samples with a gauge section 6 cm long gauge and  $13 \times 3.2 \text{ mm}^2$  in cross section. Ar-loaded samples were produced by storing samples for periods ranging from 24 hours to several weeks in an Ar atmosphere. Similarly,  $D_2O$ -loaded samples were prepared by storing samples in heavy water for a few days. The diffusion constant for Ar in polycarbonate is roughly  $D_{Ar} = 1.5 \times 10^{-8} \text{ cm}^2/\text{s}$ , while that of  $D_2O$  (which we take to be similar to that of water), should be about  $D_{H_2O} \sim 6.8 \times 10^{-8} \text{ cm}^2/\text{s}$ .<sup>8</sup> The decay constant for the removal of these volatiles from 3.2 mm-thick samples should be about two days for water and eight days for Ar. This allows more than enough time for experiments. The high solubility of water in polycarbonate (about two orders of magnitude higher than that of Ar)<sup>8</sup> results in particularly strong signals from the  $D_2O$ -loaded samples, despite the relatively fast pumpout of this material.

The samples were mounted in a tensile loading apparatus in an ultrahigh vacuum system. Typical background pressures were  $10^{-6} \text{ Pa}$ . The neutral emission was monitored with a UTI 100C quadrupole mass spectrometer (QMS). The applied load was monitored with a Scaime force transducer with a 4500 N adapter. Deformation was introduced from the outside of the vacuum through a stainless steel bellows.

**Results.** A typical mass 40 signal during loading and fracture of Ar-soaked polycarbonate appears in Fig. 1. The signal rises slowly during the drawing process and peaks sharply at fracture. A long, slow decay follows. The increase is roughly linear during cold drawing, and accelerates at the onset of strain hardening. As the increase in the length of the drawn region is roughly linear during cold drawing, an enhanced diffusion of Ar from this region would account for a linear increase in the mass 40 signal. Enhanced diffusion could be due to

heating or free volume effects, although the increase in free volume in the drawn region is expected to be minimal. A transient increase in emission at the onset of yield is barely observable in this experiment, but is readily seen in emission of D<sub>2</sub>O. The weakness of the Ar signal at the onset of yield is apparently due to the depletion of this species in the near surface region under vacuum.

The comparable mass 20 signal from D<sub>2</sub>O-soaked polycarbonate appears in Fig. 2. This sample was soaked in D<sub>2</sub>O at room temperature for four days prior to mounting in vacuum. Note the different time scale employed due to the lower strain rate. The general form of the emission is the same, although several times stronger. The principle differences between the Ar and D<sub>2</sub>O signals are that the transient increase in the D<sub>2</sub>O signal at yield is relatively much stronger, and the of the D<sub>2</sub>O signal following fracture is more rapid. As noted above, the high D<sub>2</sub>O signal strength is consistent with the high solubility of water in polycarbonate ( $S_{\text{water}} > 100 \times S_{\text{Ar}}$ ).<sup>8</sup> This more than compensates for the somewhat higher diffusion constant of water in polycarbonate ( $D_{\text{water}} \sim 4 \times D_{\text{Ar}}$ ), which allows for the rapid removal of water from the near surface region during pumpout, this is more than compensated by the much higher initial concentration. Thus the D<sub>2</sub>O concentrations in the near surface region during the experiment is much higher than the Ar concentration under typical conditions, and allows for much higher signals at the onset of yield and at other points in the loading cycle.

The intense emission accompanying fracture is due to the exposure of volatile-rich material to vacuum. The relatively fast decay of the emissions accompany fracture of the D<sub>2</sub>O-loaded samples is consistent with the somewhat more rapid diffusion of D<sub>2</sub>O in polycarbonate relative to Ar. .

A typical mass 20 signal in the region of yield is displayed in greater detail in Fig. 3. The sensitivity of the quadrupole electrometer was raised in this experiment to show the structure in this region. The signal at fracture was well off scale and is not shown. The mass 20 signal rises sharply when the stress reaches about 75% of the drawing stress. Even small bumps in the load curve are reflected in the mass 20 signal. In general, the emission increases with increasing load,

but decays under constant load. The decay at constant load is evident in Fig. 4, which shows the emissions accompanying a loading/unloading cycle at stresses somewhat below the yield stress. This is consistent with a stress-induced enhancement of D<sub>2</sub>O diffusion, mitigated by the depletion of D<sub>2</sub>O in the surface layer. The peak in D<sub>2</sub>O emission is simultaneous with the peak in load to within 50  $\mu$ s, i.e., any lag between the D<sub>2</sub>O signal and changes in load is small. This response to rapid changes in load is more evident in Fig. 5, where the load was raised quickly and quickly relaxed. Note that the background signal (56 nA) in Figs. 3-5 has been subtracted to emphasize the increase during loading. The signal of Fig. 5 is analyzed in more detail below.

A similar increase in Ar emission has been observed from polystyrene samples which had been stored in an Ar atmosphere prior to loading in vacuum. Strain enhanced permeability has been observed in polystyrene,<sup>3</sup> but much of the enhancement at high pressures can be attributed to enhanced transport through crazes. In a separate work,<sup>9</sup> we have shown that a large increase in volatile emission accompanies the growth of crazes in polystyrene in vacuum. Nevertheless, small increases are observed at low loads where crazing is not likely. Thus it appears that strain enhanced diffusion is observed in this material as well.

**Discussion.** We attribute the enhanced diffusion under load to a stress-induced increase in "free-volume" or a similar effect. The principle alternative to a free volume mechanism is thermally enhanced diffusion due to plastic deformation. However, the rapid drop in emission accompanying yield appears to rule out thermal effects as the dominant factor, as yield marks the onset of rapid (if localized) plastic deformation. Free volume effects also help explain the large, nearly reversible change in emission intensities during the transient loading of Fig. 5, as well as the relatively slow decay of the Ar signal at constant load. The temperature rise and subsequent cooling (by thermal conduction) should be comparable in these two instances, but the Ar signals differ markedly. The Ar signal primarily follows changes in the load, when account is made for depletion of Ar in the near surface region.

The strong Ar signals prior to yield are also inconsistent with thermal effects. Although a certain amount of anelastic behavior is expected prior to yield, Matsuoka and Bair report that the

surface temperature actually drops slightly (about 0.5 K), reaching a minimum near the yield point.<sup>10</sup> Although they employed much lower loading rates than those of this work ( $8.6 \times 10^{-5} \text{ s}^{-1}$  vs typically  $5 \times 10^{-2} \text{ s}^{-1}$  here), this should not affect the relationship between mechanical and thermal behavior. Any change in the mechanical behavior (e.g., a higher yield stress) will be reflected in the thermal behavior (more cooling prior to yield). Thus we expect that the temperature of the polycarbonate during the peak in Ar emission prior to yield is actually somewhat below ambient. Conversely, the high stresses immediately prior to yield are associated with a peak in the free volume. At least prior to yield, free volume effects appear to dominate any thermal effects on the diffusion of Ar in the near surface region.

To quantitatively account for the observed signals, one must account for both the diffusion of gas in the strained polycarbonate and the response of the vacuum system to transient releases of volatile material. The output of the quadrupole mass spectrometer is proportional to the density of the measured species in the quadrupole ionizer. Since volatile gasses released by the sample are eventually pumped away by the vacuum pumps, the net density in the system is determined by the competition between these two processes. The rate of change of the density may be expressed as:

$$\frac{1}{V} \frac{dN}{dt} = \frac{1}{V} \dot{N}_d - \frac{1}{V} \dot{N}_p, \quad (1)$$

where  $N$  is the number of the molecules of interest in the vacuum system,  $V$  is the volume of the vacuum system,  $\dot{N}_d$  is the rate at which molecules are emitted from the sample, and  $\dot{N}_p$  is the rate at which molecules are removed from the system by pumping. To simplify the analysis, we neglect other sources of molecules, such as the walls of the vacuum system. Although Ar and  $\text{D}_2\text{O}$  are not common vacuum system contaminants, transient adsorption on the vacuum system walls will affect the results slightly.

Assuming that the rate of emission from the sample is Fickian, the flux of particles leaving the sample surface is proportion to the product of the diffusion constant  $D$  and the



concentration gradient in the near surface region,  $\nabla C$ . The total number of particles leaving the sample is just the product of this flux and the surface area of the sample,  $A$ . Therefore,

$$\dot{N}_d = D A \nabla C, \quad (2)$$

Similarly, the rate at which molecules are pumped out of the system may be estimated from the pumping speed of the vacuum pumps,  $S$ , (units of volume per unit time) for the species of interest. This rate is given by

$$\dot{N}_p = - \frac{N S}{V} \quad (3)$$

The particle density in the system as a function of time is then given by

$$\frac{1}{V} \frac{dN}{dt} = \frac{D A \nabla C}{V} - \frac{N S}{V^2}. \quad (4)$$

Equation 4 is difficult to solve in the general case. Fortunately, the difference between the two terms on the right hand side is generally much smaller than the magnitude of either term. In this case, the particle density is well approximated by equating  $\dot{N}_d$  and  $\dot{N}_p$  and solving for  $N/V$ .

$$\frac{N}{V} = \frac{D A \nabla C}{S}. \quad (5)$$

This approximation will be valid as long as the rate of change in the measured particle density is much smaller than the rate at which particles are removed from the vacuum system, i.e.,

$$\frac{1}{V} \frac{dN}{dt} \ll \frac{N S}{V^2} \quad \text{or} \quad \frac{1}{N} \frac{dN}{dt} \ll \frac{S}{V} \quad (6)$$

The quantity  $S/V$  is characteristic of the vacuum system and the species of interest. The pumping speed of our system is typically in excess of 4000 l/s for Ar and  $D_2O$ , and the system volume is about 40 l, so that  $S/V > 100$ . As long as the fractional change in the particle density per second is much less than 100, the approximation leading to Eq. 5. is valid. In the work above, the fractional change in particle density per unit time was seldom more than  $1 \text{ s}^{-1}$ , so this condition is well satisfied.

The dependence of the diffusion constant,  $D$ , on the unknown concentration gradient,  $\nabla C$ , does not allow for an absolute measurement of  $D$  from Eq. 5. However, transient increases in  $D$  will have only small effects on  $\nabla C$ , so that to first order  $\nabla C$  will remain constant during a particular transient strain event. Thus the fractional change in the measured signal (proportional to  $N$ ) will be approximately equal to the fractional changes in  $D$  during the experiment. Since  $\nabla C$  can only decrease under these circumstances, which reduces the rate of emission, failing to account for changes in  $\Delta C$  lead to underestimates of the change in  $D$ . The other principle source of error is the contribution of gas desorbed from the walls of the vacuum system, which also leads to underestimates of the fractional change in  $D$  by lowering the fractional change in the measured signal. Thus the fractional change in  $D$  as estimated from the quadrupole signal is strictly a lower bound. Since the increase in the measured signal can be as high as the measured background, it appears that physically realizable stresses can increase  $D$  by at least a factor of two.

The dependence of the diffusion constant on the free volume may be rather simply modeled in terms of a Doolittle relation,

$$D = A \exp(-\gamma v^* / v_f) \quad , \quad (7)$$

where  $A$  and  $\gamma$  are constants,  $v^*$  is the minimum void size for molecular diffusion, and  $v_f$  is the average volume of the voids making up the free volume. In the treatment of Cohen and

Turnbull,<sup>2</sup> the voids involved in the diffusion process are created by the cooperative motion of polymer segments. They interpret  $\gamma$  as accounting for the void overlap, so that  $0.5 > \gamma > 1$ . The change in the  $D$  with changing free volume may then be expressed as

$$\frac{D_1}{D_0} = \exp\left(-\gamma v^* \left(\frac{1}{v_{f1}} - \frac{1}{v_{f0}}\right)\right) = \exp\left(-\frac{\gamma v^*}{v_{f0}} \left(1 - \frac{v_{f0}}{v_{f1}}\right)\right), \quad (8)$$

where  $v_{f0}$  and  $v_{f1}$  are the initial and final average void size, respectively. Assuming that the number of "holes" is constant during straining, the average hole size proportional to the sum of the volumes of all the holes,  $V_f$ . Then writing  $V_{f1} = V_{f0} + \delta V$ , Eq. 8 becomes

$$\begin{aligned} \frac{D_1}{D_0} &= \exp\left(-\frac{\gamma v^*}{v_{f0}} \left(\frac{\delta V}{V_{f0} + \delta V}\right)\right) \\ &= \exp\left(-\frac{\gamma v^*}{v_{f0}} \left(\frac{\delta V/V_0}{V_{f0}/V_0 + \delta V/V_0}\right)\right) \end{aligned} \quad (9)$$

where  $V_0$  is the initial volume of the sample.

The change in total free volume under uniaxial strain,  $\delta V$ , is equal to the volume change of the sample. In the limit of small strains,  $\delta V/V_0 = (1 - 2\mu)\epsilon$ , where  $\mu$  is Poisson's ration ( $\sim 0.4$  for this material) and  $\epsilon$  is the strain. Thus  $\delta V$  is readily computed from experimental measurements of stress or strain. Similarly, Eq. 5 indicates that the ratio between  $D_1$  and  $D_0$  equals the ratio of the mass spectrometer outputs, denoted  $I_1$  and  $I_0$ , respectively. These experimentally determined quantities allow us to compute the value of  $\gamma v^*/v_{f0}$ , Cohen and Turnbull take as an indication of the minimum number of polymer segments involved the cooperative motion responsible for diffusion. This quantity can be estimated from the data of Fig. 5. Near the emission peak,  $\epsilon \sim 0.030$ , so that  $\delta V \sim 6 \times 10^{-3}$ ; comparing the Ar signal at the peak with that prior to loading,  $D_1/D_0 = I_1/I_0 \sim 1.9$ . We assume that  $V_{f0}/V_0$  is about 0.025 on

the basis of experimental measurements on other material.<sup>10</sup> Substituting these values into Eq. 9 and solving for  $\gamma v^*/v_{f0}$  yields a value of 3.3. Thus it appears that at the cooperative motion of at least three or four polymer segments is required for the diffusion of D<sub>2</sub>O in this material. This is a small number relative to most other polymers, where  $\gamma v^*/v_{f0}$  is more typically between 7 and 30. However, polycarbonate is an unusual polymer being composed of unusually long, stiff segments. Small displacements of long segments readily generate large voids. However, most measurements of  $\gamma v^*/v_{f0}$  are based on permeability measurements as a function of pressure and temperature, which may probe a different set of molecular degrees of freedom. This would also help explain the apparently low value of  $\gamma v^*/v_{f0}$  in this work.

If  $v_{f0}$  is known,  $\gamma v^*$  may also be estimated. Cohen and Turnbull take  $\gamma v^*$  at a given temperature as a property of the diffusing molecule. The average void size,  $v_{f0}$ , can often be estimated on the basis of positron annihilation studies. Estimates of the void size in another commercial polycarbonate yielded  $v_f \approx 45 \text{ \AA}^3$ ,<sup>11</sup> which implies that  $\gamma v^*$  is on the order of 150  $\text{\AA}^3$ .

**Conclusion.** Measurements of Ar emission accompanying the loading of polycarbonate suggest that the diffusion of Ar is strongly enhanced under load. We attribute this enhancement to the increase in free volume which accompanies the increasing strain under load. Interpreting these results by the method of Cohen and Turnbull, we find unusually low values of  $\gamma v^*/v_{f0} \approx 3.3$  for diffusion in this material. Apparently, a relatively small number of polymer segments are involved in the molecular motion responsible for the enhancement of diffusion under load. This is consistent with the long, stiff segments which make up the backbone of the polycarbonate chain, although other factors may well be involved. Measurements of this sort may help elucidate the nature of voids in the polycarbonate and their response to changes in stress. Void growth under stress has important implications in the diffusion of gasses. Diffusion under low concentration gradients, such as those probed here, have important implication in the packaging of high-value fruits and vegetables, for instance. In addition, the growth of similar voids under load may help facilitate the molecular motions responsible for the onset of yield. Unfortunately,

relaxation effects often obscure the more elastic response responsible for the increasing free volume under load. The more elastic processes can in principle be temporally isolated from many relaxation processes by studying transient effects whose times scales are shorter than the appropriate relaxation time. Measurements of transient changes in the diffusion constant have considerable potential in this regard.

### **Emission of occluded volatiles during the fracture of polystyrene and their relation to the temperature of the fracture surface**

The fracture energy in polymeric materials is generally dominated by dissipative processes which ultimately raise the temperature of the fracture surface. This heating is also expected to substantially alter the material properties at the crack tip. Thus the temperature at the crack tip is an important parameter in models of dynamic crack growth in polymers, as well as an important test of them. Due to the fast times scales and the small amount of material involved, measurements of the temperature rise at fracture are necessarily indirect. The most common probe of crack tip temperature is the spectral distribution of the black body radiation.<sup>12-14</sup> Although the time response of this technique is excellent, it has the disadvantage of reflecting the average temperature over a rather thick surface layer of material along the fracture surface. Greater surface sensitivity is possible (with some loss of time resolution) by monitoring the velocity distribution of molecules desorbed from the surface after fracture.

We have developed a technique which allows the determination of the velocity distribution of volatile species emitted from the fracture surface immediately after fracture. These species include atmospheric gasses, impurities and additives, and products of incomplete polymerization. When fracture is performed in vacuum, the more volatile species are readily desorbed and monitored by quadrupole or time-of-flight mass spectrometry.<sup>15-17</sup> At fracture, the emission intensity spikes sharply and decays slowly. Rapidly changing emissions of this sort can often be analyzed to yield gas temperatures, assuming that the molecular velocities are described

by a Maxwell-Boltzmann distribution and that the rate of emission at the sample can be described by a simple "source function." The reliability of these analyses can be dramatically improved by utilizing simultaneous emission measurements at two different distances from the sample. This can be done by mounting two quadrupole mass filters at different distances from the sample, as shown in Fig. 1. In the early stages of emission, these signals are relatively free of interference from molecules "reflected" off the surface of the vacuum system and are readily analyzed numerically to yield the effective temperature of the surface.

**Experiment.** Compression molded bars of polystyrene, Styron 680®, were supplied by the Dow Chemical Company. Rectangular bars  $12 \times 6.3 \times 2 \text{ mm}^2$  were machined from this material and their tensile faces polished with rouge. These samples were used in the ethyl benzene measurements. Better signal to noise ratios could be obtained by using somewhat thicker samples and "loading" them with a noble gas. The relatively high solubility and diffusivity of most gasses in polystyrene allows for rather intense emissions at fracture. The thicker samples ( $12 \times 6.3 \times 3 \text{ mm}^2$ ) were cut from compression molded bars and not otherwise machined; the tensile and compressive faces of these samples were compression molded and required no polishing. The thicker samples were then loaded with Ar by storing them in Ar at atmospheric pressure for three days. The samples were then loaded into a carousel-style sample holder and mounted in a vacuum system and pumped overnight. Base pressures during testing were typically less than  $3 \times 10^{-5} \text{ Pa}$ .

The emission of volatile species accompanying fracture were made with a pair of UTI 100C quadrupole mass spectrometers mounted as shown in Fig. 6. Emissions originating from the samples passed first through Quadrupole 1, then through Quadrupole 2. In this work, the ionizers of the two quadrupoles were mounted 3 cm and 9 cm from the sample, respectively. To prevent fastest emissions from reaching the ionizers by round-about routes, each quadrupole ionizer was provided with a stainless steel shield with an aperture aligned with the sample. Samples were rotated into position for testing in the sample carousel, then loaded from behind

across a support span of 6.3 mm. The time of fracture was determined to within 20  $\mu$ s from simultaneous load measurements.

In this work, the emission rate was modeled with a source function,  $S(t)$ , of the form

$$S(t') = A (t' - t_0)^{-m} \exp\left(\frac{-\beta}{(t' - t_0)^2}\right), \quad (10)$$

where  $A$ ,  $\beta$ ,  $m$ , and  $t_0$  are adjustable parameters. This source function readily describes many peaked emissions with slow decays, and described most of our signals well. The Maxwell-Boltzmann distribution relates the source function to the observed signal,  $I(t)$ , by the relation,

$$I(t) = \sum_{t'=0}^t \frac{S(t') d^4}{T^{3/2} (t - t')^4} \exp\left(\frac{-m d^2}{2kT (t - t')^2}\right), \quad (11)$$

where  $d$  is the distance from the sample to the detector,  $T$  is the effective temperature of the emitted gas,  $m$  is the mass of the emitted molecule, and  $k$  is Boltzmann's constant. To minimize the effect of the accumulation of gas in the vacuum system on the analysis, only the leading edges of the observed signals were employed in the numerical analysis.

The model parameters were chosen to minimize the mean square deviation from the data using the simplex<sup>18</sup> and Marquardt<sup>19</sup> algorithms. The uncertainty reported in the computed coefficients is the linear "support plane limits" at the 60% level of significance.<sup>20</sup> These uncertainties assume a "worst case" correlation among the coefficients, which is seldom realized. Caution is required in their interpretation, however, in that the strong nonlinearities in the model can invalidate linear support plane limits as a reasonable error estimate in some situations.

**Results and Discussion.** Typical intensity measurements at mass 106 (ethyl benzene) are shown in Fig. 7(a). The emission has been plotted with the time of fracture as determined by load measurements at time  $t = 0$ . The rise in emission occurs quite near time  $t = 0$ , and continues

to rise for about 100  $\mu$ s. The duration of the rise is quite comparable to what one would expect for the newly formed crack to open significantly. The slow decay corresponds to the depletion of volatile material along the fracture surface. The relative amplitudes of the signals from the near and far quadrupoles were also scaled to allow both signals to contribute equally to the fitting process. Figure 7(b) shows the portion of the data used in the numerical analysis, along with model fit to the emissions. The computed source function (normalized to a convenient peak amplitude) is also shown as a dashed line. The temperature resulting from the least squares fit to the data is  $693 \pm 102$  K. The cited uncertainty represents the "support plane limits" of the curve fitting process, which, as noted above, is generally a conservative error estimate.

Similar measurements were also made at mass 40 (Ar). Occasionally the emissions from a particular fracture event appeared to yield unusually high temperatures. One of these data sets are shown in Fig. 8(a). The temperature estimated from the least squares fit was  $1060 \pm 400$  K. The unphysical nature of this analysis is evident in the source function, which does not rise significantly until 60  $\mu$ s after fracture. (The experimental error in the determination of the time of fracture is not more than 20  $\mu$ s.) In this case the model does not adequately describe the emission process.

Two samples yielded unusually high temperatures. In each case, the emissions displayed a slowly rising mass signal several tens of ms prior to fracture. Post-fracture examination of both samples revealed unusually large crazes along the fracture surface. We have recently shown that substantial emission accompanies crazing (prior to fracture) in polystyrene.<sup>21</sup> The curve fitting procedure attempts to account for this slowly rising component by making the source function rise slowly, and compensating for the delayed emission by raising the gas temperature, which reduces the time required (in the model) for the gas to travel from the sample to the detector. Presumably this situation could be remedied by finding a more flexible model for the source function.

The results of a similar analysis of seven data sets appears in Table I, along with the weighted average temperature estimate for mass 40 and mass 106 emission. The two anomalous



data sets have been excluded from the averages on the basis of the unphysical nature of their source functions; however, the computed uncertainties also leave little doubt that the anomalous data sets and the more well-behaved data sets are not members of the same population. The average temperature of the mass 40 emissions is  $481 \pm 38$  K, while the average temperature of the mass 106 emissions is  $623 \pm 98$  K. Although the difference is barely significant at the 60% level, the conservative nature of the support plane limits suggests that the difference is real. The thinner samples used in the mass 106 measurements (2 mm vs 3 mm) displayed somewhat rougher fracture surfaces; since rougher surfaces are associated with greater energy dissipation, an increased surface temperature in these fracture events is reasonable.

Table I. Temperature estimates of volatile emissions accompanying the fracture of polystyrene.

<u>Mass 40</u>			<u>Mass 106</u>		
Run #	T	$\sigma_T$	Run #	T	$\sigma_T$
*505	1060	470	515	693	102
518	503	48	*516	1177	310
520	443	47	517	563	95
<u>521</u>	<u>523</u>	<u>77</u>	<u>.....</u>		
Averages:	481	38		650	83

\*Excluded from average.

These analyses agree that the gas temperature is well above ambient, as expected on the basis of the heat generated by fracture. Fuller, Fox, and Field used an infrared detector to estimate the temperature rise the heated zone at a crack tip in polystyrene, inferring a temperature change on the order of 375 K determined about 10  $\mu$ s after the passage of the crack.<sup>1</sup> This agrees well with the temperature of the mass 106 emissions ( $\Delta T \sim 350$  K), but is somewhat higher than that of the mass 40 emissions. These different techniques probe somewhat different volumes of material and different time scales, so that some difference would be expected even if the

uncertainties involved were smaller. In all cases, the temperature estimate is well above the glass temperature of the polystyrene employed in this work (381 K), confirming that the mechanical properties at the crack tip contrast markedly with the properties of the bulk (room temperature) material.

The temperature estimates provided by this analysis are quite stable against small changes in the other model parameters. This is not true of the other model parameters, with the exception of  $t_0$  in Eq. 1. Small changes in  $A$ ,  $b$ , or  $m$  in Eq. 1 could be largely compensated by changing the other parameters. These leads to considerable uncertainty in the highly correlated parameters. The development of more tractable models would remedy this difficulty to a large degree. However, this would not necessarily improve the temperature estimate unless the model were also more physically representative of the emission process. The relatively stable behavior of temperature as a variable suggests that significant reliabilities have been attained.

**Conclusion.** We have reported temperature estimates of polystyrene fracture surfaces based on the temperature of volatile products emitted from the fracture surface. These estimates are broadly consistent with previous estimates made on the basis of infrared radiation emitted during fracture. Although improved signal-to-noise ratios can be obtained with deliberately introduced volatiles, the concentration of naturally occurring volatiles yields adequate signal intensities for the analysis. On physical grounds, this technique is expected to have excellent surface sensitivity. Although the present analysis yields only a time-averaged temperature of emissions over the first 100  $\mu$ s or so, the time resolution could be improved by incorporating temperature dependence into the source function. The high temperature of the fracture surface implies that the mechanical properties at the crack tip contrast markedly with their bulk values. A detailed understanding of the processes leading to these elevated temperatures will be required before a detailed understanding of dynamic crack growth in polymers can be achieved.

## **Electrical signals accompanying interfacial failure of metal-oxide structures**

Recent work has shown that electrical currents are produced during the interfacial failure epoxy-metal interfaces; these signals, in conjunction with previously observed electron and photon emissions, can provide useful indicators of the progress of interfacial failure.<sup>22,23</sup> In this work, we are applying similar techniques to metal-oxide-semiconductor and metal-oxide structures, which are much more readily characterized, and which have been the focus of previous studies of photon and electron emission during failure.<sup>24-26</sup> In particular, the sensitivity of the current signals allows for the detection of relatively early stages of crack growth.

**Experiment.** Metal-oxide-semiconductor structures were prepared from 10-20  $\Omega$ -cm boron-doped Si(111) wafers supplied by S.E.H. America Incorporated. A Si wafer was cleaved into sections about 1 cm<sup>2</sup> in area, etched in an HF solution, and rinsed in distilled water. They were subsequently oxidized in flowing O<sub>2</sub> at 1000 °C for two to three hours. Observation of the color of the deposited films was consistent with oxide thickness of 80-120 nm. Upon cooling, a gold film about 100 nm thick was deposited by evaporation from an alumina boat in a vacuum system maintained at a pressure of  $1 \times 10^{-5}$  Pa. The thickness of the gold layer was monitored with a quartz microbalance mounted adjacent to the samples.

Experiments were carried out with a range of oxide thicknesses. To study the effect of very thick oxides, experiments were also carried out on gold-coated fused silica plates. A conducting sheet or grid behind the plate provided a convenient reference ground for the current measurements.

Peeling was carried out by applying a drop of 5-Minute Epoxy to the gold-coated surface. The load was applied to a small nail embedded in the epoxy. The epoxy drop was often covered by a second coating of gold using a standard sputter coater. This provided a convenient electrical connection from between the gold beneath the epoxy drop and the nail, and also electrically isolated the interior of the epoxy drop from the measurement apparatus. This electrical isolation

ensured that electrical signals originating from epoxy-nail failure within the drop did not affect the current measurements.

The sample was then mounted in a vacuum system. The nail was connected to a steel cable through which the load was applied. A diagram of the peel experiment appears in Fig. 9. The peel experiment was carried out at pressures of about  $1 \times 10^{-4}$  Pa. The cable was electrically isolated from the vacuum system, allowing the current from the detached gold to be monitored by a separate electrical connection to the cable. In most experiments, the current from the undetached gold remaining on the Si wafer was also measured. Comparison between the two signals allowed the completion of the peel event to be identified with considerable precision.

Photon emission (phE) and electron emission (EE) were detected by an EMI Gencom 9924QB photomultiplier and a Galileo Electroptics Model 4821 Channeltron electron multiplier, respectively, mounted about 1 cm on either side of the sample. After suitable amplification, the phE and EE signals were digitized continuously at 5 ns intervals with LeCroy waveform digitizers. The current was also continuously digitized at 1  $\mu$ s intervals with a third waveform digitizer. The digitizers were stopped upon detection of the current accompanying the peel event.

Pb/Sn solder provided a convenient alternative to the epoxy drop, as it provided both adequate mechanical and electrical connections to a copper wire. Although these samples were coated with gold prior to the application of the solder, the metal phase in the metal-oxide structure was actually the Pb-Sn solder, which dissolved the intervening gold layer. This was evident in the steel gray color of the detached solder, and is consistent with the low temperature of the Au-Pb-Sn eutectic (well below the melting point of the solder). Application of the solder to an evaporated gold layer resulted in relatively good adhesion of the solder to the oxide layer, which difficult to obtain when solder is directly applied to the oxide surface. Due to the ability of the Pb-Sn structure to undergo large plastic deformations, failure in these samples required much longer times. This demonstrated the usefulness of current measurements in the study of slower detachment processes.

**Results.** Typical pH<sub>E</sub>, EE, and current signals accompanying the failure of an metal-oxide structure with a 120 nm oxide layer appear in Fig. 10. The current during fracture itself is negative, consistent with the relative work function of polycrystalline Au (~5.1 eV) and p-Si(111) (~4.6 eV).<sup>27</sup> As discussed below, negative charge must flow from the low work function material to the high work function material (from the Si to the Au) during metal deposition to equalize the chemical potential (Fermi energy) of electrons on either side of the interface. During fracture, electrons flow in the reverse direction (from the Au to the Si) in order to maintain this equality as the surfaces separate. The high electrical resistance of the oxide film ensures that much of the current during interfacial failure flows through the current measuring apparatus and not through the oxide itself. Thus a negative current is measured from the Au film.

The current signal displays several characteristic features. Ultimate failure is marked by the intense EE and pH<sub>E</sub> emissions at  $t = 100 \mu\text{s}$  in Fig. 10. A weak, growing current signal is typically observed some tens of  $\mu\text{s}$  prior to the onset of EE. Interestingly, a very small pH<sub>E</sub> burst coincides with the onset of detected current. Visual observation of the detached gold showed a depression near the center of the epoxy drop, immediately above the head of the embedded nail. This depression appears to be the origin of interfacial failure, with subsequent crack growth spiraling away from the center to the circumference of the drop. In these initial stages of failure, the crack is completely surrounded by intact interface, preventing the detection of EE from the growing crack. Since the epoxy drop is coated with gold, light transmission to the photomultiplier tube from the early stages of crack growth is also severely hindered; however, the gold layer on the epoxy is not entirely opaque, and would allow a small fraction of the emitted pH<sub>E</sub> to reach the detector. Nevertheless, the current signal during this period is readily detected.

The onset of detectable EE, about 50  $\mu\text{s}$  prior to ultimate failure, marks the time at which the interfacial crack first communicates with the outside world. At this point, the (negative) current increases dramatically to high values. After passing through a sharp maximum, it drops

dramatically, indicating that crack growth has slowed considerably, if not arrested. (The finite RC time constant of the load resistor-MOS structure combination limits the rate at which the current can fall.) A second "spurt" of crack growth is indicated by the shoulder in the current signal, which coincides with a burst in the EE emission. A third and final burst of crack growth is indicated by a subsequent negative current burst about 10  $\mu\text{s}$  prior to ultimate failure, (ultimate failure being marked by the intense EE and pH<sub>E</sub> emissions at  $t = 100 \mu\text{s}$  in Fig. 10).

At the completion of failure, the current signal persists for some hundreds of  $\mu\text{s}$ . We attribute this decay to the RC time constant of the detached gold-load resistor system. As noted below, the MOS structure is wired in parallel with the load resistor. Since the resistance of the MOS structure (about 52 k $\Omega$ ) is much less than that of the load resistor (1 M $\Omega$ ), the effective resistance of the circuit drops dramatically (52 k $\Omega \rightarrow 1 \text{ M}\Omega$ ) as the epoxy drop is detached from the MOS structure. This increases the RC time constant of the current measurements by about a factor of 20, which is roughly consistent with the change in decay kinetics accompanying detachment. After failure, step-like changes are occasionally observed in the current signal current, which we attribute to due to electrical breakdown and/or chance contact with surrounding surfaces.

Current measurements were also made from the undetached gold by attaching a wire to the corner of the gold-coated silicon wafer. Simultaneous current measurements accompanying the peel event of Fig. 10 are shown in Fig. 11. Although the simultaneous measurements yielded little additional information in this case, the close correspondence of these currents prior to ultimate failure ( $t = 100 \mu\text{s}$ ) indicates that the current from the undetached gold is a useful probe of the progress of peel. This is valuable in situations in which an adequate conducting path to the detached material cannot be maintained (or is not desired). (See below.)

In Fig. 11, the current from the undetached and detached portions of gold begins to diverge significantly at the first dotted line on the left (at  $t = 74 \mu\text{s}$ ), which corresponds closely to the second burst of crack growth as indicated by the EE above. This suggests that the second burst of crack growth left only a thin gold "wire" connecting the detached and detached gold.

The final burst of crack growth apparently broke the electrical connection between the detached and undetached gold completely. At the dotted line on the right, well after ultimate failure, both currents show a step-like change and afterward track each other closely, indicating that the two Au surfaces are again in contact. It was not uncommon for the epoxy drop to brush against the MOS structure as swung from the steel cable used to load the sample.

Although the pH<sub>E</sub> and EE signals are generally weaker and more erratic than the current signals, they can be quite sensitive to the rate of crack growth.<sup>28</sup> Thus pH<sub>E</sub> and EE can often be significant during transient, rapid crack growth involving very small areas. (Conversely, these signals can be quite weak during slow crack growth.) The small pH<sub>E</sub> burst coincident with the onset of weak current at  $t = 47 \mu\text{s}$  may well be due to transient, rapid crack growth at the fracture-initiating defect. A pH<sub>E</sub> burst at this point was observed several times, suggesting that the initial crack velocity was quite high despite the very small area involved. Presumably, the stress relief associated with the rapid phase of crack growth did not allow crack growth to continue at this high velocity, accounting for the drop in pH<sub>E</sub>.

Practical metal-glass composites often involve much larger oxide thicknesses. Thus current measurements were also made on fused silica plates approximately 1 mm thick. A grounded tungsten net against the back side of the plate (opposite the gold) served as a ground reference. In these geometries, the total current generated by the peel event was significantly less than that in the MOS geometry due to the decreased capacitance of the metal-oxide structure. However, in the MOS geometry, much of the current generated by peel is shunted across the relatively small resistance of the oxide layer (typically 50-60 k $\Omega$ , much less than the 1 M $\Omega$  input resistance of the digitizer). The high resistance of the fused silica plate (many M $\Omega$ ) reduced the shunted current to negligible values. Thus peel from the gold-coated fused silica samples also yielded readily measured currents.

The current measured during the removal of a Pb/Sn solder drop from a fused silica surface is shown in Fig. 12. The sign of the detected current in this case is positive, which is consistent with a low work function for the Pb/Sn solder relative to that of the W grid which

served as a reference ground. ( $\Phi_{\text{Pb}} \approx 4.2 \text{ eV}$ ;  $\Phi_{\text{Sn}} \approx 4.4 \text{ eV}$ ;  $\Phi_{\text{W}} \approx 4.4 \text{ eV}$ ). The work function difference is probably much greater than that of the component elements due to contamination of the melted solder during application to the gold surface. (Positive currents were also occasionally during the peel of "dirty" gold films sputter deposited at a pressure of 6 Pa. We attribute this positive current to a drop in the gold work function due to contamination. Gold deposited by evaporation at  $1 \times 10^{-5} \text{ Pa}$  consistently yielded negative currents during peel.)

Figure 12(a) shows an expanded view of the current from the Pb/Sn drop early in the stages of peeling. Simultaneous phE measurements show extremely intense phE bursts accompanying these current spikes, suggesting that they are produced by electrical breakdown events.

The dependence of the sign of the current upon the contact potential difference of the failed interface can occasionally be exploited to indicate the locus of failure in more complex composite systems. For instance, interfacial failure at the steel-epoxy interface inside the epoxy drop almost always preceded the failure of strong Au-oxide interfaces. When the epoxy drop is coated with Au, current signals from the steel-epoxy failure are not observed. However, positive currents are readily observed during epoxy-steel failure when the epoxy is not provided with a conductive coating.

**Discussion.** Under equilibrium conditions prior to peeling, the potential difference across the oxide is equal to the difference between the work function of the metal layer and the silicon substrate. The MOS structure can be reasonably modeled by the circuit shown in Fig. 13, which accounts for the capacitance of the MOS structure,  $C_{ox}$ , and the leakage resistance of the oxide layer,  $R_{ox}$ , as well as the potential difference between the metal and semiconducting phases,  $\Delta\phi$ . The contact potential difference is represented by a battery in series with the  $R_{ox}$  and in parallel with  $C_{ox}$ . The contact potential differences along the rest of the circuit are represented by an equal and opposite potential difference in series with the MOS structure, shown as another battery in series with the MOS structure. The potential difference  $\Delta\phi$  is associated with a charge  $Q = \Delta\phi C_{ox}$ .



During failure, the increasing separation between the metal and semiconductor surfaces decreases the capacitance of the MOS structure and reduces the charge required to maintain the potential difference  $\Delta\phi$ . Given an conducting path to ground, this results in a detectable current. In the absence of a conducting path, detached portions of gold can attain very high potentials as they are pulled away from the charged oxide surface, resulting in electrical breakdown at inhomogeneities (e.g., sharp edges) in the peeled surface.

The detected current is quite sensitive to failure along the metal-oxide interface, as indicated by the early onset of current flow in Figs. 10 and 12. Although the relation between the detected current and rate of crack growth is not simple, over short time scales the current is simply related to the total area of the fracture surface. On time scales significantly shorter than the time constant of the MOS structure ( $\tau = R_{ox} C_{ox}$ , typically  $\approx 200 \mu s$  in the MOS structures) the charge on the capacitor  $C_{ox}$  can be treated as constant, so that the potential change associated with a change in  $C_{ox}$  [ $\Delta V = \Delta(Q/C_{ox}) \approx -Q \Delta C/C_{ox}^2$ ] will appear across  $R_L$ . This resulting current is

$$i_L = \frac{\Delta V}{R_L} = \frac{Q \Delta C}{R_L C_{ox}^2} = \frac{\Delta\phi \Delta C}{R_L C_{ox}} \quad , \quad (12)$$

where use has been made of the relation  $Q = \Delta\phi C_{ox}$ , noted above. The capacitance change due to a small crack of area  $A_c$  and width  $d_c$  in a parallel plate capacitor of plate separation  $d$  is given by

$$\Delta C = \kappa \epsilon_o A_c \left( \frac{1}{d + d_c} - \frac{1}{d} \right) = \frac{\kappa \epsilon_o A_c}{d} \left( \frac{d_c}{d + d_c} \right). \quad (13)$$

Even modest crack widths of  $d_c \sim 1 \mu m$ , are much greater than the oxide thickness employed here, ( $d \sim 100 \text{ nm}$ ), so that the magnitude of the change in capacitance is essentially equal to the initial capacitance of the affected area. With  $d_c \gg d$ , the resulting current is

$$i_L = \frac{\Delta\phi \kappa \epsilon_o A_c}{R_L C_{ox} d} \quad (14)$$

Using typical values for  $\Delta\phi = \phi_{Si} - \phi_{Au} = -0.5$  V,  $\kappa_{SiO_2} = 3.8$ ,  $R_L = 1$  M $\Omega$ ,  $C_{ox} = 40$  nF, and  $d = 100$  nm,  $i_L/A_c = 4$  mA/m<sup>2</sup> fracture surface area. [In units of volts produced across the load resistor, this amounts to 4 kV/m<sup>2</sup> fracture surface area.] A crack 0.5 mm<sup>2</sup> in area thus yields a readily detectable current of 2 nA. Sensitivities 100  $\times$  greater are readily obtained with submicrosecond time resolution with fast amplifiers.

The current measured during detachment depends strongly on work function of the metal phase relative to Si. Although quantitative comparisons among different metals were not carried out in this work, qualitative measurements of the charge on detached films support a direct connection between the amplitude of the charge and the work function difference relative to the substrate.<sup>22</sup> Thus it is reasonable to expect that the sign and magnitude of the detected currents is strongly affected by the presence of contamination at the metal-oxide interface, as observed. This contamination generally degrades the mechanical strength of the interface as well, although this is in some cases low interfacial strength is desirable. For instance, low interfacial strength can greatly enhance the pullout of fibers in fiber-reinforced ceramics, greatly improving the fracture behavior of these materials. Due to the importance of interface quality to the electronics industry, an extensive array of procedures for evaluating the electrical properties of interfaces have been developed. Some of these procedures may prove valuable in evaluating metal-insulator and metal-semiconductor interfaces in structural ceramics as well.

In many cases, the integrated current accompanying film detachment can be significant. The integrated current per unit area of detached film provides a lower bound on the surface charge density on the film in the early stages of detachment, which in turn can provide a lower bound on the electrostatic contribution to the adhesion of the metal to the oxide in a MOS structure. For instance, the integrated current from the failure event of Fig. 10 is readily estimated to be on the order of 200 nC, which corresponds to a charge density of about 10

mC/m<sup>2</sup>. The electrostatic force per unit area associated with a vacuum gap in a parallel plate capacitor in this geometry is  $\sigma^2/\epsilon_0$  or about 100 kPa. This is a substantial contribution to the adhesive force in the case of Au-oxide interfaces. The work done against the associated electric field by opening the crack 1  $\mu\text{m}$  is 1 J/cm<sup>2</sup>, suggesting that electrostatic forces can contribute substantially to the resistance to rapid crack growth by hindering the separation of the two crack surfaces. We expect the effect of electrostatic forces to be smaller in the case of much slower crack growth, in which the charge on either side of the crack has adequate time to dissipate; i.e., the growth of the crack is slow relative to the decay time for charge across the crack ( $\tau = R_{ox} C_{ox}$ ).

**Conclusions.** Currents produced by interfacial failure can be employed to monitor the course of interfacial failure, often with  $\mu\text{s}$  time resolution. Readily detected currents may be observed many tens of  $\mu\text{s}$  prior to ultimate failure, and fluctuations in the observed current apparently reflect periods of rapid and slow crack growth.

In the model system treated above, the utility of these currents to predict the time of failure is limited to time scales of hundreds of  $\mu\text{s}$ . However, in practical ceramic-metal composites, it is reasonable to expect that interfacial metal-ceramic failure within structural members can precede ultimate failure of by usefully long time scales. In such case cases, electrical transducers coupled to a conducting phase could in principle yield useful warnings in the form of identifiable currents or current fluctuations, such as those produced by stick-slip processes accompanying fiber pullout.

### **Chemi-emission of electrons from titanium metal as a probe of deformation processes**

Although the ceramics have many desirable mechanical properties, especially at high temperatures, their use in structural applications is often limited by their characteristic brittleness. This brittleness can often be mitigated in ceramic-metal composites, which take advantage of the fracture toughness of the metal phase while retaining much of the hardness and stiffness of the

ceramic phase. However, in many cases the ductility of metal-ceramic composites is highly localized, making an overall assessment of the degree of metallic deformation associated with a particular fracture event difficult to assess. Since plastic deformation generally produces fresh metallic surfaces on the sample surface, one strategy for assessing the overall amount of plastic deformation accompanying fracture is to measure the amount of fresh metal surface created during a testing cycle. The following work describes a preliminary assessment of the use of the electron emission accompanying the reaction of Ti with O<sub>2</sub> on fresh titanium surfaces as a means of estimating the surface area of freshly exposed titanium surface exposed during deformation and fracture. The results suggest that most of the electron emission accompanying deformation and fracture in appropriate oxygen atmospheres is indeed produced by a chemi-emission mechanism and is related simply to the amount of fresh titanium metal exposed to this atmosphere during deformation and fracture.

**Experiment.** Titanium sheets of 99.7% purity were used. The principal impurities are probably oxygen or nitrogen. Dogbone samples were cut from 0.67 mm sheet to produce a gauge section with dimensions 50 × 6.25 mm<sup>2</sup>. The samples were mounted in vacuum and strained at a rate of 1.5% s<sup>-1</sup>. Elongations at fracture were typically about 9 mm, or 18%. All samples were fractured at room temperature in various partial pressures of oxygen. The base vacuum pressure was approximately 3 × 10<sup>-4</sup> Pa. Assuming that the residual gasses in the chamber were due to leakage around a rubber O-ring, the partial pressure of oxygen in the system would be 4-5 × 10<sup>-6</sup> Pa prior to the introduction of additional oxygen. For testing purposes we raised the oxygen partial pressure to either 5 × 10<sup>-5</sup> or 3 × 10<sup>-4</sup> Pa.

**Results and Discussion.** Figure 14 shows typical EE and load data taken during loading in the presence of 5 × 10<sup>-5</sup> Pa O<sub>2</sub>. The electron emission starts to rise as the load starts to drop; visual observations indicate that this load drop corresponds to the onset of necking in the sample. About 100 ms prior to fracture the EE increases at a more rapid rate, with an approximately exponential rise. This increase is more evident in machine loaded samples (constant strain rate) than in samples loaded by turning the loading apparatus by hand (roughly constant load). At

fracture the emission spikes sharply for a few tenths of a second and subsequently decays. Just after fracture, the EE often plateaus briefly; during this period the EE is fairly constant but may show some fluctuations in intensity. The count rates immediately after fracture are sufficiently low to ensure that the electron multiplier is not saturated for more than a few microseconds; thus the total number of EE counts observed should closely reflect the actual number of electrons reaching the detector. Generally about 10 times more counts are observed after fracture than are observed before fracture.

The intensity of the EE observed following fracture depends strongly upon the partial pressure of oxygen in the system. Figure 15 shows EE data taken during fracture, where a leak valve connected to an oxygen tank was used to raise the partial pressure of oxygen in the system to  $5 \times 10^{-5}$  Pa midway through the EE decay following fracture. As the partial pressure of oxygen is raised, the EE count rate increases dramatically. The EE count rate soon reaches a maximum and subsequently decays at a rate several times faster than the decay prior to the introduction of the additional oxygen.. The total number of EE counts observed following fracture is not greatly changed by the admission of additional oxygen. Thus the total number of EE counts observed appears to be a function of the sample surface and not the oxygen partial pressure. However, the observed count rates and the duration of the emissions are strong functions of oxygen partial pressure.

As indicated in Fig. 15, the EE time required for the decay of EE following fracture depends strongly on the partial pressure of oxygen in the system. This is displayed more systematically in Fig. 16, which shows EE decays recorded at three different oxygen partial pressures. The time required for the EE decay is roughly equal to the time required for the formation of a monolayer of oxygen on the titanium surface at the indicated partial pressures. However, the total number of observed EE counts does rise slightly with oxygen pressure, implying that other (background) gasses, such as water or nitrogen, are absorbing on reactive surface sites at the lower oxygen partial pressures.

The relationship between deformation and the observed chemi-emission is perhaps most clearly established by Fig. 17, which shows the EE and load signals during repeated deformation cycles with a partial pressure of oxygen of  $5 \times 10^{-5}$  Pa. In between cycles, the EE was allowed to decay to near-background levels. The second and third deformation cycles involved extensions of about 1.25 mm, with the third deformation cycle producing fracture. The EE decays following the first two deformation cycles are quite similar to that following fracture, which is consistent with a decay limited by the rate at which oxygen adsorbs onto reactive surface sites produced by deformation. In particular, this is inconsistent with the possibility that the EE observed during loading is due to fracto-emission from cracking of a surface oxide layer. The EE following fracture of the titanium metal is clearly related to an oxygen reaction, and it is unlikely that the emission during deformation would have similar decay kinetics if another emission mechanism were operative.

**Conclusions and Further Work.** The above data indicate that the observed EE is due to chemi-emission from fresh metal surfaces exposed to oxygen during deformation and fracture. The similarities of the decays accompanying deformation prior to fracture with the decay following fracture suggests that amount of deformation may be determined as a function of time by numerically "deconvoluting" the emission decay from the observed signal. By exposing a known amount of fresh titanium to an oxygen ambient, we expect to be able to calibrate the observed emissions, although even relative measures of surface formation would prove useful.

The utility of chemi-emission in the study of deformation in composite materials will be assessed in simple glass-titanium composites. The thermal expansion of titanium and ordinary soda-lime glass is quite similar, facilitating the construction of these samples. In composite materials, the constraint of the ceramic phases hinders deformation in the metallic phase, suggesting that the EE decay following fracture of these materials will be considerably less than that observed from titanium metal alone. Visual observations of similar metal-glass fracture surfaces suggest that interfacial failure generally leaves the metal phase covered with an oxide. If this observation proves general, interfacial failure will yield little chemi-emission. In this case,

EE measurements in the presence and absence of oxygen may allow us to assess the amounts of interfacial failure and deformation separately.

### **Imaging Point Defect Clusters Generated by Plastic Deformation in Inorganic Materials.**

When semi-brittle inorganic crystals are deformed, stresses during indentation, at pre-existing flaws, and at moving crack tips result in significant dislocation generation and motion. The field of moving atoms associated with a variety of dislocation structures (e.g., jogs) in turn produce point defects in surprising abundance. We have developed a method using an excimer laser to image the photoluminescence generated by these defects. In MgO, this results in a distinct 400 nm emission band which is due principally to clusters of oxygen vacancies occupied by electrons (F-Centers). This type of luminescence has been previously observed in doped CaO by Chen et al.<sup>29</sup> Unique patterns of these clusters occur on cleavage surfaces with strong correlation with regions of high densities of dislocation concentrations. These patterns can be observed using the imaging system shown in Fig.18. Using pulses of unfocused 248 nm (ultraviolet light) from a KrF excimer laser, defects associated with a wide variety of deformation induced dislocations can be viewed and recorded through an optical microscope. All scattered UV is absorbed in the microscope optics. Currently, magnifications up to 250X have been used. [With a CCD camera, much higher magnifications could be achieved.]

Alignment of clusters of such point defects are observed along cleavage steps as seen in Fig. 19. Cleavage steps are generated by cracks running in parallel but on different crystal planes. Swain, Lawn, and Burns<sup>30</sup> have analyzed the process of step formation, finding that adjacent but non-coplanar crack will tend to overlap prior to ultimate failure (see Fig. 20).

The overlapped material experiences extreme shear stresses, and in semibrittle materials can be extensively deformed and therefore produce rows of dislocations along the cleavage steps. Often, undercutting occurs which produces highly deformed "platelets" one of which is seen in the luminescent image shown in Fig. 19(a).

Diamond tip indentations, scratch marks, polishing grooves, and regions involving tribological interactions lead to extensive concentrations of luminescent centers due to the associated plastic deformation. and serve as a means of mapping and monitoring energy dissipative processes occurring during mechanical and fracture phenomena. Such patterns are seen in Fig. 21. Real time information (with  $\mu\text{s}$  time resolution) can also be obtained by replacing the imaging system with integrating optics and a fast photomultiplier tube. These measurements allow us to see visually where plastic deformation is occurring during loading and fracture--in transparent, wide bandgap materials this includes well below the surface. It can also serve as a way of detecting damage on a ceramics surface where flaws are often the cause of failure, as well as coupling laser energy into these defect clusters for the purposes of healing microcracks and other flaws by preferential melting and annealing. We have recently made direct measurements of the role of these defects on the mechanically induced decomposition of the surface of ceramics which has importance concerning wear during tribological loading.

## REFERENCES

1. V. Stannett, in *Diffusion in Polymers*, edited by J. Crank and G. S. Park, (Academic Press, London, 1968), pp. 41-73.
2. C. A. Kumins and T. K. Kwei, in *Diffusion in Polymers*, edited by J. Crank and G. S. Park, (Academic Press, London, 1968), pp. 107-140.
3. Bernard Rosen, *J. Polym. Sci.* **47**, 19 (1960).
4. H. Yasuda, V. Stannett, H. L. Frisch, and A. Peterlin, *Macromol. Chem.* **73**, 188 (1964).
5. M. A. Grayson, C. J. Wolf, R. L. Levy, and D. B. Miller, *J. Polym. Sci. Polym. Phys.* **14**, 1601 (1976).
6. N. S. Enikolopian, L. S. Zarkhin, and E. V. Prut, "Primary molecular products of mechanical fracture of polymers," *J. Appl. Polym. Sci.* **30**, 2991 (1985).



7. V. R. Regel, T. M. Muinov, and O. F. Pozdnyakov, "A mass spectrometric study of volatile products evolving in degradation of solids," in *Physical Basis of Yield and Fracture*, edited by A. C. Stickland, (Institute of Physics, London, 1966), pp. 194-199.
8. F. J. Norton, *J. Appl. Polym. Sci.* **7**, 1649 (1963).
9. J. T. Dickinson, L. C. Jensen, S. C. Langford, and R. P. Dion, work in progress.
10. S. Matsuoka and H. E. Bair, "The temperature drop in glassy polymers during deformation," *J. Appl. Phys.* **48**, 4058 (1977).
11. B. D. Malhotra and R. A. Pethrick, *Eur. Polym. J.* **19**, 457 (1983).
12. K. N. G. Fuller, P. G. Fox, and J. E. Field, *Proc. Royal. Soc. London* **341**, 537 (1975).
13. R. Weichert and K. Schonert, *J. Mech. Phys. Solids* **26**, 151 (1978).
14. P. J. Miller, C. S. Coffey, and V. F. DeVost, *J. Appl. Phys.* **59**, 913 (1986).
15. V. R. Regel, T. M. Muinov, and O. F. Pozdnyakov, in *Physical Basis of Yield and Fracture*, edited by A. C. Stickland, (Institute of Physics, London, 1966), pp. 194-199; 295-296.
16. M. A. Grayson, C. J. Wolf, R. L. Levy, and D. B. Miller, *J. Polym. Sci. Polym. Phys. Ed.* **14**, 1601 (1976).
17. N. S. Enikolopian, L. S. Zarkhin, and E. V. Prut, *J. Appl. Polym. Sci.* **30**, 2291 (1985).
18. M. S. Caceci and W. P. Cacheris, *Byte* (May 1984) 340.
19. D. W. Marquardt, *SIAM J. Appl. Math.* **11**, 431-441 (1963).
20. W. H. Press, B. P. Flannery, S. A. Teukolsky, and W. T. Vetterling, *Numerical Recipes in Pascal*, (Cambridge University Press, Cambridge, 1989), pp. 580-590.
21. J. T. Dickinson, L. C. Jensen, S. C. Langford, and R. P. Dion, "Emission of occluded volatiles accompanying the crazing of polystyrene and high impact polystyrene," manuscript in preparation.

22. K. A. Zimmerman, S. C. Langford, and J. T. Dickinson, *J. Appl. Phys.* **70**, 4808 (1991).
23. Z.-Y. Ma and J. T. Dickinson, *Appl. Phys.* **70**, 4797 (1991).
24. D. L. Doering, J. T. Dickinson, S. C. Langford, and P. Xiong-Skiba, *J. Vac. Sci. Technol. A* **8**, 2401 (1990).
25. P. Xiong-Skiba, D. L. Doering, and K. H. Siek, *J. Vac. Sci. Technol. A* **9**(4), 2563-2565 (1991).
26. L. A. K'Singam, J. T. Dickinson, and L. C. Jensen, *J. Am. Ceram. Soc.* **68**, 510 (1985).
27. *CRC Handbook of Chemistry and Physics*, 71st Edition, edited by David R. Lide, (CRC Press, Boca Raton, 1991), p. 12.84-12.85.
28. K. A. Zimmerman, S. C. Langford, J. T. Dickinson, and R. P. Dion, "Electron and photon emission accompanying deformation and fracture of polycarbonate, to appear in *J. Polym. Sci. Polym. Phys. Ed.*
29. Y. Chen, W. P. Unruh, M. M. Abraham, T. J. Turner, and C. M. Nelson, *J. Am. Ceramics Soc.* **56**438 (1973).
30. M. V. Swain, B. R. Lawn, and S. J. Burns, *J. Mat. Sci.* **9**, 175-183, (1974).

## FIGURE CAPTIONS

- FIG. 1. (a) Mass 40 and (b) load signals accompanying the fracture of polycarbonate in tension.
- FIG. 2. (a) Mass 20 and (b) load signals accompanying the fracture of polycarbonate in tension.
- FIG. 3. (a) Mass 20 and (b) load signals accompanying the loading of polycarbonate in tension prior to fracture.
- FIG. 4. (a) Mass 20 and (b) load signals accompanying one loading/unloading cycle in polycarbonate prior to yield, where the maximum load was held briefly prior to unloading. A 56 nA background signal has been subtracted from (a).
- FIG. 5. (a) Mass 20 and (b) load signals accompanying another loading/unloading cycle in polycarbonate. Again, a 56 nA background signal has been subtracted from (a).
- FIG. 6. A diagram of the apparatus used to make simultaneous emission measurements at two distances from the sample.
- FIG. 7. (a) Mass 106 signals detected by the two-quadrupole apparatus, and (b) the leading edges of the two signals (asterisks) plotted with the least squares fit (continuous lines) of the model to the data. The heights of the two signals in (b) have been scaled to yield equal weights in the sum of squares. The dark curve is a normalized plot of the source function employed in the curve fitting routine.
- FIG. 8. (a) Anomalous mass 40 signals detected by the two-quadrupole apparatus, and (b) the leading edges of the two signals (asterisks) plotted with the least squares fit (continuous lines) of the model to the data. The heights of the two signals in (b) have been scaled to yield equal weights in the sum of squares. The dark curve is a normalized plot of the source function employed in the curve fitting routine.
- FIG. 9. Diagram of sample geometry. Typically a photomultiplier tube and a Channeltron electron multiplier would be mounted on either side of the sample.

FIG. 10. (a) pH<sub>E</sub>, (b) EE, and (c) current accompanying detachment of a gold film from a MOS structure. The weak signals early in the detachment process are shown on expanded scales; these signals have been displaced vertically for ease of visualization.

FIG. 11. Current from (a) detached and (b) undetached gold from the experiment shown in Fig. 2. The first vertical line shows the end of the peel event, where the two signals begin to show divergent behavior. The second vertical line shows the contact of the two gold surfaces, where the two signals again become identical. Contact is remade when the epoxy drop falls against the sample.

FIG. 12. Current accompanying the peel of a Pb/Sn solder drop from a gold-coated silica surface (a) in the early stages of detachment and (b) during and after detachment. The step-like drops in current in (a) were accompanied by intense pH<sub>E</sub>, consistent with electrical breakdown (sparks). Measurements of the current drops at these points indicate that fully 60% of the charge on the solder drop was lost in the breakdown events.

FIG. 13. Schematic diagram of the MOS equivalent circuit used to model the current signals during and after detachment.  $\Delta\phi$  is the potential difference between the gold and the silicon required for chemical and physical equilibrium.

FIG. 14. (a) Load and (b) electron emission accompanying the deformation and fracture of titanium sheet in the presence of  $5 \times 10^{-5}$  Pa O<sub>2</sub>.

FIG. 15. (a) Load and (b) electron emission accompanying the deformation and fracture of titanium in vacuum. At the time indicated by the arrow, the partial pressure of oxygen was raised from about  $5 \times 10^{-6}$  Pa to  $5 \times 10^{-5}$  Pa.

FIG. 16. Electron emission following the fracture of titanium at oxygen partial pressures of (a)  $5 \times 10^{-7}$  Pa, (b)  $5 \times 10^{-6}$  Pa, and (c)  $3 \times 10^{-4}$  Pa.

FIG. 17. (a) Load and (b) electron emission accompanying repeated tensile deformation of titanium at an oxygen partial pressure of  $5 \times 10^{-6}$  Pa.

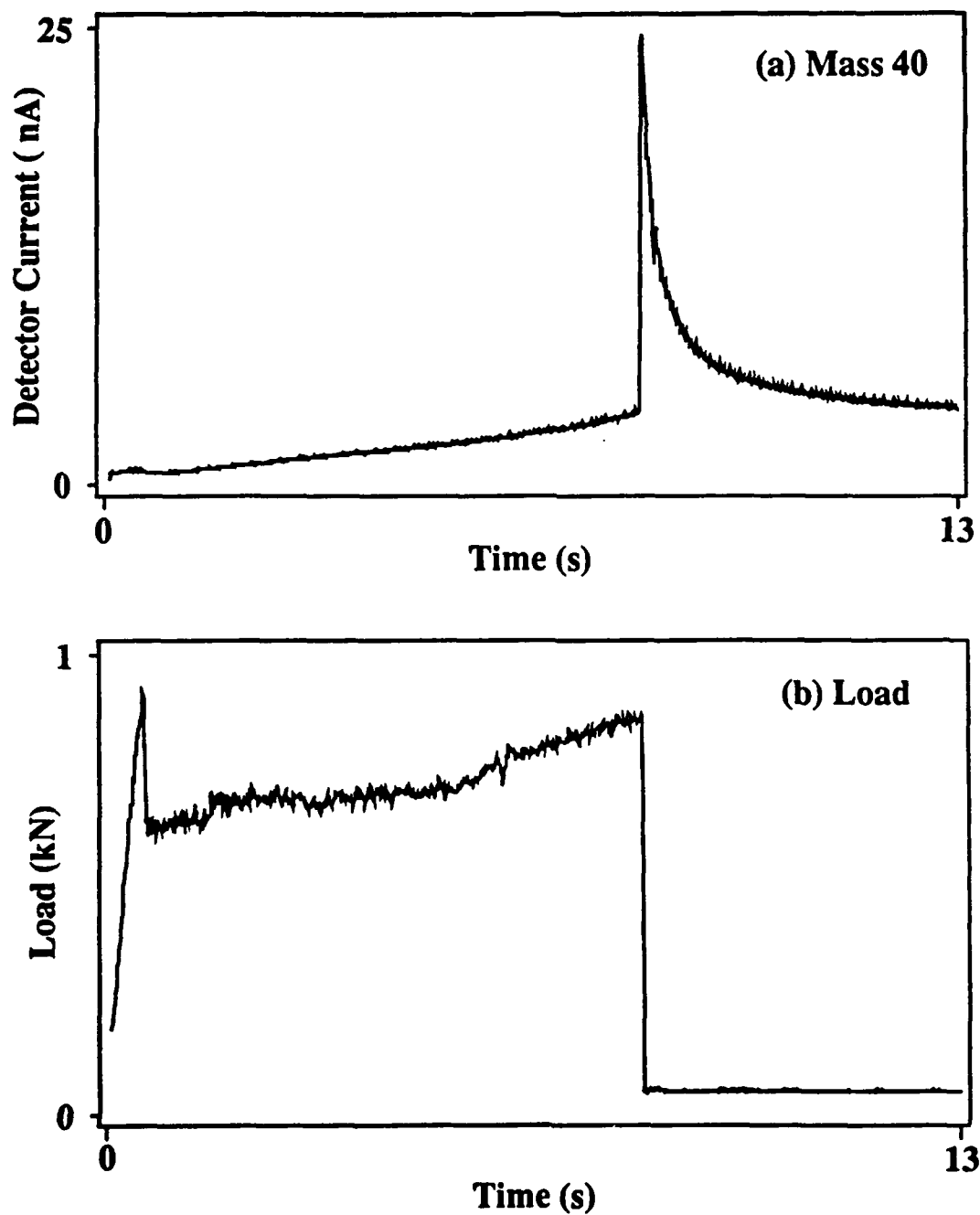
**FIG. 18** Schematic diagram of photoluminescence imaging system using an excimer laser as an intense excitation source along with schematic representations of the vacancy formation mechanism and a simple MgO crystal defect model.

**FIG. 19.** (a) Photoluminescence image of a cleavage surface of MgO. Note cleavage steps and the very bright "flap" which indicates extensive plastic deformation. (b) SEM photograph of the same surface.

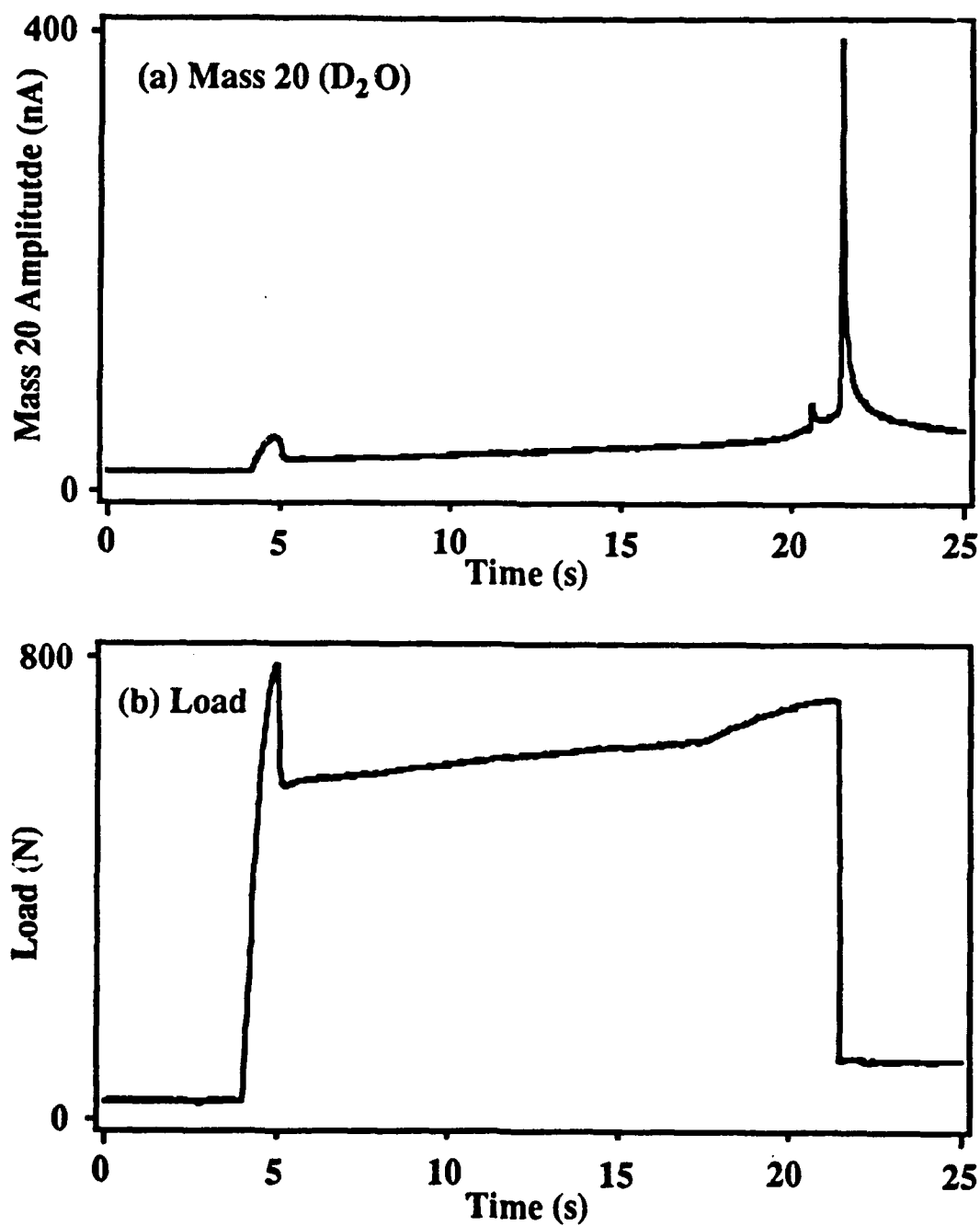
**FIG. 20** Diagram of plastic deformation induced dislocations at cleavage steps.

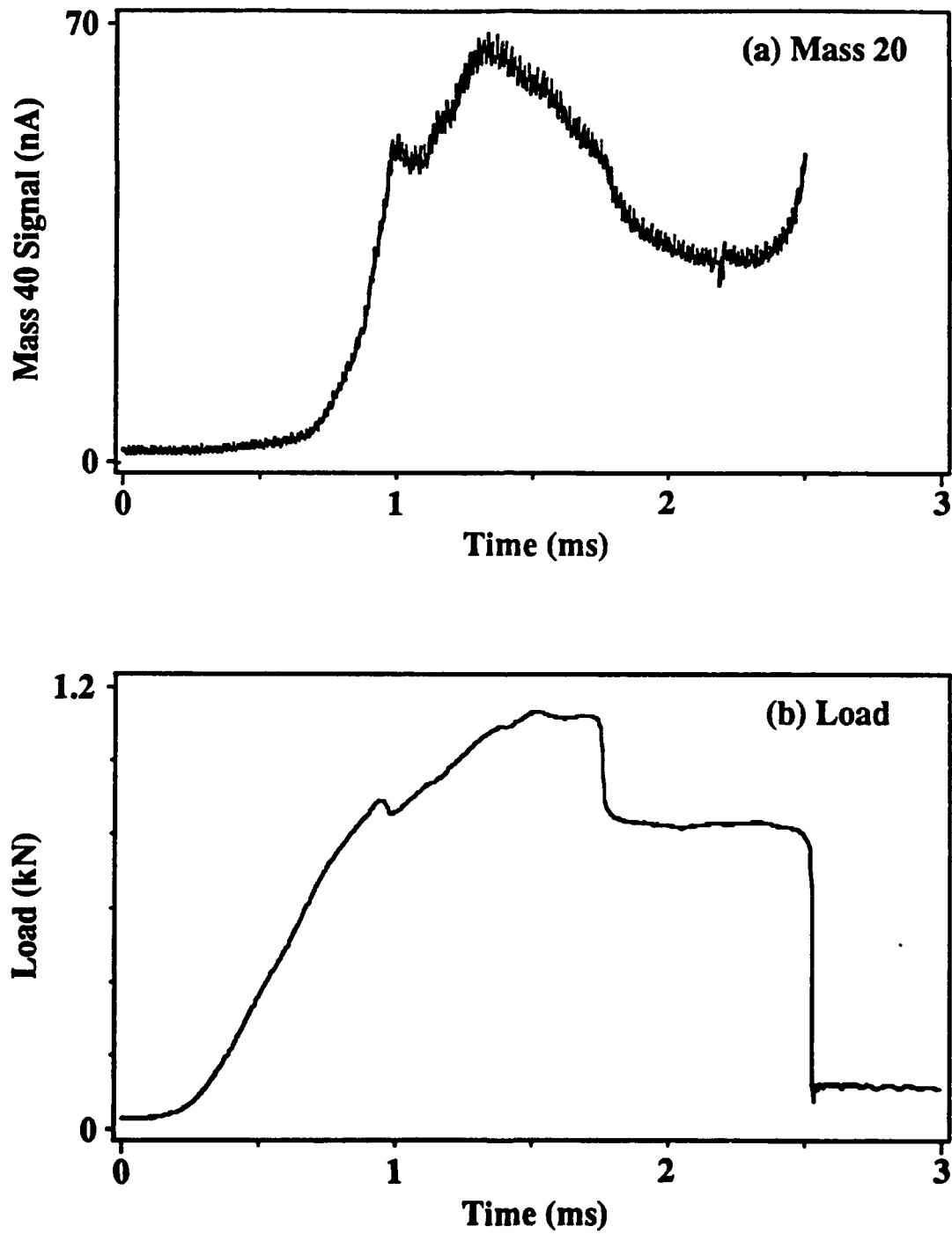
**FIG. 21.** White light image and photoluminescence image of several diamond indents on a cleaved MgO surface.

**Mass 40 and Load During the  
Tensile Fracture of Polycarbonate**

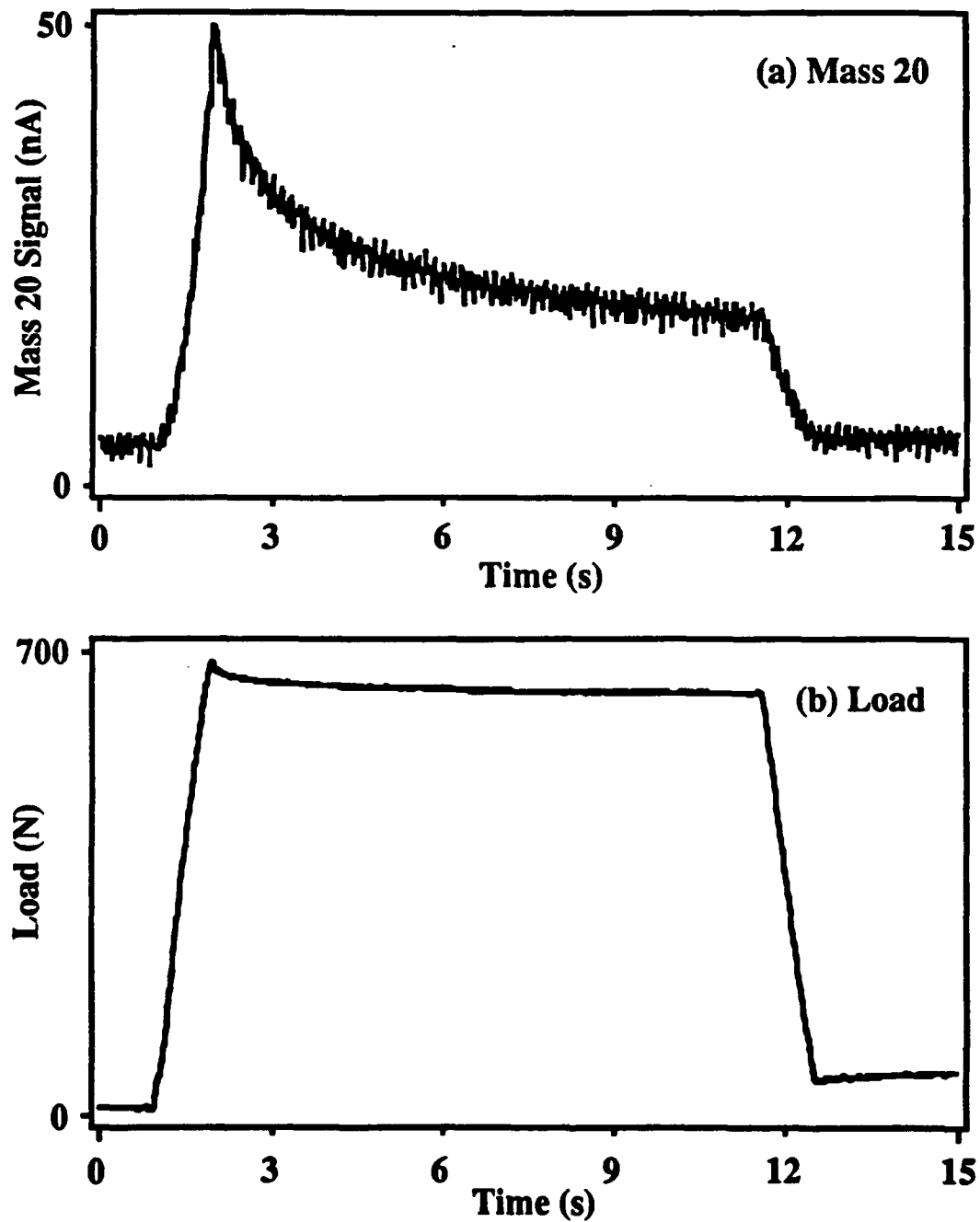


**FIG. 1**

**Mass 20 and Load During the Tensile Fracture of Polycarbonate****FIG. 2**

**Mass 20 Signal and During Loading of Polycarbonate****FIG. 3**

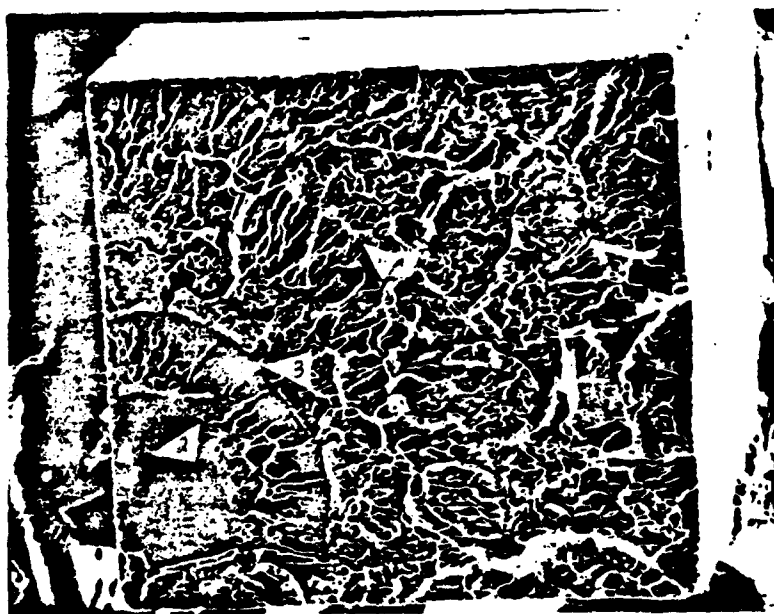


**Mass 20 and Load During the Elongation of Polycarbonate****FIG. 4**

## SEM Micrographs of PS Fracture Surfaces



**Heavily Crazed**

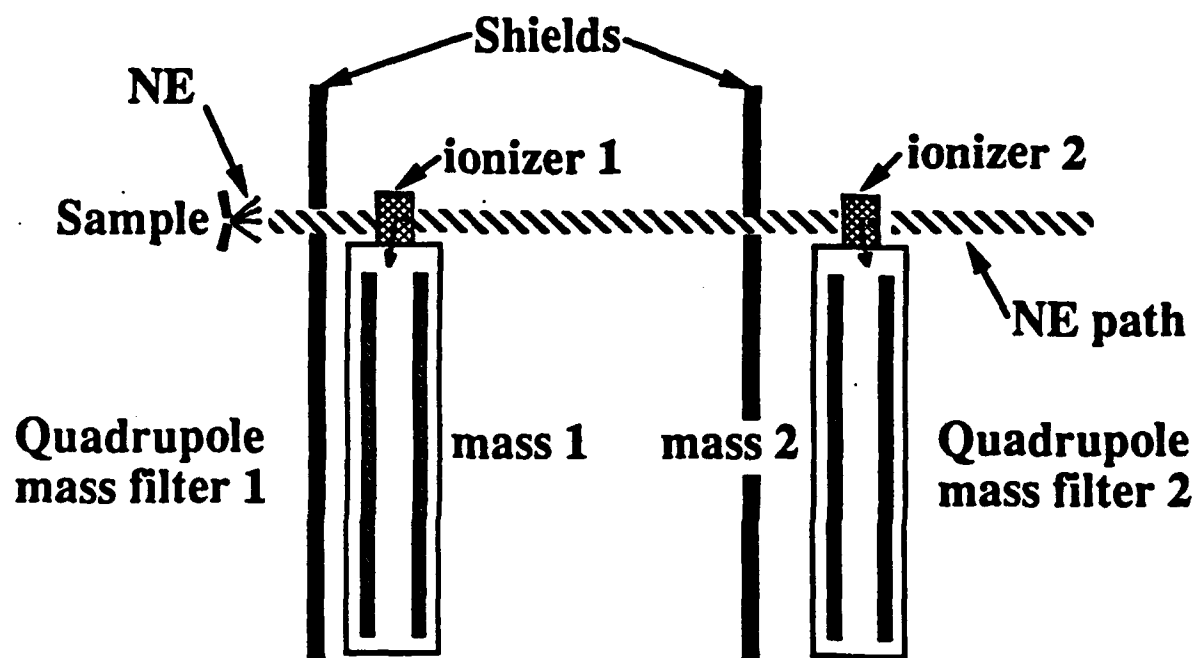


**Lightly Crazed**

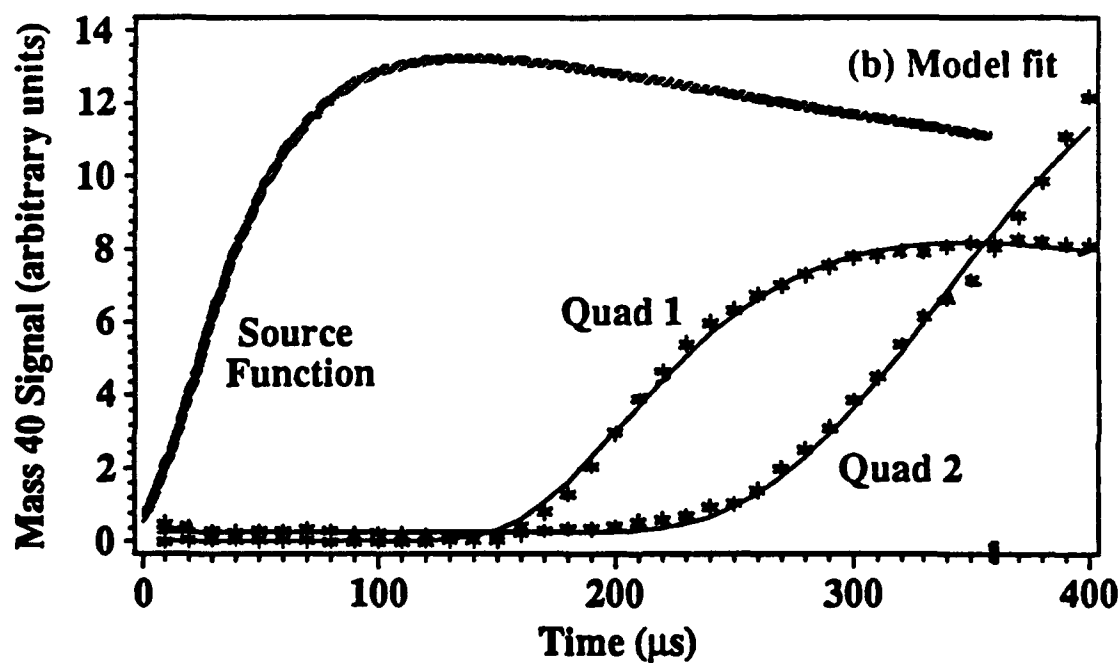
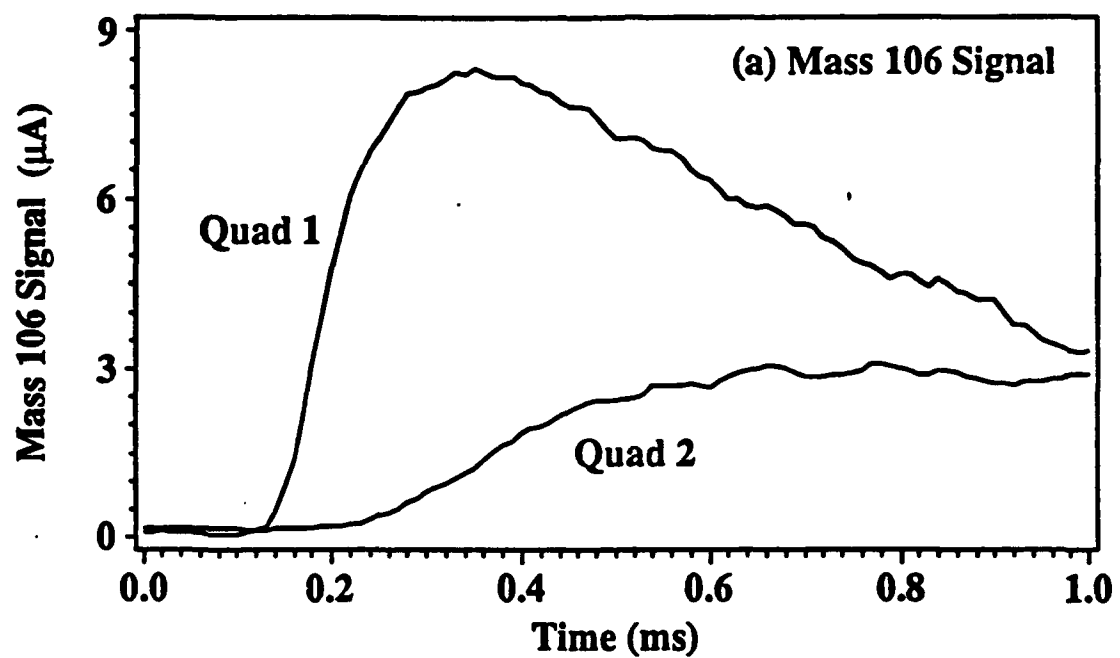


**FIG. 5**

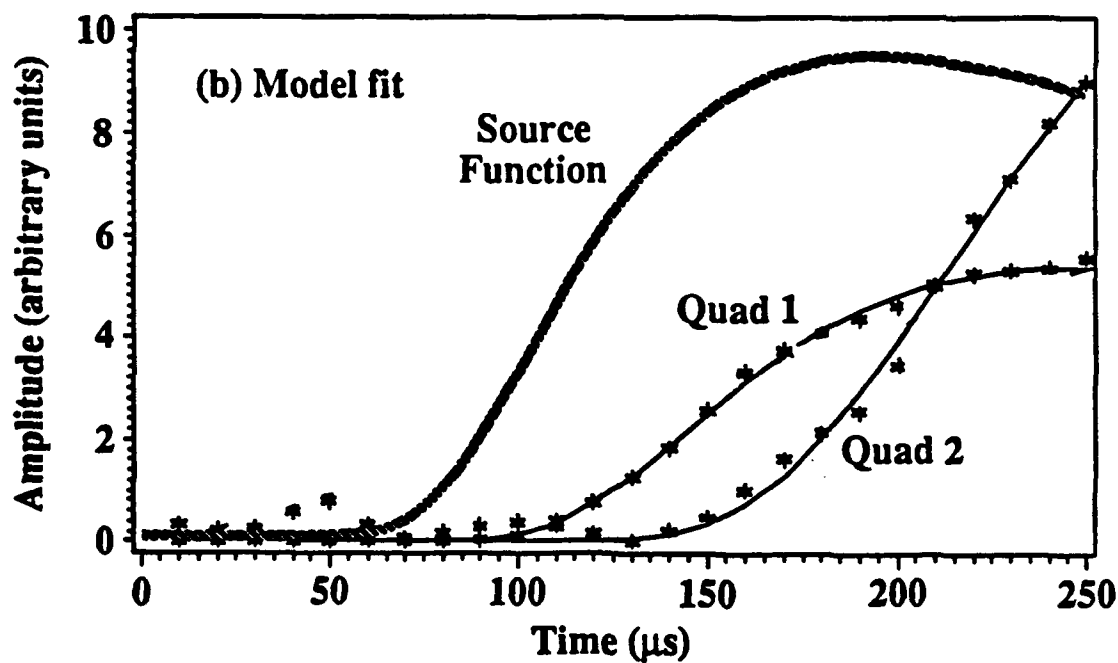
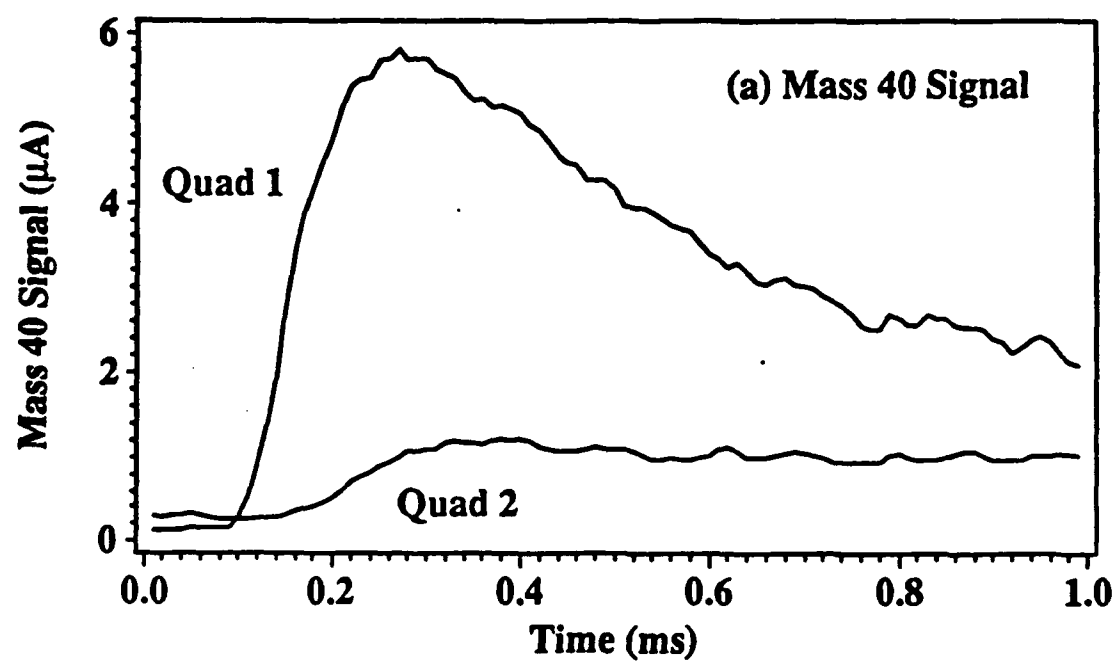
## Sequential Quadrupole Experiment



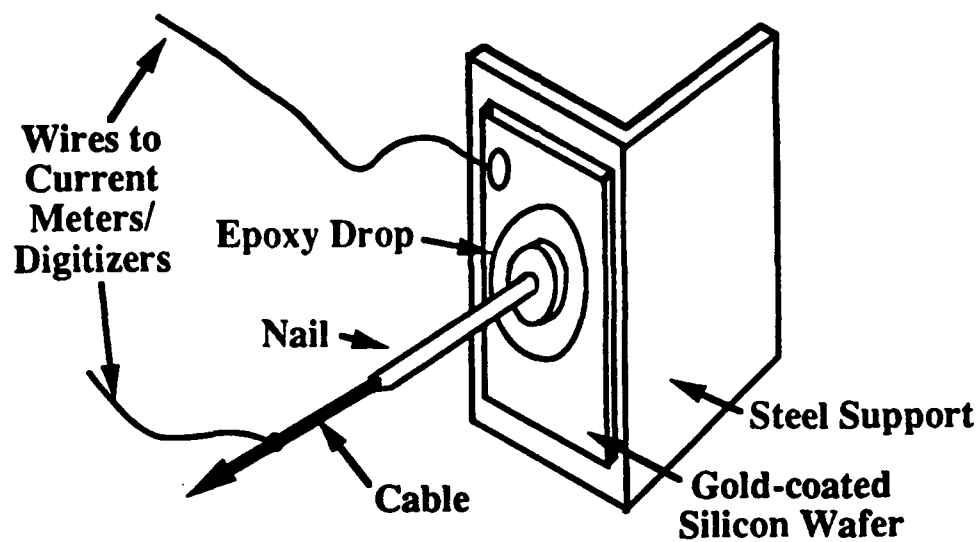
**FIG. 6**

**Two-Quadrupole Mass 106 Signals from Polystyrene****FIG. 7**

### Two -Quadrupole Mass 40 Signals from Polystyrene

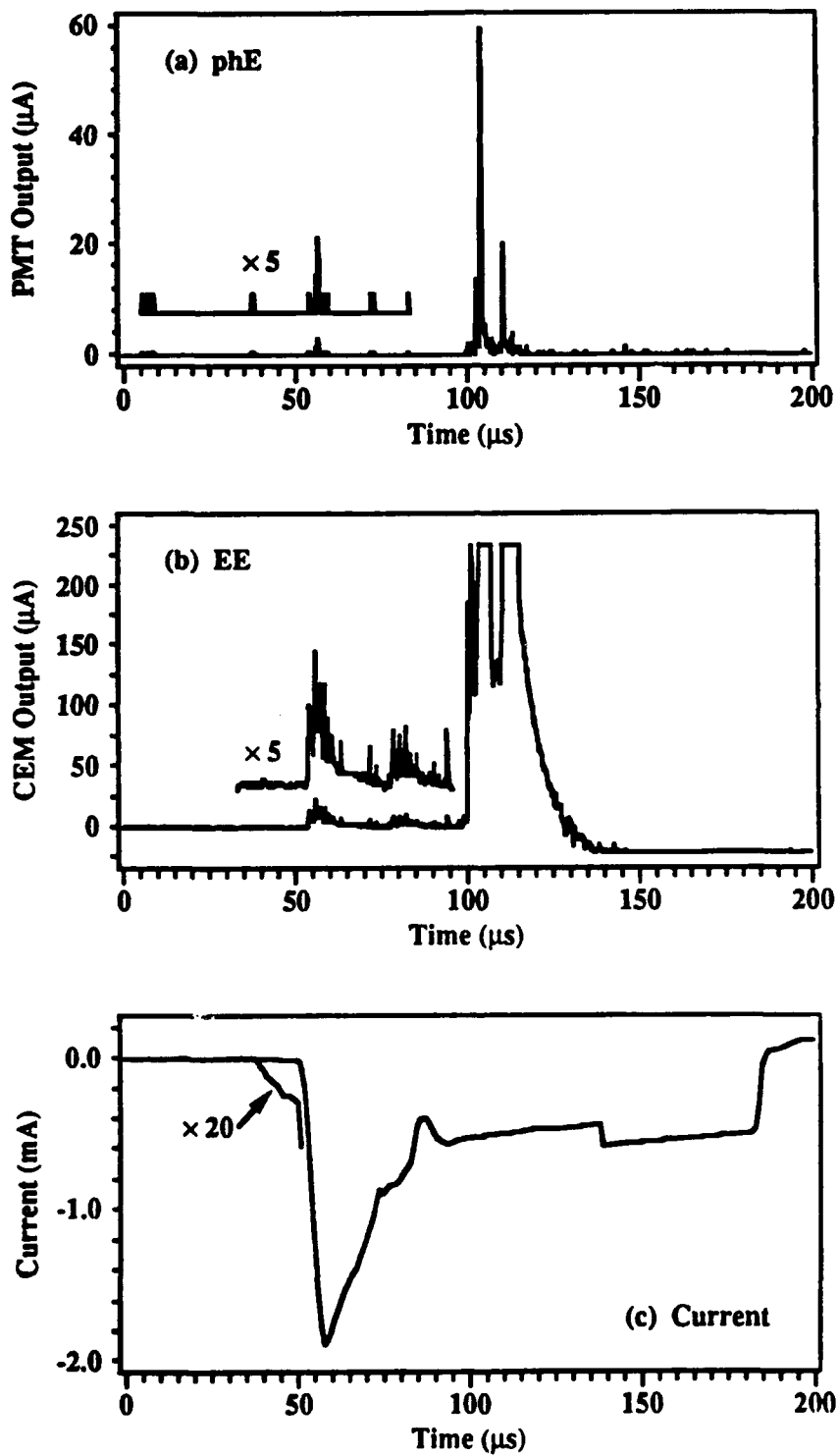
**FIG. 8**

## Sample Geometry



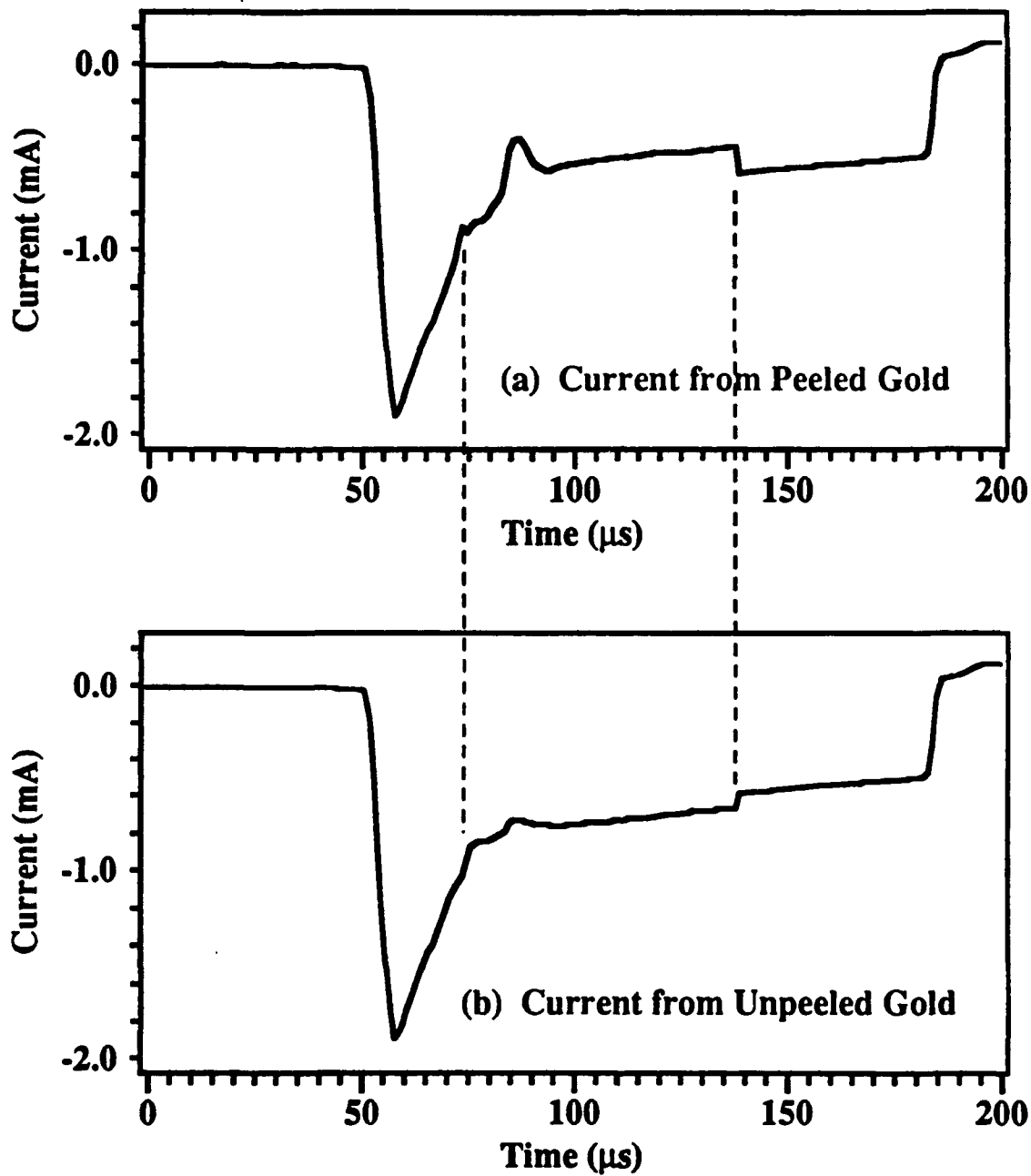
**FIG. 9**

phE, EE, and Current Accompanying Peel of MOS Structure  
(Gold Coated Epoxy Drop)



**FIG. 10**

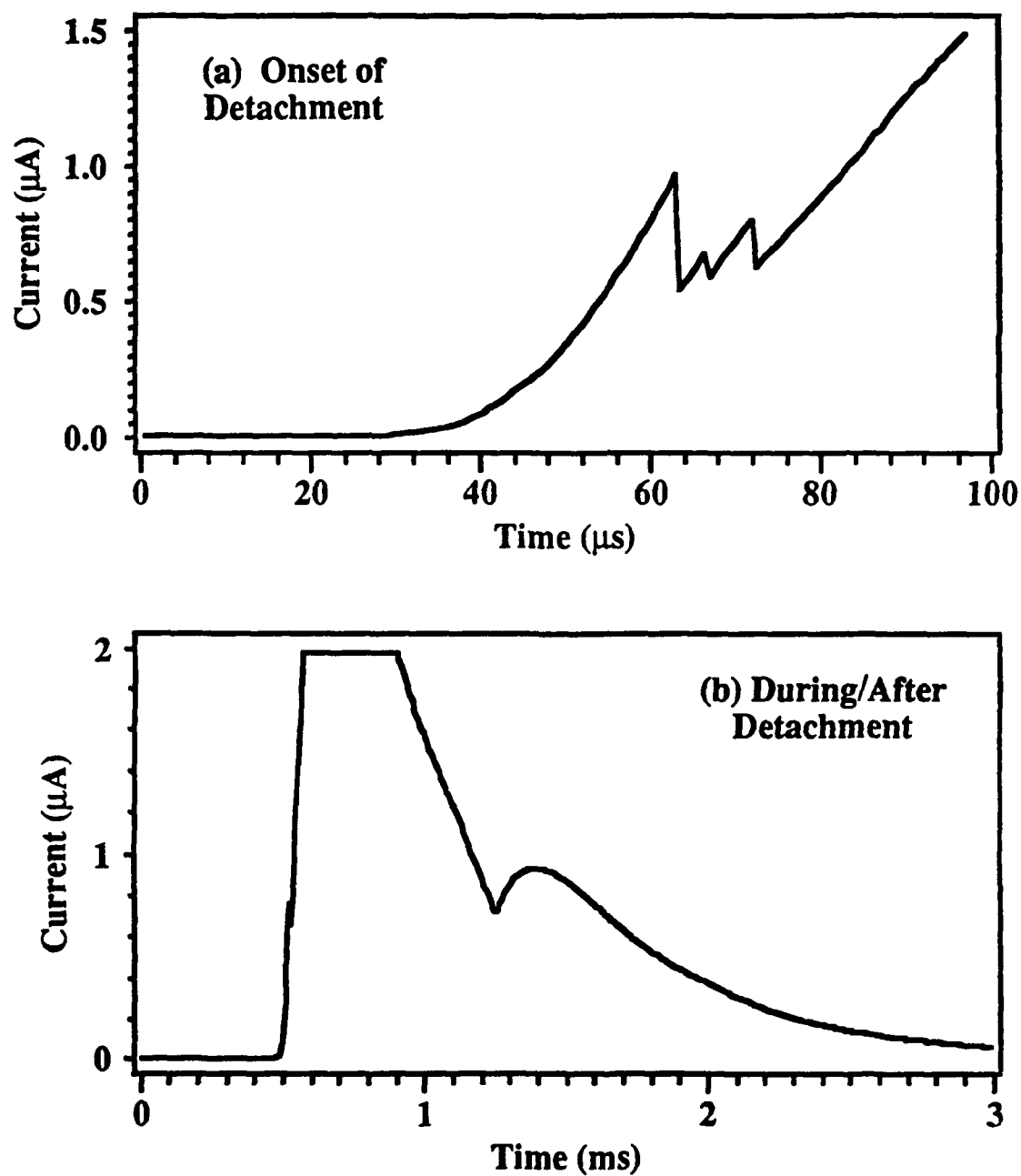
**Current from Peeled and Unpeeled Portion of Gold  
Accompanying Peel of MOS Structure**



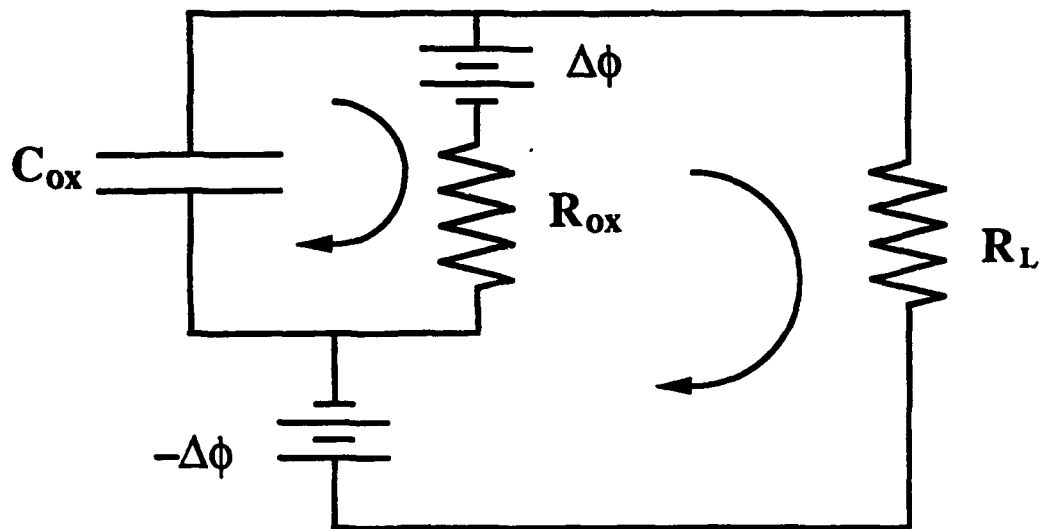
**FIG. 11**



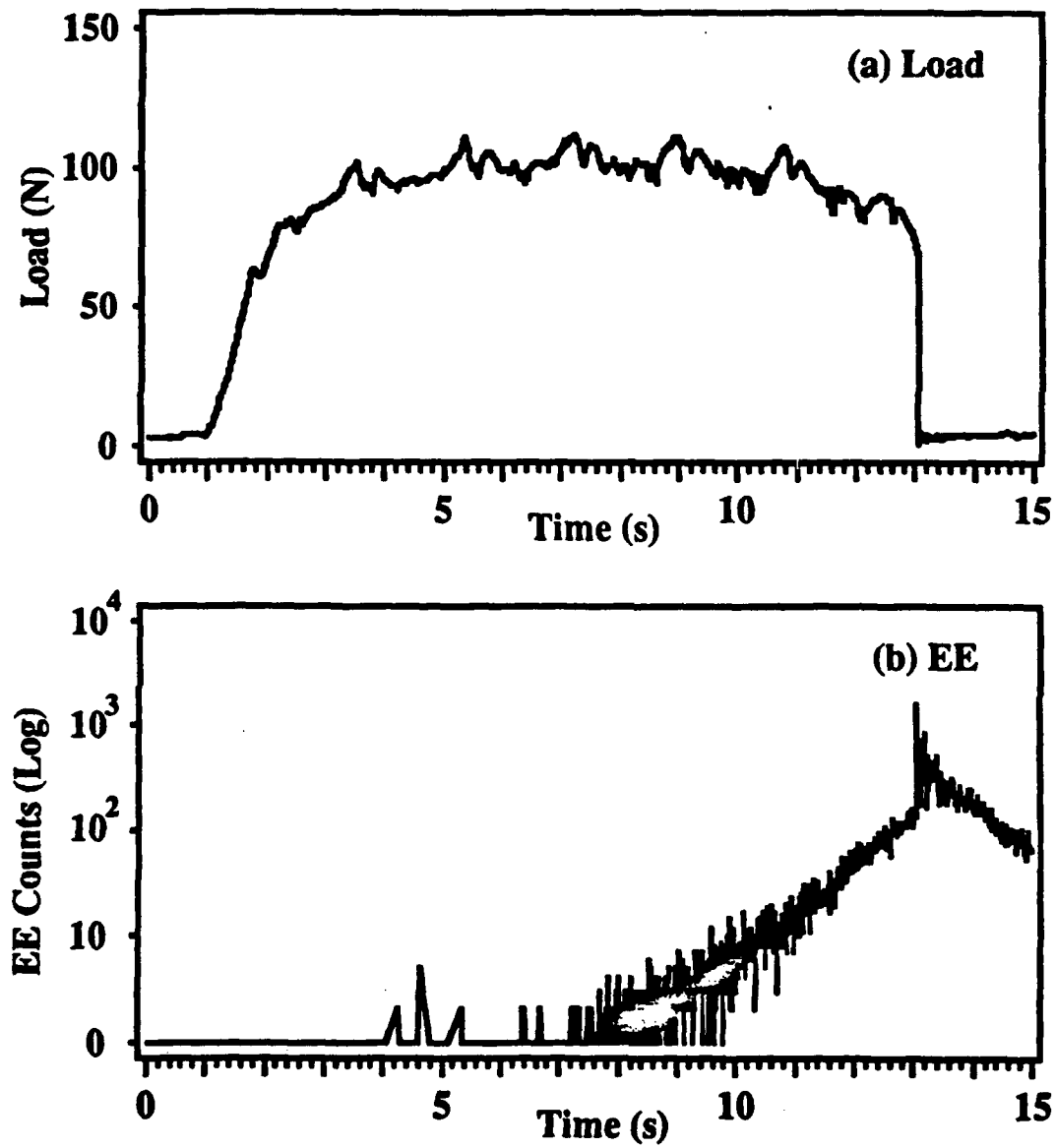
### Current Accompanying Peel of Pb/Sn from Silica

**FIG. 12**

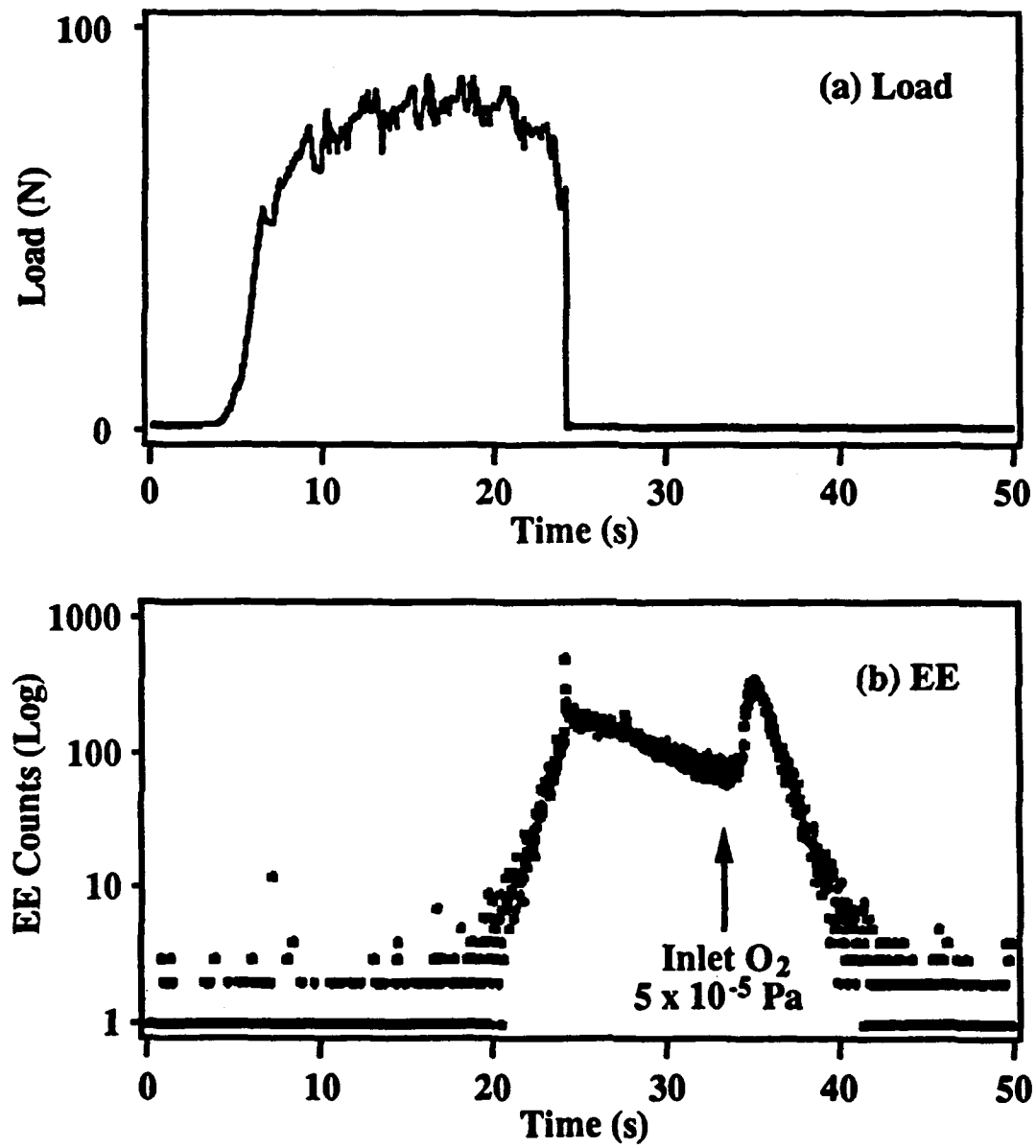
### Schematic Diagram of MOS Circuit

**FIG. 13**

### Load and Electron Emission During Loading and Fracture



**FIG. 14**

**Load and EE Intensity, Introducing Oxygen After Fracture****FIG. 15**

## Electron Emission After Fracture as a Function of Oxygen Pressure

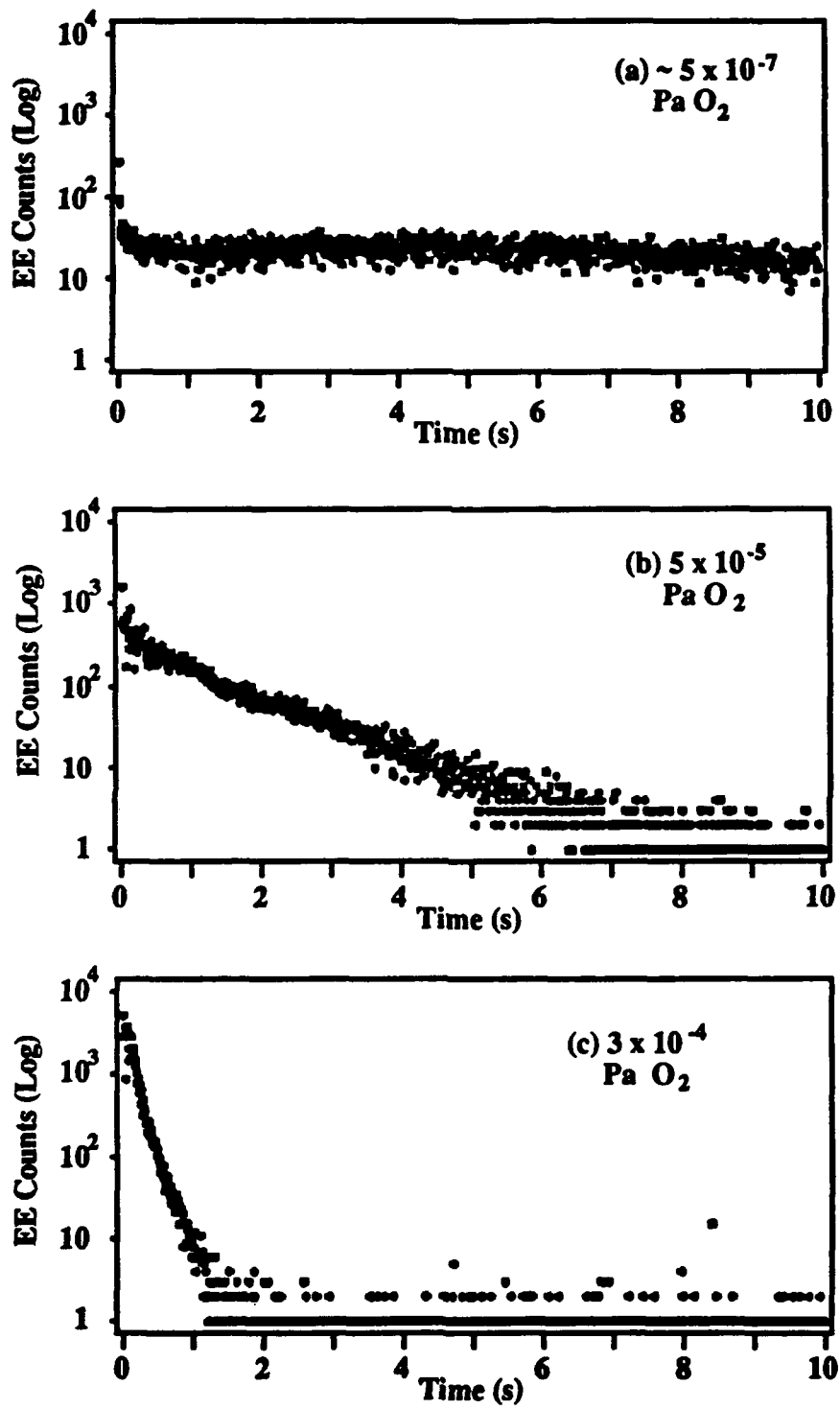
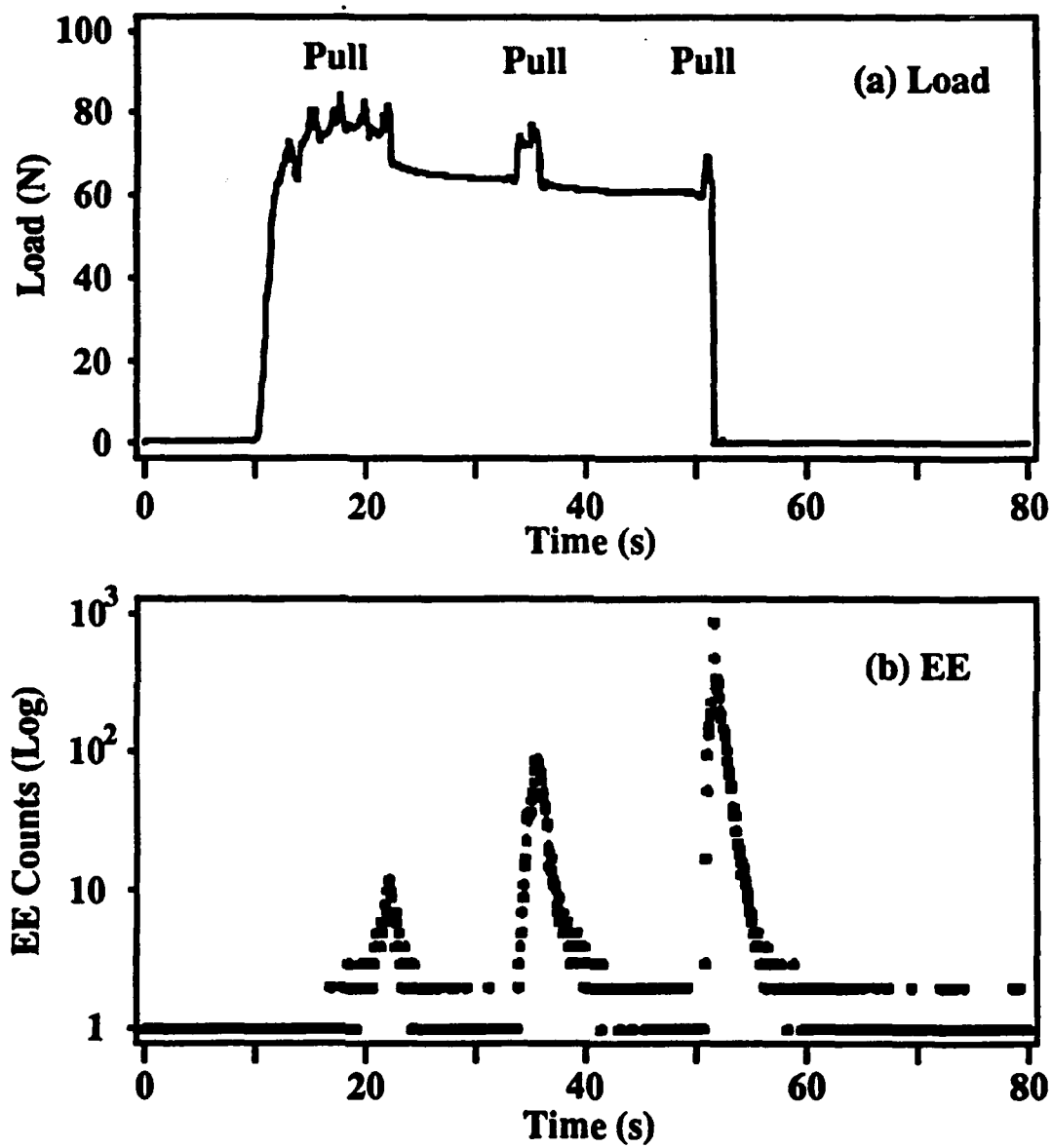
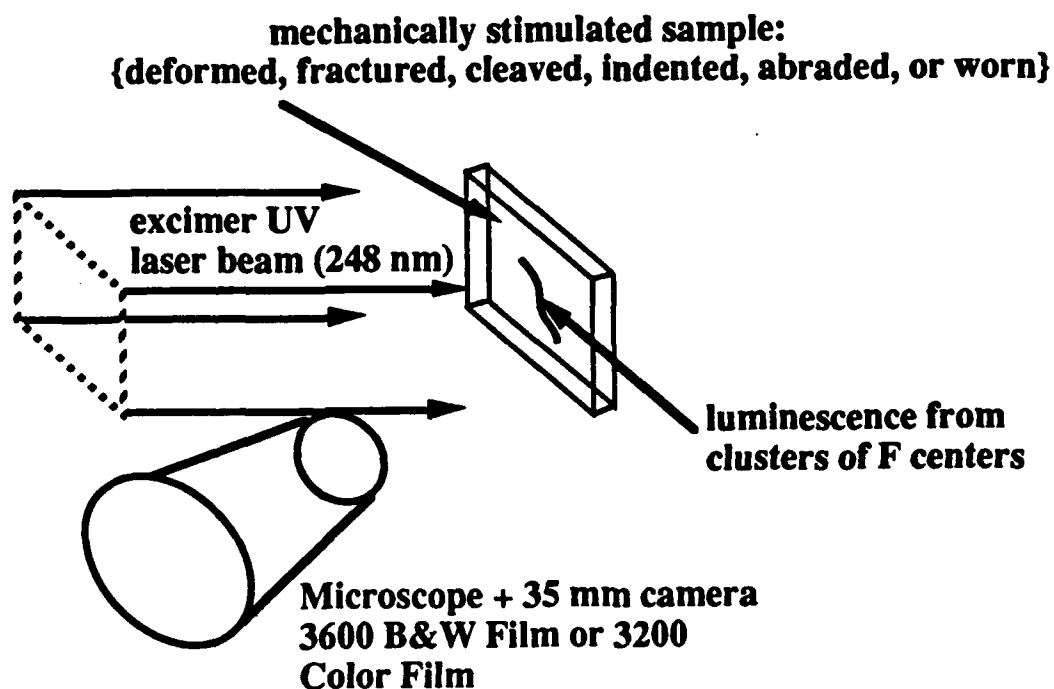


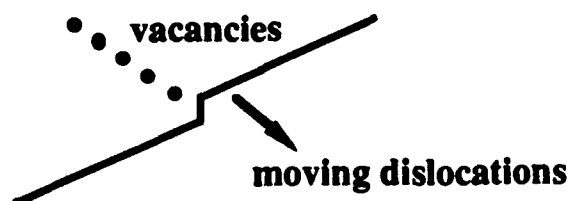
FIG. 16

**Load and Electron Emission in  $5 \times 10^{-5}$  Pa Oxygen****FIG. 17**

## System for Imaging F-Center Cluster Luminescence



**Plastic Deformation of MgO Produces Vacancies.**  
One mechanism is glide of jogged screw dislocations.



**Oxygen Vacancies + electrons  $\rightarrow$  F Centers**

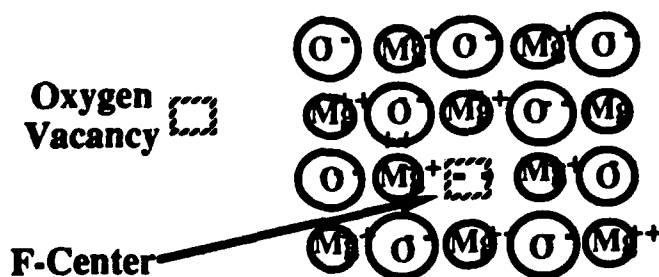
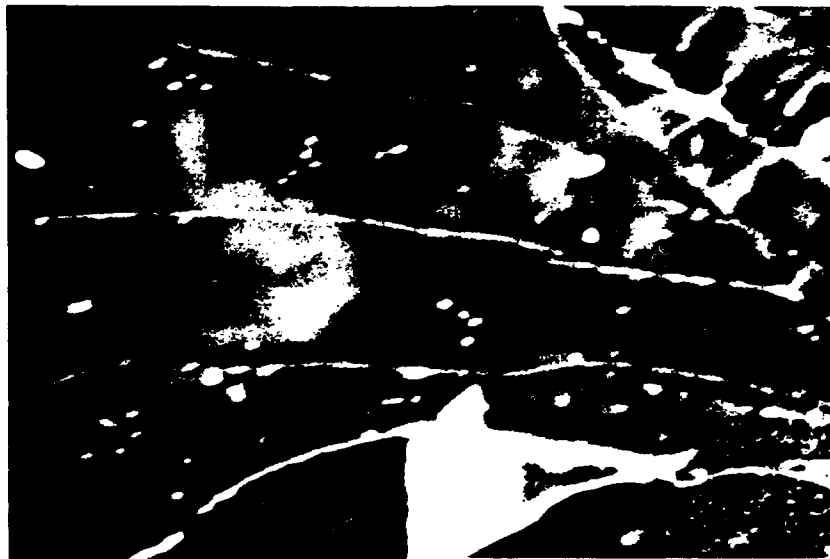


**FIG. 18**

# Imaging of Plastic Deformation in MgO with Photoluminescence



Photoluminescence (note "flap" at bottom)

100  $\mu\text{m}$



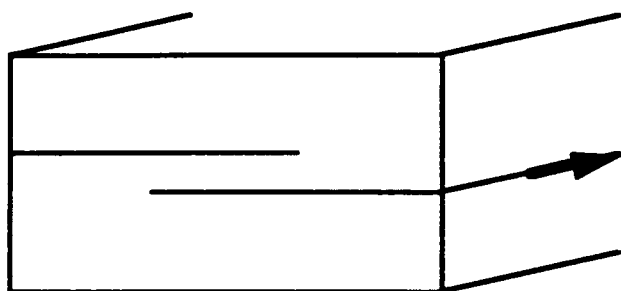
SEM of Cleavage Surface of MgO

100  $\mu\text{m}$

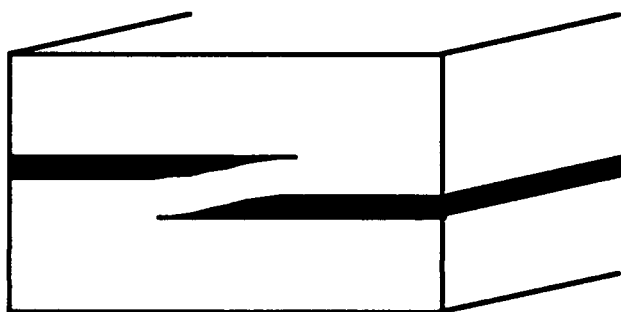
**FIG. 19**



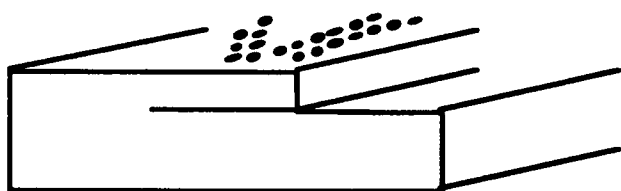
## Cleavage Step Deformation



**Steps are formed when adjacent "fingers" of advancing crack move on different planes.**



**The sliver of material between the overlapping cracks can be highly deformed before the completion of fracture.**



**The dislocations responsible for this deformation can be revealed by dislocation etchants.**

**Point defects produced by dislocation motion in MgO luminesce under UV illumination.**

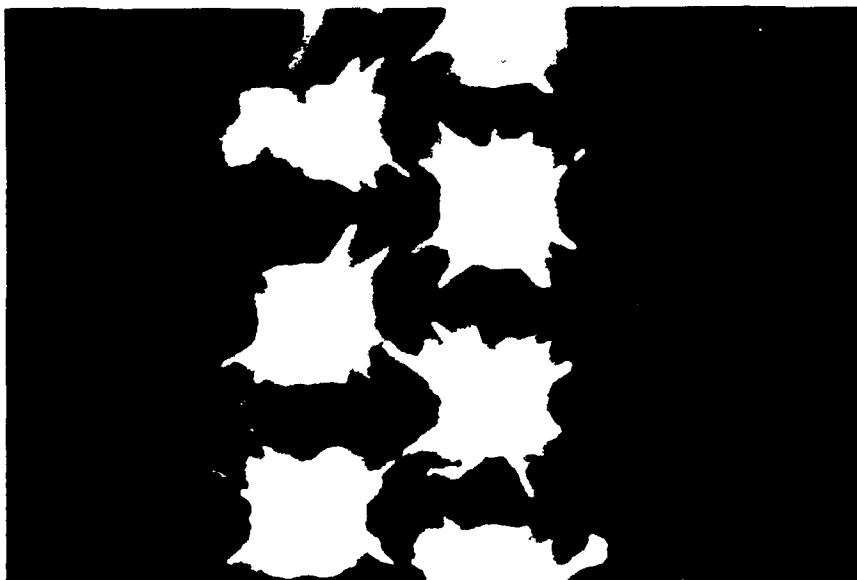
**FIG. 20**

## Photoluminescence of Indented MgO



**Cleaved (001) MgO surface  
with indentations imaged  
under white light.**

500  $\mu\text{m}$



**Luminescence resulting  
from 248 nm laser  
irradiation at <200  
mJ/sq.cm. Indentations and  
part of large cleavage step  
are seen to luminesce.**

**Fig. 21**